Undular bore development over coral reefs

An experimental study

Jochem M. Dekkers

Section of Environmental Fluid Mechanics
Faculty of Civil engineering & Geosciences
Delft University of Technology

Undular bore development over coral reefs

An experimental study

by

Jochem M. Dekkers

in partial fulfillment of the requirements for the degree of

Master of Science

in Coastal Engineering

at the Delft University of Technology,

to be defended publicly on Tuesday July 17, 2018 at 10:00 AM.

Student number:	1323881	
Thesis committee:	Prof. dr. ir. A.J.H.M. Reniers,	TU Delft
	Dr. ir. M. F. S. Tissier,	TU Delft
	Dr. ir. A. R. van Dongeren,	Deltares
	Dr. ir. J. D. Bricker,	TU Delft
	Ir. S. G. Pearson,	TU Delft

TU Delft

Preface

This thesis completes the Master of Science in Coastal Engineering at the Delft University of Technology. The past year I have spent my time at the Environmental Fluid Mechanics section, studying the fascinating phenomenon called the undular bore.

I would like to thank my thesis committee; Ad Reniers, Marion Tissier, Jeremy Bricker, Stuart Pearson and Ap van Dongeren, for their patience and constructive feedback. Thank you Marion, for your daily supervision and enthusiasm throughout the project. Thank you Stuart, for the spontaneous meetings. Thanks for everyone at the Water Laboratory: Sander de Vree for providing all the support I needed and making sure as many instruments as possible were allocated to de Lange Speurwerkgoot, Frank Kalkman for making sure the instruments were properly functioning and Arno Doorn for constructing the reef structure. Thanks go also out to my fellow students, for the interesting discussions and the countless cups of coffee.

Last but not least, I would like to thank my dear family and friends for their support. I want to thank my parents for raising the way they did, and for always giving me good advice. Thank you Koen and Thijs, my two great brothers. Special thanks go to Wanchen, for believing in me, and for always being there to support me by providing me with a myriad of different Asian snacks I did not even know existed.

Jochem M. Dekkers
Delft, July 2018

Summary

Low-lying coral reef-islands are extremely vulnerable to wave-induced flooding. Particularly, low frequency waves are known to drive significant wave run-up. Undular bores are tsunami-like breaking long waves, and feature a train of short waves at the bore front. They are frequently observed on coral reefs.

Undular bore development over fringing coral reefs is experimentally investigated in largest wave flume of Environmental Fluid Mechanics Laboratory at the TU Delft.

A series of laboratory experiments were designed for a schematized 1/20 fringing reef. Both regular and bichromatic wave experiments were carried out. Bichromatic wave experiments were not analyzed in detail in this thesis; the focus lies on the regular waves experiments. Six regular wave experiments were carried out during which cnoidal waves were generated at the wave paddle. Those were of two types:

- Swell scale: wave height of 4-8 cm for a period of 5 s in model scale, corresponding to 0.8-1.6 m for 22 seconds at prototype scale (long swell)
- IG-scale: wave height of 2-4 cm for periods of 10-20 s in model scale, corresponding to 0.4-0.8 m for 44-90 seconds at prototype scale (IG-cale)

High-resolution collocated measurements of surface elevation and velocity allowed the proper separation of incoming and outgoing wave components at 11 positions along the reef. This made a detailed analysis of wave transformation over the reef flat and run-up measurements on the beach possible.

A collocated decomposition method has been developed which takes into account the effects of nonlinearity and dispersion (non-hydrostatic pressure), and can be used for deforming waves on the reef flat. The method requires further specification of the vertical distribution of horizontal velocity. The method can be used for experimental investigation if specification is based on the Boussinesq theory (i.e. a parabolic velocity profile is assumed), whereas it can be used for non-hydrostatic model output if both the depth-integrated velocity and non-hydrostatic pressures (at the layer interfaces) are specified. The incoming and outgoing waves are given in terms of discharge or surface elevation. The method is valid up to a relative depth of $kd \approx 1$, and for nonlinear waves up to $H/d \approx 0.5$.

For all wave conditions, well-developed undular bores are observed at the beach toe. For all these cases, a train of undulations develops behind the leading front over the reef flat. The processes leading to the development of the undulations are however quite different for the different wave conditions. For the swell cases, the wave front steepens considerably on the fore-reef slope and the waves subsequently break violently at the reef crest. The breaking bore then decays progressively until it stops breaking and start forming undulations at mid reef, similar to field observations by Gallagher [Gallagher, 1972].

The IG-scale waves stay relatively symmetric about the vertical during the shoaling process on the fore-reef. The front only becomes steeper on the reef flat, and does not break turbulently for all IG-scale cases. For some cases the steepening process continues and is directly followed by formation of undulations. For the more energetic IG-scale cases the front first breaks turbulently. The rate at which the waves steepen on the reef flat depends as expected on the wave height and wave length. This is in concordance with the theory of [Stoker, 1957]; larger and shorter waves steepen faster than smaller and longer waves. Consequently, the former group starts forming undulations earlier on and features more developed undulations (larger crest elevation and deeper troughs) when they arrive at the beach.

The cross-shore evolution of the total variance clearly reflects these differences in behavior. The cases involving strong breaking (swell cases) show a rapid decrease of the variance at the outer reef flat, while the IG wave cases involving no breaking experience a slow decay of energy, most probably due to bottom and wall friction. The leading undulation is generally the largest and propagates faster than the trailing undulations due to amplitude dispersion. As a result the wave length of the undulations increases while propagating towards the beach. The leading undulation progressively separate from the rest of the wave train, and ultimately resembles a solitary wave when it arrives at the toe of the beach.

Nonlinear steepening is associated with generation of higher harmonics at a multiple of the primary frequency. The undulations are also higher harmonics, but form a secondary peak instead a tail of decreasing

energy in the spectrum. This secondary peak shifts towards lower frequencies as the undular bore travels over the reef. Morover, the reflection coefficient is larger for a larger offshore period and wave height.

The relative magnitude of HF bulk energy with respect to energy in the LF band near the beach differs per experiment. For the swell waves and IG-scale waves with smaller periods, the major part of LF energy is transferred to the HF band due to undular bore formation. For the cases that involve wave breaking, energy dissipation is, at least initially, the main mechanism for energy loss in the LF band. However, as energy decay continues and the bore becomes weaker, radiation of energy at the front by means of formation of undulations can take over this role.

The undulations break while running up the beach. The signature of the first undulations is clearly visible in the run-up signal. It is shown that the leading undulation governs maximum run-up. More specifically, we demonstrate that empirically derived formulas for the run-up of breaking solitary waves are able to predict the maximum run-up accurately, when the characteristics of the leading undulation at the beach toe are used. The solitary wave breaker parameter of [Grilli et al., 1997] should be used for parametrization of run-up for both breaking and non-breaking solitary waves.

Two types of empirical formulations were presented, of which only requires a single parameter to be estimated from data. This empirical formula, formally valid for solitary waves, can be used for run-up estimation of undular bores. Given the current fit, maximum run-up can be estimated for a given reef if the beach slope is known.

Table of Contents

List of Symbols

x	horizontal position
z	vertical position
t	time
h	total water depth, $h(x,t) = d(x) + \zeta(x,t)$
k	wave number, also used for layer number
ω	radial frequency, also used for velocity of propagation of a wave-volume element
c	propagation velocity, alternatively called wave celerity or phase speed
c_b	bore speed
c_w	propagation velocity of a breaking wave
E	wave energy
F	(wave) energy flux
F_p	external pressure-induced force
u	horizontal (particle) velocity
w	vertical (particle) velocity
U	depth-averaged velocity
U_k	layer-averaged velocity
Q	discharge (per unit width), alternatively called volume flux
Q_k	layer-averaged discharge
d	depth with respect to still water or mean water level
ζ	free-surface elevation
N_{Ursell}	Ursell number
F_r	Froude number
p	(total) pressure
q	non-hydrostatic pressure, also used for specific discharge
ψ	stream function
B	Fourier coefficients used for stream function
X	wave paddle displacement
ξ	Surf similarity parameter or Irribarren number

1 Introduction

When a long wave travels to the shore, it steepens and forms a bore. The shape of the resulting wave front depends on the complex balance between non-linearity, dispersive effects and energy dissipation. In its most common form, a bore consists of a turbulent, breaking front. However, in some cases a train of well-formed, quasi-periodic undulations develop behind the leading bore front. This type of bore is called an undular bore [Peregrine, 1966], [Treske, 1994]. A well-known example of an undular bore is the tidal bore, which forms when a tidal wave propagates in a funnel-shaped estuary in which the leading edge of the incoming tide forms an undular bore. Undular bores have also been observed near tsunami wave fronts, and during lock-exchange in channels.

In this project, we focus on the transformation of a different type of long wave, the infragravity waves, over fringing coral reefs. Reef profiles are typically characterized by a fast transition from one horizontal section with depth h_1 to another horizontal section with depth $h_2 < h_1$. Such a bathymetry is known to enhance the growth of the undulations on top of the primary long waves [Madsen and Mei, 1969]. The formation of undular bores could therefore be an important process for infragravity waves over coral reefs. As reef-fronted coastlines are particularly vulnerable to flooding Cheriton [2016], a good understanding of long wave transformation, and their potential transformation into undular bores, is crucial. [Gawehn et al., 2016] recently classified low frequency waves on coral reef flats. Progressive low frequency waves were either put in the progressive dissipative, or the progressive growing class. How important is undular bore formation, and can a shoreward decay of low frequency energy and increase in higher frequencies partly be explained by undular bore formation? A few laboratory (e.g. [Nwogu and Demirbilek, 2010]) and numerical studies [Pearson, 2016] reported the development of undular bores over the reef flat, but these were not analyzed in detail.

1.1. Problem definition & research goal

The main objective of this study is to identify the conditions under which undular bores develop over fringing reef profiles and to analyze the consequences in terms of run-up.

The following research questions are formulated:

- Under what conditions does a long wave transform into a periodic undular bore over the reef flat?
- Are undular bores important for wave-induced flooding; what are the key parameters effecting run-up of undular bores?
- How is the frequency distribution of energy changing across the reef flat?
  - Can undular bore development lead to a significant decrease in infragravity wave energy?
  - What is the spectral signature of the undulations; how can we identify an undular from the wave spectrum?

1.2. Thesis outlines

Ch. 2 starts of with a short literature review. A physical decription of undular bores is given, the concept of radiation of energy is introduced and run-up of undular bores is discussed. Ch. 3 described the experimental

setup. The fringing reef scale model design is presented, the long wave generation method is discussed and the test conditions are subsequently given. Ch. 4 discusses collocated decomposition methods and presents the techiques used in this thesis. Data processing is treated in Ch. 5. The results are discussed in 6, 7 and 8. Finally, the most important conclusions are discussed in Ch. 9, where also recommendations are given for future investigation.

2

The undular bore

2.1. Introduction

Hydraulic bores are steep propagating wave fronts, and are (for example) frequently observed on coral reef flats. Its simplest description is a transition between two different uniform flows [Peregrine, 1966], [Bjørkavåg and Kalisch, 2011]. Bores, surges and moving hydraulic jumps are synonyms. In this chapter we focus on advancing (or positive) surges (as opposed to negative, or retreating surges). Bores are formed under a variety of different circumstances and in different settings. For example in open channel flows, bores develop due to a sudden increase in discharge (e.g. during lock-exchange [Treske, 1994] or after failure of a dam). Bores may reflect against closed ends, overtake or propagate on top of other bores, or meet opposing (possibly reflected) bores.

Classical turbulent bores are well-known and well-documented. Calculations are relatively simple and quite effective; solutions follow directly from the balance principles (of mass and momentum), see for example [Chow, 1959] or Appx. B.

In the coastal setting, turbulent bores can be observed in the surf-zone due breaking of sea-swell. On the reef flat of coral reefs, bore formation is also a common phenomenon. These bore-like broken waves form not only due to turbulent breaking of swell waves, but also infra-gravity waves (and low frequency waves in general) can develop steep turbulent bore fronts. Even resonantly generated very low frequency waves deform and turn into bore-like surges (see [Gawehn et al., 2016] for a recent overview on very low frequency waves on reefs).

While turbulent bore fronts develop when the bore is strong, their less energetic counterpart is the intriguing undular bore. Undular bore formation on a coral reef flat of about one meter deep was analyzed by [Gallagher, 1972], based on photographic evidence."The nearshore topography plays a dominant role in the creation of the observed [undulations], both during and after the breaking of the incident swell on the outer reef edge", [Gallagher, 1972]. Hence the fact that undular bores are of the weaker bore class doesn't necessarily mean they should be disregarded instantly. Moreover, if a tsunami wave-front becomes sufficiently steep, it turns into an undular bore, see [Grue et al., 2008], [Madsen et al., 2008]. The relevance of undular bores on reefs will be investigated in detail during the course of this thesis, supported by the literature presented in this chapter.

Section **??** starts with the classification of bores based on the bore strength, which has been pioneered by [Favre, 1935] trough physical model testing. Section 2.3 gives a physical description of the formation of an undular bore. Curvature of the free surface and deviations from the hydrostatic pressure distribution (due to vertical accelerations) at the wave front seem to be inextricably linked with the formation of undulations [Peregrine, 1966], [Soares Frazao and Zech, 2002]. On a different note, it is commonly said that as waves or bores break in a dispersive manner, excess energy is radiated away from the wave-front by formation of undulations. Section 2.4 introduces the concept of radiation of energy using the theory of [Lemoine, 1948] supplemented with key observations by [Benjamin and Lighthill, 1954] and [Ali and Kalisch, 2010]. The impact of tsunami's has contributed to the vast amount of literature available on undular bores, which is shortly discussed in section 2.5.

2.2. Classification of bores

Citing [Treske, 1994], systematic experimental investigation on undular bores was first done by [Favre, 1935], who studied the behavior of bores in a long rectangular flume. Favre classified bores propagating in based on bore strength; the ratio of the water depth increment (the difference between mean upstream depth and the undisturbed depth downstream, $\Delta h = h_1 - h_0$) and the initially undisturbed water depth (h_0). On the extremes, the bores can be either purely undular ($\Delta h/h_0 < 0.28$), characterized by a smooth but wavy transition between the undisturbed water and the upstream flow, or fully turbulent ($\delta h/h_0 > 0.5$ to 0.75) with a highly turbulent roller at the front and a flat back. The intermediate regime has features of both; smooth trailing undulations, with one or more leading undulations breaking at the front.

The Froude number defines the type of bore (undular, transition, or turbulent). This has been used extensively in experimental research on undular bores [Favre, 1935], [Binnie and Orkney, 1955], [Wilkinson and Banner, 1977], [Treske, 1994], [Soares Frazao and Zech, 2002], [Koch and Chanson, 2008]. For example, relevant quantities for undular bores, such as amplitude a_w (of the first undulation) and wave length L_w (the distance between the first two crests) are often plotted against the Froude number (or bore strength r). Favre's $r = 1.28$ (or $\Delta h/h_0 = 0.28$) corresponds to $F_{r,1} = 1.21$, while the value for the transition between undular turbulent and fully turbulent by Binnie and Orkney [1955], $r = 1.75$, gives $F_{r,1} = 1.55$. In the same manner, measurements can be compared against analytical solutions (e.g. the theory of [Lemoine, 1948], see next section), or they can be used to validate numerical models (see [Soares-Frazão and Guinot, 2008] or [Tissier, 2011]).

Furthermore, classification of bore strength is often based on Froude number, which follows from the classical turbulent bore problem, which is presented for convenience in Appx. B.

2.3. Physical description of the formation of an undular bore

2.3.1. Deviation from hydrostatic pressure

The initial formation and further development an undular bore can be described and modeled by means of the balance equations of mass and momentum. By inclusion of a dispersion term in the model equations (resulting in Boussinesq-type of equations), Peregrine [1966] was able to take "the effect of vertical acceleration of the water on the pressure" into account. Quoting [Soares Frazao and Zech, 2002], "The growth of an undular bore is due to the free-surface curvature, inducing extra horizontal pressure gradients as a consequence of the vertical acceleration of the water".

The deviation of pressure from a hydrostatic pressure distribution is commonly referred to as non-hydrostatic pressure. Because non-hydrostatic pressure plays a crucial role in the formation and growth of undular bores, a suitable set of model equations to describe the initial formation process are the nonlinear shallow water (NLSW) equations *including non-hydrostatic pressure*. The NLSW equations form the governing set of equations of non-hydrostatic models such as SWASH [Zijlema et al., 2011] and XBeach-NH, which are frequently applied in reef hydrodynamics studies (see e.g. [Zijlema, 2012], [Pearson, 2016]), and might be familiar to the target audience of this thesis. These equations will used in this section to support the physical interpretation, which aided by a SWASH simulation. For a description of the model, the reader is referred to [Zijlema et al., 2011]. For a short introduction to the non-hydrostatic model equations, the reader is referred to Appx. A.

The competing forces acting on the fluid ultimately determine the transformation of a long wave into an undular bore, and it is therefore useful to cover the most important contributions in detail. Instead of considering a balance in every point in the fluid, the mass and momentum equations are integrated over depth. The depth-integrated NLSW equations can be written as:

$$\frac{\partial \zeta}{\partial t} + \frac{\partial Q}{\partial x} = 0 \tag{2.1}$$

$$\frac{\partial Q}{\partial t} + \underbrace{gd\frac{\partial \zeta}{\partial x}}_{F_0} + \underbrace{\frac{\partial}{\partial x}\left(\underbrace{\frac{Q^2}{h}}_{M_a} + \underbrace{\frac{1}{2}g\zeta^2}_{M_g} + \underbrace{\frac{1}{2}\frac{q_b}{\rho}h}_{M_q}\right)}_{\Delta F = F_a + F_g + F_q} = 0 \tag{2.2}$$

$$q_b = \frac{1}{2}\rho h \frac{\partial w_\zeta}{\partial t} \tag{2.3}$$

For simplicity, the bottom is assumed to be flat (which seems reasonable, since undular bores are formed on the reef flat). The horizontal momentum balance (Eq. 2.2) states that the flow is accelerated by horizontal

pressure gradients, which are here split in hydrostatic ($F_0 + F_g$) and non-hydrostatic pressure (F_q) contributions. From the depth-integrated continuity equation, it can be determined how the resulting flow leads to deformation of the free surface — it is after all the continuously deforming wavy free surface that defines the undular bore.

Eq. 2.3 is essentially the vertical momentum equation. If the vertical hydrostatic balance is substracted, the vertical momentum equation reduces to a balance between vertical non-hydrostatic pressure gradient and vertical acceleration. Eq. 2.3 is the depth-integrated version of this reduced vertical momentum equation. Because non-hydrostatic pressure and vertical acceleration are assumed to vary linearly over depth, non-hydrostatic pressure at the bottom can be directly linked to vertical acceleration at the surface. The concept that a "horizontal non-hydrostatic pressure gradient induces "additional" horizontal acceleration of the flow, and, by continuity (Eq. 2.1), associated gradients in the flow result in "extra" deformation of the surface" now hopefully becomes more credible.

In the next sections, for a simple discharge wave, the mechanism initiating the formation of an undular bore is demonstrated and explained using Eq. 2.1 - 2.3.

2.3.2. A wave of positive elevation & steepening of the front

The textbook example to demonstrate undular bore formation uses a gentle transition between uniform flow and still water as the initial waveform (see e.g. [Peregrine, 1966], [Wei et al., 1995], [Soares Frazao and Zech, 2002] or [Tissier et al., 2011b]). [Keulegan and Patterson, 1940b] note that such a surge may also be generated by a rise in discharge at either ends of a flume. A discharge wave is here generated by imposition of a hyperbolic tangent boundary condition at the left boundary of the computational domain:

$$U(0,t) = \frac{1}{2}U_1\left(1 + \tanh\left(a\left(t-b\right)\right)\right) \tag{2.4}$$

where U_1 is the final uniform upstream depth-averaged velocity, calculated using Eq. B.9. $a = 2\pi/T$, where T is the characteristic time scale of the front. T is taken sufficiently large to ensure a gentle flow increase ($T = 10$ s) such that vertical acceleration is negligible and the pressure distribution is practically hydrostatic. At $t = b$, the center of the front passes, i.e. $U(0,t) = \frac{1}{2}U_1$ at $t = b$. b is taken equal to T. From the toe up to the center, the resulting profile is convex (◟), while the higher elevated portion of the profile is concave (◝).

Because the horizontal length scale is much larger than the depth, the pressure distribution is hydrostatic and velocity is uniform over depth; the motion can initially be described by the shallow water equations. As shown by Airy almost two centuries ago, the front of any wave of elevation described by the shallow water equations will steepen and ultimately break. This is due to nonlinear effects; i.e. the combined effects of advection and the nonlinear contribution due to hydrostatic pressure.

Of special interest is the flow region near the front of wave; it is there where the first undulation is formed. Long before a wave breaks, long wave theory breaks down. At a certain moment, as the surge travels across the flume, the front is sufficiently steep so that dispersive effects ($\mu^2 = {h_0}^2/L^2$) and nonlinear effects ($\epsilon = \Delta h/h_0$) become of comparable magnitude [Peregrine, 1966]. In other words, from that moment on, vertical acceleration cannot be neglected and non-hydrostatic pressure has to be taken into account in the SWASH simulation.

Fig. 2.1 shows snapshots of the free surface near the bore front, taken at consecutive moments in time. While dispersion might initially be small compared to nonlinearity, after traveling some distance across the flume, the accumulated effect of dispersion manifests as additional deformation of the free surface (Fig. 2.1a). To highlight this, the results of the non-hydrostatic simulation (SWASH) is compared with an analytical solution to the NLSWE (hydrostatic).

Method of characteristics

The NLSWE are solved using the method of characteristics (MoC), see Appx B. Alternatively, an additional SWASH simulation could have been carrier out, identical to the first but without resolving the vertical momentum balance. The tangent hyperbolic velocity boundary condition is used to calculate the characteristic curves issued from the boundary (Eq. B.25). The free surface elevation (calculated using Eq. B.26) is shown up to the time step just before the front becomes vertical (Fig. 2.1g). Physically, this represents turbulent wave breaking, but it is also referred to as gradient catastrophe or breaking of the hyperbolic kind [Whitham, 1974]. It can be seen from Fig. 2.1g), that just before breaking, the rate of change in time of the free surface ($\partial_x \zeta_{MoC}$) approaches infinity near the front.

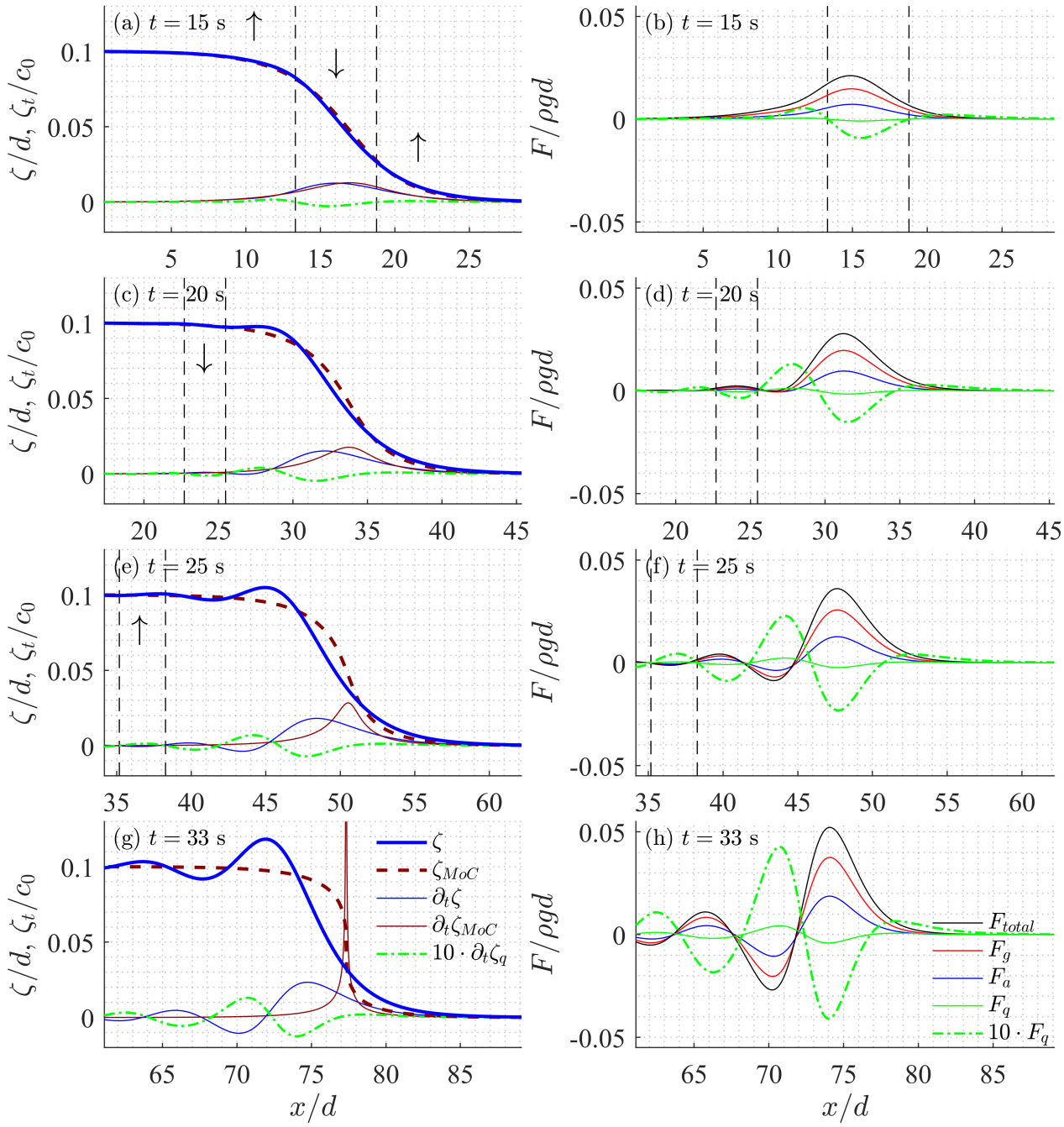

Figure 2.1: Formation of the initial wave. The left plots shows (quantities related to) the free surface elevation: (solid blue line) free surface elevation (SWASH), (dashed dark red) free surface elevation (MoC), (thin blue line) rate of surface rise (SWASH), (thin red line) rate of surface rise (MoC), (dash-dotted green line) rate of surface rise due to non-hydrostatic pressure (SWASH). The right subplots show the magnitude forcing terms due to: (red) advection, (blue) gravity or hydrostatic pressure, (dash-dotted green) non-hydrostatic pressure, (black) F_{total}.

2.3.3. Vertical acceleration & formation of the initial undulations

In reality, turbulent breaking of the front only happens if the bore is strong; i.e. if nonlinearity is dominating over dispersion. Non-hydrostatic pressure has a stabilizing effect which effectively postpones the onset of breaking [Smit et al., 2013]. For weak bores this is large enough to prevent turbulent wave breaking at all from happening. Instead, an undular bore breaks in a dispersive manner, which can be referred to as dispersive wave breaking. It is said that energy is carried away by the undulations forming behind the bore front, rather than dissipated through turbulent breaking [Benjamin and Lighthill, 1954]. By evaluating both the forcing terms (Fig. 2.1b,d,f,h) and the resulting deformed free surface (Fig. 2.1a,c,e,g) near the front, this mechanism can be investigated in detail, see also [Peregrine, 1966] and [Soares Frazao and Zech, 2002].

From the figure it can be seen that "additional elevation" is present where the horizontal non-hydrostatic pressure gradient is positive. Since curvature seems to be a good proxy for non-hydrostatic pressure, this is approximately where the curvature of the free surface decreases. The free surface is lowered (a relative depression compared to a hydrostatic flow computation) where the horizontal non-hydrostatic pressure gradient is positive.

[Madsen and Mei, 1969] note that Peregrine's stepped bore (with horizontal back) is actually the limiting case for all kinds of undular bore-like phenomena where steepening of the front and flattening of the back occurs prior to disintegration, and therefore the physical interpretation given by Peregrine should hold universally.

2.3.4. Further growth of the undulations

In the previous section, depth-integrated forces and the resulting surface deformation were discussed up to the breakpoint. Results of a hydrotatic and non-hydrostatic computation were shown alongside each other. In this section, the non-hydrostatic simulation is continued to see how the undulations further develop. The flow is be partitioned according to the contribution momentum fluxes. The discharge (per unit width, i.e. volume flux) is used for this purpose, and is calculated using Eq. D.48:

$$Q = \underbrace{c_0\zeta}_{Q_0} + \underbrace{\frac{1}{2c_0}\left(\underbrace{\frac{Q^2}{h}}_{M_a} + \underbrace{\frac{1}{2}g\zeta^2}_{M_g} + \underbrace{\frac{1}{2}\frac{q_b}{\rho}h}_{M_q}\right)}_{\Delta Q = Q_a + Q_g + Q_q}$$

This approximation is essentially due to Boussinesq (although here based on the non-hydrostatic equations), and is valid for a disturbance propagating in an undisturbed shallow layer of water. $Q_0 = c_0\zeta$ is the familiar expression for the discharge of a long wave of negligible height, and is due to hydrostatic pressure (or gravity). ΔQ is assumed to be small with respect to Q_0, and takes the effects of nonlinearity and dispersion into account. Specifically, the considered contributions to ΔQ are due to:

- Q_g — hydrostatic pressure (nonlinear part)
- Q_a — advection of momentum
- Q_q — non-hydrostatic pressure (due to vertical acceleration)

Fig. 2.2 shows the contributions at several time instances. The shaded areas represent the mentioned flow contributions. Q_{Airy} and $Q_{\text{Boussinesq}}$ are combinations of these flow contributions, and are here defined by:

- $Q_{\text{Airy}} = Q_0 + Q_a + Q_g$
- $Q_{\text{Boussinesq}} = Q = Q_0 + \Delta Q = Q_{\text{Airy}} + Q_q = Q_0 + Q_a + Q_g + Q_q$

As mentioned earlier, the effects of advection and gravity both contribute to "additional" flow. Because the free surface is largest near the crests of the undulations, these contributions are largest there. In contrast, non-hydrostatic pressure is linked to vertical acceleration, which does not always work in the same direction. Non-hydrostatic pressure is negative near the concave crests, and positive near the convex parts of the profile. At the toe of the surge and in the troughs between the crests of the undulations, non-hydrostatic pressure "enhances" the effects of advection and the non-hydrostatic pressure force, while near the crests of the undulations — where advection and gravity are largest — it causes a "reduction" in discharge.

Any local section of the undular bore, defined such that the volume ahead of it stays constant, moves with the speed $\omega = Q/\zeta$ (see Appx. D). Due to the stabilizing effects of non-hydrostatic pressure, there is a

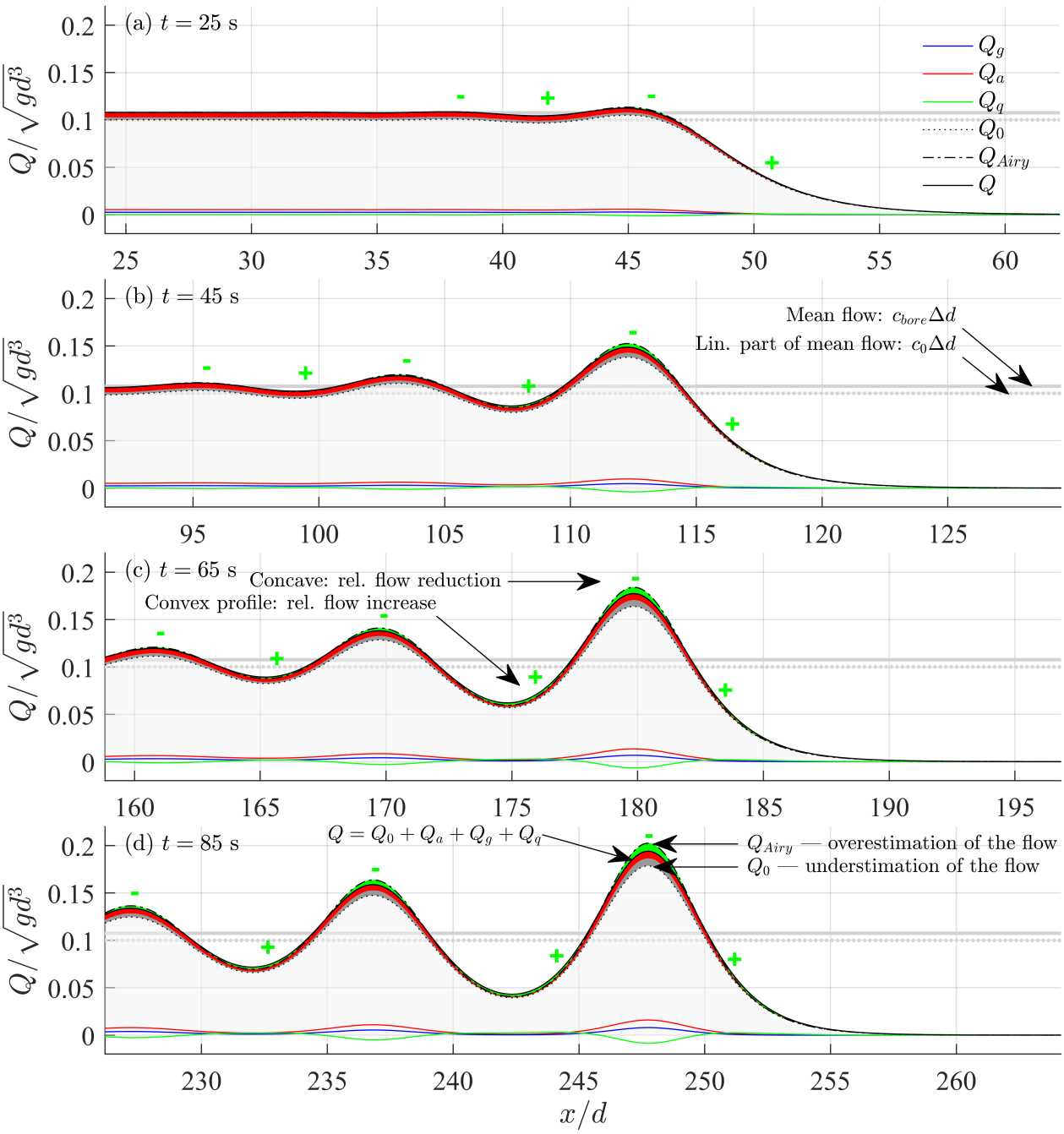

Figure 2.2: Further development of the undular bore in terms of the state variable discharge. The total discharge is partitioned into the following contributions due to: (blue) gravity, (red) advection, (green) non-hydrostatic pressure. The flow is reduced where the profile is concave (-) and increased where the profile is convex (+). Linear theory (Q_0) underestimates the total flow, whereas Q_{Airy} overestimates the discharge due inclusion of non-linear effects ($Q_a + Q_g$) but omission of dispersive effects (Q_q). The shaded areas show the incremental contributions.

tendency for ω to become constant as the undular bore continues to propagate. If $\partial_x \omega = 0$, all sections move with the same constant speed. "There is only one steady translational solution with still water in front of a wave, that is the solitary wave" [Peregrine, 1966]. [Peregrine, 1966] suggest that "The most likely behaviour for an idealized inviscid bore is that the leading waves slowly draw away from each other, so that the bore tends to become a succession of solitary waves".

2.4. Radiation of energy

For a strong turbulent bore, in the ideal case where it is schematized as a discontinuity (or shock wave), [Rayleigh, 1914] fount that by conservation of mass and momentum across the bore (using the de Saint-Venant equations), energy must be dissipated at the bore discontinuity (see also Appx. B). In reality, this energy is dissipated through the turbulent motion at the bore front. The shallow water equations and classical bore theory are presented in Appx. B.

In an undular bore, energy is assumed to be radiated away through undulations forming behind the bore front, rather than dissipated through turbulent motion at the front. This is especially important since this wave train is present in all but very strong bores [Benjamin and Lighthill, 1954]. According to [Benjamin and Lighthill, 1954] the wave-train absorbs almost the entire amount of energy "otherwise liberated at the bore" (the dissipation found by Rayleigh) [Benjamin and Lighthill, 1954]. They studied the first undulation of an undular bore and found that it closely resembles a solitary wave. Furhermore they showed that a solitary wave is the only form where mass, momentum and energy are preserved, and if energy is lost at the first wave of an undular bore, it must wave must be of cnoidal type.

[Ali and Kalisch, 2010] studied the energy loss in undular bores and concluded that there is no energy loss if dispersion is accounted for. The net influx of energy, lost at the bore front in the classical situation (calculated by Rayleigh using the shallow water equations), equals the production of energy through generation of dispersive waves (calculated using dispersive theory) [Ali and Kalisch, 2010]. For a undular bore, according to Ali and Kalisch [2010], the rate of change of energy (in a control volume surrounding the undular bore) is equal to the net influx of energy. An undular bore conserves energy (one could say that D_b is accounted for through formation of undulations).

Lemoine [1948] already implicitely assumed that an undular bore conserves energy at the front, and provided a practical solution for characteristics of secondary wave field. Lemoine's approach relies heavily linear wave theory and on the classical turbulent bore description. While not able to describe the initial formation or the further development of an undular bore, the theory of Lemoine [1948] provides a practical description of the energy budget of undular bores using concepts familiar to most coastal engineers.

2.4.1. Undular bore theory [Lemoine, 1948]

Lemoine [1948] was the first to derive an analytical expression for both the wavelength and amplitude of the leading undulation, assuming linear wave theory. He made the following assumptions in order to derive analytical expressions for a_w and L_w for an undular bore:

1. Relations derived for a classical turbulent bore (see Appx. B) are still valid for an undular bore, provided that the mean motion is considered.
2. The undulations propagate at the same speed as the bore front c_b.
3. Furthermore, the undulations are small enough (a_w small w.r.t. h_1 and L_w) such that linear wave theory can be used (in the reference frame moving with the flow; i.e. with respect to u_1).

The phase velocity (in the reference frame moving with u_2) is given by:

$$c_p = \frac{\omega}{k} = \sqrt{\frac{g}{k}\tanh(kh_2)}, \qquad k = \frac{2\pi}{L_w} \tag{2.5}$$

Similarly, group velocity c_g in the same reference frame can be written as:

$$c_g = \frac{\partial \omega}{\partial k} = \frac{1}{2}\left(1 + \frac{2kh_1}{\sinh 2kh}\right)c_p = nc_p \tag{2.6}$$

In an absolute, or fixed frame of reference, the undulations propagate at speed:

$$c_{p,\text{abs}} = c_p + u_1 \tag{2.7}$$

Now, making use of assumption (2), the absolute phase speed of the undulations is equated to the absolute bore speed:

$$c_{p,\text{abs}} = c_b \tag{2.8}$$

The classical bore speed (the velocity of propagation of a moving hydraulic jump) is given by:

$$c_b = u_1 + \sqrt{g\frac{h1+h0}{2}\frac{h_0}{h_1}} \tag{2.9}$$

see Appx. B. By subsitution of 2.7 and 2.9 in 2.8, we obtain:

$$\frac{L_w}{h_1}\tanh\left(h_1\frac{2\pi}{L_w}\right) = \pi\frac{h_0}{h_1}\left(1+\frac{h_0}{h_1}\right) \tag{2.10}$$

from which the wave length of the undulations can be easily calculated (given certain values for upstream and downstream water levels, h_2 and h_1, respectively). The amplitude a_w follows from an energy balance. The energy radiated away from the front by the undulations, P_{radiated}, is assumed to be equal to the dissipation rate of a bore, denoted by D_b:

$$P_{\text{radiated}} = D_b \tag{2.11}$$

The Rayleigh dissipation was given in Appx. B (Eq. B.17), and repeated for convenience:

$$D_b = \frac{1}{4}\rho g\sqrt{\frac{g\,(h_0+h_1)}{2h_0h_1}}(h_1-h_0)^3 \tag{2.12}$$

In concordance with linear wave theory (see e.g. [Holthuijsen, 2007]), energy is solely transported by the work done by wave-induced pressure. The energy transport (or energy flux) is given by:

$$P_{\text{energy}} = \overline{\int_{-h}^{0} p_w u dz} = \left(\frac{1}{2}\rho g {a_w}^2\right)\frac{1}{2}\left(1+\frac{2kh_1}{\sinh 2kh_1}\right)c_p = Enc_p = Ec_g \tag{2.13}$$

a net time-averaged transport of energy in propagation direction. The energy radiated away from the front is associated with the undulations in the frame of reference moving with the bore front:

$$P_{\text{radiated}} = Ec_{g,\text{front}} = \frac{1}{2}\rho g {a_w}^2 c_{g,front} \tag{2.14}$$

The group velocity with respect to the bore speed is:

$$c_{g,\text{front}} = c_{g,\text{abs}} - c_b \tag{2.15}$$

and the group velocity in a fixed frame of reference is given by:

$$c_{g,\text{abs}} = c_g + u_1 \tag{2.16}$$

thus the group velocity at the front can be related to the bore speed and the group velocity in reference frame moving with u_1:

$$c_{g,\text{front}} = c_g + u_1 - c_b \tag{2.17}$$

Again we use assumption (2) ($c_b = c_{p,\text{abs}}$):

$$c_{g,\text{front}} = c_g + u_1 - (c_p + u_1) = c_g - c_p \tag{2.18}$$

Substituting the expressions for c_g and c_p in equation 2.18, we get:

$$c_{g,\text{front}} = (n-1)\,c_p = \frac{1}{2}\left(\frac{2kh_1}{\sinh(2kh_2)}-1\right)c_p \tag{2.19}$$

Subsequently, subtituting this expression for c_g in equation 2.14, to get a final expression for the radiation of energy due to the undulations, and using the energy balance (equation 2.11) equating this radiation to the Rayleigh dissipation rate D_b yields:

$$\frac{1}{4}\rho g {a_w}^2\left(\frac{2kh_1}{\sinh(2kh_1)}-1\right)c_p = \frac{1}{4}\rho g\sqrt{\frac{g\,(h_0+h_1)}{2h_0h_1}}(h_1-h_0)^3 \tag{2.20}$$

Finally, an expression for the amplitude is given by:

$$\frac{a_w}{h_1} = \frac{h_1 - h_0}{h_1}\left(\frac{h_1 - h_0}{h_0}\right)^{\frac{1}{2}}\left(1 - \frac{2kh_1}{\sinh(2kh_1)}\right)^{-\frac{1}{2}} \tag{2.21}$$

Several authors have discussed and build upon the work of Lemoine using steady wave theories, such as [Benjamin and Lighthill, 1954] using cnoidal theory, and [Wilkinson and Banner, 1977] using the integral flux equations by [Whitham, 1962] that correspond to second order Stokes theory [Sobey and Dingemans, 1992].

The approach of [Sobey and Dingemans, 1992] is especially interesting. Like Lemoine, it is assumed that the the flow is steady and uniform near the bore front (which seems reasonable, looking at Favre's results). Their "rapidly varried flow analysis" of is based on the (exact) integral flux equations for mass, momentum and energy, which are expressed in terms the water depth, the uniform current, and familiar integral properties of the wave field such as the mass flux, radiation stress, kinetic energy, potential energy, and energy flux [Sobey and Dingemans, 1992], see also Appx.G. The problem is transformed to a reference frame moving with the bore front. Like Lemoine, the undulations are assumed to be trapped on the subcritical flow, and move with the bore speed. Shock conditions are formulated, which form the system to be solved. Based on their observation that the mean terms, corresponding to the mean flow, dominate over the wave-related parts, they split the set of equations to be solved in a Rayleigh balance (the turbulent bore problem) and a residual balance (corresponding to a radiated wave related part and wave-current interaction terms). The integral properties are given in terms of integral parameters (given by [Longuet-Higgins, 1975]), such as the wave phase speed, the free surface stream function, and the Bernoulli constant. Only then they choose the desired (steady) wave theory (which provides expressions for the integral parameters) and the dissipation model. Hence up to specification if these integral parameters, the analysis is independent of the chosen wave theory. Higher order Stokes theory is used in their comparison with experimental data, but it is Fourier theory (stream function theory) is proposed as the most appropriate theory. Choosing the formulation independent of steady wave theory is motivated by experimental evidence which suggests that undular bores occur in transitional water depths, and observed amplitudes are quite large (with respect to depth). In other words, small amplitude shallow water theory might not be appropriate.

[Sobey and Dingemans, 1992] comment on the work by Lemoine and Wilkinson, that even though their solutions match observations well, their set of equations not consistent with the set of integral flux equations. Only by including dissipation they should have obtained a solution. Instead, a slight inconsistency in their equations allowed them to obtain a solution without any form of dissipation. Whether or not this is true remains unclear (to the author), since there seems to be no broad consensus on this matter. However, in the approach of [Lemoine, 1948], no energy balance needs to be considered to obtain an expression for the wavelength (it directly follows from the trapped wave condition (2)); hence Eq. should be unaffected by the mentioned inconsistency in the formulation of the problem. In this thesis we will settle with the theory of [Lemoine, 1948] because:

- the theory agrees reasonably well with observations,
- it explains the concept of radiation of energy through formation of secondary waves (the undulations),
- it does so using concepts familiar to most coastal engineers (bore theory and linear wave theory).

Where necessary, the analysis of the experimental results can be augmented with SWASH simulations. Since SWASH is based on the full balance equations for mass and momentum, it does not have any of restrictions of steady wave theory or small amplitude shallow water theory; SWASH allows for time and space varying solutions of highly non-linear waves in intermediate water depths.

The most important thing relevant for coastal engineering is that most energy is not dissipated at the bore front, but radiated away from front through the undulations. These undulations might be observable in the wave spectrum as energy at higher frequencies, which under investigation.

2.5. Run-up of undular bores on reef-fronted beaches

Coastal flooding of reef-fronted beaches due to run-up of infragravity and very low frequency waves has been investigated by numerous authors REF. In general, most reef hydrodynamics studies focus on energy transfer from waves the incident wave band to low frequency waves, or the resonance phenomenon, see for example [Gawehn et al., 2016].

Run-up predictions are often based on spectral estimates of key wave parameters; either offshore or local estimates. It is most often implicitly assumed that waves have a sinusoidal shape. [Gawehn et al., 2016] however mention that very low frequency waves for which energy increases over the reef flat, most of the time appear as bore-shaped waves in time series. It was suggested that these bores most likely have a larger impact on the shoreline than sinusoidal waveforms.

Run-up of waves on a fringing reef has been experimental studied, see for example [Demirbilek et al., 2007] and the follow-up study [Nwogu and Demirbilek, 2010]. While it was mentioned in [Nwogu and Demirbilek, 2010] that undular bores appear on the reef flat, their potential relevance regarding run-up was not investigated.

To predict coastal flooding and point out the key variables,[Pearson, 2016] and [Pearson et al., 2017] recently investigated run-up on reef-fronted beached using a numerical model, which was validated based on the data of [Demirbilek et al., 2007]. The run-up results were analysed using a probabilistic model (a Bayesian network). Using the Bayesian network [Pearson et al., 2017] found information on water levels and waves to be most important, followed by the reef width. [Pearson, 2016] suggested that a subsequent study should clarify whether undular bores lead to greater run-up and flooding than their turbulent counterpart.

Empirical parametrizations for run-up of ocean waves on beaches involve estimation of both wave-induced setup and the local spectral estimates (i.e. on the inner reef flat) based on offshore conditions, see e.g. [Stockdon et al., 2006]. In contrast, tsunami run-up prediction studies are concerned with the detailed description of wave transformation process over the continental shelve, and finding a suitable prototype wave, which can then be used for further run-up studies [Madsen et al., 2008]. Furthermore, the run-up of tsunamis on a beach is usually treated as a deterministic process, while run-up of a spectrum of waves on natural beaches is assumed to be a stochastic process. Hence the use of a run-up exceeding value (i.e. $R_{2\%}$). However, in both cases, the surf-similarity seems to be the key parameter to translate local wave conditions into run-up (see e.g. [Fuhrman and Madsen, 2008]).

In this thesis the focus lies on understanding the run-up process for given undular bores on the inner reef flat. Below follows an overview of run-up related research, relying heavily on tsunami theory.

2.5.1. Run-up of classical undular bores

Run-up of undular (and turbulent) bores was first systematically investigated by [Miller, 1968], and later by [Yeh et al., 1989]. In these experimental investigations, bores were studied with a large range of Froude numbers (and thus also included intermediate and turbulent bores). [Miller, 1968] made several key observations on the run-up of undular bores. While (for a given slope) dimensionless run-up (R/h_0) of purely undular and fully developed turbulent bores almost linearly depends on the Froude number (or h_1/h_0), there is a distinct transition zone for intermediate bores (i.e. breaking undular bores). The lower bound of this transition zone coincides with the "abrupt drop in height and celerity that follows the first appearance turbulence on the leading undulation" (the transition between the purely undular and intermediate bore region, $h_1/h_0 \approx 0.28$).

[Miller, 1968] states that the maximum run-up is "achieved by the second or third undulation, rather than by the leading undulation". However, it has to be noted that, for [Miller, 1968], the horizontal section (between the wave plate attached to the piston and the beach toe) is in the order of three depths h_0, hence the undular bores studied are most likely not fully developed (i.e. the leading undulation is far from a solitary wave). The same hold for the experimental setup by [Yeh et al., 1989]; the gate is placed almost directly against the start of the slope.

2.5.2. Run-up of tsunami waves

While a great deal can be learned from run-up of positive surges, in relatively few experimental investigations feature a large horizontal sections (think reef flat). These experiments are most likely designed with a sandy beach type of setting in mind, where sea-swell waves break and evolve into (periodic) bores on the beach. As mentioned before, bores have been observed on the reef flat. The observation that (undular) bores develop before they reach the beach should thus be taken into consideration. There are few run-up experiments akin to the those of Favre, where the positive surge has sufficient space to develop significant undulations.

In other words, the first questions that need to be answered are: under what initial wave conditions and for what geophysical scales do long waves transform into an undular bores over the reef flat. Subsequently, it should be investigated what a suitable prototype wave is in order to systematically study run-up.

Prototype wave and geophysical constraints

While the relevance of the solitary wave paradigm was questioned by [Madsen et al., 2008] for tsunamis due to geophysical constraints, here it is hypothesized that the solitary wave might still be a viable mathematical model for run-up of the leading undulation on a reef-fronted beach.

Solitary waves

Here, solitary wave solutions are presented. Solitary waves are waves with appreciable height and curvature, which are propagated with no deformation (i.e. they are of constant form). Such an infinitely long shallow water wave, that is elevated entirely above the undisturbed water level, was already observed by Scott Russell in 1834 in a real channel [Svendsen, 2006]. Solitary waves are the result of a balance between dispersion and nonlinearity, and "can travel considerable distances without appreciable deformation, a property called longevity" [Keulegan and Patterson, 1940b]. There are various solitary wave solutions (for different sets of equations, see e.g. [Dingemans, 1997]), but the most well are those of [Boussinesq, 1872] and [Rayleigh, 1876]. Both solutions have the following same functional form:

$$\zeta = H\,\mathrm{sech}^2\left(\beta\theta\right), \quad \text{where} \quad \theta = x - ct \quad \text{and} \quad c = \sqrt{g\,(d+H)} \tag{2.22}$$

but the outskirts decay coefficient, denoted by β, differs [Katell and Eric, 2002]:

$$\beta_{\text{Boussinesq}} = \frac{1}{d}\sqrt{\frac{3}{4}\frac{H}{d}}, \qquad \beta_{\text{Rayleigh}} = \frac{1}{d}\sqrt{\frac{3}{4}\frac{H}{d+H}} \tag{2.23}$$

While [Katell and Eric, 2002] mention that solitary waves generated using the solution of Rayleigh are more pure[1], Boussinesq's solution is more often used in practice (and thus most run-up results are obtained using $\beta_{\text{Boussinesq}}$). Moreover, [Goring, 1979] studied the generation of solitary waves in detail and noted that solutions obtained from higher order theories do not fit experimental data any better than the solution of Boussinesq.

Solitary wave are infinitely long cnoidal waves. Nonlinearity and the horizontal length scale of the wave are tied [Madsen and Schäffer, 2010]. However, following [Madsen et al., 2008], the effective duration and effective length scale can be defined as:

$$L_s = \frac{2\pi}{\beta} \quad \text{and} \quad T_s = \frac{2\pi}{\beta c} \tag{2.24}$$

also called the effective period and wavelength.

Run-up of breaking solitary waves and the surf similarity parameter

Much attention has been given to finding analytical solutions for run-up of non-breaking waves on plane beaches, see for example [Madsen and Schäffer, 2010] for a general overview. These theoretical results have been used to point out the key parameters affecting run-up of, not only non-breaking, but also of breaking waves.

Over the past decades, there has been a significant amount of effort directed towards studying run-up of breaking and non-breaking solitary waves, such as [Synolakis, 1987], [Li, 2000], [Hsiao et al., 2008] [Lo et al., 2013] and [Pujara et al., 2015].

Empirical run-up formulae for breaking waves have been developed from experimental investigations or numerical simulations, in combination with regression analysis. [Kobayashi and Karjadi, 1995] and later [Fuhrman and Madsen, 2008] explored the possibility of using a surf similarity parameter to describe the run-up heights of breaking solitary waves. [Lo et al., 2013] even investigated the use of such a parameter for double solitary waves with varying amplitudes and separation times.

An analytic expression is available for the maximum run-up of a (non-breaking) solitary wave, which was presented by [Synolakis, 1987]:

$$\frac{R}{d} = 2.831\,s^{-\frac{1}{2}}\epsilon^{\frac{5}{4}} \tag{2.25}$$

where s is the beach slope and $\epsilon = H/d$ the wave height to depth ratio (or nonlinearity parameter). This expression is commonly referred to as the run-up law for non-breaking solitary waves. The corresponding breaking criterion during run-up is given by:

$$\epsilon > \epsilon_b \quad \text{where} \quad \epsilon_b = 0.8183\,s^{\frac{10}{9}} \tag{2.26}$$

[1] By pure it is meant that minimal trailing waves are present and the amplitude is stable during propagation.

i.e. for a given slope, waves are breaking if $\epsilon > \epsilon_b$. Instead of normalizing by the depth, Eq. 2.25 can be written as an amplification factor:

$$\frac{R}{H} = 2.831 s^{-\frac{1}{2}} \epsilon^{\frac{1}{4}} \tag{2.27}$$

The former ratio (Eq. 2.25)is referred to as dimensionless run-up, and the latter (Eq. 2.27) as fractional run-up. [Fuhrman and Madsen, 2008] explain that the ratio of the two parameters, s and ϵ,

$$\xi_s = \frac{s}{\epsilon} \tag{2.28}$$

can be considered as the solitary wave equivalent to the surf similarity parameter for periodic waves. Using this definition of ξ_s, they show that the solution of [Synolakis, 1987] can be rewritten as:

$$\frac{R}{H} = 2.831 \epsilon^{-\frac{1}{4}} \xi_s^{-\frac{1}{2}} \tag{2.29}$$

As discussed in [Madsen and Fuhrman, 2008], this becomes apparent when Eq. 2.29 is compared with the expression for run-up of non-breaking periodic waves:

$$\frac{R}{H} = 2\pi^{\frac{3}{4}} \epsilon^{-\frac{1}{4}} \xi^{-\frac{1}{2}} \quad \text{where} \quad \xi = s\left(\frac{H}{L_0}\right)^{-\frac{1}{2}} \tag{2.30}$$

which follows from the solution of [Carrier and Greenspan, 1958]. H is the local wave height at the toe of the slope, and L_0 is the linear deep-water wave length. [Fuhrman and Madsen, 2008] finally show that fractional run-up is uniquely defined by yet another run-up similarity or surf similarity parameter:

$$\frac{R}{H} = 2.831 \chi_s^{-\frac{1}{2}} \quad \text{where} \quad \chi_s = s\epsilon^{-\frac{1}{2}} \tag{2.31}$$

χ_s has been discussed by [Pujara et al., 2015], who advocated that χ_s provides a credible parametrization for both run-up and breaker type. The latter is motivated by the study of [Grilli et al., 1997], who, using fully non-linear potential flow theory, show that χ_s defines the solitary wave breaker type. [Lo et al., 2013] give a slightly different definition for the solitary surf similarity parameter than [Kobayashi and Karjadi, 1995] and [Fuhrman and Madsen, 2008], which is more in line with the breaking criterion (Eq. 2.26):

$$\varsigma_s = s\epsilon^{-\frac{9}{10}} \tag{2.32}$$

In other word, the breaking limit can be expressed as a constant value of the surf similarity parameter of [Lo et al., 2013]:

$$\varsigma_{s,b} = 0.8183^{-\frac{9}{10}}$$

The breaking limit in terms of ξ_s is not constant, but is slope dependent. Substituting ϵ_b in Eq. 2.28, we get:

$$\xi_{s,b} = \frac{1}{0.8183} \cdot s^{-\frac{1}{9}} = 1.22205 \cdot s^{-\frac{1}{9}} \tag{2.33}$$

Beyond the breaking limit, i.e. for $\varsigma_s < \varsigma_{s,b}$, the run-up law is not valid. By several researchers it was proposed to write the fractional run-up of breaking solitary waves as a power function of a solitary surf similarity parameter:

$$\frac{R}{H} = \alpha S^{\beta}, \quad \text{for} \quad S < S_b \tag{2.34}$$

where for S we can substitute any of the alternative solitary similarity parameters. The scaling coefficient α and power β are free parameters. The following empirical curves were given by [Kobayashi and Karjadi, 1995], [Fuhrman and Madsen, 2008] and [Lo et al., 2013] respectively:

$$\left(\frac{R}{H}\right)_{KE} = 2.955 \cdot \xi^{0.395} \tag{2.35}$$

$$\left(\frac{R}{H}\right)_{FM} = 3.9 \cdot \xi^{0.42} \tag{2.36}$$

$$\left(\frac{R}{H}\right)_{LPL} = 4.5 \cdot \varsigma_s^{0.5} \tag{2.37}$$

Finally, an alternative empirical formulation, which considers the parameters s and ϵ separately (i.e. they are not combined into a single surf similarity parameter) was given by [Hsiao et al., 2008]:

$$\frac{R}{d} = 7.712 s^{0.632} \sin(\epsilon)^{0.618}$$

which for $\frac{R}{H}$ yields:

$$\frac{R}{H} = 7.712 s^{0.632} \sin(\epsilon)^{-0.382} \tag{2.38}$$

3

Experimental Setup

The experiments are performed in the largest flume (Lange Speurwerkgoot) of the Fluid Mechanics Laboratory at Delft University of Technology. The present chapter describes the experiments conducted in the flume: the physical setup, which includes a general description of the flume and instrumentation, and proves the instrumentation layout; and the testprogramme for both regular and bichromatic wave experiments, in which the test conditions are detailed.

3.1. Objectives

The research questions, defined in the introduction, are translated into more practical objectives:

1. To acquire experimental data of sufficiently high quality and resolution, to study the (trans)formation of undular bores on fringing reefs, under different test conditions.
2. To enable comparison of the monochromatic results (at both swell and infra-gravity time-scale) with the results of the bichromatic wave experiments.
3. To allow for separation of shore- and seaward traveling waves or undular bores.
4. To be able to translate the hydrodynamic conditions at the toe of the beach into wave run-up.

The exact methodology, i.e. how the experiments are set up and which techniques are used, is subject of this chapter.

3.2. Physical Setup

The flume is roughly 38 m long (measured from wave paddle zero position to the end of the flume), 0.8 m wide and 1 m high (which can effectively accommodate a water depth of approximately 0.85 m). The scale model design, wave board properties and measurement instruments are discussed in this section.

3.2.1. Fringing reef scale model

To investigate wave transformation and undular bore formation on fringing reefs, a wooden fringing reef is constructed on scale and placed in the flume. The bathymetry of L. Phan Khanh — originally designed and constructed for mangrove experiments — has been adapted to incorporate a beach slope, resulting in typical fringing reef geometry. Moreover, the fore-reef slope has been adjusted; the composite slope used by L. Phan Khanh has been replaced by a plain slope. The fringing reef model is characterized by a fore-reef slope of approximately 1:10 (1:10.09), and a beach slope of 1:5 (1:4.79). The reef flat is 21.202 m wide and elevated 51.9 cm[1] above the flume bottom. For the majority of the experiments the offshore water level (the water level near the wave paddle) is set at 60 cm, hence the still water depth on the reef flat 8.1 cm. Given a scale factor of 20, the model dimensions translate to a reef flat in prototype of roughly 400 m wide and 1.6 m deep. This classifies as an average fringing reef (see for example Quataert [2015] for typical reef dimensions cited in literature). A horizontal section (dubbed "offshore") of roughly 10 m (9.61 m) is reserved to for wave

[1] The reef structure was initially planned to be elevated 50 cm above the flume bottom.

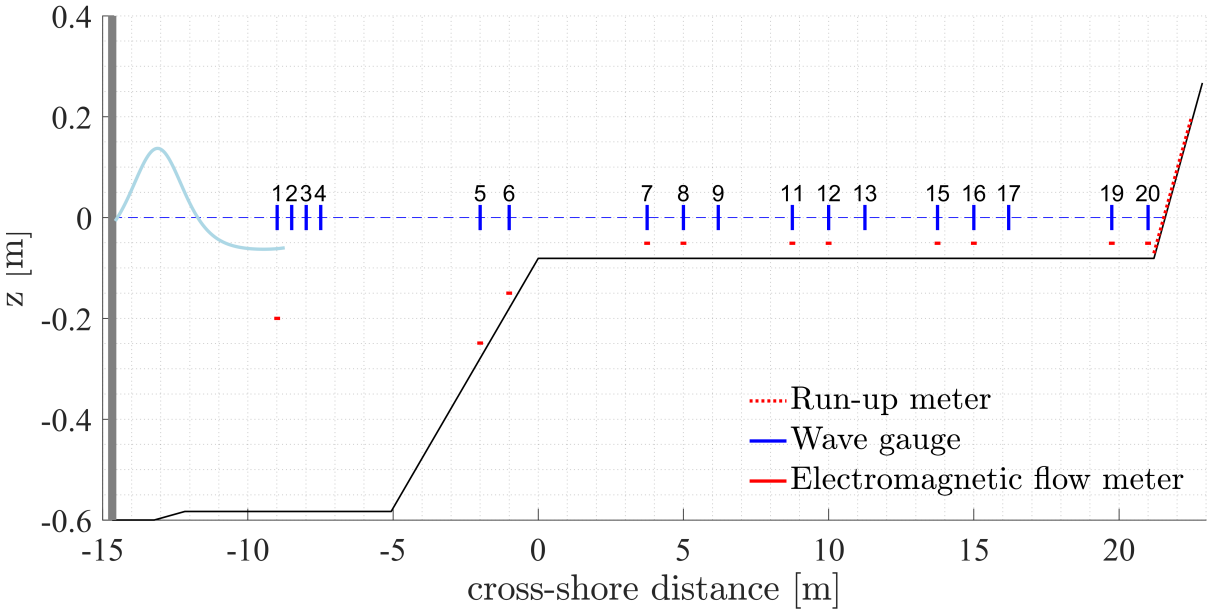

Figure 3.1: Schematized bathymetry and instrument positions. The depth is given with respect to the still water level for the reference case (d_0 = 0.6 m). Wave board zero position: x = -14.67 m; reef flat length: 21.202 m; reef flat depth in reference case: 0.081 m; fore-reef slope: 1:10; beach slope: 1:5. The following instruments are installed and the indicated positions: (blue vertical lines) wave gauge, (red horizontal lines) electromagnetic flow velocity meter, (dotted red) run-up meter.

generation. The bathymetry is schematized for modeling purposes, see Table 3.1. The schematized profile is depicted in Fig. 3.1.

Table 3.1: Schematized bathymetry of the fringing reef, defined by a set of straight lines. The horizontal position of each vertex, x, is measured from the reef crest. The vertical position, z, is measured with respect to the flume bottom at the wave maker zero position.

	Wave paddle	**-**	**-**	**Fore-reef toe**	**Reef crest**	**Beach toe**	**-**
x [m]	-14.670	-13.224	-12.169	-5.065	0.000	21.202	22.870
z [m]	0.000	0.000	0.017	0.017	0.519	0.519	0.867

The reef structure is made of smooth fiberboard slabs, supported by a wooden frame. Consequently, water is present under the reef structure. To prevent circulation under the reef structure and to avoid sloshing of water through the gaps (between the glass flume wall and the wooden slabs), the gaps are sealed with sealant (reef flat) and clay (fore-reef and beach slope). The type of fiberboard used is waterproof; the material is known not to expand when submerged in water for a longer period of time.

3.2.2. Wave generator

The flume is equipped with a piston-type wave generator. The wave board has a maximum stroke of 2 m. Wave generation is based on second order theory, which allows for the generation of regular waves (according to linear or Stokes' wave theory), bichromatic wave trains, or irregular (multichromatic) waves. Second order theory is not well suited for generation of non-linear long waves (e.g. Cnoidal waves). Appx. E is devoted to long wave generation and its implementation.

Wave generation and absorption occur concurrently. Active reflection compensation[2] (ARC) is activated to make sure reflections (seaward traveling waves originating from reflection against the fore-reef and beach slope) are not re-reflected against the wave-board. While the paddle position — associated with the to-be-generated incident waves — is predetermined, adjustments to the board position are calculated numerically in real-time (using the feedback of wave gauges mounted on the wave board). The ARC implemented in the software is independent of chosen wave generation theory.

[2]ARC mode: SHORTWAVE-THEORY-2D, see [Verhage and Dongeren, 2003].

Table 3.2: Identifiers of the used wave gauges: wave gauge sensors and their control units.

No.	**1**	**2**	**3**	**4**	**5**	**6**	**7**	**8**	**9**
WG sensor	G23	G27	G26	G25	G22	G21	G20	G19	G18
WG control unit	G23	G27	G26	G25	G22	G21	G20	G19	G18

Table 3.3: Identifiers of the used EMF: electromagnetic flow meters and their control units.

No.	**1**	**2**	**3**	**4**	**5**	**6**
EMF sensor	E02	E06	E08	E11	E12	E13
EMF control unit	E03	E06	E08	'E11	E04	E12

3.2.3. Instrumentation

Nine wave gauges wave gauges were available to measure the free surface elevation. A good understanding of the transformation process of long waves over reefs requires decomposition of the total wave field into incident and reflected waves.

The choice of instrument type is largely dictated by the signal decomposition technique used. Anticipating the use of a co-located signal decomposition method, co-located wave gauge and electromagnetic flow meter pairs are placed throughout the flume (for free surface elevation and horizontal velocity measurements, respectively). The most obvious advantage of such methods is great flexibility with regard to positioning of the instruments. Since the long waves are transforming (changing shape) while propagating over the reef profile, co-located methods are most likely more appropriate than array methods. The main advantage is that the required information is gathered by both sensors at the same (horizontal) position. In other words, co-located methods are in general not affected by spatial variations in the wave field.

Furthermore, [Lin and Huang, 2004] state that co-located gauge methods "have a potential for accounting for the propagating waves over a bed with arbitrary bathymetry". In good faith of this notion, we do not restrict placement of co-located pairs to the horizontal sections (offshore section and reef flat); co-located instrument pairs are also placed on the fore-reef slope.

Details on the used decomposition techniques (with their respective assumptions and limitations) are presented in Ch. 4. Section 3.3 details the instrument layout.

Wave Gauges (WG)

Resistive type gauges are installed at a total of 20 (17 for the regular wave tests) different positions throughout the flume. The gauges measure the conductivity of water by two parallel submerged stainless steel rods, acting as electrodes. The probes are manufactered by Deltares and characterized by: a large (0.5 m) range; a fast dynamic response; automatic compensation for conductivity variation (using a reference electrode); high linearity [Deltares, 2016b]. The accuracy is 0.5 % of measuring range. Because the analogue output signal is linearly proportional to the water level (in between the two stainless steel rods/electrodes), calibration is trivial and requires the determination of a single calibration coefficient. Compensation for variation in conductivity avoids the need to re-calibrate the wave gauges. The sensors are accompanied by a control unit for signal amplifications and zeroing. Table 3.2 lists the identifiers of the sensors and control units used in this study.

Electromagnetic Flow Meters (EMF)

The co-located decomposition method requires horizontal velocity in cross-shore direction. Hence in addition to the nine wave gauges, a total of six electromagnetic velocity meters (EMS or EMF) are installed for flow-measuring purposes. The EMFs measure water velocity in two perpendicular directions. A magnetic field is induced by the probe, and two platinum electrodes measure the induced voltages produced by the flow past the probe. The flow velocity is proportional to these voltages. See [Deltares, 2016a] for the complete specification.

In this study the instruments are mounted vertically to measure horizontal particle velocities. The measuring directions are aligned with the flume coordinate system; u_x is measured along the flume, while u_y is the velocity in perpendicular direction. u_y is only recorded during the validation tests (section 5.1.2).

Because of interference with the wave gauges, the wave gauges were set to operate at 7 kHz (away from the default 5 kHz). This way, the noise would fall within the filter of the EMF, and two type of instruments could be used in in co-located setup, close to each other, without interference.

Run-up Measurements (WRM)

A wave run-up meter (WRM) [3] is placed centrally on the beach slope. The device measures run-up through an array metal pins, spaced 2.5 cm apart. The instrument is positioned such that its measuring range can register the complete shore-line motion along the transect, from minimum run-down to maximum run-up.

A thin steel cable is stretched parallel to the array of pins (separated around 2-3 mm from the pins). Once a pin becomes wet, a current starts flowing between pin and the cable, and the control unit registers an increase in voltage of around 150 mV per wet pin. This output can be converted to the shoreline motion at the beach. By taking the exact position of the pins on the 1:5 beach slope into account, the horizontal and vertical components of the shoreline-motion can be calculated. In this thesis, the vertical component of the swash-motion (shoreline elevation) it is simply referred to as "the run-up". Run-up measurements will be available for all the regular experiments; and for a subset of the bichromatic experiments.

The meter is accompanied by a simple "action camera", which records video at a vertical resolution of 1080p at 30 FPS. These recordings can be used for qualitative description of run-up, but are unfortunately not of sufficiently high quality for accurate run-up calculation.

3.3. Layout & Testprogramme

In reality, reef hydrodynamics involves a variety of complex phenomena (shoaling, wave-breaking, wave interactions, resonance, etc.). Instead of dealing with all phenomena at once, we like to follow the "keep it simple" principle, which is possible in a controlled environment that is a wave flume in a hydraulic laboratory. Simple and systematic investigation is accomplished by performing regular and bichromatic experiments, using the same bathymetry.

The first test-series is composed of regular wave experiments (denoted with a prefix R for regular), thereby reducing the complexity of wave-interactions. In these experiments we study long wave transformation — characterized by non-linear steepening of the long wave (due to self-self interaction) and the subsequent undular bore formation — and run-up on reefs, without too many other processes involved. Reflection, which inevitably happens on the fore-reef and beach slope, is something one almost cannot (and in our case we do not want to) completely avoid[4]. To be able to focus on the shore-wards propagating waves, considerable effort is directed towards decomposition techniques (see Ch. 4).

It is assumed that infra-gravity waves, generated on the reef flat by the time-varying breakpoint mechanism, behave as free long waves. Using this similarity, we aim to use the knowledge gained in the analysis of long wave transformation (using the regular wave experiments) in the analysis of infra-gravity waves on reefs (generated in the bichromatic experiments).

The second series of tests included in the testprogramme, the bichromatic wave experiments, is denoted by prefix B. A bichromatic wave train is the most basic case where infra-gravity waves are generated. Since only two primary wave-components (with frequency f_1 and f_2) are present in the incident signal, the number of interactions (sum and difference interactions) is limited[5], and thus the measurements are relatively easy to investigate using spectral analysis (and therefore readily compared with theory, using the theories established by e.g. [Hasselmann, 1962] and [Longuet-Higgins and Stewart, 1962]).

The generation of the bound waves is related to the group frequency (see [Longuet-Higgins and Stewart, 1962] for theoretical background, or Noorloos [2003] for an experimental investigation). To make intercomparison of free long waves and infra-gravity waves possible, the frequency of the bichromatic primary waves are chosen such that the infra-gravity time-scale matches the period of the long wave in the regular experiments.

3.3.1. Regular wave experiments

[3] Also referred to as the wave rake, from the Dutch name *golfhark*; the name given to this discrete run-up meter because of its resemblance with a garden rake (due to the long pins).

[4] It is chosen not to install a wave absorber. First of all, because it would not totally absorb long waves, and thus it would unnecessarily add another unknown (the reflection coefficient of the absorber). This would complicate calibration of numerical models. Moreover, since the waves would still not have a purely propagating character, decomposition would still be required. Secondly, the investigation of run-up of undular bores is one of the main research questions, and publicly available experimental run-up data of undular bores is scarce. Finally, including a beach slope is much closer to a true reef setting; reflection of waves resulting in a standing wave pattern is an inherent feature of reef hydrodynamics. Ignoring it would oversimplify the situation.

[5] In contrast to a bichromatic wave trains, the sheer number of interactions present in an irregular wave field makes analysis increasingly difficult. Nonetheless, it is encouraged for a next student or researcher to analyse undular bores originating from an irregular (or multichromatic) offshore wave field.

Test conditions

For all the regular wave experiments, the depth is kept the same, $d_0 = 60$ cm (from which follows, $d_r = 8.1$ cm). Cnoidal waves are generated using the method of [Goring, 1979] as discussed in Appx. E. Table 3.4 lists the test conditions and some relevant parameter estimates based on the offshore wave conditions. For estimation of the wavelength and celerity, cnoidal wave theory is used (see [Svendsen, 2006]). Table 3.5 lists some estimates of relevant parameters on the reef flat, based on linear long wave theory (i.e. $c_0 = \sqrt{gd}$). The conditions are set up such that:

- The long wave steepens enough such that it breaks on the reef flat ($x_b < W$).
- Either purely undular ($H_r/d_r < 0.3$), or transient regime bores ($H_r/d_r < 0.75$) are to-be-expected over the reef flat.

The reef structure was planned to be elevated 50 cm above the flume bottom, such that for an offshore depth of $d_0 = 60$ cm, the reef depth would be would be 10 cm. However, the reef structure turned out to be 2 cm higher, and as a consequence the reef is shallower than planned. This has the following consequences, which will be discussed in detail in Ch. 2. Because the reef depth is smaller:

- the breakpoint estimate x_b is smaller, which means the long waves travel a shorter distance before breaking, hence the undular bores that develop over the reef flat have a longer distance to develop significant undulations,
- the bore strength, $\Delta h/d_r$, is larger than planned, hence the undular bore the develop over the reef depth are all (at least initially, before energy is significantly dissipated due to turbulent wave-breaking) in the transient or turbulent bore regime.

Table 3.4: The test conditions for all six regular wave experiments, the corresponding parameter estimates, and dimensionless are given. For all regular wave experiments, the offshore depth is $d_0 = 60$ cm.

Experiment	Scale	Wave conditions		Par. estimates		Dim. parameters		
	T		H	c_{cn}	L_{cn}	H/d	L/d	U
R1	5	Swell	0.04	2.401	12.01	0.067	20.01	27
R2	5	Swell	0.08	2.438	12.19	0.133	20.32	55
R3	10	IG	0.02	2.429	24.29	0.033	40.49	55
R4	10	IG	0.04	2.454	24.54	0.067	40.90	112
R5	20	IG	0.02	2.448	48.96	0.033	81.60	222
R6	20	IG	0.04	2.480	49.60	0.067	82.67	456

Table 3.5: Parameter estimates on the reef flat based on linear long wave theory and Green's shoaling law. For all experiments, the still water depth on the reef flat is $d_r = 8.1$ cm.

Experiment	Par. estimates					Dim. parameters			
	K_{shoaling}	H_r	c_r	L_r	x_b	H_r/d_r	L_r/d_r	U_r	x_b/W
R1	1.65	0.066	0.892	4.46	1.161	0.815	7.43	2467	0.05
R2	1.65	0.132	0.892	4.46	0.581	1.629	7.43	4935	0.03
R3	1.65	0.033	0.892	8.92	4.645	0.407	14.86	4935	0.22
R4	1.65	0.066	0.892	8.92	2.322	0.815	14.86	9870	0.11
R5	1.65	0.033	0.892	17.83	9.289	0.407	29.72	19740	0.44
R6	1.65	0.066	0.892	17.83	4.645	0.815	29.72	39479	0.22

Instrumentation Layout

For all regular wave experiments, two sessions will be carried out in order to increase the spatial resolution (increase the number of measurements per experiment). The experiments are repeated two times using identical test conditions, but with measurements taken at different locations. The instruments positions were already shown in Fig. 3.1. In Table 3.6 and 3.7 they are given for either session, respectively. The instrument numbers of both wave gauges and EMF are listed, and the exact locations of the sensors are included.

Table 3.6: Instrument layout for the first session of the regular wave experiments. The following information is listed: instrument position numbers, instrument numbers and instrument positions.

Position No.	1	2	3	4	6	8	12	16	20
WG No.	1	2	3	4	5	6	7	8	9
x [m]	-8.99	-8.49	-7.99	-7.49	-1	5	10	15	21
y [m]	0.325	0.4	0.4	0.4	0.325	0.325	0.325	0.325	0.325
z [m]	-0.2	-0.3	-0.3	-0.3	-0.18	-0.081	-0.081	-0.081	-0.081
EMF No.	1	-	-	-	2	3	4	5	6
x [m]	-8.99	-	-	-	-1	5	10	15	21
y [m]	0.475	-	-	-	0.475	0.475	0.475	0.475	0.475
z [m]	-0.2	-	-	-	-0.15	-0.051	-0.051	-0.051	-0.051

Table 3.7: Instrument layout for the second session of the regular wave experiments. The following information is listed: instrument position numbers, instrument numbers and instrument positions.

Position No.	1	5	7	9	11	13	15	17	19
WG No.	1	5	6	2	7	3	8	4	9
x [m]	-8.99	-2	3.75	6.2	8.75	11.25	13.75	16.2	19.75
y [m]	0.325	0.325	0.325	0.4	0.325	0.4	0.325	0.4	0.325
z [m]	-0.2	-0.279	-0.081	-0.081	-0.081	-0.081	-0.081	-0.081	-0.081
EMF No.	1	2	3	-	4	-	5	-	6
x [m]	-8.99	-2	3.75	-	8.75	-	13.75	-	19.75
y [m]	0.475	0.475	0.475	-	0.475	-	0.475	-	0.475
z [m]	-0.2	-0.249	-0.051	-	-0.051	-	-0.051	-	-0.051

3.3.2. Bichromatic Wave-trains

Test conditions

For the larger part of the bichromatic experiments, the depth is kept the same as in the regular wave experiments ($d_0 = 0.6$ m and $d_r = 0.081$ m). The test conditions for the Bichromatic experiments are given in Table 3.8. To investigate the influence of the reef depth on hydrodynamic processes on the reef flat, the reef depth is reduces by 2 cm ($d_r = 0.061$ m and $d_0 = 0.58$ m) for experiments B5-B8. This is expected to enhance nonlinear wave steepening and undular bore formation. Due to the reduced offshore depth, the wave height is also reduced slightly, such that the short wave components are still within the second order Stokes' region of validity.

The primary wave frequencies f_1 and f_2 are supplied to the wave generation software. The test-conditions are defined by the combination of a mean short-wave frequency $f_{\text{mean}} = (f_1 + f_2)/2$ and a difference (or group) frequency $f_g = f_1 - f_2$. The mean short-wave period is $T_{\text{mean}} = 1.5, 2.0$ or 2.5, while the group period is $T_g = 10$ or 20.

For all experiments, the wave height of the two primary wave components are kept equal. For some experiments, a second session was carried out, denoted by HR.

Table 3.8: Test conditions for the bichromatic wave experiments.

Experiment	resolution	depth		wave height	frequency		period	
		d_0 [cm]	d_r [cm]	$H_1 = H_2$ [cm]	f_1 [Hz]	f_2 [Hz]	T_{mean} [s]	T_g [s]
B1	60	HR	8.1	8	0.55	0.45	2.0	10
B2	60	HR	8.1	8	0.526	0.476	2.0	20
B3	60	LR	8.1	8	0.716	0.616	1.5	10
B4	60	LR	8.1	8	0.692	0.642	1.5	20
B5	58	HR	6.1	8	0.55	0.45	2.0	10
B6	58	HR	6.1	8	0.526	0.476	2.0	20
B7	58	LR	6.1	8	0.716	0.616	1.5	10
B8	58	LR	6.1	8	0.692	0.642	1.5	20
B9	60	LR	8.1	6	0.55	0.45	2.0	10
B10	60	LR	8.1	6	0.526	0.476	2.0	20
B11	60	LR	8.1	6	0.426	0.376	2.5	20

4

Decomposition techniques using collocated free surface and flow measurements

Breaking down complex and seemingly chaotic free surface elevation measurements into simpler components or signals is an essential step in most reef hydrodynamics studies. The first step is usually to separate incident (shorewards-traveling) and reflected (seawards-traveling) waves. Choosing appropriate techniques is necessary for proper estimation of these more manageable signals. Array methods, utilizing an array of wave gauges carefully spaced apart, are most commonly used. Alternatively, collocated methods can be used, which are not necessarily better or worse.

Collocated methods require at least two variables to be measured at the same cross section. In this chapter, several collocated decomposition techniques are investigated, together with their assumptions and limitations. The two main variables used for decomposition of the wave field are velocity and free surface elevation.

First, in section 4.1, the general concept of decomposition is introduced. Subsequently, in section 4.2 and 4.3, shallow water wave theory is treated, which yields a decomposition method for experimental investigation based on the Boussinesq-type of equations of [Nwogu, 1993]. Because the decomposition equations are given in a more general form, they can also be used with numerical model output. The method obtained can be seen as an extension to the method of [Guza et al., 1984], which is widely used for decomposition of waves on reefs. As will be shown in the next chapter, highly dispersive reflected undulations are registered at the deeper offshore section. It is shown that the linear dispersion relation associated with the Boussinesq method is (in present form) not accurate enough for such waves, hence the method of [Hughes, 1993] is discussed, which is based on (fully dispersive) linear wave theory (subject of section 4.4). In the last section this method is modified to account for the fact that the incident wave is a regular wave of the cnoidal type.

4.1. Collocated decomposition

The wave-field can be separated into incoming and an outgoing waves, assuming linear superposition:

$$\zeta - \overline{\zeta} = \zeta^+ + \zeta^- \quad \text{and} \quad Q - \overline{Q} = Q^+ + Q^- \tag{4.1}$$

as is done in [van Dongeren et al., 1996] and [Noorloos, 2003] for long waves, and for example in Buckley et al. [2015] for the total wave-field (which is assumed to be linear). In the following, ζ is chosen with respect to the mean water level ($\overline{\zeta} = 0$). The time-mean discharge can be set to zero ($\overline{Q} = 0$) in a flume type of setting; once steady state conditions are reached, there is no net flow. By application of the kinematic relation between discharge and surface elevation, Eq. D.16, for both the incoming and reflected waves,

$$Q^+ = c^+\zeta^+ \quad \text{and} \quad Q^- = c^-\zeta^- \tag{4.2}$$

the following expressions for ζ^+ and ζ^- can be obtained:

$$\zeta^+ = \frac{Q - c^-\zeta}{c^+ - c^-} \quad \text{and} \quad \zeta^- = \frac{Q - c^+\zeta}{c^- - c^+} \tag{4.3}$$

Instead of Eq. D.16, Eq. D.13 can be used, which results in an equation of the same form as Eq. 4.3, but written in terms of ω. Here ω denotes the velocity of propagation of a local cross section, such that the volume of the anterior portion of water stays constant in time (see Appx. D). Using this definition for the propagation velocity, the constant form assumption is not required for decomposition.

The key difficulties of collocated methods are the estimation of propagation velocity and discharge. From numerical models, the discharge Q can usually be directly requested as an output, whereas in the flume (and in prototype) it has to be estimated, based on velocity measurements (and the free surface elevation).

4.2. Decomposition of long waves of negligible height

The collocated decomposition method in this section based on linear shallow water theory. Linear long waves are governed by the following set of equations:

$$\begin{aligned} \zeta_t + dU_x &= 0 \\ U_t + g\zeta_x &= 0 \end{aligned} \tag{4.4}$$

which follows from the full balance equations if both nonlinear and dispersion terms are omitted.

4.2.1. Total discharge for waves of negligible curvature

Initially, no assumption is made on either the height of the waves and curvature of the streamlines. The discharge is defined as:

$$Q \equiv \int_{-d}^{\zeta} u \, \mathrm{d}z = U(d+\zeta) \tag{4.5}$$

where U is the depth-averaged velocity. For long waves of negligible curvature but significant height (i.e. nonlinear shallow water waves), the velocity profile is approximately uniform over depth, which simplifies things greatly. The discharge can then be approximated from:

$$Q = U(d+\zeta) \tag{4.6}$$

if the depth-averaged velocity is replaced by $u_\alpha = u(x, z_\alpha, t)$; the horizontal velocity measured at an arbitrary vertical position $z = z_\alpha$ in the water column.

4.2.2. Method of [Guza et al., 1984]

If the studied long waves are additionally of negligible height, the discharge reduces to:

$$Q \approx Ud \tag{4.7}$$

which is the expression according linear shallow water wave theory. Again, u_α can be substituted for U. Linear shallow water waves are non-dispersive, and propagate with the shallow water wave speed, $c_0 = \sqrt{gd}$. Using these approximations, Eq. 4.3 reduces to:

$$\zeta_0^+ = \frac{1}{2}\left(\zeta + U\sqrt{\frac{d}{g}}\right) \quad \text{and} \quad \zeta_0^- = \frac{1}{2}\left(\zeta - U\sqrt{\frac{d}{g}}\right) \tag{4.8}$$

as presented by [Guza et al., 1984]. Decomposition can now, most conveniently, be carried out in the time domain. The corresponding expressions for U_0^+ and U_0^- are:

$$U_0^+ = \frac{1}{2}\left(U + \zeta\sqrt{\frac{g}{d}}\right) \quad \text{and} \quad U_0^- = \frac{1}{2}\left(U - \zeta\sqrt{\frac{g}{d}}\right) \tag{4.9}$$

In terms of discharge, 4.8 is given by:

$$\zeta_0^+ = \frac{1}{2}\left(\zeta + \frac{Q}{c_0}\right) \quad \text{and} \quad \zeta_0^- = \frac{1}{2}\left(\zeta - \frac{Q}{c_0}\right) \tag{4.10}$$

The corresponding expressions for Q_0^+ and Q_0^- are:

$$Q_0^+ = \frac{1}{2}(Q + c_0\zeta) \quad \text{and} \quad Q_0^- = \frac{1}{2}(Q - c_0\zeta) \tag{4.11}$$

Eq. 4.8 and 4.10 are valid for long waves of small amplitude. If strictly used under such conditions, these equations should give the same results.

4.3. Decomposition of long waves of appreciable height and curvature

Waves observed over the reef flat are nonlinear and dispersive. In practice, decomposition in reef hydrodynamics studies often done using the linear method of [Guza et al., 1984], even though highly nonlinear waves and bores are frequently observed over reef flats.

Construction of a decomposition method (based on collocated velocity and free surface measurements) for waves that are nonlinear, dispersive and deforming, requires one to be familiar with a higher order theory, such as the theory of [Boussinesq, 1872]. For example, [Mattioli, 1998] decomposed the Boussinesq equations in a pair of coupled Korteweg-de Vries-type of equations, that explicitly show the dynamics of the incident and reflected waves. The result is two complicated partial differential equations with nonlinear and dispersive terms, from which the incident and reflected waves (ζ^+ and ζ^-) can not be obtained directly. This section intents to shed some light on the question whether a method akin to the method of [Guza et al., 1984] can be developed, which takes into account the effect wave height and dispersive effects.

4.3.1. Total discharge estimate based on a quadratic velocity profile

Eq. 4.5 states that the discharge is the product of depth-averaged velocity and the local water depth. Using the mean depth instead leads to an underestimation near the crests and an overestimation near the troughs of waves with significant amplitudes.

Furthermore, significant curvature of streamlines (of which the free surface is one) implies that the horizontal velocity varies over depth. In the present experiments, the horizontal velocity measured on the reef flat, is taken relatively close to the bottom. In such a case, approximating the depth-averaged velocity by its locally measured value could lead to a significant underestimation, especially near the crests of the undulations.

To approximate the discharge more accurately, one needs to account for the velocity distribution and use the instantaneous depth $(d+\zeta)$. Using a Taylor series expansion about the bottom yields the following expression for $u = u(x,z,t)$, which satisfies the Laplace equation and the bottom boundary condition:

$$u = u_b + \frac{1}{2}\left(d^2 - z^2\right)\frac{\partial^2 u_b}{dx^2} - (d+z)\frac{\partial^2 (d\,u_b)}{dx^2} + \mathcal{O}\left(\mu^4\right) \quad \text{where} \quad \mu = L/d \tag{4.12}$$

where $u_b = u(x,-d,t)$ is the velocity at the bottom. See for example [Svendsen, 2006] for details. For a horizontal bottom (d = constant), Eq. 4.12 reduces to:

$$u = u_b - \frac{1}{2}(d+z)^2\frac{\partial^2 u_b}{dx^2} + \mathcal{O}\left(\mu^4\right) \tag{4.13}$$

No additional assumptions have to be introduced in the derivation of Eq. 4.12, and the main error source will therefore be due to truncation of the series [Madsen et al., 1991]. If the $\mathcal{O}\left(\mu^4\right)$ terms and higher are dropped, the vertical structure is quadratic.

As shown in [Nwogu, 1993], u can similarly be expressed in terms of $u_\alpha = u(x,z_\alpha,t)$:

$$u = u_\alpha + \frac{1}{2}\left(z_\alpha^2 - z^2\right)\frac{\partial^2 u_\alpha}{dx^2} + (z_\alpha - z)\frac{\partial^2 (d\,u_\alpha)}{dx^2} + \mathcal{O}\left(\mu^4\right) \tag{4.14}$$

This has been used by [Nwogu, 1993] to improve the dispersion properties of his Boussinesq model[1]. Eq. 4.14 has been used in the reef hydrodynamics study [Nwogu and Demirbilek, 2010], and forms an important building block of the higher-order Boussinesq model of [Wei et al., 1995], which has been used to simulate the evolution of an undular bore (using the test case of [Peregrine, 1966]).

Eq. 4.14 can be used in conjunction with a Boussinesq model to obtain the velocity distribution of horizontal velocity from the computational velocity variable u_α (which is simply the computed horizontal velocity at the depth z_α). In the present thesis u_α represents the measured velocity and will be used to obtain an estimate for the discharge, as well as other quantities. Integrating Eq. 4.14 over depth yields for the discharge [Nwogu, 1993]:

$$Q \approx u_\alpha\left(d+\eta\right) + \left(\frac{1}{2}z_\alpha^2 d - \frac{1}{6}d^3\right)\frac{\partial^2 u_\alpha}{dx^2} + \left(z_\alpha d + \frac{1}{2}d^2\right)\frac{\partial^2 (d\,u_\alpha)}{dx^2} \tag{4.15}$$

which simplifies for a horizontal bottom to:

$$Q \approx u_\alpha\left(d+\eta\right) + \left(\frac{1}{3}d^3 + z_\alpha d^2 + \frac{1}{2}z_\alpha^2 d\right)\frac{\partial^2 u_\alpha}{dx^2} \tag{4.16}$$

[1] By choosing z_α such that the error with respect to the linear dispersion relation is minimized.

Note that higher order terms are discarded. [Quinn et al., 1994] experimentally investigated the "reverse problem", i.e. to obtain the velocity profile based on the depth-averaged velocity and its second order derivative. It was found that agreement of the quadratic velocity profile with the measured profile was particularly good near the bed. Since in our case the velocity is measured relatively close to the bed ($z_\alpha \approx -5/8d$), we also expect Eq. 4.16 to give good results.

4.3.2. Governing equations

In the previous section it was suggested that Eq. 4.16, which is due to [Nwogu, 1993], provides a sensible estimate for the discharge in case velocity is measured at a single position in the water column. In fact, the full balance equations of mass and momentum based on Nwogu's formulation provide a natural starting point for a decomposition method for experimental investigation.

In contrast, direct application of the non-hydrostatic model *equations* to measurements is perhaps are not so useful (at least not using the present data set). However, non-hydrostatic *models* are of course extremely versatile; they are the model type of choice of many coastal engineers due to the striking balance between model complexity and performance.

The aim is to present the decomposition method in a general framework, which can be used for both measurements (based on Boussinesq theory) and numerical model output (either from a non-hydrostatic or a Boussinesq-type model). Because both the non-hydrostatic model equations and the Boussinesq equations of [Nwogu, 1993] are essentially based on the incompressible Euler equations, it would be logical to choose this set of equations as a starting point.

Depth-integrated incompressible Euler equations

The incompressible Euler equations are integrated over depth. A horizontal bottom is assumed. The depth-integrated continuity equation is given by:

$$\frac{\partial \zeta}{\partial t} + \frac{\partial Q}{\partial x} = 0 \quad \text{where} \quad Q = \int_{-d}^{\zeta} u \, \mathrm{d}z \tag{4.17}$$

The depth-integrated horizontal momentum balance (per unit density) can be written as:

$$\frac{\partial Q}{\partial t} + \frac{\partial M}{\partial x} = 0 \quad \text{where} \quad M = \int_{-d}^{\zeta} \left(u^2 + p^{'} \right) \mathrm{d}z \quad \text{and} \quad p^{'} = \frac{p}{\rho} \tag{4.18}$$

M is the total momentum flux per unit density. The total pressure is split in a hydrostatic and non-hydrostatic part:

$$M = \int_{-d}^{\zeta} \left(u^2 + g\left(\zeta - z\right) + q^{'} \right) \mathrm{d}z = \int_{-d}^{\zeta} u^2 \, \mathrm{d}z + \frac{1}{2} g \left(d + \zeta\right)^2 + \int_{-d}^{\zeta} q^{'} \, \mathrm{d}z \quad \text{where} \quad q^{'} = \frac{q}{\rho} \tag{4.19}$$

The hydrostatic pressure is split in a linear and nonlinear part, which yields the excess momentum flux[2] in the following (general) form:

$$M = \underbrace{g d \zeta}_{M_0} + \overbrace{M_a + \underbrace{\frac{1}{2} g \zeta^2}_{M_g} + M_q}^{\Delta M} \tag{4.20}$$

4.3.3. Expressions for the momentum flux terms

The vertical distribution of the variables needs to be known in order to evaluate the integrals occurring in the depth-integrated equations. The vertical distribution of horizontal velocity was already touched upon in section 4.3.1. Here the depth dependence of the other variables is investigated. In addition to the discharge, expressions for the integrals M_a and M_q will be provided for the two chosen theories.

Boussinesq theory

The integrals are first evaluated following the approach of [Nwogu, 1993], which is consistent with Boussinesq theory. It is assumed that $\mathcal{O}\left(\mu^2\right) << 1$, where $\mu = d/L$ is a measure for dispersion. $\epsilon = H/d$ is a measure for

[2] The term $\frac{1}{2} g d^2$ has been discarded, such that only the wave-induced momentum flux is accounted for. Note that if M is averaged over a wave, the radiation stress is obtained.

nonlinearity, and it is assumed that $\mathcal{O}(\epsilon) = (\mu^2)$. Note that this means that the (Stokes-)Ursell number is $N_{\text{Ursell}} = \frac{\epsilon}{\mu} = \mathcal{O}(1)$.

For a horizontal bottom, Nwogu's expressions for the horizontal and vertical velocity are:

$$\begin{aligned} u &\approx u_\alpha + \left[\frac{1}{2}\left(\frac{z_\alpha^2}{d} - \frac{z^2}{d}\right) + (z_\alpha - z)\, d\right] u_{\alpha,xx} \\ w &\approx -(d+z)\, u_{\alpha,x} \end{aligned} \tag{4.21}$$

The vertical velocity has been obtained by substituting u in the (local) continuity equation, followed by subsequent integration over depth and application of the bottom boundary condition. In the current approximation (to $\mathcal{O}(\mu^2)$), the horizontal velocities vary quadratically over the depth and the vertical velocities vary linearly over depth [Nwogu, 1993]. The vertical distribution of pressure is also quadratic. The pressure field is obtained from the depth-integrated vertical momentum balance, the free surface boundary conditions, and the expressions for u and w given above. For brevity, the vertical momentum equation is not given, only the resulting expression for non-hydrostatic pressure is given. Non-hydrostatic pressure is given by:

$$q' = \left(zd + \frac{1}{2}z^2\right) u_{\alpha,xt} \tag{4.22}$$

and is independent of z_α. The discharge is obtained by integrating the horizontal velocity over depth:

$$Q = \int_{-d}^{\zeta} u\,\mathrm{d}z \approx u_\alpha\,(d+\zeta) + \left(\alpha + \frac{1}{3}\right) d^3 u_{\alpha,xx} \quad \text{where} \quad \alpha = \left(\frac{z_\alpha}{d}\right) + \frac{1}{2}\left(\frac{z_\alpha}{d}\right)^2 \tag{4.23}$$

as given in the previous section. If higher order terms are discarded, the advection term is given by:

$$M_a = \int_{-d}^{\zeta} u^2\,\mathrm{d}z \approx u_\alpha^2\,(d+\zeta) \tag{4.24}$$

The non-hydrostatic pressure term becomes:

$$M_q = \int_{-d}^{\zeta} q'\,\mathrm{d}z \approx -\frac{1}{3} d^3 u_{\alpha,xt} \tag{4.25}$$

Hence Boussinesq scaling finally yields for the momentum flux:

$$M_B \approx g d\zeta + u_\alpha^2\,(d+\zeta) + \frac{1}{2} g\zeta^2 - \frac{1}{3} d^3 u_{\alpha,xt} \tag{4.26}$$

which is consistent with [Ali and Kalisch, 2012], apart from the higher-order term $u_\alpha^2\zeta$. As suggest by [Ali and Kalisch, 2012], this higher order term can be included such that the momentum flux reduces to the shallow-water flux if the dispersion term is omitted.

Non-hydrostatic theory

In SWASH the governing equations are integrated over K layers, see e.g. [Zijlema and Stelling, 2005]. The dependent variables can be requested as model output at the cell faces and layer interfaces, from which the integrals of interest can be determined. An integral is approximated by a finite sum. The discharge can be determined directly from the depth-averaged velocity, or from the layer-averaged velocities by a summation over the layers:

$$Q = U\,(d+\zeta) = \sum_{k=1}^{K} u_k h_k \tag{4.27}$$

where h_k is the layer thickness; the distance between two consecutive layer interfaces. u_k is the layer-averaged velocity at the cell face. The advection term is given by:

$$M_a = \int_{-d}^{\zeta} u^2\,\mathrm{d}z \approx \sum_{k=1}^{K} u_k^2 h_k \tag{4.28}$$

As mentioned in Appx. A, dispersion — due to deviations from the layer-averaged velocities — is neglected. Note that there may be some discrepancy in the numerical treatment of certain terms because SWASH uses

a staggered grid arrangement, whereas the present method is based on collocated measurements. For a horizontal bottom, the momentum flux due to non-hydrostatic pressure is given by:

$$M_q = \int_{-d}^{\zeta} q' \, \mathrm{d}z \approx \frac{1}{2\rho} \sum_{k=1}^{K} \left(q_{k-\frac{1}{2}} + q_{k+\frac{1}{2}} \right) h_k \tag{4.29}$$

where $q_{k\pm\frac{1}{2}}$ are the non-hydrostatic pressures at the layer interfaces ($q = 0$ at the surface). Note that for $K = 1$, M_q reduces to the depth-averaged expression, $M_q = \frac{1}{2}\frac{q_b}{\rho} h$. The total excess momentum flux can finally be expressed as:

$$M_{NH} = g d\zeta + \sum_{k=1}^{K} u_k^2 h_k + \frac{1}{2} g \zeta^2 + \frac{1}{2\rho} \sum_{k=1}^{K} \left(q_{k-\frac{1}{2}} + q_{k+\frac{1}{2}} \right) h_k \tag{4.30}$$

4.3.4. Discharge and depth-averaged velocity of the incident and reflected waves

It turns out that expressions for the discharge of the incident and reflected waves is more easily obtained than the free surface elevation. ω, the velocity of propagation of a wave volume-element (see [Keulegan and Patterson, 1940b] or section Appx. D for a physical account) plays a central role in the derivation. The procedure builds op results obtained in section D.4.2 (most importantly, Intermezzo D.1). We start with the depth-integrated momentum equation (Eq. 4.18). Replacing the total discharge by the sum of the discharges associated with the incident and reflected waves (Eq. 4.1), we get:

$$\frac{\partial Q^+}{\partial t} + \frac{\partial Q^-}{\partial t} = -\frac{\partial \Delta M}{\partial x} - g d \frac{\partial \zeta}{\partial x} \tag{4.31}$$

In order to integrate this equation, both time derivatives, Q_t^+ and Q_t^-, have to be replaced by spatial derivatives. This can be done making use of the continuity written in terms of ω (Eq. D.13). ω^+ and ω^- are written as a sum of the linear shallow water speed and a small quantity:

$$\omega^+ = c_0 + \Delta\omega^+ \quad \text{and} \quad \omega^- = -(c_0 + \Delta\omega^-) \tag{4.32}$$

as was assumed in section D.4.2 for ω^+ only. Eq. D.45 provides an approximate expression for $\partial_t Q^+$, written in terms of spatial derivatives:

$$\frac{\partial \left(\omega^+ \zeta^+\right)}{\partial t} + c_0^2 \frac{\partial \zeta^+}{\partial x} + 2c_0 \frac{\partial \left(\Delta\omega^+ \zeta^+\right)}{\partial x} = 0 \tag{4.33}$$

Similarly, for $\partial_t Q^-$ we get:

$$\frac{\partial \left(\omega^- \zeta^-\right)}{\partial t} + c_0^2 \frac{\partial \zeta^-}{\partial x} + 2c_0 \frac{\partial \left(\Delta\omega^- \zeta^-\right)}{\partial x} = 0 \tag{4.34}$$

In this form, these two equations will be used later to decompose the free surface. Eq. 4.33 and Eq. 4.34 are revisited in intermezzo 4.1. Additionally, it is shown that the unknowns $\Delta\omega^\pm$ can be eliminated.

Intermezzo 4.1: approximations for Q_t^+ and Q_t^-

Eq. 4.33 is revisited. 4.1.A simply states a procedure to obtain the desired result, whereas 4.1.B gives a more detailed treatment. The reader could choose skip the second part.

4.1.A: The short version

Sommerfeld's radiation condition, applied to linear long waves, is given by:

$$\frac{\partial \zeta^+}{\partial t} + c_0 \frac{\partial \zeta^+}{\partial x} = 0 \tag{4.35}$$

Similarly, one could write for the discharge:

$$\frac{\partial Q^+}{\partial t} + c_0 \frac{\partial Q^+}{\partial x} = 0 \tag{4.36}$$

If Eq. 4.35 is multiplied by c_0 and subtracted from Eq. 4.35, we get:

$$\frac{\partial Q^+}{\partial t} + c_0 \frac{\partial Q^+}{\partial x} - c_0 \frac{\partial \zeta^+}{\partial t} - c_0^2 \frac{\partial \zeta^+}{\partial x} = 0 \tag{4.37}$$

Making use of the continuity equation to replace ζ_t by $-Q_x$, the second and third term can be combined, and the desired result is obtained:

$$\frac{\partial Q^+}{\partial t} + 2c_0 \frac{\partial Q^+}{\partial x} - c_0^2 \frac{\partial \zeta^+}{\partial x} = 0 \tag{4.38}$$

The equation reduces to Eq. 4.36 if $Q^+ = c_0\zeta^+$, which holds for long waves of small amplitude. It turns out that Eq. 4.38 is more accurate than Eq. 4.36 if waves are not strictly linear shallow water waves. A similar expression as Eq. 4.38 can be obtained for left-traveling waves:

$$\frac{\partial Q^-}{\partial t} - 2c_0 \frac{\partial Q^-}{\partial x} - c_0^2 \frac{\partial \zeta^-}{\partial x} = 0 \tag{4.39}$$

Eq. 4.38 and Eq. 4.39 can be used to integrate the momentum equation. The next part reveals which terms have actually been neglected by directly assuming the shallow water wave speed in Eq. 4.35 and Eq. 4.36.

4.1.B: The long version

A new quantity is introduced, denoted by Ω^+, which is the speed of a local cross-section such that:

$$\frac{\partial}{\partial t} \int_{x=\Omega^+ t}^{\infty} Q^+ \, dx = 0$$

which yields an equation in similar form as Eq. D.6:

$$\frac{\partial Q^+}{\partial t} + \frac{\partial \left(\Omega Q^+\right)}{\partial x} = 0 \tag{4.40}$$

If it is used to eliminate Q^+ in the momentum equation (Eq. 4.18), we a wave traveling in the positive direction (exactly):

$$\Omega^+ Q^+ = M^+ \tag{4.41}$$

Because Ω^+ is unknown, the result obtained is not very useful in present form. To approximate Eq. 4.40, it is assumed that Ω^+ is not much larger than the shallow water wave speed. We write:

$$\Omega^+ = c_0 + \Delta\Omega^+$$

Making use of Eq. D.13, one can consequently write for Q_t:

$$\frac{\partial Q^+}{\partial t} = -c_0 \frac{\partial Q^+}{\partial x} - \frac{\partial \left(\Delta\Omega^+ Q^+\right)}{\partial x}$$

Using Eq. D.13 and Eq. 4.32 this can be further written as:

$$\frac{\partial Q^+}{\partial t} = -c_0^2 \frac{\partial \zeta^+}{\partial x} - c_0 \frac{\partial \left(\Delta\omega^+ \zeta^+\right)}{\partial x} - c_0 \frac{\partial \left(\Delta\Omega^+ \zeta^+\right)}{\partial x} - \frac{\partial \left(\Delta\Omega^+ \Delta\omega^+ \zeta^+\right)}{\partial x}$$

or even:

$$\frac{\partial Q^+}{\partial t} = -c_0^2 \frac{\partial \zeta^+}{\partial x} - 2c_0 \frac{\partial \left(\Delta\omega^+ \zeta^+\right)}{\partial x} - \frac{\partial \left(\left(\Delta\omega^+\right)^2 \zeta^+\right)}{\partial x} - c_0 \frac{\partial \left(\left(\Delta\Omega^+ - \Delta\omega^+\right)\zeta^+\right)}{\partial x} - \frac{\partial \left(\left(\Delta\Omega^+ - \Delta\omega^+\right)\Delta\omega^+ \zeta^+\right)}{\partial x} \tag{4.42}$$

Eq. 4.42 is compared with the expression for a wave of constant form:

$$\frac{\partial Q^+}{\partial t} = -\left(c_0 + \Delta c^+\right)\frac{\partial Q^+}{\partial x} = -\left(c_0 + \Delta c^+\right)^2 \frac{\partial \zeta^+}{\partial x} = -c_0^2 \frac{\partial \zeta^+}{\partial x} - 2c_0 \Delta c^+ \frac{\partial \zeta}{\partial x} - \left(\Delta c^+\right)^2 \frac{\partial \zeta^+}{\partial x} \quad \text{if} \quad \Delta c^+ = \text{constant}$$

If $\Delta\omega^+$ is constant, it is equal to Δc^+, and consequently it can be placed outside of the derivative. The first three terms on the RHS of Eq. 4.42 are then equal to the constant form expression. From the remaining two terms, it becomes clear that if a wave is indeed of constant form, $\Delta\Omega = \Delta\omega = \Delta c^+$[a].

A slowly deforming wave is assumed, hence last two terms in Eq. 4.42 are neglected:

$$\frac{\partial Q^+}{\partial t} \approx -c_0^2 \frac{\partial \zeta^+}{\partial x} - 2c_0 \frac{\partial \left(\Delta\omega^+ \zeta^+\right)}{\partial x} - \frac{\partial \left(\left(\Delta\omega^+\right)^2 \zeta^+\right)}{\partial x} \quad \text{if} \quad \Omega^+ \approx \omega^+ \tag{4.43}$$

Because it is assumed that $\Delta\omega^+$ is small, the last term of Eq. 4.43, which involves $\left(\Delta\omega^+\right)^2$, is discarded as well. There is no reason to believe that for a deforming wave this term is larger than the two terms neglected previously.

The remaining expression is simply Eq. 4.33. $\Delta\omega^+$ is unknown, but can be eliminated if $\partial_x\left(\Delta\omega^+\zeta^+\right)$ is replaced by $Q_x^+ - c_0\zeta_x^+$. If this substitution is performed, Eq. 4.38 is obtained. Unlike Eq. D.7, Eq. 4.38 is not exact. However, it does not require ω^+ to be known, and, as mentioned before, it is more accurate than Eq. 4.36.

[a] It is interesting to note that since $\omega = \frac{Q}{\zeta}$ and $\Omega = \frac{M}{Q}$, $\Delta\Omega - \Delta\omega = \frac{Q}{\zeta} - \frac{M}{Q}$. Hence if a unidirectional wave is of constant form, $M\zeta - Q^2 = 0$ (and vice versa).

Subtitution of Eq. 4.38 and 4.39 into Eq. 4.31 yields:

$$2c_0 \frac{\partial \left(Q^+ - Q^-\right)}{\partial x} - c_0^2 \frac{\partial \left(\zeta^+ + \zeta^-\right)}{\partial x} = \frac{\partial \Delta M}{\partial x} + gd\frac{\partial \zeta}{\partial x} \tag{4.44}$$

Eq. 4.1 ($\zeta = \zeta^+ + \zeta^-$) can be used to combine the second term on the LHS and the linear hydrostatic pressure term on the RHS:

$$\frac{\partial \left(Q^+ - Q^-\right)}{\partial x} = c_0 \frac{\partial \zeta}{\partial x} + \frac{1}{2c_0}\frac{\partial \Delta M}{\partial x} \tag{4.45}$$

On integrating each side of Eq. 4.45 with respect to x we have:

$$Q^+ - Q^- = c_0\zeta + \frac{\Delta M}{2c_0} \tag{4.46}$$

If made use of Eq. 4.1 ($Q = Q^+ + Q^-$), one obtains for Q^+ and Q^-:

$$Q^+ = \underbrace{\frac{1}{2}\left(Q + c_0\zeta\right)}_{Q_0^+} + \frac{\Delta M}{4c_0} \quad \text{and} \quad Q^- = \underbrace{\frac{1}{2}\left(Q - c_0\zeta\right)}_{Q_0^-} - \frac{\Delta M}{4c_0} \tag{4.47}$$

The second term in Eq. 4.47 can be seen as a correction to Guza's linear expression (Eq. 4.11) and accounts for nonlinearity (advection of momentum and nonlinear effects due to hydrostatic pressure) and dispersion (due to nonuniformity of velocities and deviation from hydrostatic pressure).

Note that no expression for Q and ΔM have been assumed yet. In this thesis, either Nwogu's expressions are substituted (Eq. 4.23 and Eq. 4.26), or the non-hydrostatic equivalents (Eq. 4.27 and Eq. 4.30). One is free to insert other suitable expressions for Q and ΔM accordingly.

One might prefer to have an expression for the velocity instead of discharge, for example to determine the velocity skewness and asymmetry of the incident waves. The depth-averaged velocities U^+ and U^- can be obtained simply by dividing these discharges by the total depth:

$$U^+ = \frac{Q^+}{d+\zeta} \quad \text{and} \quad U^- = \frac{Q^-}{d+\zeta} \tag{4.48}$$

Weakly reflective boundary condition for non-hydrostatic models

The expression for Q^- in Eq. 4.47 could potentially be incorporated in a weakly reflective boundary condition for non-hydrostatic models, such as SWASH. The discharge (or depth-averaged velocity) to-be-specified at the open boundary, is then given by:

$$Q_b = Q_w^+ + Q^- \quad \text{or} \quad U_b = \frac{Q_w^+ + Q^-}{d+\zeta} \tag{4.49}$$

where Q_w^+ is discharge according to a wave theory of choice (such as linear, Stokes', cnoidal or stream function wave theory) of the incident waves entering the domain, and Q^- is given by Eq. 4.47. Q and ΔM are given by Eq. 4.27 and Eq. 4.30.

The advantage of Eq. 4.49 is that it will most likely perform better than the radiation condition if reflections are weakly dispersive and/or weakly nonlinear. The disadvantage is that it is approximate and consequently, even if there there are no reflections present at the boundary, Q^- will not be exactly zero. For a weakly nonlinear (dispersive) wave field the error might be small. However, in case there are no reflections, but the incident waves are highly nonlinear (dispersive), they may be attenuated, or more generally, incorrectly specified at the boundary.

4.3.5. Estimation of the second-order derivatives

For the current application it is more convenient to evaluate temporal derivatives. For Boussinesq systems, it is customary to interchange spatial and temporal derivatives if the order of the error in the approximation does not change. Hence, the first order relations, Eq. 4.4, are used to replace:

$$\begin{aligned} u_{\alpha,xx} \quad &\text{by} \quad \frac{1}{gd}u_{\alpha,tt} \\ u_{\alpha,xt} \quad &\text{by} \quad -\frac{1}{d}\zeta_{tt} \\ \zeta_{\alpha,xt} \quad &\text{by} \quad -\frac{1}{g}u_{\alpha,tt} \end{aligned} \tag{4.50}$$

$u_{\alpha,xx}$ occurs in the expression for the discharge (Eq. 4.23). $u_{\alpha,xt}$ is used to approximate the momentum flux contribution due to non-hydrostatic pressure M_q (Eq. 4.25), which occurs in Eq. 4.47. The last substitution will be made later (Eq. 4.74).

The second-order derivatives in time are approximated numerically from the velocity measurements using a Savitzky-Golay filter (a digital filter). A Savitzky-Golay filter can be thought of as a generalized moving average. Because a polynomial is used, a high level of smoothing can be obtained without attenuation of data features. The standard Matlab function sgolayfilt is used with a polynomial order of 5 and a frame length of 25 (i.e. 0.25 seconds). This gives good results for waves on the reef flat.

One might wonder if the method can be extended to field scale. Typically, the sampling rate of measurements taken in the field are in the order of 1-10 Hz. Using the scale factor of 20, our sampling rate of 100 Hz at model scale corresponds to a sampling rate of approximately 22 Hz in prototype. The reef depth scaled to prototype is $d_{r,p} = 20 \cdot d_{r,m} \approx 1.6$ m. If it is assumed that a typical undulation has a wavelength of five to ten times the depth, then the typical period is approximately $2-4$ s. Furthermore, the effective period of a solitary wave (Eq. 2.24) with nonlinearity $\epsilon = 0.6$ yields $T_s = 3$ s. Suppose measurements are obtained at a rate of 10 Hz. Then the number of samples per typical undulation is around 20-40. This resolution is lower than the resolution of our laboratory data, but it should still suffice to accurately approximate the second-order derivatives.

Recently, [Bonneton et al., 2018] presented a local time discretization method for reconstruction of the surface from pressure measurements (sampled at 10 Hz). Derivatives were approximated using appropriate numerical schemes. Subsequently a moving average filter was used to reduce noise. The method gave good results for field data (obtaiend at the French Atlantic coast), even for the crest elevation of the highest waves observed. The mean water depth was 2.25 m, which would not be uncommon for a typical reef flat. For this depth, the effective period of a solitary wave with nonlinearity within the range $\epsilon = 0.3-0.6$ is $T_s = 3.55-5.56$ s. Furthermore, applying our rule of thumb for the wavelength of a typical undulation yields a period of $2.4-4.8$ s. From their Fig. 8 it can be seen that time-scale of the front of the highest wave observed in a wave group is approximately 2 s. Because the observed scales of the highest waves are of similar order of magnitude as can be expected for undulations, it should also be feasible to determine first- and second-order derivatives from measured time series on a typical reef flat, of course provided the sampling rate is high enough (preferably > 10 Hz).

4.3.6. Verification of the decomposition method

The decomposition method (Eq. 4.47) is considered for verification. First, the depth dependence of the variables is based on Boussinesq theory; Eq. 4.26 will be used for the momentum flux term and Eq. 4.23 is substituted for the discharge. The discrepancy with respect to the linear dispersion relation is determined. Subsequently, it is assessed whether nonlinear properties are satisfactory.

Finally, Eq. 4.47 calculated based on the output of a SWASH simulation. Reflection of an undular bore against a closed wall is used as a test case. Eq. 4.30 will be used for the momentum flux term and 4.27 is substituted for the discharge.

Linear dispersion properties of the Boussinesq decomposition method

The decomposition method is essentially based on Eq. 4.45, hence this equation will be investigated further. A dispersion relation is usually obtained by substituting a right-traveling wave,

$$\begin{aligned} \zeta &= a sin(\omega_f t - kx) \\ u_\alpha &= \hat{u} sin(\omega_f t - kx) \end{aligned} \tag{4.51}$$

in the linearized version of the governing equations and setting the determinant to zero. Since a right-traveling wave is considered, ζ^- and Q^- in Eq. 4.45 are initially set to zero. If the continuity equation is used to replace Q_x^+ by $-\zeta_t^+$, and all nonlinear terms are omitted, we get:

$$\zeta_t^+ + c_0 \zeta_x^+ - \frac{1}{6}\frac{d^3}{c_0} u_{\alpha,xxt}^+ = 0 \tag{4.52}$$

Because we have two variables (ζ^+ and u_α^+) and only one equation, this equation alone is not very useful. An additional equation is required to determine the dispersion relation. This second equation can be found in the continuity equation, with Eq. 4.23 substituted for the discharge. However, because Nwogu's expression for the discharge is merely approximate, it will affect the dispersion relation. Therefore, instead of using the continuity equation, we make use of the linear solution to rewrite the last term of Eq. 4.52 in terms of ζ^+. Doing so, one can determine the dispersion relation-like equation associated with Eq. 4.52. The velocity amplitude, according to linear theory, is given by:

$$\hat{u} = \omega_f a K_u \quad \text{and} \quad K_u = \frac{\cosh(k(d+z_\alpha))}{\sinh(kd)} \tag{4.53}$$

If the plane wave expressions, Eq. 4.51, are substituted in Eq. 4.52, with Eq. 4.53 for the velocity amplitude, the following dispersion relation can be obtained:

$$c = \frac{\omega_f}{k} = c_0 \frac{\sqrt{6(kd)^3 K_u + 9} - 3}{(kd)^3 K_u} \tag{4.54}$$

Eq. 4.54 can be compared with the exact linear dispersion relation,

$$c_{\text{linear}} = \sqrt{\frac{g}{k}\tanh(kd)} \tag{4.55}$$

for different values of z_α (and thus K_u). However, since Eq. 4.47 is used for decomposition, ζ^- and Q^- were not set to zero in its derivation. Instead, ζ^- and Q^- were replaced by $\zeta - \zeta^+$ and $Q - Q^+$. Substitution of Eq. 4.47 in the continuity equation yields:

$$\zeta_t^+ + \frac{1}{2}c_0\zeta_x + \frac{1}{2}d u_{\alpha,x} + \frac{1}{2}\left(\alpha + \frac{1}{3}\right) d^3 u_{\alpha,xxx} - \frac{1}{12}\frac{d^3}{c_0} u_{\alpha,xxt} = 0 \tag{4.56}$$

This equation should be examined if one would like to assess up to which kd-value Eq. 4.47 gives accurate answers.

As discussed in the previous section, for practical reasons, spatial derivatives are replaced by time derivatives. If $u_{\alpha,xt}^+$ is replaced by $-\frac{1}{d}\zeta_{tt}^+$, Eq. 4.52 can be written as:

$$\zeta_t^+ + c_0\zeta_x^+ + \frac{1}{6}\frac{d^2}{c_0}\zeta_{xtt}^+ = 0 \tag{4.57}$$

with the associated dispersion relation:

$$c = \frac{\omega_f}{k} = c_0 \frac{\sqrt{6(kd)^2 + 9} - 3}{(kd)^2} \tag{4.58}$$

Notice that Eq. 4.58 is independent of z_α. Eq. 4.57 is closely related to the (linearized versions of the) KdV and BBM equation (it only requires application of the first order relations for the dispersion term). In a similar way as Eq. 4.57 follows from Eq. 4.52 , Eq. 4.56 yields:

$$\zeta_t^+ + \frac{1}{2}c_0\zeta_x + \frac{1}{2}d u_{\alpha,x} - \frac{1}{2}\left(\alpha + \frac{1}{3}\right)\frac{d^2}{g} u_{\alpha,xtt} + \frac{1}{12}\frac{d^2}{c_0}\zeta_{xtt} = 0 \tag{4.59}$$

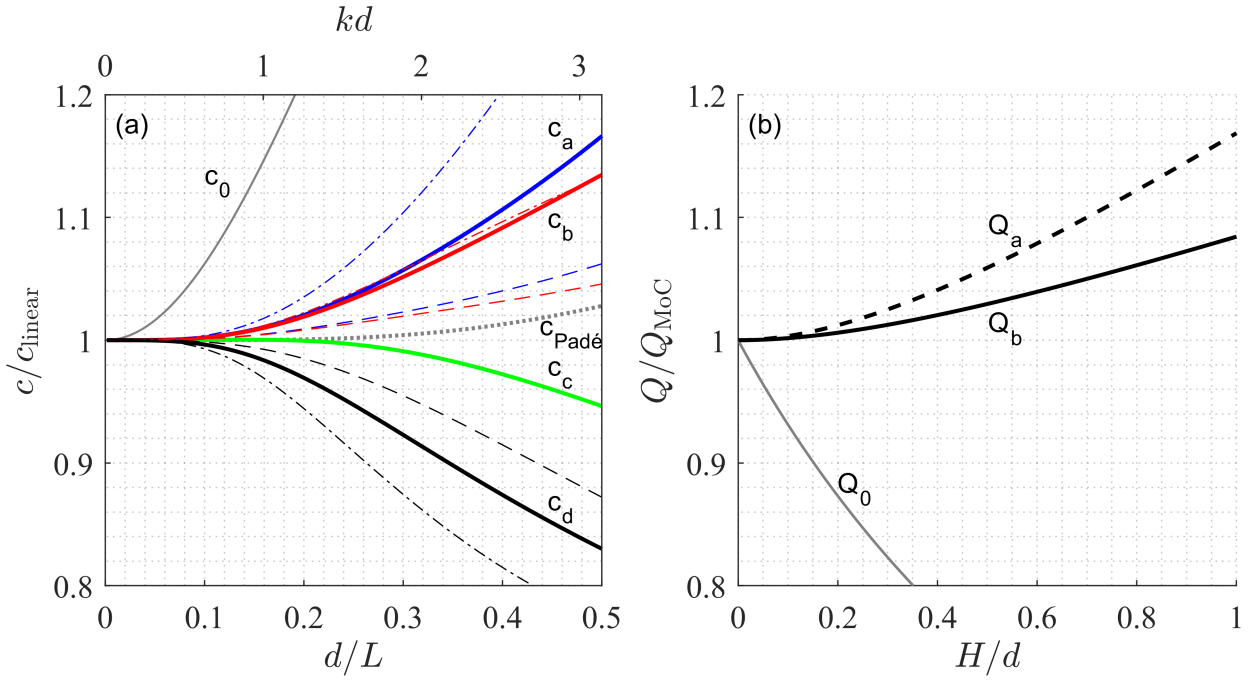

Figure 4.1: Subplot (a) normalized phase speed. Legend: (blue) Eq. 4.52 (c_a), (red) Eq. 4.56 (c_b), (green) Eq. 4.57 (c_c), (black) Eq. 4.59 (c_d), (solid grey) (1,1) Padé expansion ($c_{\text{Padé}}$), (grey dotted) linear shallow water wave speed (c_0). The normalized phase speed is plotted for different values of z_α: (solid lines) $z_\alpha = -\frac{5}{8}d$, (dashed) $z_\alpha = -\frac{1}{2}d$ (dash-dotted) $z_\alpha = -d$. Subplot (b) Ratio approximate discharge over exact discharge, the latter computed using the method of characteristics. Legend: (black solid) Eq. 4.60 (Q_b), (dashed) Eq. 4.61 (Q_a), (grey) $Q = c_0\zeta$.

if spatial derivatives are replaced by temporal derivatives. The dispersion relation of this equation finally determines whether the decomposition method (Eq. 4.47, with substitution of Eq. 4.50) is viable in intermediate water depths. The dispersion relations associated with Eq. 4.52, Eq. 4.56, Eq. 4.57 and Eq. 4.59 are shown in Fig. 4.1a (denoted by c_a, c_b, c_c and c_d, respectively). The phase speeds for different values of z_α, normalized with respect to the exact linear phase speed (c_{linear}), are plotted as a function of relative depth (d/L). The corresponding kd-value is shown on top. In addition to the value $z_\alpha = -\frac{5}{8}d$, which is used during the experiments, lines for $z_\alpha = 0, -\frac{1}{2}d, -d$ are shown. For reference, the linear shallow water wave speed (c_0) and the (1,1) Padé expansion of the exact linear phase speed ($c_{\text{Padé}}$) have been included in the figure. The decomposition method should not be used for waves with kd-values much larger than $kd \approx 1$. Accuracy can be increased by strategically placing the EMF water column. In the present study the EMFs on the reef flat are not positioned any higher than $z_\alpha = -\frac{5}{8}d$ out of fear that the probes fall dry.

Nonlinear properties of the Boussinesq decomposition method

Undular bores can be significantly nonlinear; it has to be assessed whether Eq. 4.47 is still accurate if the height of the undulations is significant. The method of characteristics provides an analytical solution to the NLSWE (see section B.5 of Appx. B) and will be used for the assessment. The depth-averaged velocity of a nonlinear long wave propagating in quiescent waters is given by Eq. B.23, which is repeated for convenience:

$$U_{MoC} = 2\left(\sqrt{g\,(d+\zeta)} - \sqrt{gd}\right)$$

The corresponding discharge can be computed by $Q_{MoC} = U_{MoC}\,(d+\zeta)$, which is exact and is thus considered as the benchmark. Because only nonlinear effects are considered, the dispersion term in Eq. 4.47, hence:

$$Q^+ = \frac{1}{2}\,(Q + c_0\zeta) + \frac{U^2\,(d+z) + \frac{1}{2}g\zeta^2}{4c_0} \tag{4.60}$$

Since only right-traveling waves are considered, we might as well assume unidirectional propagation from the start, and write:

$$Q^+ = c_0\zeta^+ + \frac{\left(U^+\right)^2\left(d+z^+\right) + \frac{1}{2}g\left(\zeta^+\right)^2}{2c_0} \tag{4.61}$$

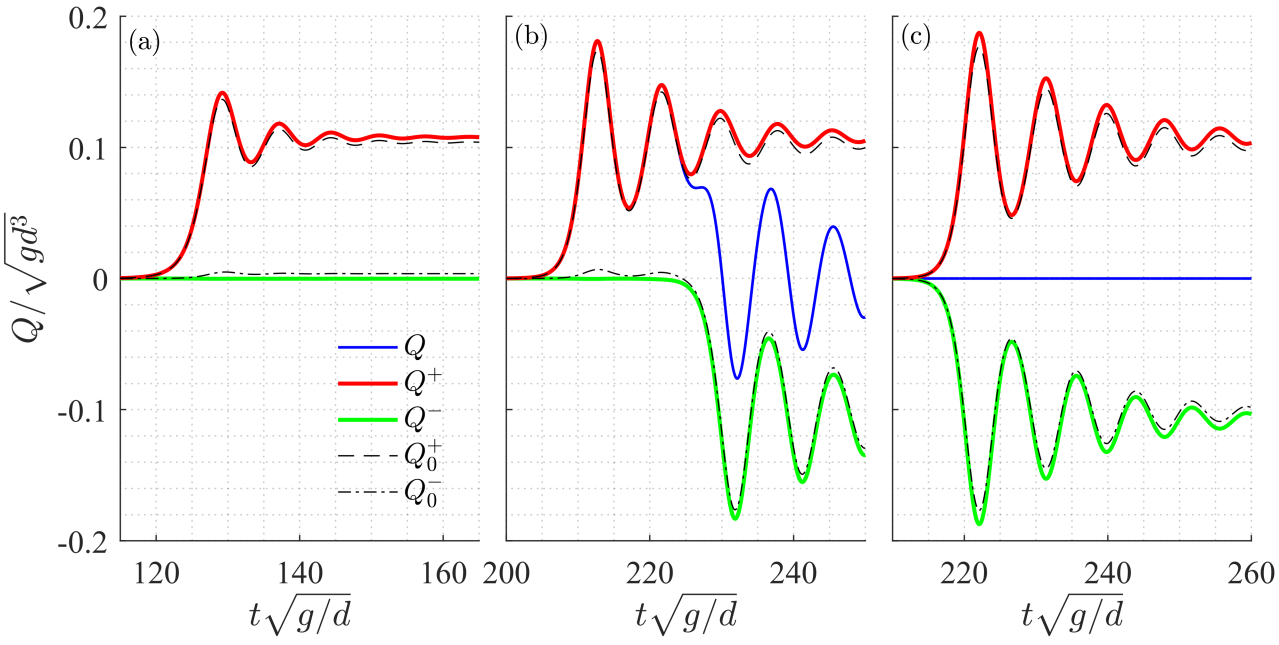

Figure 4.2: Decomposition of an undular bore. The time-series of discharge are show at: (a) at $x = 100d$, before the undular bore has reflected against the closed end, (b) at an arbitrary distance, $x = 190d$, after the bore has reflected and (c) at the closed end at $x = 200d$, where we have full reflection ($Q^+ = -Q^-$). Legend: (blue) total discharge, Q, (red) incident discharge, Q^+, decomposed using Eq. 4.47, (green) reflected discharge, Q^-, (black dashed line) incident discharge, Q_0^+, decomposed using the method of [Guza et al., 1984], (black dash-dotted line) reflected discharge, Q_0^-.

For wave heights up to the water depth, the two the discharge estimates for the incident wave (Eq. 4.60 and Eq. 4.61) are compared with Q_{MoC}. Fig. 4.1b shows the ratio Q^+/Q_{MoC} for $0 < H/d < 1$. The linear expression, $Q^+ = c_0\zeta^+$, is also included in the figure. It can be seen that linear wave theory significantly underestimates the discharge. Furthermore, Eq. 4.60 (denoted by Q_b) overestimates the discharge, but is closer to the exact discharge expression than Eq. 4.61 (Q_a). This is due to decomposition; part of the error will be visible in the reflected wave signal (which is suppose to be zero). It can be concluded that up to $H/d \approx 0.5$, Eq. 4.47 should give accurate results as far as nonlinearity is concerned.

SWASH test case: reflection of an undular bore against a vertical wall

To investigate whether Eq. 4.47 is suitable for usage with a non-hydrostatic model, a test case is set up (similar to Appx. C). SWASH is run in depth-averaged mode. A positive surge ($\Delta h/d = 0.1$) propagates into quiescent waters. After traveling a certain distance, undulations start to develop at the bore front. The eastern boundary (at $x = 200d$) is a closed one and causes the incident bore to reflect (full reflection). The simulation is halted after the first few undulations have reflected. Fig. 4.2 shows the discharge time-series at the following three locations:

1. at $x = 100d$, where the reflected undular bore is not yet visible in the time-series,
2. at $x = 190d$,
3. and at the closed end $x = 200d$.

At the first location, one would expect $Q^+ = Q$, because $Q^- = 0$ (no reflection). At the closed end, $Q^+ = -Q^-$, because $Q = 0$ (full reflection).

The discharge is decomposed both using Eq. 4.47 and by application of the method of [Guza et al., 1984]. The depth-averaged velocity is provided, hence the total discharge can be determined directly from Eq. 4.27. The momentum flux terms are calculated from Eq. 4.30. Note that in depth-averaged mode, M_q reduced to $M_q = \frac{1}{2}\frac{q_b}{\rho}h$, and $M_a = U^2(d+\zeta) = Q^2/(d+\zeta)$.

It can be seen that the present method correctly decomposes a right-traveling undular bore (Fig. 4.2a). The method of [Guza et al., 1984] causes some artificial reflection, especially near the crests of the incident

undulations. From Fig. 4.2c, it can be seen that, for both methods, $Q^+ = -Q^-$, which is to be expected in case of full reflection. The difference is that the present method gives larger (absolute) values for Q^+ and Q^-, which is supposedly correct. Fig. 4.2b shows the decomposed time series at an arbitrary location near the closed end. It becomes clear that the method of [Guza et al., 1984] generally underestimates the discharge.

To shows that Eq. 4.47 is equally valid for long waves that steepen and form undulations, a SWASH simulation is carried out with a sinusoidal long wave specified at the left boundary ($T = 10$ s, $a/d = 0.1$ and $d = 1$ m). A ramping function is applied over the first wavelength to smoothly start the simulation. The eastern boundary at $x = 200d$ is again a closed boundary. The model is this time run with a higher vertical resolution (6 layers). Fig. 4.3 shows the results of the decomposition. The difference between the present method and the linear method of [Guza et al., 1984] is overall not significant for the this test case, however the discrepancy is noticeable near the crests of the undulations. The difference is expected to increase as waves become more dispersive and/or nonlinear.

4.3.7. Decomposition of the free surface

So far, decomposition was performed in terms of discharge. In reef hydrodynamic studies it is typically the free surface that is decomposed; wave statistics are mostly based on the free surface elevation.

Decomposition based on the discretized continuity equation

ζ^+ and ζ^- could be determined numerically by discretizing the continuity equation. This requires Eq. 4.47 to be determined at two adjacent locations. For example, using central differences in space and midpoint rule in time:

$$\frac{\zeta^{\pm}_{x,t+1} - \zeta^{\pm}_{x,t-1}}{2\Delta t} + \frac{Q^{\pm}_{x+1,t} - Q^{\pm}_{x-1,t}}{2\Delta x} = 0 \quad \text{with} \quad \zeta^{\pm}_{t=0} = 0 \tag{4.62}$$

To determine the discharge at two locations, both velocity and elevation (and pressure, if used with non-hydrostatic model output) needs to be known there. This poses no problems if the free surface is indeed decomposed based on model output. However, from a practical point of view, this approach not seem to be very convenient for experimental investigation. This is especially true because, in order to accurately approximate the gradients numerically, the two collocated pairs should be placed closely together. This will inevitably lead to problems such as interference. Therefore, in the following section, a method is presented which requires only a single collocated instrument pair.

Decomposition based on Boussinesq theory

It is attempted to find expressions for ζ^+ and ζ^- based on the theory of Boussinesq. Let us reconsider Eq. 4.31. Substitution of the kinematic relation, Eq. D.13, for both Q^+ and Q^- gives:

$$\frac{\partial\left(\omega^+\zeta^+\right)}{\partial t} + \frac{\partial\left(\omega^-\zeta^-\right)}{\partial t} = -\frac{\partial \Delta M}{\partial x} - gd\frac{\partial \zeta}{\partial x} \tag{4.63}$$

Subsequent substitution of Eq. 4.33 and 4.34 into Eq. 4.63 yields:

$$c_0^2\frac{\partial \zeta}{\partial x} + 2c_0\frac{\partial\left(\Delta\omega^+\zeta^+ + \Delta\omega^-\zeta^-\right)}{\partial x} = \frac{\partial \Delta M}{\partial x} + gd\frac{\partial \zeta}{\partial x} \tag{4.64}$$

This makes integration possible. The first term on the LHS and the linear hydrostatic pressure term (M_0) cancel. Carrying out the integration (setting the integration constant to zero) we get:

$$\Delta\omega^+\zeta^+ + \Delta\omega^-\zeta^- = \frac{\Delta M}{2c_0} \quad \text{or} \quad \omega^+\zeta^+ - \omega^-\zeta^- = \frac{M}{2c_0} \tag{4.65}$$

There seems to be no simple way of calculating ω^+ if ω^- is unknown (and vice versa). It is attempted to split the total momentum flux term ΔM into M^+ and M^-. M^+ is then the momentum flux contribution associated with the shoreward-traveling waves and M^- is associated with the seaward-traveling waves. By substituting Eq. 4.1 in Eq. 4.26, the (wave-induced) momentum flux can be decomposed:

$$\begin{aligned}\Delta M = M^+ + M^- + M^i = &\underbrace{\left(U^+\right)^2\left(d+\zeta^+\right) + \frac{1}{2}g\left(\zeta^+\right)^2 + M_d^+}_{M^+} + \underbrace{\left(U^-\right)^2\left(d+\zeta^-\right) + \frac{1}{2}g\left(\zeta^-\right)^2 + M_d^-}_{M^-} \\ &+ \underbrace{2dU^+U^- + g\zeta^+\zeta^- + 2\zeta^+U^+U^- + 2\zeta^-U^+U^- + \zeta^+\left(U^-\right)^2 + \zeta^-\left(U^+\right)^2}_{M^i}\end{aligned} \tag{4.66}$$

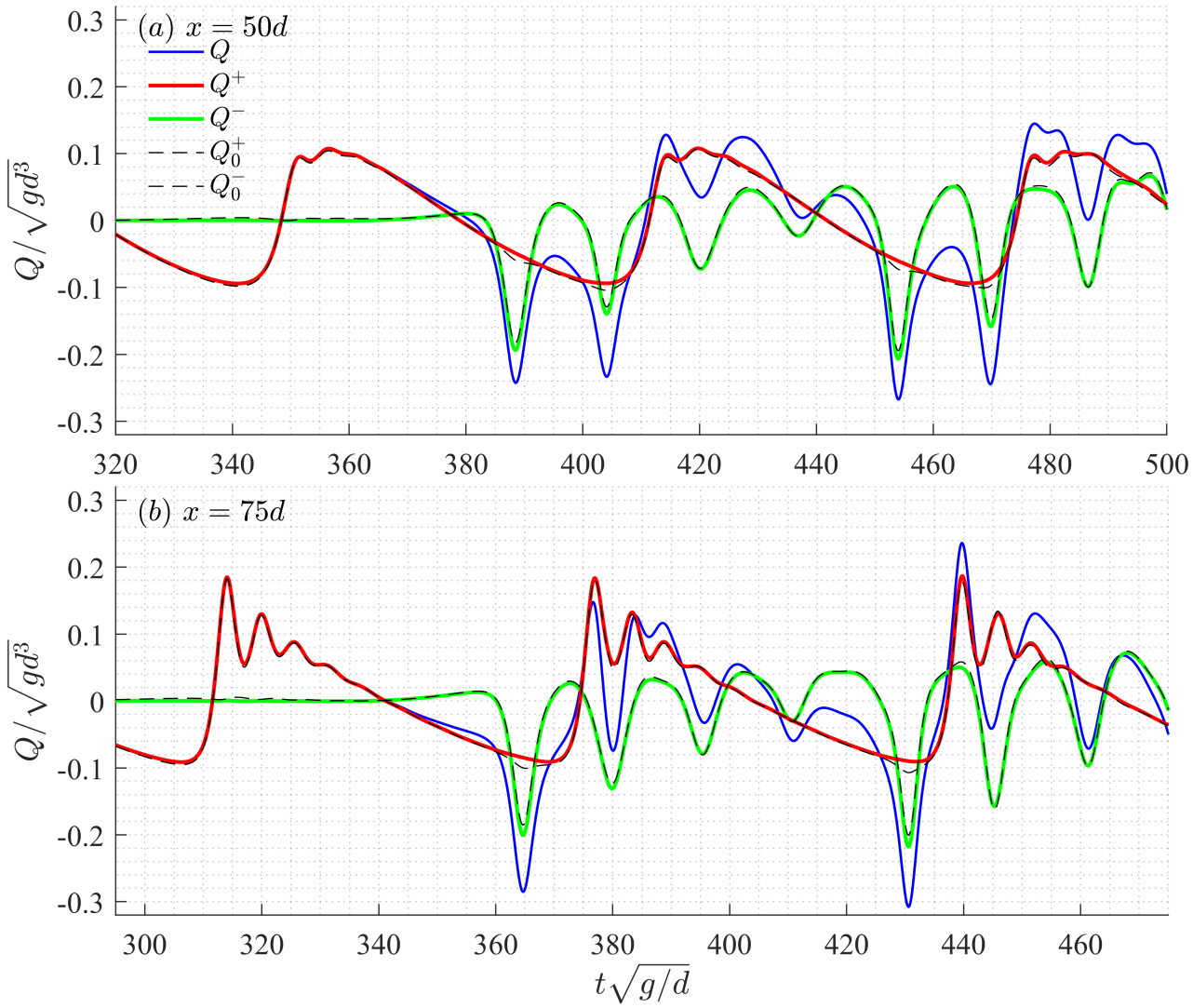

Figure 4.3: Decomposition of a dispersively breaking long wave. The time-series of discharge are show at: (a) at $x = 50d$, where the incident wave just starts to develop undulations and (b) at $x = 70d$, where the incident undulations are more developed. Legend: (blue) total discharge, Q, (red) incident discharge, Q^+, decomposed using Eq. 4.47, (green) reflected discharge, Q^-, (black dashed line) incident discharge, Q_0^+, decomposed using the method of [Guza et al., 1984], (black dash-dotted line) reflected discharge, Q_0^-.

A third term arises, denoted M^i, which is due to interaction between waves coming from the two directions. Because the dispersion term is linear in the present approximation, it does not contribute to the interaction. If higher order terms are dropped, we get:

$$\Delta M \approx \underbrace{\left(U^+\right)^2 d + \frac{1}{2} g \left(\zeta^+\right)^2 + M_d^+}_{M^+} + \underbrace{\left(U^-\right)^2 d + \frac{1}{2} g \left(\zeta^-\right)^2 + M_d^-}_{M^-} + \underbrace{2 d U^+ U^- + g \zeta^+ \zeta^-}_{M^i} \tag{4.67}$$

In the present approach, the interaction term, M^i, is ignored. Substituting $\Delta M = M^+ + M^-$ in Eq. 4.65 yields:

$$\Delta\omega^+ \zeta^+ + \Delta\omega^- \zeta^- = \frac{M^+ + M^-}{2c_0} \tag{4.68}$$

It is deduced that:

$$\Delta\omega^+ \zeta^+ = \frac{M^+}{2c_0} \quad \text{and} \quad \Delta\omega^- \zeta^- = \frac{M^-}{2c_0} \tag{4.69}$$

Consequently, $\omega^\pm$ can then be written as:

$$\omega^+ = c_0 + \Delta\omega^+ = c_0 + \frac{M^+}{2c_0\zeta^+} \quad \text{and} \quad \omega^- = -\left(c_0 + \Delta\omega^+\right) = -c_0 - \frac{M^-}{2c_0\zeta^-} \tag{4.70}$$

Substituting $\Delta M = M^+ + M^-$ in Eq. 4.47 and making use of the kinematic relation (Eq. D.13) yields for $\zeta^\pm$:

$$\zeta^+ = \frac{1}{2}\left(\frac{Q}{c_0} + \zeta\right) + \frac{M^- - M^+}{4c_0^2} \quad \text{and} \quad \zeta^- = \frac{1}{2}\left(\zeta - \frac{Q}{c_0}\right) + \frac{M^+ - M^-}{4c_0^2} \tag{4.71}$$

$M^\pm$ can be determined using Guza's first order expressions for $\zeta^\pm$ and $U^\pm$ (section 4.2.2):

$$M^\pm = \left(U_0^\pm\right)^2 d + \frac{1}{2} g \left(\zeta_0^\pm\right)^2 + M_d^\pm = \frac{3}{8} U^2 d + \frac{3}{8} g \zeta^2 \pm \frac{3}{4} \zeta U \sqrt{gd} + M_d^\pm \quad \text{where} \quad M_d^\pm = -\frac{1}{6} d^3 \left(U_{xt} \pm \sqrt{\frac{g}{d}} \zeta_{xt}\right) \tag{4.72}$$

For completeness, the interaction term[3] is also given (but not used). The quantities $M^- - M^+$ and $M^+ - M^-$ in Eq. 4.71 can now be written as:

$$M^- - M^+ = -\frac{3}{2}\zeta U\sqrt{gd} + \frac{1}{3} d^3 \sqrt{\frac{g}{d}} \zeta_{xt} \quad \text{and} \quad M^+ - M^- = \frac{3}{2}\zeta U\sqrt{gd} - \frac{1}{3} d^3 \sqrt{\frac{g}{d}} \zeta_{xt} \tag{4.73}$$

and Eq. 4.71 is finally written as:

$$\zeta^+ = \frac{1}{2}\left(\frac{Q}{c_0} + \zeta\right) + \frac{\frac{1}{3} d^2 \zeta_{xt} - \frac{3}{2}\zeta U}{4c_0} \quad \text{and} \quad \zeta^- = \frac{1}{2}\left(\zeta - \frac{Q}{c_0}\right) + \frac{\frac{3}{2}\zeta U - \frac{1}{3} d^2 \zeta_{xt}}{4c_0} \tag{4.74}$$

From Eq. 4.74, together with Eq. 4.16 for Q, the free surface can be decomposed, taking into account the effect of nonlinearity and dispersion. As mentioned earlier, $\zeta_{\alpha,xt}$ is replaced by $-\frac{1}{g} u_{\alpha,tt}$.

4.4. Decomposition of linear waves

Waves in deep water are dispersive. The method presented in the previous section is valid up to $kd \approx 1$. As will be shown in Ch. 6 reflected undulations, dispersing in deeper water, have larger kd-values. This is also true for some of the primary incident wave components in the bichromatic experiments. The method of [Hughes, 1993], presented below, is based on linear wave theory, and is exact for linear, fully dispersive waves.

According to linear wave theory, each wave component i (with frequency f_i) in a wave-field satisfies the dispersion relation:

$$\omega_i^2 = g k_i \tanh\left(k_i d\right) \tag{4.75}$$

and propagates freely with its own phase speed. Moreover, the velocity distribution of a deep water wave is far from uniform over depth. The horizontal particle velocity of a progressive harmonic wave $\zeta(x,t) = a\cos\psi$ (with $\psi = kx - \omega t$) is given by:

$$u = \frac{\partial\phi}{\partial x} = \frac{\partial}{\partial x}\left(a\frac{g}{\omega}\frac{\cosh k(d+z)}{\cosh kd}\sin\psi\right) = \frac{gk}{\omega}\underbrace{\frac{\cosh k(d+z)}{\cosh kd}}_{K_u}\underbrace{a\cos\psi}_{\zeta} = \frac{g}{c} K_u \zeta \tag{4.76}$$

[3] $M^i = 2U_0^+ U_0^- d + g\zeta_0^+\zeta_0^- = \frac{1}{4}U^2 d - \frac{1}{4} g\zeta^2 = \frac{1}{4} g\zeta^2$

See [Dean and Dalrymple, 1984] or [Holthuijsen, 2007] for details on linear wave theory. K_u is called the velocity response function. Equation 4.76 can be used together with the kinematic relation between the discharge and surface elevation (equation D.17) to obtain an expression for the discharge Q, as a function of (among others) the horizontal velocity u:

$$Q = c\zeta \approx \frac{c^2}{g}\frac{u}{K_u} \tag{4.77}$$

By substitution of the result for Q, for both incoming and outgoing linear waves, Eq. 4.3 becomes:

$$\zeta^+ = \frac{\frac{c}{g}\frac{u}{K_u} + \zeta}{2} \quad \text{and} \quad \zeta^- = \frac{-\frac{c}{g}\frac{u}{K_u} + \zeta}{2} \tag{4.78}$$

A Fourier transform (of both the measured surface elevation and velocity) is required to perform the decomposition for all components/frequencies, as done in [Hughes, 1993] and [Buckley et al., 2015][4].

4.5. Decomposition of nonlinear regular waves

In this section, we seek a method to accurately separate the incident cnoidal waves, which are generated at the wave paddle, from the seaward traveling undulations. The method is to-be-used at the initial horizontal section of the flume (near the wave paddle).

The decomposition method outlined in section 4.3 is based on the theory of Boussinesq. Application of this method would be perfectly justified if reflected waves would be long or even weakly dispersive (as is the case up to one minute). However, kd-values of the reflected undulations, dispersing into deeper water, can be much larger than one[5], such that application Boussinesq's theory (in presented form) is not justified.

Non-linear periodic, such as cnoidal waves, waves can be thought of to be composed of a primary wave component, and its bound higher harmonics. This contradicts the assumptions on which the linear decomposition method is based on; it was assumed in the previous section that all waves are free waves, which follow the linear dispersion relation. Since cnoidal waves are generated at the wave board, the linear method of [Hughes, 1993] has to be modified.

The present method is based on the following assumptions:

- all waves are of constant form,
- both the period (frequency) and wave height of the incident wave are known,
- all harmonics at multiples of the primary frequency are bound to the incident primary wave,
- all reflected waves are linear waves, and follow the linear dispersion relation,
- there is no interaction between the incident and reflected waves.

It is thus implicitly assumed that wave generation and absorption are perfect, and that no re-reflection occurs at the wave paddle (which would result in incident free waves). Moreover, the reflected undulations, dispersing in deeper water, are assumed to be well described by linear wave theory, which means the amplitudes have to be relatively small with respect to depth.

The last assumption should not introduce huge errors; Mei, [1983] states that (under certain conditions) two permanent non-linear waves which do not travel in the same direction may be superimposed. For example, standing waves may be constructed by superimposing two opposite-going cnoidal waves.

[4] After applying the fast Fourier transform (FFT) to both η and u, in order to obtain $\mathscr{F}_u$ and $\mathscr{F}_u$, Buckley et al. [2015] carry out the calculations for $\mathscr{F}_\eta^+$ and $\mathscr{F}_\eta^-$ in the frequency domain. The inverse Fourier transformation of $\mathscr{F}_\eta^+$ and $\mathscr{F}_\eta^-$ gives η^+ and η^-. The equivalent of Eq. 4.76 in the frequency domain is:

$$\mathscr{F}_u^+ = \frac{g}{c}K_u\mathscr{F}_\eta^+ = \frac{gk}{2\pi f}K_u\mathscr{F}_\eta^+ \quad \text{and} \quad \mathscr{F}_u^- = -\frac{g}{c}K_u\mathscr{F}_\eta^+ = -\frac{gk}{2\pi f}K_u\mathscr{F}_\eta^+$$

where $k_i = k(f_i)$ and $K_{u_i} = K_u(f_i)$. Similar to equation 4.78, $\mathscr{F}_\eta^+$ and $\mathscr{F}_\eta^-$ can be computed from

$$\mathscr{F}_\eta^+ = \frac{\frac{gk}{2\pi f}\frac{\mathscr{F}_u}{K_u} + \mathscr{F}_\eta}{2} \quad \text{and} \quad \mathscr{F}_\eta^- = \frac{-\frac{gk}{2\pi f}\frac{\mathscr{F}_u}{K_u} + \mathscr{F}_\eta}{2}$$

[5] A linear short wave with $T = 1$ s (note that even smaller periods have been observed for the reflected undulations) at the offshore section ($d = 0.6$ m) already gives $kd \approx 2.5$.

Because free and locked modes do not have to be isolated, it is only necessary to specify one wave number per combination of frequency and propagation direction (k_i^+ for the incident components and k_i^- for the reflections). For a given frequency, the wave number of the incident component can be calculated using the known phase speed of the incident wave:

$$k_i^+ = \omega_i^+ / c^+ \quad \text{where} \quad c^+ = f(\omega_{i,primary}^+, d, H^+) \tag{4.79}$$

The phase speed of the incident wave, c^+, is calculated according to first order cnoidal theory Mei, [1983]. The same value for T, d and H^+ used for wave generation are provided. Based on the stated assumptions, total free surface can be approximated by:

$$\begin{aligned}
\zeta &= \underbrace{\zeta_{primary}^+ + \sum_{i=2}^{N} \zeta_{i,bound}^+}_{\zeta^+} + \underbrace{\sum_{i=2}^{N} \zeta_{i,free}^-}_{\zeta^-} \\
&= a_{primary}^+ \cos\left(k_{primary}^+ x - \omega_{primary} t + \phi_{primary}^+\right) \\
&+ \sum_{i=2}^{N} a_{i,bound}^+ \cos\left(k_{i,bound}^+ x - \omega_i t + \phi_{i,bound}^+\right) \\
&+ \sum_{i=2}^{N} a_{i,free}^- \cos\left(k_{i,free}^- x + \omega_i t + \phi_{i,free}^-\right)
\end{aligned} \tag{4.80}$$

where the angular frequencies of the higher harmonics are given by: $\omega_i = i \cdot \omega_{primary}$. Because bound harmonics are taken into account for the incident waves, the wave numbers (k_i^+ and k_i^-), and therefore also the velocity response functions for the incident and reflected waves (K_i^+ and K_i^-), differ for a given frequency f_i. The wave numbers of free waves are determined from linear dispersion relation, while those of bound waves are a multiple of the primary wave number (Eq. 4.79). Let $K^\pm$ be the velocity response functions for the non-linear incident and linear reflected wave, such that for each frequency (subscript i is dropped):

$$Q^+ = K^+ u^+ \quad \text{and} \quad Q^- = K^- u^- \tag{4.81}$$

Eq. 4.1, 4.3, and 4.81 are combined to obtain the following result:

$$\zeta^+ = \frac{u - \frac{c^-}{K^-}\zeta}{\frac{c^+}{K^+} - \frac{c^-}{K^-}} = \frac{K^- u - c^- \zeta}{c^+ \frac{K^-}{K^+} - c^-} \quad \text{and} \quad \zeta^- = \frac{u - \frac{c^+}{K^+}\zeta}{\frac{c^-}{K^-} - \frac{c^+}{K^+}} = \frac{K^+ u - c^+ \zeta}{c^- \frac{K^+}{K^-} - c^+} \tag{4.82}$$

where K^- is the linear velocity response function, discussed previously. A velocity response function for the incident cnoidal wave can be based on the definition of the stream function (see Appx. F):

$$K = Q/u = \frac{\sinh k(d+\zeta)}{k \cosh k(d+z)} \tag{4.83}$$

For a certain frequency, ζ^+ is calculated using Eq. 4.82, with substitution of Eq. 4.83 for K^+ and the linear velocity response function for K^-. Note that Eq. 4.83 is almost identical to the expression for K^-, but in contrast, K^+ now depends on the free surface elevation. As a result, Fourier components $\mathscr{F}_\zeta^+$ and $\mathscr{F}_\zeta^+$ cannot be calculated directly in frequency domain. The decomposition method thus follows the following procedure:

- De-mean the total free surface elevation (and add $\overline{\zeta}$ to the depth d). It is assumed that $\overline{Q} = 0$.
- Continue by Fourier transforming both ζ and u, to obtain $\mathscr{F}_\zeta$ and $\mathscr{F}_u$.
- Use the Inverse Fourier transform for each frequency separately, to obtain time-series of u and ζ per frequency.
- Compute, for each frequency, the wave numbers $k^+ = \omega / c_{cn}$ (with c_{cn} the cnoidal wave celerity) and $k^- = f(\omega, d)$ (according to the linear dispersion relation).
- Subsequently, compute the corresponding velocity response functions, $K^+ = f(d, k^+, z, \zeta)$ and $K^- = f(d, k^-, z)$, per frequency.

- Solve Eq. 4.82 (in the time domain) for each frequency, which yields time-series for both ζ^+ and ζ^- per frequency.
- Sum up the time-series for each direction to get the total incident and reflected free surface elevation, ζ^+ and ζ^-, respectively.

5

Data Processing

5.1. Calibration of instruments

5.1.1. Calibration of wave Gauges

As mentioned before, the analogue output of the wave gauge is linearly proportional to the water level, which means determination of only a single calibration coefficient is required per wave gauge. Compensation for variation in conductivity avoids the need to re-calibrate the wave gauges. The wave gauges are calibrated by lowering the water level 10 cm and registering the difference in voltage. For redundancy reasons, calibrated coefficients are determined a total of three times for each instrument. The calibration coefficients are listed in Table . The averaged value, rounded to three significant digits, is used during the experiments.

Table 5.1: Calibration coefficients taken on the following dates: (K_1) 06-02-2017, (K_2) 10-02-2017, (K_3) 17-02-17.

No.	**1**	**2**	**3**	**4**	**5**	**6**	**7**	**8**	**9**
WG sensor	G23	G27	G26	G25	G22	G21	G20	G19	G18
K_1 [m/V]	0.02588	0.02419	0.02352	0.02440	0.02346	0.02418	0.02649	0.02311	0.02532
K_2 [m/V]	0.02606	0.02400	0.02381	0.02399	0.02331	0.02420	0.02629	0.02270	0.02527
K_3 [m/V]	0.02625	0.02420	0.02414	0.02445	0.02381	0.02439	0.02668	0.02318	0.02541
Used value	0.0261	0.0241	0.0238	0.0243	0.0235	0.0243	0.0265	0.0230	0.0253

5.1.2. Calibration of electromagnetic flow meters

The electromagnetic flow velocity meters (EMF) have not been calibrated since 2005. A consistency check has been performed to expose any differences among the six instruments. It was found that there was considerable variation in signal strength between the sensors, and thus a commonly used conversion factor between voltage and velocity (0.1 m/s/V) was though of to be too inaccurate. Proper re-calibration (using towing-tank tests) requires an empty flume and is time-consuming. Instead, preliminary calibration is performed by using results of the regular wave experiments, in combination with shallow water wave theory. If deemed necessary, towing-tank tests can be performed at a later stage.

Correction factor

To determine the correction factor, the same regular wave test was repeated for each flow velocity meter. Linear waves would be simplest to analyze, however, the measured orbital velocities would be small with respect to the noise present in the EMF signal (i.e. a small signal-to-noise ratio). Moreover, because relatively large waves are generated during the bichromatic experiments, it is preferred to calibrate the instruments at higher velocities. Stokes' waves are generated for with a period of 2 s, a wave height of 0.1 m, at a depth of 0.75 m.

The resulting Ursell number $U = HL^2/d^3$ of such a wave is approximately 5, well below the demarcation line between Stokes' and cnoidal theory ($U = 26$) and below the maximum value of $U = 10$ recommended in

Holthuijsen [2007]. The steepness H/L is around 0.021, below maximum steepness, as advised in the Coastal Engineering Manual[1];

A single EMF is placed close to the wave maker, at $x = 6$ m. At this distance, evanescence modes are negligible [Noorloos, 2003]. The probe is placed centrally, and at mid water depth ($z = 0.375$ m)[2].

It was mentioned that during manufacturing of the instrument, the box with electronics mounted on top of the EMF was carefully aligned with the direction of the electrodes at the bottom of the probe. The effect of possible small deviations in orientation of the instrument (rotation with respect to the flume x-direction) on the measurements should be negligible [3], therefore the correction factors are calculated directly based on the x-channel output.

After the correction factors are determined for each probe, it is only necessary to calibrate a single EMF to obtain the calibration factor for each probe. The reference probe is chosen to be probe EMF02. The signals of the flow meters have been synchronized by maximizing cross-correlation with respect to EMF02. Any inconsistency with respect to the reference probe is expressed in a factor different from unity. The correction factor is defined by:

$$V_{x,i} = V_{x,1} C \tag{5.2}$$

where $V_{x,1}$ and $V_{x,i}$ and are column vectors, which are the time series recorded by EMF02 and one of the other five EMF, respectively. C is the correction factor calculated in the least squares sense. The results are given in Table 5.2.

Table 5.2: Correction factors for each EMF.

No.	**1**	**2**	**3**	**4**	**5**	**6**
EMF sensor	E02	E06	E08	E11	E12	E13
C [-]	1	1.20	1.05	1.06	1.07	1.05

Calibrating EMF using long wave theory

For purely propagating waves, horizontal velocity and free surface elevation are in phase. This fact could be used to calibrate an EMF, based on an already calibrated wave gauge. It was planned to use the Stokes' wave experiments, not only as a consistency check among the flow meters, but also for calibration purposes. In the seventh run, a wave gauge was installed for free surface elevation measurements. A ramping function is by default applied to smoothly start wave generation. As a consequence, reflections are already present in the signal before the incident waves are at full height. In other words, Stokes ' theory for unidirectional waves cannot be used. Moreover, the velocity measurements were slightly asymmetric (about the vertical), while the wave gauge registered a symmetric signal, which is most likely due to reflection against the fore reef slope. Based on these two observations, it was decided that calibration using the Stokes' wave measurements would be too complicated. The velocity measurements of the Stokes' wave experiments are nonetheless useful to determine the correction factor (previous section); as long as the test conditions are consistent, they can be used for the determination of the correction factor.

Calibration based on long wave theory is perhaps more suitable and generally less complex. The fact that for long waves the horizontal velocity is almost uniform over depth has obvious advantages. First of all, since vertical velocities are small, the streamlines are approximately aligned with the horizontal plane through the disk-shaped probe, similar to towing-tank tests (where the probe is moved in the horizontal xy-plane through

[1] The maximum steepness is often calculated as the steepness for which the magnitude of the third stokes expansion term is less than 1% of the second term: $H/L = 1/7 \sinh(kd)^3/\sqrt{(1+8\cosh(kd)^3)}$ see Coastal Engineering Manual EM 1110-2-1100 part 2 equation II-1-113.

[2] The probe could have been positioned higher up in the water column at, close to the surface, where orbital velocities are highest. However, because of the curvature of the horizontal velocity profile (for waves in deep water, but also in intermediate water depths), the vertical gradient in horizontal velocity is significantly larger near the surface than lower in the water column. Near the surface, a slightly incorrect vertical position of the probe would result would result in a significant error in measured orbital velocities (larger than 1% per mm).

[3] From the EMF y-channel it was found that some probes were most likely installed under a slight angle (with respect to the flume x-axis), because the y-signal clearly showed oscillations associated with the waves. Using standard trigonometry:

$$V_{x,flume} = V_{x,EMF}\frac{1}{\cos\theta} \quad \text{or} \quad V_{x,flume} = V_{y,EMF}\frac{1}{\sin\theta} \tag{5.1}$$

Any possible angle between instrument and flume x-direction is small ($|\theta| < 5°$), and the resulting error in the measurements is effectively negligible (relative error < 0.5%). For small angles, $V_{x,flume} \approx V_{x,EMF}$

the electrodes). Secondly, the discharge can be easily calculated based on the velocity measurements, without taking any velocity distribution into account.

As stated by the manufacturer, the measured voltages are proportional to the liquid velocity parallel to the plane of the electrodes:

$$u = KV_x. \tag{5.3}$$

where K is the calibration coefficient and V_x is x-channel output in volt. If we assume that the generated waves are purely propagating waves, the calibration factor could be calculated directly using the free surface elevation measurements[4]. More so than with short generation, reflections pose a significant problem. Since the flume length is limited (especially in our case, with the reef already in place) and wavelengths are in the order of tens of meters, waves are already partially reflected during generation.

If both the incident long wave and outgoing reflections would be known, it would be possible (using Eq. E.3 for both the incoming and outgoing wave) to calculate the total depth averaged velocity:

$$U_\zeta = \frac{Q^+ + Q^-}{d+\zeta} = \frac{c^+\zeta^+ + c^-\zeta^-}{d+\zeta} \tag{5.6}$$

By equating this to the measured velocity, the calibration factor between voltage and velocity could be computed. In the regular long wave experiments, only the *total* free surface is known (measured by the offshore wave gauge). To overcome this, it is assumed that the generated Cnoidal wave is indeed a permanent wave (there is only a difference in phase between wave paddle and wave gauge). Thus we have for the outgoing waves:

$$\zeta^- = \zeta - \zeta^+ \tag{5.7}$$

where ζ^+ is the free surface elevation according to cnoidal wave theory (used earlier to calculate the paddle motion). Substition of this expression in Eq. gives:

$$U_\zeta = \frac{Q^+ + Q^-}{d+\zeta} = \frac{c^+\zeta^+ + c^-\left(\zeta - \zeta^+\right)}{d+\zeta} = \frac{\left(c^+ - c^-\right)\zeta^+ + c^-\zeta}{d+\zeta} \tag{5.8}$$

which can be equated to the unknown measured velocity, Eq. 5.3, to calculate the calibration coefficient of the EMF using a wave field with incident and outgoing long waves:

$$K = \frac{1}{V_x}\frac{\left(c^+ - c^-\right)\zeta^+ + c^-\zeta}{d+\zeta} \tag{5.9}$$

c^+ is the cnoidal wave speed, and c^- is the shallow water wave speed $\sqrt{gd}$. For calibration, only the regular long wave tests with the largest period and smallest wave height have been used, namely experiments C3 and R5. It has been verified with stream function theory that vertical variations in horizontal velocity should be negligible for these test conditions.

For reference, a similar procedure is followed, but now based on the theory of Boussinesq (Eq. 4.47). The resulting discharge is divided by the theoretical cnoidal wave speed $c^+ = c_{cn}$, which yields the incident free surface elevation. This is compared with the free surface elevation according to cnoidal theory. The calibration coefficient is calculated using a non-linear least squares method. For each experiment, resulting calibration coefficients for probe EMF02 are shown in Table 5.3. The average of 0.103 is finally chosen to be the calibration coefficient for EMF02. Table 5.4 gives the calibration coefficients (including correction factor) for the other five probes.

[4]Making use of the relation between depth averaged velocity and surface elevation from the previous chapter, Eq. E.3, the calibration coefficient can be determined by equating this expression to the measured x-velocity:

$$u = U_\zeta \tag{5.4}$$

where U_ζ is the depth averaged velocity. The subscript signifies that it is based on surface elevation measurements. The calibration coefficient is calculated using a least squares method from:

$$K = \frac{1}{V_x}\frac{c\zeta}{d+\zeta} \tag{5.5}$$

Table 5.3: Calibration coefficient for probe EMF02, for each experiment. The results are given for the two different methods.

Experiment	**R1**	**R2**	**R3**	**R5**	**R7**
K [m/s/V]	-	-	0.1034	0.1009	0.1039
$K_{Boussinesq}$ [m/s/V]	0.1007	0.1017	0.1052	0.1025	0.1038

Table 5.4: Calibration coefficient for each probe.

No.	**1**	**2**	**3**	**4**	**5**	**6**
EMF sensor	E02	E06	E08	E11	E12	E13
K [m/s/V]	0.103	0.124	0.108	0.109	0.110	0.108

5.2. Verification of the Boussinesq decomposition method

Now the calibration coefficients for both the wave gauges and flow velocity meters are known, it is possible to verify the decomposition method outlined in section 4.3 using experimental data. For long waves of small amplitude, we have following estimates for the discharge:

$$Q_0 = Ud \quad \text{and} \quad Q_0^+ = c_0\zeta$$

Based on velocity and surface elevation measurements of a right-traveling wave one can use these estimates to verify whether the method of [Guza et al., 1984] is applicable.

The undular bores observed on the reef are highly nonlinear and dispersive. The propagation velocity is not constant; waves are deforming because nonlinear and dispersive effects are not exactly in balance. To assess whether the Boussinesq decomposition method can be used with data, Nwogu's expression for the discharge (Eq. 4.23) is compared with our expression for the incident discharge, Q^+:

$$Q^+ = c_0\zeta + \frac{M}{2c_0} \quad \text{where} \quad M = u_\alpha^2 h + \frac{1}{2}g\zeta^2 + \frac{1}{3}d^2\zeta_{tt}$$

Note that this follows from Eq. 4.47 if Q^- is set to zero. To first order, $Q = Ud$ and $Q^+ = c_0\zeta$. In other words, Q is mainly determined by the flow velocity measurements, whereas Q^+ is dictated by the free surface measurements. The advective term has been approximated by $u_\alpha^2 h$. As mentioned in section 4.3, second-order derivatives in space are replaced by derivatives in time, which are in subsequently approximated making use of a digital filter (a Savitzky–Golay filter).

For verification, both long wave theory and the theory of Boussinesq are applied to the regular wave experiments. For a duration of approximately 23.5 seconds, the wave field on the reef flat can be characterized as unidirectional (purely incident)[5]. Neglecting any form of dissipation, this means that the free surface elevation and the discharge are in phase during this time interval.

For all experiments, Fig. 5.1 shows the two estimates, for the discharge of the first wave propagating over the reef flat. Measurements obtained at position 7 and 8, 11 and 12, 15 and 16 are used. Measurements obtained at position 19 and 20 are not used because the instruments are located too close to the beach; reflections are almost immediately visible in the time series.

Agreement is quite good. First of all, there is some minor discrepancy near the troughs of the undulatons. Secondly, at location 7 and 8, for experiment 3, 5 and 6, Q is larger than Q^+ for the falling part of the time series (corresponding to the back of the wave profile). Overall, we feel confident that the Boussinesq decomposition procedure should give accurate estimates for Q^+ and Q^-. Possible error sources include:

1. Fundamental errors:
    - assumption that motion is irrotational; the effects of bottom friction and turbulence due to wave breaking are neglected

[5] The reef flat is approximately 21 m wide and 8.1 cm deep. The duration it takes for a wave to travel from the reef crest to the beach toe can be estimated by:

$$\Delta t = \frac{\Delta x}{\sqrt{gd}} \tag{5.10}$$

which is approximately 23.5 s in the present case. However, it does takes some additional time for the reflected wave to reach a certain wave gauge. Hence for the instruments at the first position on the reef flat (position 7), no reflections are present in the time series up to approximately 40 seconds.

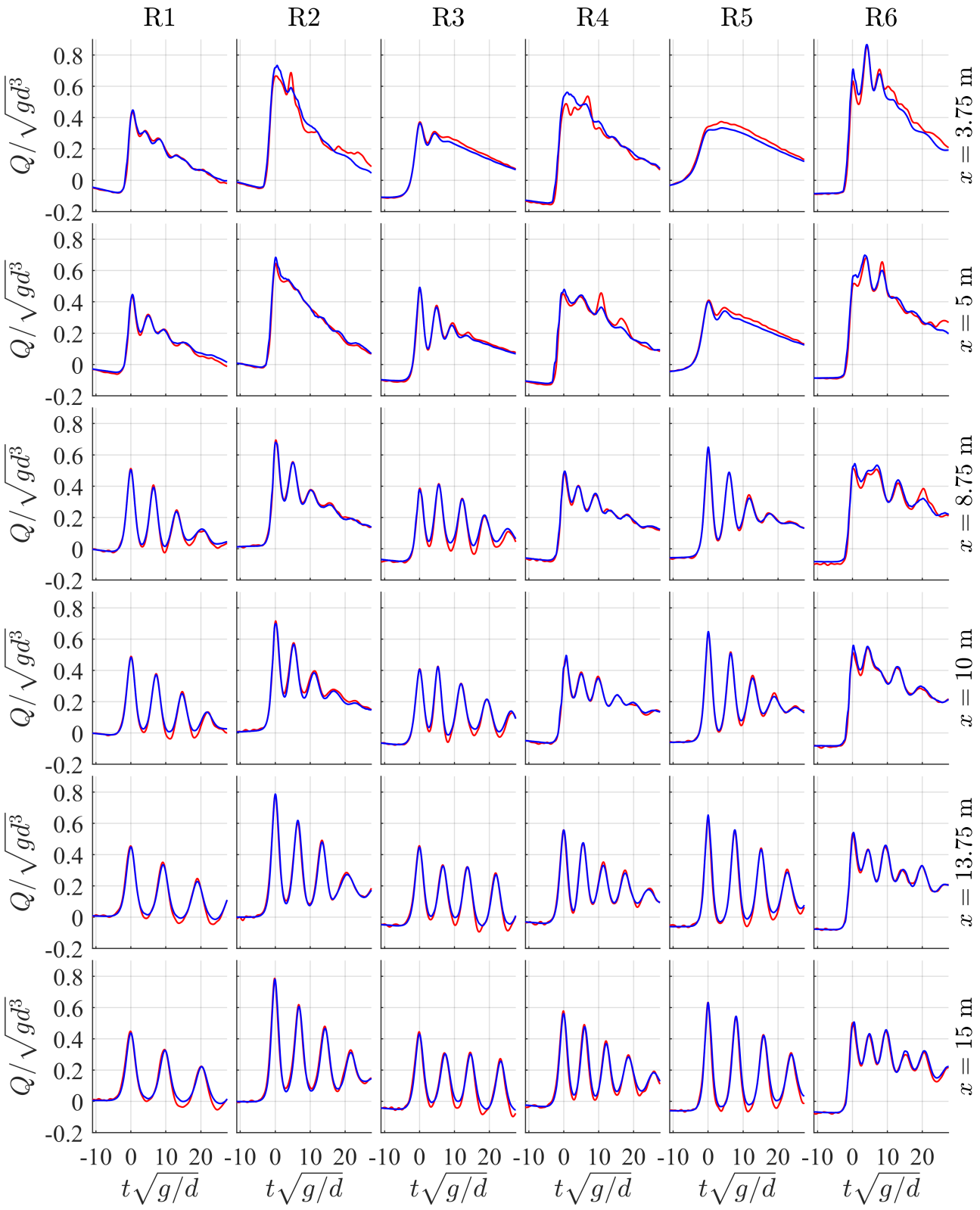

Figure 5.1: Decomposition of an undular bore. The time-series of the surface elevation (top) and discharge (bottom figures) are show at: (left) at $x = 100d$, before the undular bore has reflected against the closed end (middle) at an arbitrary distance, $x = 190d$, after the bore has reflected and (right) at the closed end at $x = 200d$, where we have $Q^+ = -Q^-$ and $\zeta^+ = -\zeta^-$.

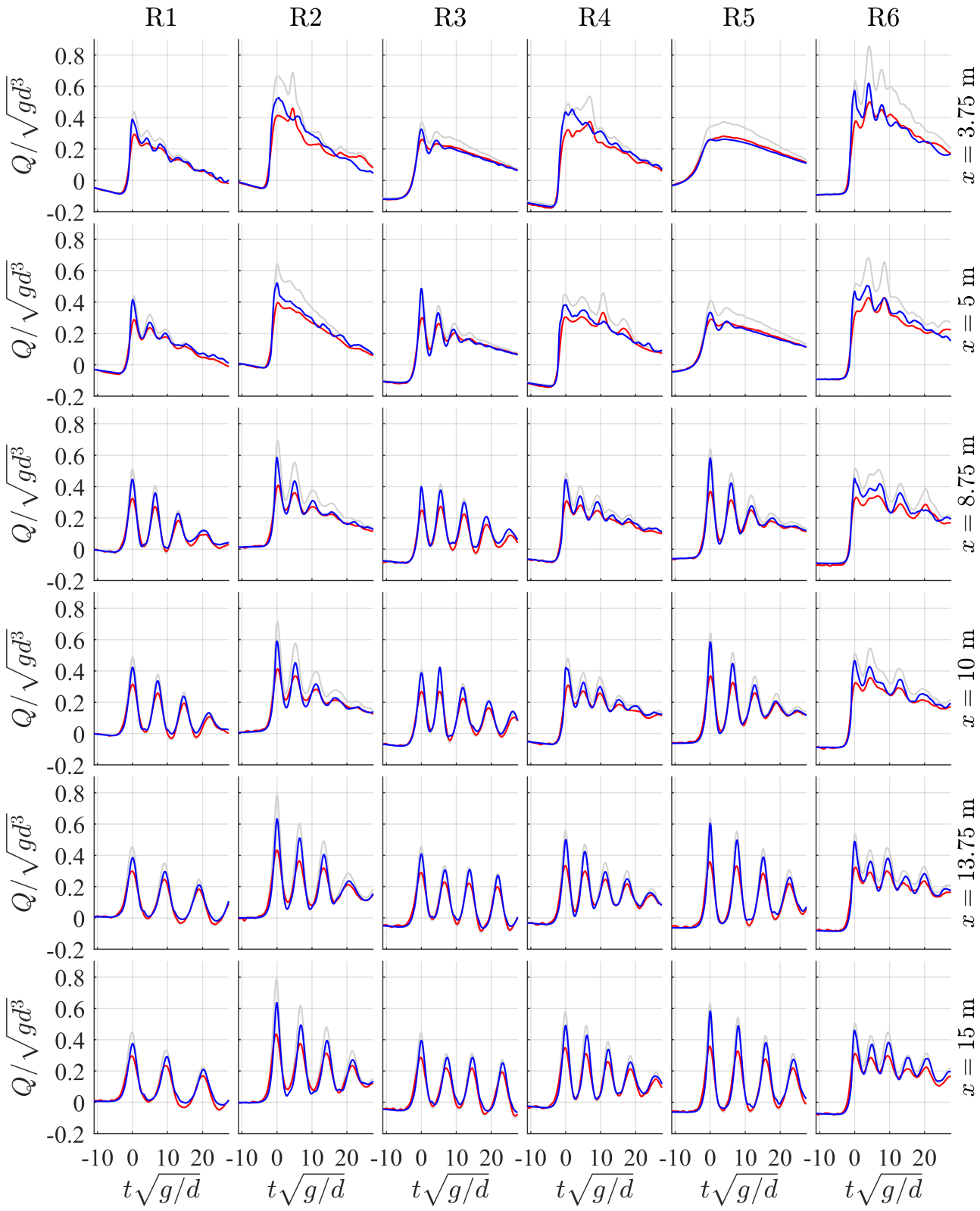

Figure 5.2: Decomposition of an undular bore. The time-series of the surface elevation (top) and discharge (bottom figures) are show at: (left) at $x = 100d$, before the undular bore has reflected against the closed end (middle) at an arbitrary distance, $x = 190d$, after the bore has reflected and (right) at the closed end at $x = 200d$, where we have $Q^+ = -Q^-$ and $\zeta^+ = -\zeta^-$.

2. Further approximations and truncation errors:

   - truncation of higher order terms (for example in Eq. 4.16)
   - assumption that the deviation from the linear shallow water wave speed is small (Eq. 4.32)
   - replacing second-order derivatives in space by temporal derivatives
   - numerically approximated second-order derivatives

3. Measurement errors

   - inaccuracies in calibration values
   - inaccuracies in the measured signals
   - inaccuracies in the measured depth
   - inaccurate placement of the instruments; EMF and wave gauge were sometimes slightly spaced apart in horizontal direction (up to 0.5 cm).

A combination of these errors explains the mentioned discrepancies. Both linear estimates, $Q_0 = u_\alpha d$ and $Q_0^+ = c_0\zeta$, consistent with the method of [Guza et al., 1984], are show in Fig 5.2. Q and Q^+ have been included for reference. At the outer reef flat, where nonlinearity dominates over dispersion, Q_0 and Q_0^+ both underestimate the discharge. For significantly developed undulations, for example at the mid to inner reef flat, especially Q_0 results in a significant underestimation.

5.3. Wave run-up meter

Smooth time-series of the shoreline position have to be derived from the discrete run-up measurements. First, the measured output is converted to the "number of wet pins", by dividing the output by 150 mV and appropriately rounding off the result to yield an integer number per time sample.

While the original raw signal is recorded at 100 Hz, this does not mean that every sample can be converted to shoreline elevation. When the shoreline position is located between two pins, a constant voltage is recorded, associated with the highest wet pin. This results in a staircase-like signal. Only during a change in voltage (or equivalently, a change in wet pin number), the position of the free surface at the beach slope (the shoreline position) is known. Hence, only the value at that moment is stored during post-processing, while the remaining samples are discarded. Both during the run-up and run-down process, only the highest value is saved when the number of wet pins increases.

The vertical elevation of the free surface at the shore-line is obtained from the time-series of wet pin number in time. To convert between pin number and elevation, the exact location of the pins has to be known. The first pin is located 22.5 cm from the beach toe (measured along the slope). Using the known spacing between the pins (2.5 cm), the excursion of the remaining pins can be readily calculated. As the bathymetry at the beach is measured every 10 cm, the vertical position of a pin is obtained by means of interpolation.

The last step is to resample the time-series at 100 Hz, here done using shape-preserving piecewise cubic interpolation; a standard Matlab function. The final results are time-series of the horizontal and vertical components of the instantaneous shoreline position, the latter here simply called "the run-up".

A few practical remarks follow:

1. It was observed in the flume that the shoreline motion has a 3D character. As the instrument only measures along a transect (in cross-shore direction) along the beach, and it only registers a single value in time, it does not capture the true 3D characteristics of the shore-line motion. The run-up meter only registers the (current) highest elevated wet pin in time, along the transect.

2. The pins have a plastic cap (for insulation) of around 1-2 mm, which means that the resulting time-series can be considered to be a slight underestimation of the "real" run-up.

3. Small plastic grains were present in the water tank. Floating grains would sometimes wash ashore, and could possibly get stuck between a pin and the cable.

5.4. Composition of synchronized time series

For all regular wave experiments, two sessions were carried out in order to increase the spatial resolution (number of measurements per experiment). The experiments were repeated using identical test conditions, but the instruments were moved. The same was done for 4 out of the 11 bichromatic experiments. The free surface elevation signals of the first wave gauge, obtained during session 1 and 2 respectively, were synchronized by maximizing cross-correlation.

5.5. Steady state conditions & Phase averaging

Steady state conditions are reached for all experiments within the first 15 minutes. The last $D = 1000$ s (i.e. 100 wave lengths for case R3 and R4) are used for in the frequency domain section for spectral analysis. The time domain analysis requires phase averaging, which is also done over duration D. Phase averaging is performed to average out all variably, in order to get the mean wave profile. This is especially important when wave-breaking is involved due to its stochastic nature. Unfortunately, a small but constant time-lag ($0.5 \cdot 10^{-}4$ s per second) was observed, which complicated phase-averaging. It is unclear if the consistent error is of physical nature: for example the wave-generation method (or active reflection compensation), or perhaps it is due to a circulation under the reef structure.

6

Undular bore formation over a fringing reef: a time domain analysis

In the present chapter, undular bore formation on a fringing reef is studied in detail in the time domain. Ch. 7 continues with a detailed spectral analysis, which is complementary to the present analysis. In general, one can directly extract characteristics of individual waves from the measurements in the time domain. A spectral analysis provides us information about the harmonic components (such as amplitudes and phases) and the energy distribution.

The undulations are often collectively referred to as the secondary wave field. In the early stages of the dispersive long wave breaking process, an undulating periodic bore can be thought of as a short wave structure riding on top of an underlying long wave. The transformation of a long wave into an undular bore is clearly visible in the time domain. Since growth of the leading undulation leads to an increase in height of the wave front, we focus on the leading undulation in the time domain analysis. The growth of undulations and decay of the underlying long wave can be seen as a redistribution of energy; energy transfer from low to high frequencies. This can be analyzed in detail in the frequency domain.

First, the decomposed time series will be shown at several successive locations throughout the flume (section 6.1). The surface elevation measurements of two representative tests will be shown side-to-side, to point out qualitative differences and similarities between undulating swell and IG-scale waves. To give a clear overview of both classes of waves, the measured surface elevation will be visualized in space-time diagrams. The incident signal, will be highlighted in section (6.2). A Hovmöller diagram will be used to describe the wave transformation process, that both swell waves and IG-scale waves undergo as they propagate across the reef flat towards the beach, in detail. The most important characteristics of the leading undulations are given in the following section (6.4). In section 6.5, special attention is given to the velocity of propagation.

6.1. An introduction to the results

For the first six regular wave tests (R1-6), cnoidal waves were generated at the wave paddle. Tests R1 and R2 represent swell wave cases, while R3-R6 represent IG-scale waves.

The evolution of free surface for a typical IG-scale wave test (R5) is shown on the left side of Fig. 6.1. A typical swell case (R2) is shown on the right side, at the same successive wave gauges throughout the flume. Note that the stationary part of the time-series is ensemble-averaged (for more robust statistics) and repeated for several wavelengths (for visualization purposes). The subplots correspond to the following cross-reef locations: (a,b) offshore, (c,d) at the fore-reef slope, (e-n) at the reef flat and (o,p) at the shore-line. In addition to the total free surface elevation (shown in blue), the decomposed incident (red) and reflected waves (green) are included in the figure (except at the shoreline, where only the swash motion is shown).

Test R5 has been chosen in this introductory paragraph, because incident cnoidal wave has the longest period (converted to prototype, $T_p \approx 90$ s or $f_p \approx 0.011$ Hz) and smallest offshore wave height ($H_p \approx 0.4$ m) considered in the regular wave tests. Due to the moderate wave height, test R5 involves little to no turbulent wave-breaking; it is expected that the major part of the net influx of energy supplied to the front, is radiated away by means of formation of undulations (as opposed to being dissipated through generation turbulence). In contrast, the cnoidal waves generated during test R2 have typical swell wave scales; a period in sea-swell

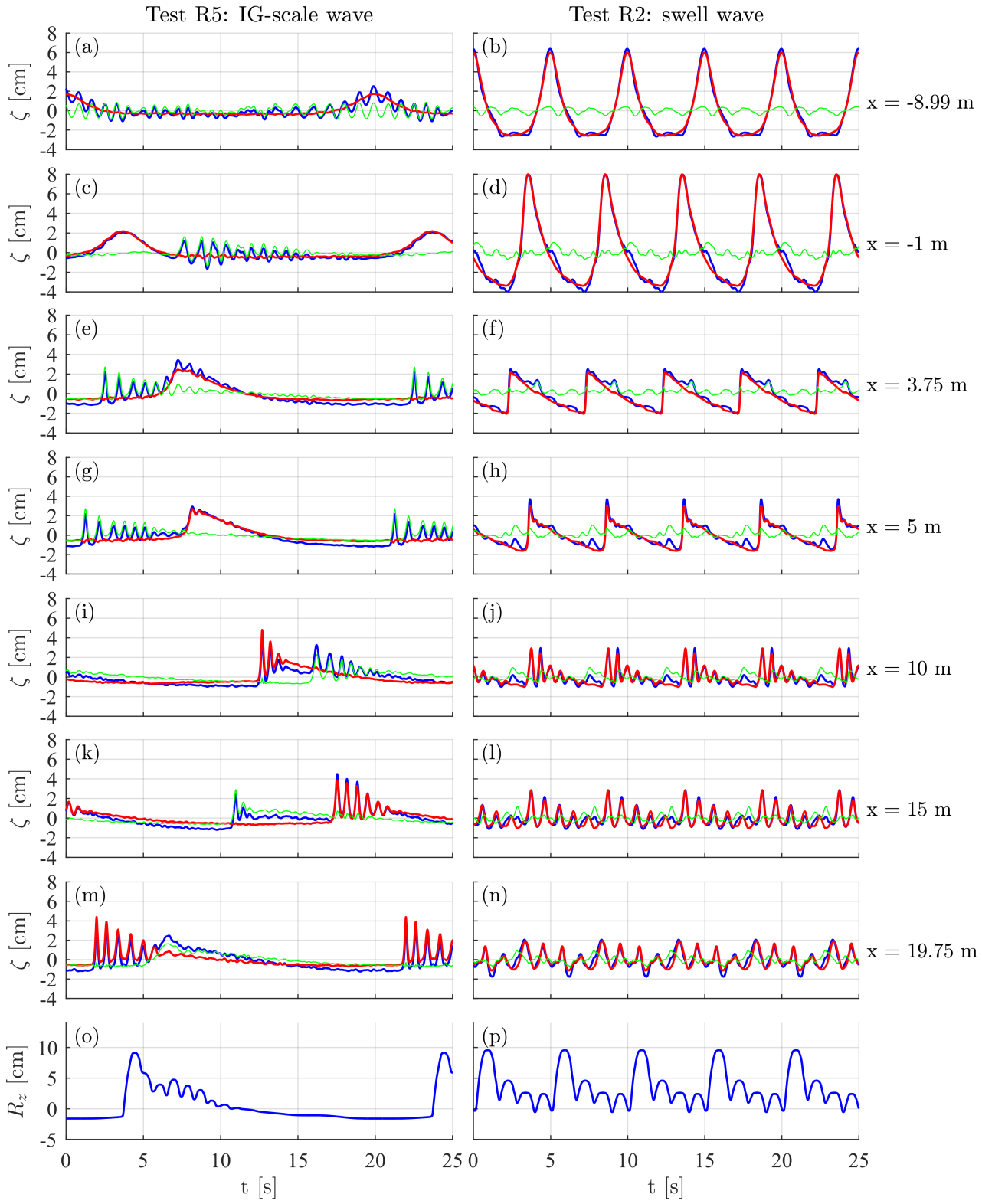

Figure 6.1: Wave transformation and undular bore formation over the fringing reef profile. (left) IG-scale test, R5 ($T = 20$ s, $H = 2$ cm), (right) swell wave test, R2 ($T = 5$ s, $H = 8$ cm). The surface elevation is shown at several cross-reef locations: (a,b) offshore, (c,d) fore-reef slope, (e-p) reef flat, (q,r) shore-line. The following ensemble-averaged signals are plotted: (blue) total free surface elevation with respect to mean water level, $\zeta - \bar{\zeta}$, (red) incident signal, ζ^+, (green) reflected signal, ζ^-. The last two plots (q,r) show the vertical elevation of the free surface at the shore-line in time, denoted by R_z.

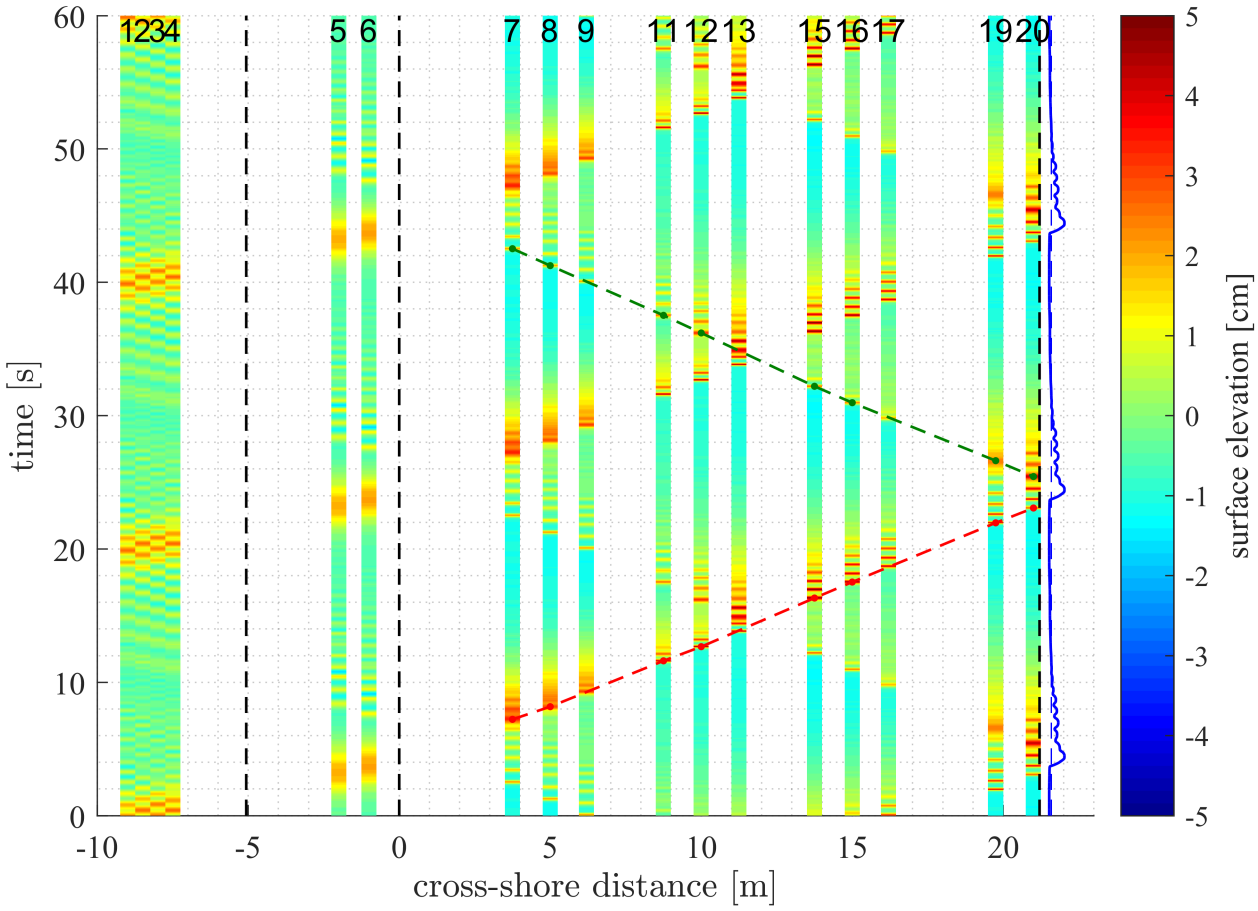

Figure 6.2: Space-time (or Hovmöller) diagram of free surface elevation for experiment R5. The color intensity of each time-slice represents the (total) free surface elevation at that location. The instrument location numbers are shown on top of each time-slice. The trajectory of this leading crest is shown: (red) incident long wave, (green) reflected long wave. At the beach, the horizontal component of the swash motion is given.

part of the spectrum ($T_p \approx 22$ s or $f_p \approx 0.045$ Hz), and a considerable wave height ($H_p \approx 1.6$ m). As a consequence of the large wave height to reef depth ratio (slightly larger than one), these swell waves break violently around the reef crest. From here on, all parameters are given in model scale.

A quick glance at the time-series of either test R2 or R5 reveals that undulations are formed over the reef flat. Where the incident waves initially had a single crest, halfway the reef flat, at $x = 10$ m, multiple prominent crests can be observed. In fact, for all six regular wave tests considered, the shoreward traveling long wave eventually transforms into an undular bore over the reef flat. Interestingly, not only the incident wave, but also the reflected wave transforms into undular bore while propagating across the reef flat. We will come back to undular bore formation in extensive detail later.

Let us for now focus on the most offshore wave gauge (Fig. 6.1a,b). At first sight, the total free surface elevation at the horizontal offshore section only vaguely resembles a permanent cnoidal wave. As becomes clear, the reflected waves contribute significantly to the total surface elevation, and the free surface could be seen as a superposition of approximately linear reflected waves on the incident cnoidal wave signal. Indeed, the decomposed shoreward traveling wave does match the permanent cnoidal wave form forced at the wave paddle. Reflection is especially significant for the IG-scale cases, see Fig. 6.1a. It is clear that decomposition is crucial to properly analyze wave transformation.

The reflected wave signal at the offshore location can be further broken down in a long wave reflection and a high frequency part. The incident cnoidal wave is reflected against the fore-reef slope, which causes a seaward traveling small amplitude long wave. The high frequency reflections are actually the undulations, which originate from the incident undular bore reflecting against the beach. They seem to get a more linear character as they leave the reef flat and disperse into deeper water.

On the fore-reef slope (Fig. 6.1b,c), the shoaling process is apparent, noticeable by the increase in wave

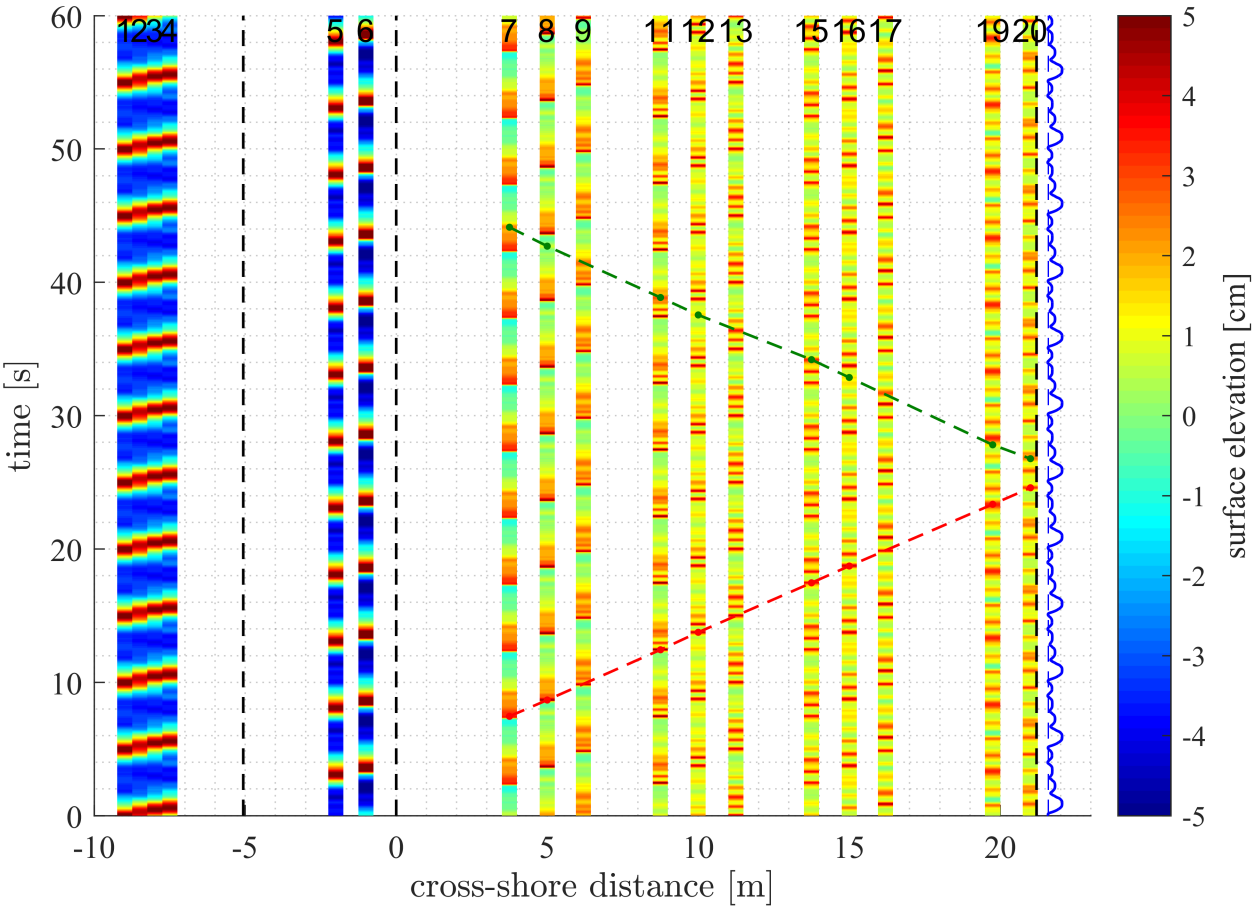

Figure 6.3: Space-time diagram of free surface elevation for experiment R2. See caption Fig. 6.2.

height, which is known to be accompanied by a decrease in wavelength. While the front of the swell wave steepens considerably on the slope, the incident wave for the IG-scale experiment stays reasonably symmetric around the vertical. Skewness and asymmetry are subject of section 6.3.2.

For a clear spatial overview, the measured surface elevation is visualized in space-time diagrams (Fig. 6.2 and 6.3). A space-time diagram (alternatively named Hovmöller diagram), lends itself perfectly for a "birds-eye view" of the hydrodynamic processes on the reef. For each so-called time-slice, the instrument location number is shown on top. The color intensity of each time-slice represents the (total) free surface elevation at that location. The first four wave gauges in Fig. 6.2 show a "checkerboard pattern", instead of a smooth cnoidal wave shape. As explained earlier in this section, the cnoidal wave shape is masked by the significant superimposed reflections, associated with the seaward traveling undular bore. Section 6.4 shows Hovmöller diagrams for the decomposed incident signal, which corroborates this. The wave transformation process can be investigated in space-time by following a wave across the reef flat. For this purpose, the crest of the leading undulation is tracked in space and time, as will be detailed in section 6.4. Each Hovmöller diagram shows the trajectory of this leading crest, both for the incident and reflected long wave.

6.2. Undular bore formation over the reef flat

The qualitative description continues with a focus on wave transformation over the reef flat, where the long wave transforms into an undular bore. Even though for every test undular bores are observed, the exact point on the reef flat where undular bore formation is initiated depends on the wave conditions. The transformation process is governed by the complex competition between non-linearities, dispersive effects and energy dissipation [Tissier et al., 2011b].

Table 6.1 re-states the test conditions and gives a classification of the long waves. The breaker types are based on the Iribarren number (calculated using the fore-reef slope and the offshore wave steepness). Furthermore, the table provides the resulting bore types observed at different sections of the reef flat. The bore

Table 6.1: Classification of the breaking long waves. The test conditions are re-stated (d_{reef} = 8.1 cm for all cases and has thus not been specified). The breaker types and bore types are listed. The latter is separately determined for each reef flat section (outer, mid and inner reef).

Test case	wave type	T [s]	H [cm]	Fore-reef	Outer reef	Mid reef	Inner reef
R1	swell	5	4	plunging	turbulent	interm./undular	undular
R2	swell	5	8	plunging	turbulent	interm./undular	undular
R3	IG-scale	10	2	-	undular	undular	undular
R4	IG-scale	10	4	-	intermediate	undular	undular
R5	IG-scale	20	2	-	undular	undular	undular
R6	IG-scale	20	4	-	intermediate	intermediate	intermediate

types are separately determined for the outer, mid and inner reef. This is visually determined and based on the measured profiles. Remember that bores classified as intermediate, are undular bores with breaking fronts.

6.2.1. IG-scale waves

The four IG-scale wave tests (R3-6) are treated first. Fig. 6.4 shows the incident waves at each location side-by-side, to enable a direct comparison among the four different IG-scale wave cases. For all four cases, the long wave breaks on the outer reef; it seems that nonlinearity is large enough for the long wave to steepen and break at the outer reef.

During test R3 and R5, long waves were generated with relatively small wave heights. These long waves transform smoothly into undular bores with little to no *turbulent* wave breaking involved. At the outer reef flat, non-linearity dominates over dispersion; the wave front steepens (and at the same time the back flattens). As the front becomes steeper, dispersion becomes increasingly important. At a certain point, the front slope reaches a maximum and the long wave breaks in a dispersive manner. This marks the start of *dispersive* long wave breaking. For case R3 the wave breaks approximately at x = 3.75 m (Fig. 6.4g), while for case R5 the first undulations start to appear in Fig. 6.4j (x = 5 m). Breaking happens earlier for waves with a smaller wavelengths (or periods), which is in quantitative agreement with the solution of [Stoker, 1957], discussed in intermezzo 6.1.

Intermezzo 6.1: Dispersive wave breaking

The observation that shorter and higher waves break earlier agrees qualitatively with the formula of [Stoker, 1957]. The breakpoint of a sinusoidal wave, $x_{b,sin}$, is given by:

$$\frac{x_{b,sin}}{d} = \frac{2}{3\pi}\frac{T\sqrt{gd}}{H}$$

The expression is based on the method of characteristics (see Appx. B), solving the nonlinear shallow water equations. Dispersion is disregarding completely. Numerical simulations confirm that up to the breakpoint, it provides a good approximation for long waves, see for example [Madsen et al., 2008]. The table below compares Stoker's formula with the observed breakpoints. $x_{\mathrm{b,obs,1}}$ is derived from the free surface time-series. It is based on the rate of surface rise (ζ_t) for the turbulent/intermediate bores (R4 and R6) and based on the appearance of undulation for the undular bores (R3 and R5). $x_{\mathrm{b,obs,2}}$ is the breakpoint of the turbulent breaking waves (R4 and R6), as observed in the flume; the distance from the reef crest where we first observe air entrainment. The wave-height on the reef, H_{reef}, is estimated by application of Green's shoaling law. Between parentheses, an alternative value is given for H_{reef}, based on the concept of wave transmission and reflection at a abrupt junction (see [Madsen et al., 2008]).

Test case	T [s]	$\mathbf{H}_0$ [cm]	$\mathbf{H}_{\mathrm{reef}}$ [cm]	$\mathbf{x}_{\mathrm{b,sin}}$ [m]	$\mathbf{x}_{\mathrm{b,cos}}$ [m]	$\mathbf{x}_{\mathrm{b,obs,1}}$ [m]	$\mathbf{x}_{\mathrm{b,obs,2}}$ [m]
R3	10	2	3.3 (2.9)	4.67 (5.24)	3.60 (4.27)	≈ 3.75	-
R4	10	4	6.6 (5.9)	2.33 (2.62)	0.65 (1.02)	< 3.75	≈ 2.30
R5	20	2	3.3 (2.9)	9.30 (10.48)	7.16 (8.54)	≈ 5.00	-
R6	20	4	6.6 (5.9)	4.65 (5.24)	1.28 (2.05)	$5 > x > 3.75$	≈ 3.95

It turns out to be that a sine wave breaks at its foot ($\zeta = 0$), while a cosine wave becomes vertical at a

position much lower elevated in the wave profile (close to the trough), since the complete front is included. As a result, breaking happens after a shorter distance for the latter wave profile. $x_{b,cos}$ is also included in the comparison table (the breakpoint has been computed numerically). See figure below for an illustration of the breakpoint in both cases (for test R7).

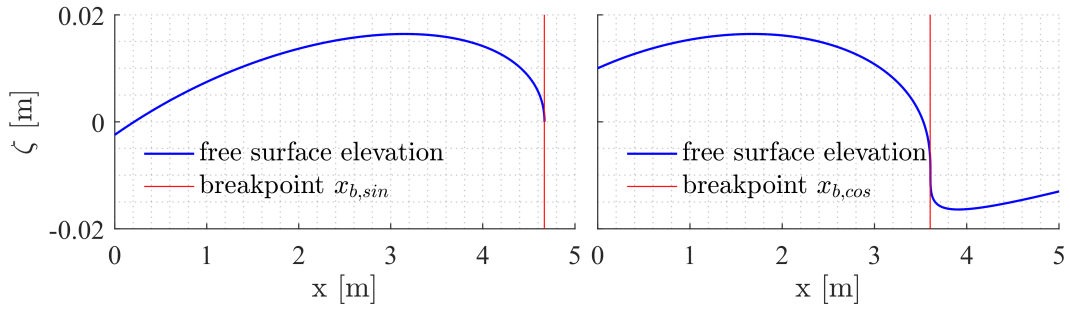

As can be seen from the table, neither method for the breaking distance consistently produces accurate results. This comes as no surprise because Stoker's expressions assumes:

- a sinusoidal wave shape,
- uni-directional wave propagation,
- and a horizontal bottom.

Hence if these conditions are not met, the formula should not be used for quantitative analysis (as we have done here). The major error sources seem to be of fundamental nature: the mismatch in wave shape (sinusoidal versus cnoidal) and the oversimplification of the shoaling process of long waves (for example, the increase in asymmetry about the vertical is completely ignored up to the reef crest).

Test R3, R3 and R4 are modeled using SWASH to clarify this matter. The measurements are compared with the SWASH results. Subsequently it is investigated if the MoC is a reasonable method to estimate the breakpoint. We focus on the initial part of the measurements ($t < 45$ s), such that no reflections are visible yet.

In the figure below, both the modeled free surface (SWASH) and measured surface elevation is shown at six subsequent wave gauges. The modeled free surface (shown in red) agrees well with the measured free surface (blue). The HFA appromation of [Smit et al., 2013] is used; the breaking process is initiated in SWASH $\frac{\partial \zeta}{\partial t}/c_0 > 1.0$. The breaking front is shown in green. The analytical solution according to the method of characteristics is also included, for which the boundary condition is taken from the SWASH simulation (the free surface at the reef crest). Up to the breakpoint the method of characteristics agrees well with model results and measurements. Hence the start of dispersive wave breaking can be determined from the NLSWE

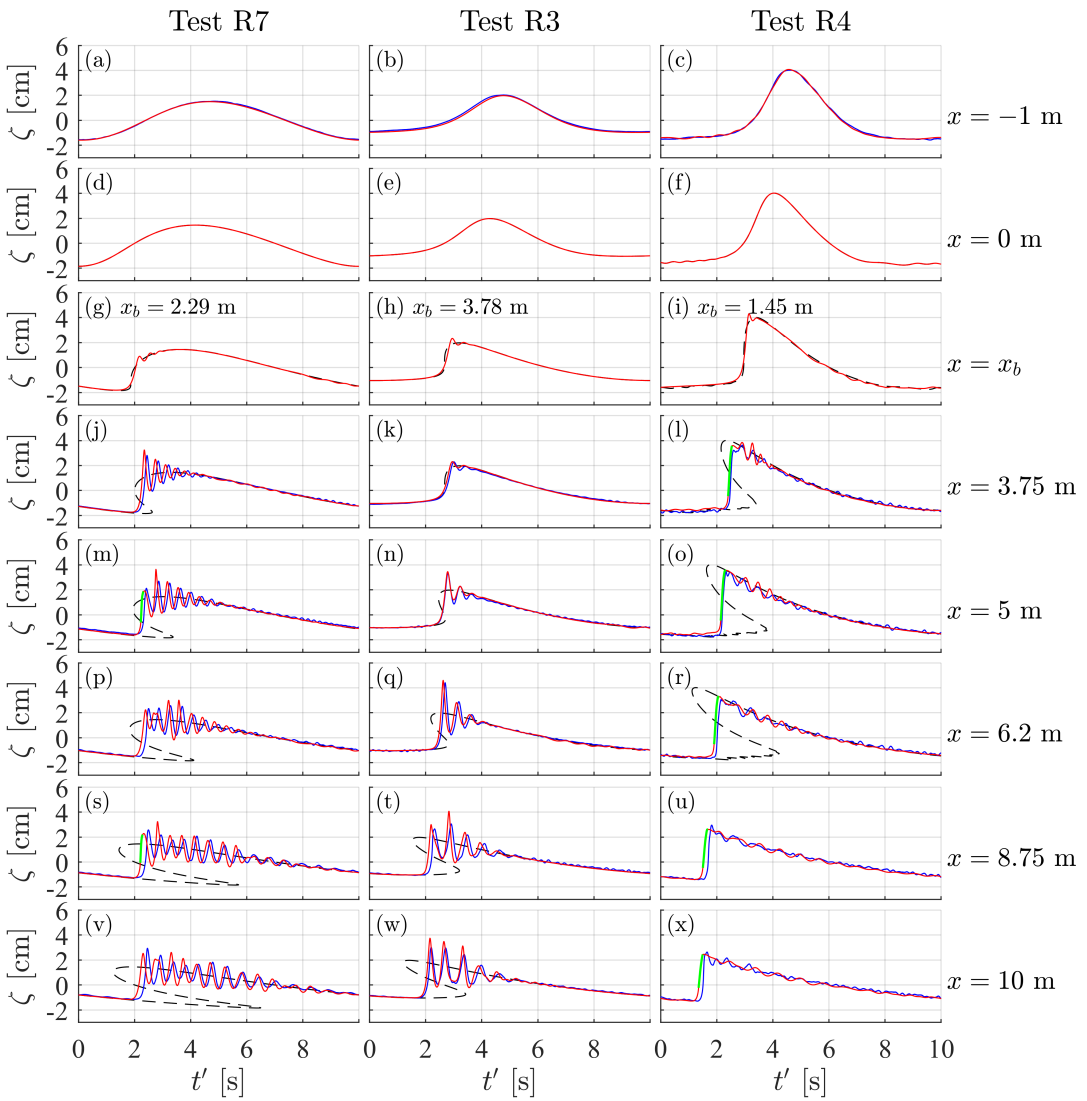

Following the bore front on the reef flat, the situation resembles the formation of a classical undular bore (from a transition between two states of uniform flow). The wavelength (of the underlying long wave) is much larger than the reef depth ($L/d > 200$), as a result the back of the breaking wave is mildly sloping. Hence it is no surprise that the behavior (near the front) is — at least in a qualitative sense — largely similar to the classical stepped bore case[1]. For such a stepped bore it is known that the resulting bore is of the purely undular type (no turbulent wave-breaking) if the bore strength $H/d = 0.3$. For test case R5 around the breakpoint, $H/d \approx 0.35$, which means that (according to Favre's classification[2]) the bore has to be classified in the intermediate (or transient) bore regime.

A stepped bore has a flat back and a constant net influx of energy, which is carried away by the undulations developing behind the front. The absence of a constant supply of energy to the front in the long wave case might modify Favre's classification (the conditions for which undular, intermediate and turbulent bores develop). This could potentially explain fact that little to no wave-breaking is involved in our long wave case $H/d = 0.35$. Unfortunately this is merely speculation. To properly classify undular and turbulent breaking long waves in a similar to what [Favre, 1935] did for stepped bores, would require a larger number of experiments with varying H/d and L/d.

The remaining subplots of Fig. 6.4 show the development of the undular bore up to the beach. Energy continues to be radiated away from the wave front. Quantitatively, wave transformation on the reef for test R3

[1] According to [Madsen and Mei, 1969], the stepped bore, with its horizontal back, is the limiting case for all other undular bore phenomena.

[2] Recall that the intermediate bore regime is experimentally determined by Favre within the range $H/d = 0.28 - 0.75$.

and R5 is similar. The general undular bore shape is familiar, a large leading undulation, followed by smaller trailing undulations decreasing in size. The crest heights of the leading and trailing undulations increase as the undular bore travels across the reef. In general we can conclude that as undular bores travel a longer distance they become more developed; not only the the amplitudes, but also wavelengths of the undulations increase. The underlying long wave becomes increasingly less visible.

The leading trough (behind the first crest) seems to reach a minimum and becomes approximately equal to the base just in front of the first undulation. This again agrees with a stepped bore, for which the troughs ultimately reach the downstream level.

Because the breakpoint is earlier for waves with smaller wavelengths, at any location the undulations are more developed for case R3 than for R5. Near the beach the undular bores are well developed in both cases. There, for case R3, the effect of the undulations is visible over about half of the wavelength, while for case R3 it (almost) extends over the full length of the underlying long wave.

The more energetic IG-scale waves (test R4 and R6) can be classified (initially) in the intermediate bore regime ($H/d \approx 0.6-0.7$ around the reef crest); with both features of undular and turbulent bores. After steepening around the reef crest, the long waves transform into spilling breakers.

For test R6 at the first the wave gauge on the reef flat (Fig. 6.4h, $x = 3.75$ m), two well pronounced undulations are visible, which appear to be are broken at the subsequent location (Fig. 6.4j). For case R4 at the first gauge on the reef flat, there are no significant undulations visible in the incident signal for (Fig. 6.4g). Breaking of the leading undulations seems to have happened already, which is not surprising since the theoretical breakpoint x_b is earlier. In both experiments, short, small amplitude trailing undulations are visible in the measurements around the breakpoint. After dissipating a sufficient amount of energy, around mid-reef the bores, the bores transform into undular bores (Fig. 6.4k-v).

The leading undulation in case R6 seems to be peaking and breaking multiple times on the reef flat. Breaking leads to a reduction in crest elevation. The subsequent trough seems to be raised due to the breaking process. As a result the leading undulation is overtaken by and merged with the second undulation (Fig. 6.4t,v). R6 never leaves the intermediate bore regime. At the beach, the underlying long wave is much more pronounced for case R6 than for case R4, for the latter the undulations are more developed. In case R4 the breaking undular bore dissipates a sufficient amount on the reef flat that it would classify as a purely undular bore near the beach. Near the beach there is not much difference in between R3 and R4; the undular bores are surprisingly similar.

The difference in maximum front slope[3] between undular bores (R3 and R5) and their turbulent counterparts (R4 and R6, up to $x = 10$ m) is notable. Turbulent fronts are considerably steeper. However, the described transition from a turbulent to undular bore goes together with a reduction in front slope steepness.

We speculate that if the reef depth would have been significantly larger (or wave height significantly smaller), non-linearity would have been reduced and the reef would not have been wide enough for the long wave to steepen and break. If non-linearity would have been much larger, turbulent bore would have developed. In the extreme (but realistic) case, non-linearity would have dominated over the whole width of the reef flat, with a turbulent bores observed from reef crest up to the beach.

In contrast if the reef width would have been reduced (for example half of the present width), or reef depth would have been increased slightly, undulations would most likely have still developed. Moreover, we can imagine that waves with even longer periods (possibly even VLF waves) break and form undulations on reefs with similar reef width to depth ratio's (recall, here $W_r/d_r \approx 20/0.08 = 250$).

6.2.2. Swell waves

The swell waves (R1 and R2) break more violently on the reef crest as plunging breakers. They appear as a characteristic sawtooth-shaped breaking waves in the measured time-series of free surface elevation at the outer reef (Fig. 6.1f). The resulting turbulent bores dissipate energy at a rapid rate.

Ultimately, even these (initially) highly energetic waves form well pronounced undulations (Fig. 6.1 j), which underlines the importance of understanding the processes involved. It turns out to be the case that — even though the swell initially break turbulently around the reef crest by forming plunging breakers — undular bores still occur around mid reef (after a sufficient amount energy has been dissipated due to turbulent wave-breaking). In contrast with the IG-scale wave cases, the wavelength of the underlying long wave is small enough for the leading undulation to start overtaking the trailing undulations of the undular bore ahead of it, before it reaches the beach.

[3] It is not surprising that [Bonneton et al., 2015] considers well developed undular tidal bores based on the maximum front slope.

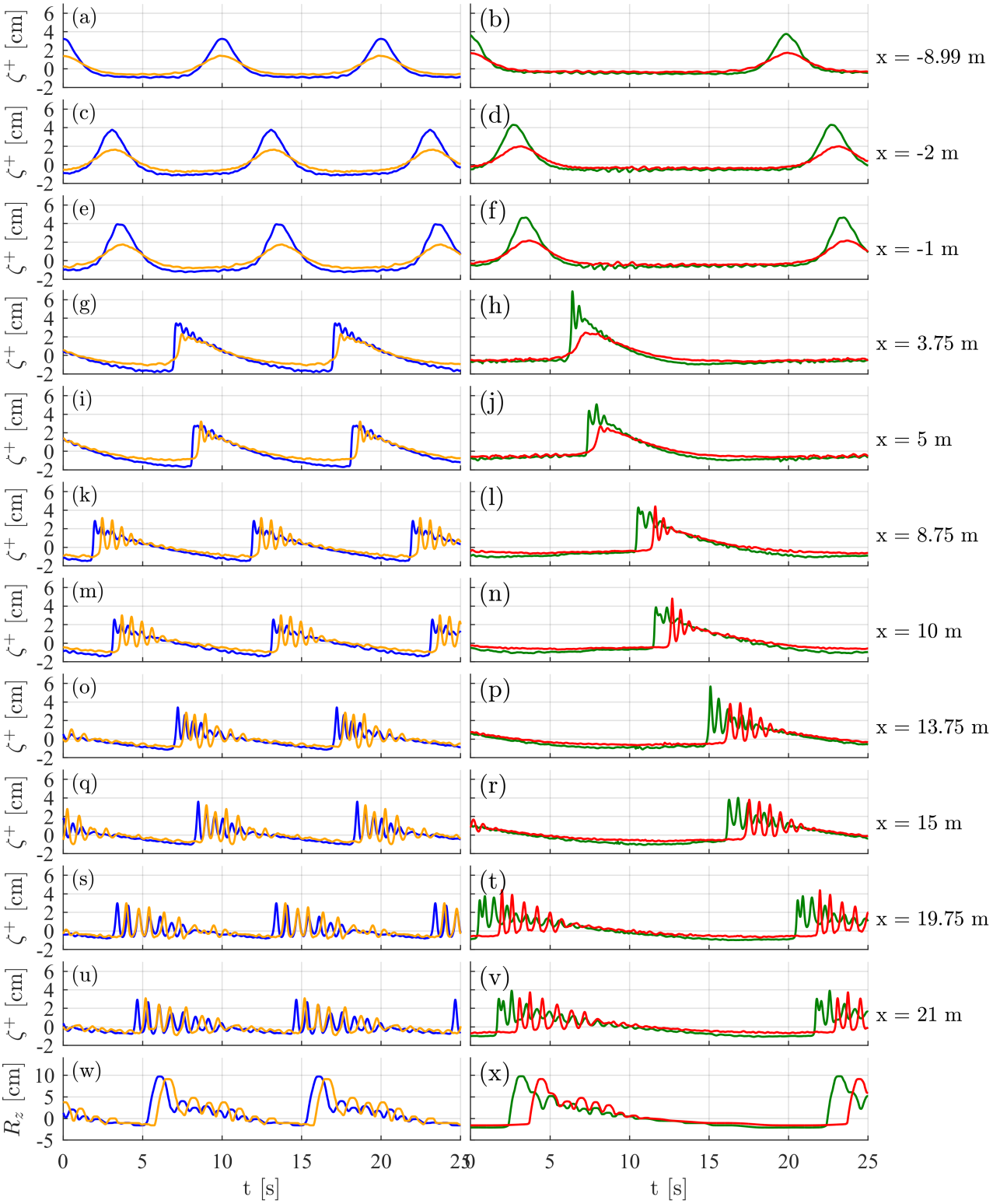

Figure 6.4: Comparison of the transformation process (of the incident long wave, denoted by ζ^+) among the four different IG-scale wave cases, R3-6. On the left, the cases are shown with $T = 10s$: (orange) case R3: $T = 10$ s, $H = 2$ cm, (blue) R4: $T = 10$ s, $H = 4$ cm. On the right, the larger period IG-scale cases are shown: (red) case R5: $T = 20$ s, $H = 2$ cm, (green) R6, $T = 20$ s, $H = 4$ cm. The last two figures show the vertical elevation of the free surface at the shore-line in time, R_z.

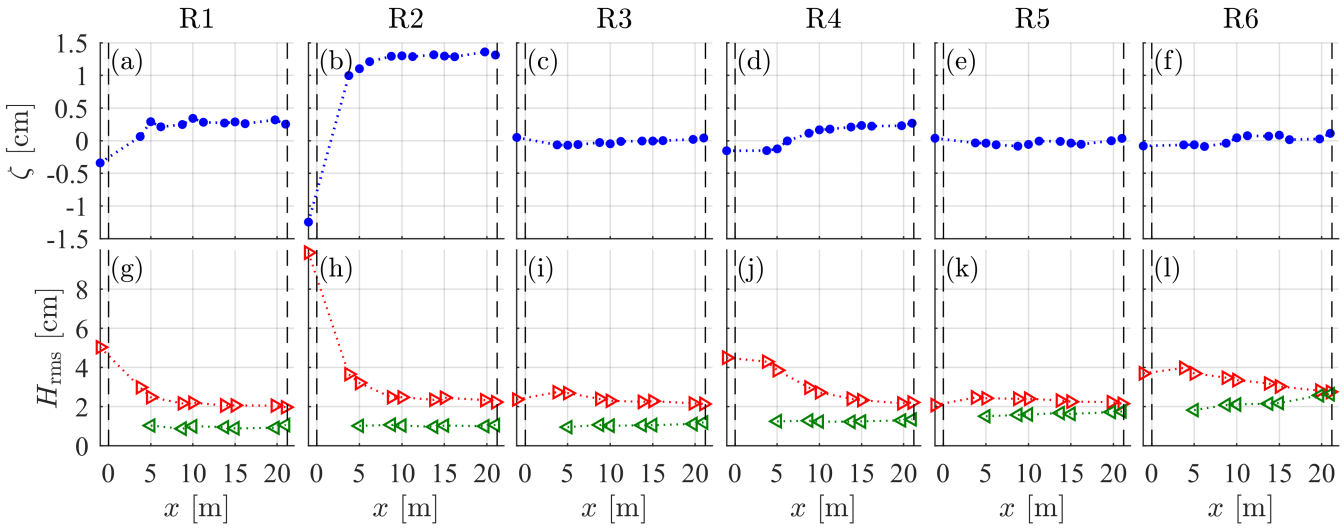

Figure 6.5: In top plots, the he wave-induced set-up, $\overline{\zeta}$ is shown. The root-mean-square wave height, H_{rms}, is shown for both the incident and reflected waves in the bottom figures.

The fact that the undulations spread out is due to amplitude dispersion. Near the beach toe, the highly non-linear leading undulations are clearly interacting with more dispersive trailing undulations. For the IG-scale cases, the length scale (or time scale) of the bores is such that the the front does not interact with trailing waves.

6.3. Bulk wave parameters

The two previous sections provided a qualitative description of the hydrodynamic processes on the reef. To make a first quantitative comparison among the six different regular wave tests, several bulk wave parameters are considered.

6.3.1. Wave height and wave-induced set-up

It is well-known that depth-induced wave breaking of swell waves drives an onshore flow over the reef crest, which leads to a water level increase over the reef flat. While wave-induced setup is not of particular interest in this study, it has to be taken into account in the run-up parametrization (8). The root-mean-square wave height, H_{rms}, and wave-induced set-up, $\overline{\zeta}$, are shown side-by-side for all experiments in Fig. 6.5. The root mean squared wave height is calculated based on the variance of the detrended (incident and reflected) free surface elevation:

$$H^{\pm}_{\text{rms}} = \sqrt{8\,\langle(\zeta^{\pm})^2\rangle} \tag{6.1}$$

where $\langle ... \rangle$ represents time-averaging. For the less energetic IG-scale cases (R3 and R5) H^{+}_{rms} decreases only slightly across the reef flat (from the reef crest to beach toe), indicating that the majority of energy is conserved on the reef flat. Little energy is dissipated due to wave-breaking. The transformation into an undular bore does not lead to a rapid decrease in total variance, as is the case for turbulent bores.

For the more energetic IG-scale case, R6, H^{+}_{rms} decreases at a higher rate at the outer and mid reef, due to turbulent wave-breaking. However, at the inner reef the variance decreases at a rate reminiscent to purely undular (or intermediate) bores. A sufficient amount of energy has been dissipated while propagating over the reef, and the bore is not strong enough to keep the steepening process going; it starts breaking in a dispersive manner by forming undulations.

6.3.2. Wave-form characteristics

Skewness and asymmetry are important for sediment transport studies [Ruessink et al., 2012]. Qualitatively, the processes responsible for asymmetry of the wave shape about the horizontal and vertical have been described. Here, two waveform characteristics are used to characterize the transforming waves observed along

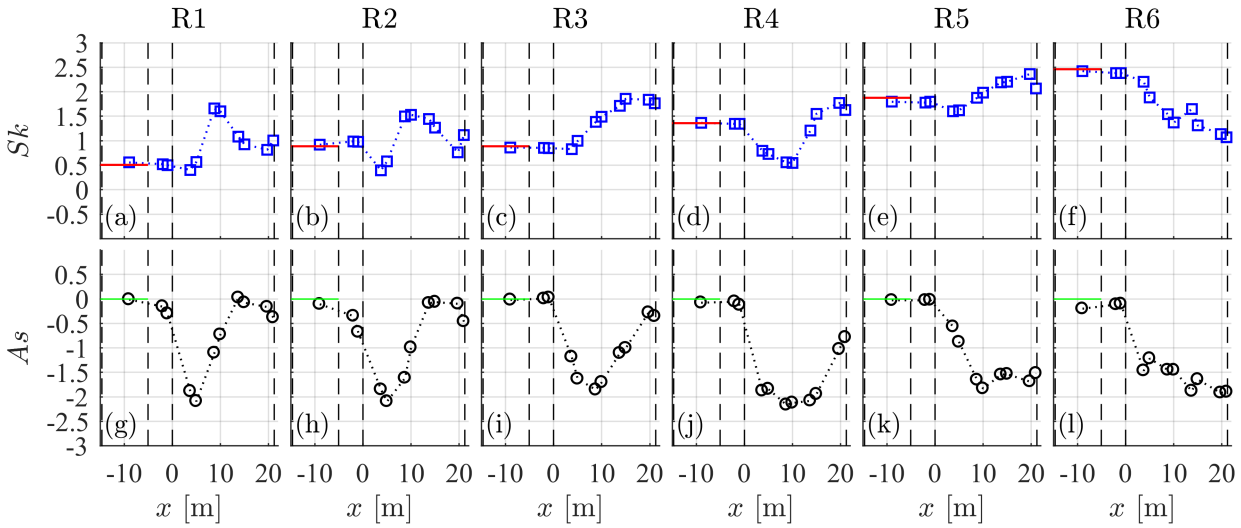

Figure 6.6: Evolution of skewness and asymmetry across the reef. The upper plots show skewness of the incident wave. The theoretical skewness value of the incident cnoidal wave is shown in red. The bottom plots show asymmetry of the incident wave.

the reef: skewness Sk and asymmetry As, defined as:

$$Sk = \frac{\langle \eta^3 \rangle}{\langle \eta^2 \rangle^{3/2}} \quad As = \frac{\langle \eta^3_{\text{Hilbert}} \rangle}{\langle \eta^2 \rangle^{3/2}} \tag{6.2}$$

where η_{Hilbert} is the Hilbert transform of η and $\langle ... \rangle$ denotes time-averaging. Both parameters have been investigated in recent research on infra-gravity waves on reefs, see [Cheriton, 2016] [Pearson, 2016]. Skewness (or asymmetry about the vertical) is the gradual peaking of the wave crest and flattening of the trough, while asymmetry is the steepening of the face and flattening of the back (resulting in a pitched-forward or sawtooth wave-shape). Both parameters are usually used to describe the shoaling process up to the point where the waves break. Since undulations are formed during the (dispersive) wave breaking process around the moment where the steepness front is maximum, it is interesting to analyze both skewness and asymmetry even after the undular bore has formed.

Fig. 6.6 shows both parameters for the incident signal. Cnoidal waves are permanent waves with peaked crests and flat troughs and thus have a certain skewness. Asymmetry about the vertical is initially zero. The theoretical skewness is shown in the figure at the offshore section, which agrees well with observations. For the more energetic cases (R2, R4 and R6) both skewness and asymmetry decrease at the outer to mid reef due to nonlinearity. This process continues at the inner reef for case R6, while for case R2 and R4 skewness and asymmetry increase at the mid to inner reef. Dispersive effects counteract steepening and peaking.

For the less energetic cases (R3 and R5 and also R1), asymmetry decreases due to nonlinear effects, but skewness barely decreases. The onset of formation of undulations goes paired with an increasing skewness and asymmetry.

Note that in the regular wave experiment, we can directly calculate the skewness and asymmetry based on the (incident) velocity or free surface measurements. To calculate these parameters for infra-gravity waves, one has to retain the bound higher harmonics in the calculation of the low frequency elevation. Simply low-pass filtering would not suffice, since it also removes the bound higher harmonics, which are responsible for the asymmetric shape of the wave.

6.4. Characteristics of the undulations

6.4.1. Crests, troughs, and periods

For the description of ocean waves, the wave period is most commonly calculated by a zero-crossing analysis, or calculated using spectral methods. For undular bores it is common practise to identify the crests of the undulations, and subsequently calculate parameters of interest (e.g. wave period, wavelength) based on the location of the crests. Figure 6.7 shows the definitions of these characteristics based on an incident undular bore. A trough is defined are defined as the minimum between two subsequent crests. Here, the wavelength

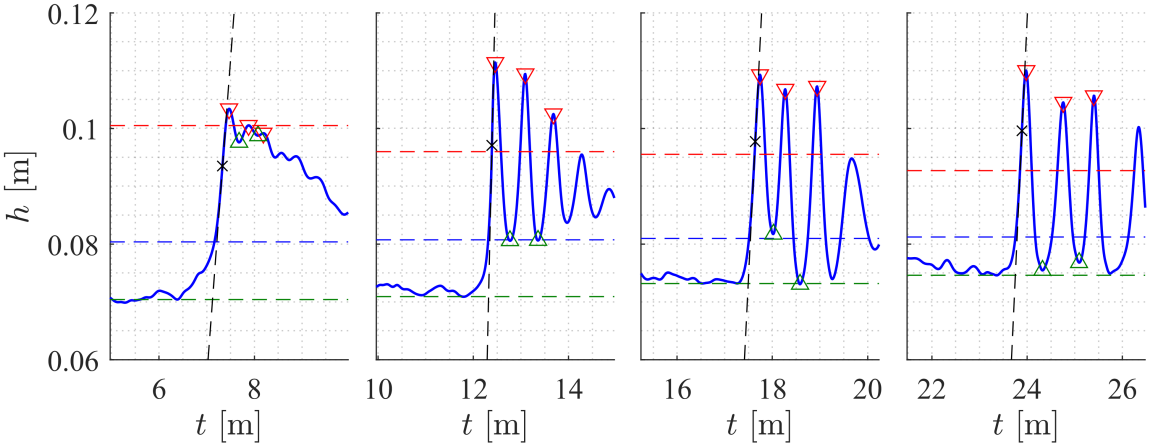

Figure 6.7: Definition characteristic parameters: (red triangle) crests undulation, (green triangle) troughs undulations, (red dashed line) mean elevation of the bore front h_1 (green dashed line) base level just in front of the bore front h_0.

is defined as the length between two subsequent crests at a certain moment in time, and the period is defined as the separation time of two crests at a certain location (difference in arrival time between the crests).

The crests of the first three undulations are tracked using a simple algorithm similar to [Tissier et al., 2013]. The crests of the leading undulations is marked at the first gauge after the reef crest ($x = 3.75$ m). It is tracked towards the shore by requiring (for each stretch between two gauges) that its propagation speed is $c_1 < 1.5\sqrt{gd}$. For the subsequent undulations we require $c_n > 0.8\sqrt{gd}$, in addition to the requirement that an undulation may not overtake the undulations ahead of it.

Figure 6.8 shows space-time diagram of the incident long wave, together with the the tracked crests and wave trajectories of the undulations. Overlaid are the trajectories which correspond to a wave traveling with a constant speed, $c = \sqrt{1+\epsilon}\sqrt{gd}$, where $\epsilon = 0 - 0.4$[4].

The characteristic parameters of the incident undular bore at several locations on the reef flat (locations $x = 3.75, 8.75, 13.75, 19.75$ m, from session 2[5]) are listed in Table x. For all experiments, it contains the crest and trough levels, the associated periods, and the maximum rate of surface rise $\max(\frac{\partial \zeta}{\partial t})$.

T_u and $\frac{\partial \zeta}{\partial t}$, are readily estimated from the free surface elevation time-series at a certain location. While the spatial resolution of the free surface and flow measurements are high enough to analyze formation of undular bores in sufficient detail, direct calculation of the wavelength of the leading undulation L_u, and the (maximum) steepness of its front, $\frac{\partial \zeta}{\partial x}$, requires a denser spacing.

Both parameters L_u and $\frac{\partial \zeta}{\partial x}$ can be approximated, if the celerity of the undular bore is known. The listed values in Table 6.2 are approximated using the linear shallow water wave speed: $c_0 = \sqrt{gd}$. $L_u = c * T$, and $\frac{\partial \zeta}{\partial x} = -\frac{\partial \zeta}{\partial t} / c_0$. In the next section, we will examine if this is sufficiently accurate.

6.5. Velocity of propagation

To properly characterize a dispersively breaking long waves, it is important to estimate the velocity of propagation with sufficient accuracy. The propagation velocity of the leading undulation that appears at the front of the long wave is of particular interest. We would like start by making the following statements:

- Deviation from hydrostatic pressure results in a significantly (relative) reduction of the propagation velocity.
- Properly accounting for this fact can yield accurate predictions.

These hypotheses are to be validated in this section. The current analysis has to be performed independent from the decomposition procedure, for which we have used the shallow water wave speed. To avoid the complication that reflection entails, we focus on the first (positive) disturbance that enters still water and travels across the reef flat.

[4] Note that $\epsilon = H/d$ would correspond to a solitary wave

[5] The analysis which follows is based on session 2 in order to avoid errors and/or confusion. Slight inconsistencies between the results of the two sessions might lead to erroneous interpretations.

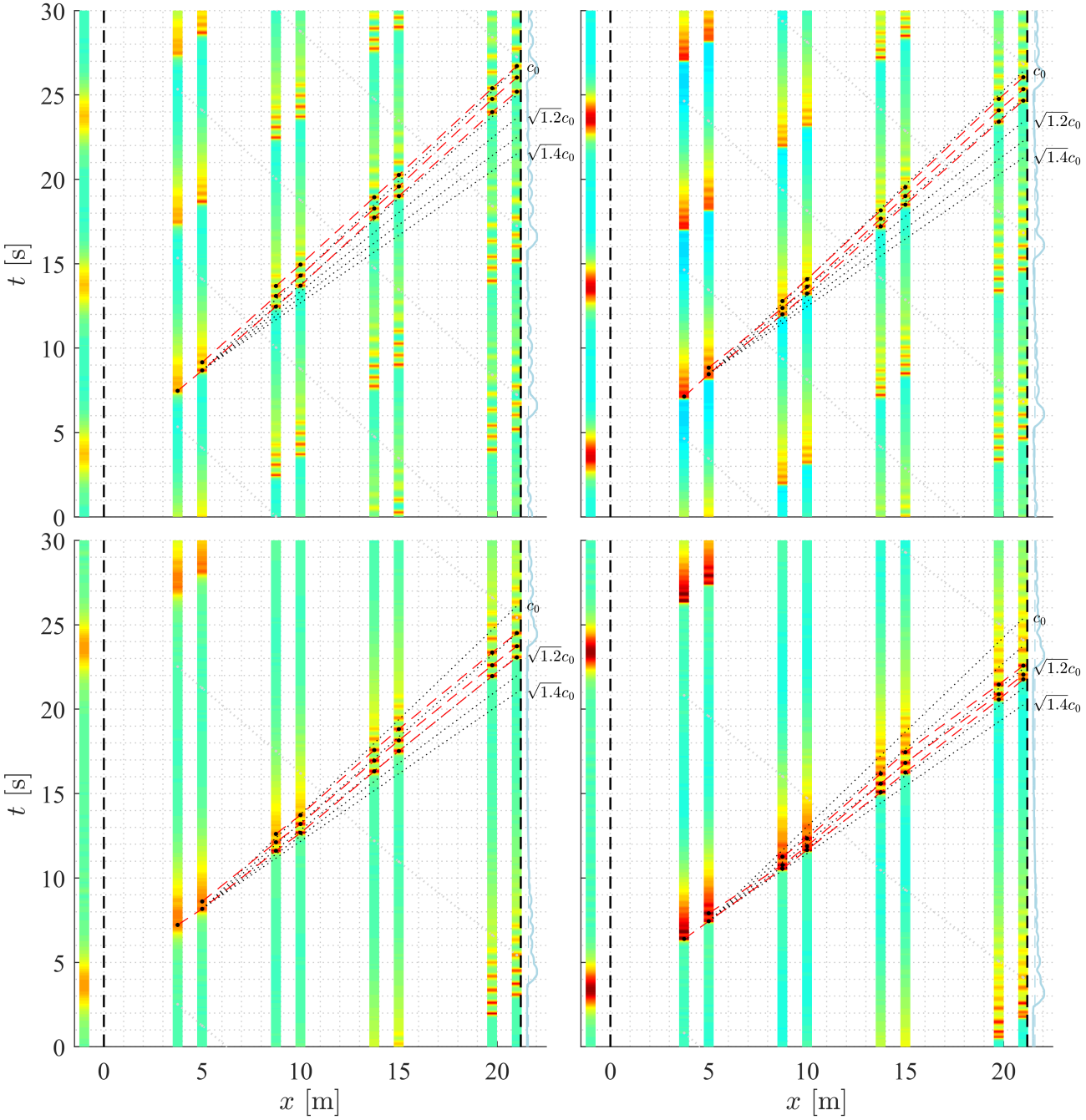

Figure 6.8: Trajectories of the first three undulations overlaid on the space-time diagram of the incident waves, for test R3-6.

Table 6.2: Characteristics of the shoreward traveling undular bore.

	R3				R4			
x_{reef} [m]	3.75	8.75	13.75	19.75	3.75	8.75	13.75	19.75
d [m]	0.080	0.081	0.081	0.081	0.080	0.082	0.083	0.083
$h_{crest,1}$ [m]	0.103	0.111	0.109	0.110	0.114	0.110	0.116	0.112
$h_{crest,2}$ [m]	0.101	0.109	0.107	0.104	0.115	0.105	0.109	0.109
$h_{crest,3}$ [m]	0.099	0.102	0.107	0.106	0.110	0.100	0.102	0.105
$h_{trough,1}$ [m]	0.098	0.081	0.082	0.075	0.114	0.098	0.085	0.077
$h_{trough,2}$ [m]	0.099	0.081	0.073	0.077	0.105	0.096	0.085	0.078
T_1	0.41 [s]	0.63	0.53	0.78	0.22	0.38	0.46	0.68
T_2	0.31 [s]	0.59	0.67	0.64	0.39	0.41	0.49	0.67
$(\frac{\partial \zeta}{\partial t})_{1,max}$ [-]	0.11	0.37	0.17	0.18	0.40	0.35	0.24	0.19
$L_1 = c_0 T_1$ [m]	0.37	0.56	0.47	0.70	0.20	0.34	0.41	0.61
$L_2 = c_0 T_2$ [m]	0.28	0.53	0.60	0.57	0.35	0.37	0.44	0.60
$(\frac{\partial \zeta}{\partial x})_{1,max}$ [-]	-0.12	-0.42	-0.19	-0.20	-0.45	-0.39	-0.26	-0.22
$\overline{h_0}$ [m]	0.070	0.071	0.073	0.075	0.063	0.068	0.072	0.075
$\overline{h_1}[m]$	0.101	0.096	0.096	0.093	0.114	0.104	0.101	0.095
	R5				R6			
x_{reef} [m]	3.75	8.75	13.75	19.75	3.75	8.75	13.75	19.75
d	0.081	0.080	0.081	0.081	0.080	0.081	0.082	0.081
$h_{crest,1}$ [m]	0.106	0.123	0.119	0.123	0.150	0.123	0.138	0.113
$h_{crest,2}$ [m]	0.104	0.111	0.119	0.119	0.135	0.120	0.125	0.118
$h_{crest,3}$ [m]	0.104	0.102	0.114	0.111	0.121	0.119	0.114	0.117
$h_{trough,1}$ [m]	0.104	0.089	0.082	0.079	0.112	0.119	0.091	0.099
$h_{trough,2}$ [m]	0.104	0.095	0.080	0.079	0.119	0.103	0.089	0.086
T_1 [s]	0.42	0.51	0.63	0.64	0.42	0.22	0.51	0.32
T_2 [s]	0.13	0.49	0.63	0.76	0.35	0.49	0.59	0.57
$(\frac{\partial \zeta}{\partial t})_{1,max}$ [-]	0.05	0.30	0.20	0.36	0.85	0.46	0.49	0.40
$L_1 = c_0 T_1$ [m]	0.37	0.45	0.56	0.57	0.37	0.20	0.45	0.29
$L_2 = c_0 T_2$ [m]	0.12	0.44	0.56	0.68	0.31	0.44	0.53	0.51
$(\frac{\partial \zeta}{\partial x})_{1,max}$ [-]	-0.05	-0.34	-0.22	-0.40	-0.95	-0.52	-0.55	-0.44
$\overline{h_0}$ [m]	0.078	0.076	0.075	0.075	0.074	0.075	0.073	0.072
$\overline{h_1}$ [m]	0.105	0.106	0.101	0.101	0.131	0.121	0.114	0.106

6.5.1. Observed propagation speed

Several formulations for the propagation velocity will be benchmarked against the observed speed at which the leading crest travels. The observed mean propagation speed of an undulation over a stretch A-B is approximated by:

$$c_{obs} = \frac{dx}{dt} \approx \frac{\Delta x}{\Delta t} \tag{6.3}$$

By dividing the traveled distance of an undulation (the distance between gauge A and B, $\Delta x = x_{AB}$) by the travel time of that undulation (the difference in arrival time, evaluated at the moment the crest passes, $\Delta t = t_{c,B} - t_{c,A}$), we obtain its average propagation speed. Fig. 6.11 shows the derived values, together with the chosen predictors.

6.5.2. Predictors for the propagation speed

First it is described how wave transformation processes (e.g. the process of steepening, breaking or undulating) stand in relation to the propagation speed. The following description is based on test R4, since it involves both significant wave-breaking and undular bore formation. It should make clear which predictors are considered and why.

Subsequential to shoaling on the fore-reef slope, the long wave appears in shallow water on the reef flat. Near the reef crest, non-linearity dominates over dispersion and the front quickly steepens. Perhaps, over a very short distance, an estimate based on the method of characteristics (Eq. D.20) gives a reasonable estimate for the speed of the front. However, since the front rapidly breaks, this predictor is not tested. A turbulent bore front forms at the outer reef, which is not surprising considering the bore strength, $H/d \approx 0.5$. Hence we expect a bore model, such as [Svendsen et al., 1978], to be a good predictor for the speed of the front. An alternative would be the one-way celerity model of [Bonneton, 2005], because it might be that the trough is not significantly influenced by the formation of the shock (see Ch. D). In other words, the trough does not travel with the speed of the front as assumed by [Svendsen et al., 1978]. Well-pronounced — but not yet fully developed — undulations appear around the mid reef. We known that non-hydrostatic pressure plays an important role from the moment the front becomes relatively steep. This is furthermore revealed by the formation of undulations. Predictors that do not take this into account are expected to overestimate the celerity if non-hydrostatic pressure is indeed significant. To properly account for this one could:

1. use a predictor for the propagation speed which includes the effect of non-hydrostatic pressure (and optionally non-uniformities in the velocity profile),
2. assume a developed leading undulation — a solitary wave propagation about its background — and apply the corresponding expression[6]
3. or apply one of the available bore formulae (that assume a hydrostatic pressure distribution and uniform velocity) with h_1 taken at a point where pressure is locally hydrostatic.

[Svendsen et al., 1978] discussed the effect of non-hydrostatic pressure and non-uniformity of velocities in the wave motion on the velocity of propagation. In other words, they investigated option (1). Their expression for the velocity of propagation is based on the theory of Boussinesq. However, for their dataset, simply assuming the hydrostatic pressure distribution and a uniform velocity profile gave better results than taking into account the deviation of pressure and velocity.

Here option (3) is pursued, involving the hydrostatic point. See Fig. 6.9 for the definition of the hydrostatic point. To find the hydrostatic point — which seems to be located approximately halfway the first crest and the subsequent trough — we make use of Eq. D.54. The derivatives in this expression for non-hydrostatic pressure (at the bottom) are approximated numerically from the surface elevation measurements.

6.5.3. Comparison between predicted and observed propagation speed

Three bore type of predictors are selected, namely: classical bore theory (see Appx. B), the breaking wave theory of [Svendsen et al., 1978] and the one-way celerity model of [Bonneton, 2005]. For each model, h_1 is either evaluated at the crest of the leading undulation, or at the hydrostatic point near the crest. Additionally,

[6] The speed of a solitary wave propagation about its background is given by:

$$c_s = \sqrt{g\left(\overline{d} + H\right)} + \overline{U} \tag{6.4}$$

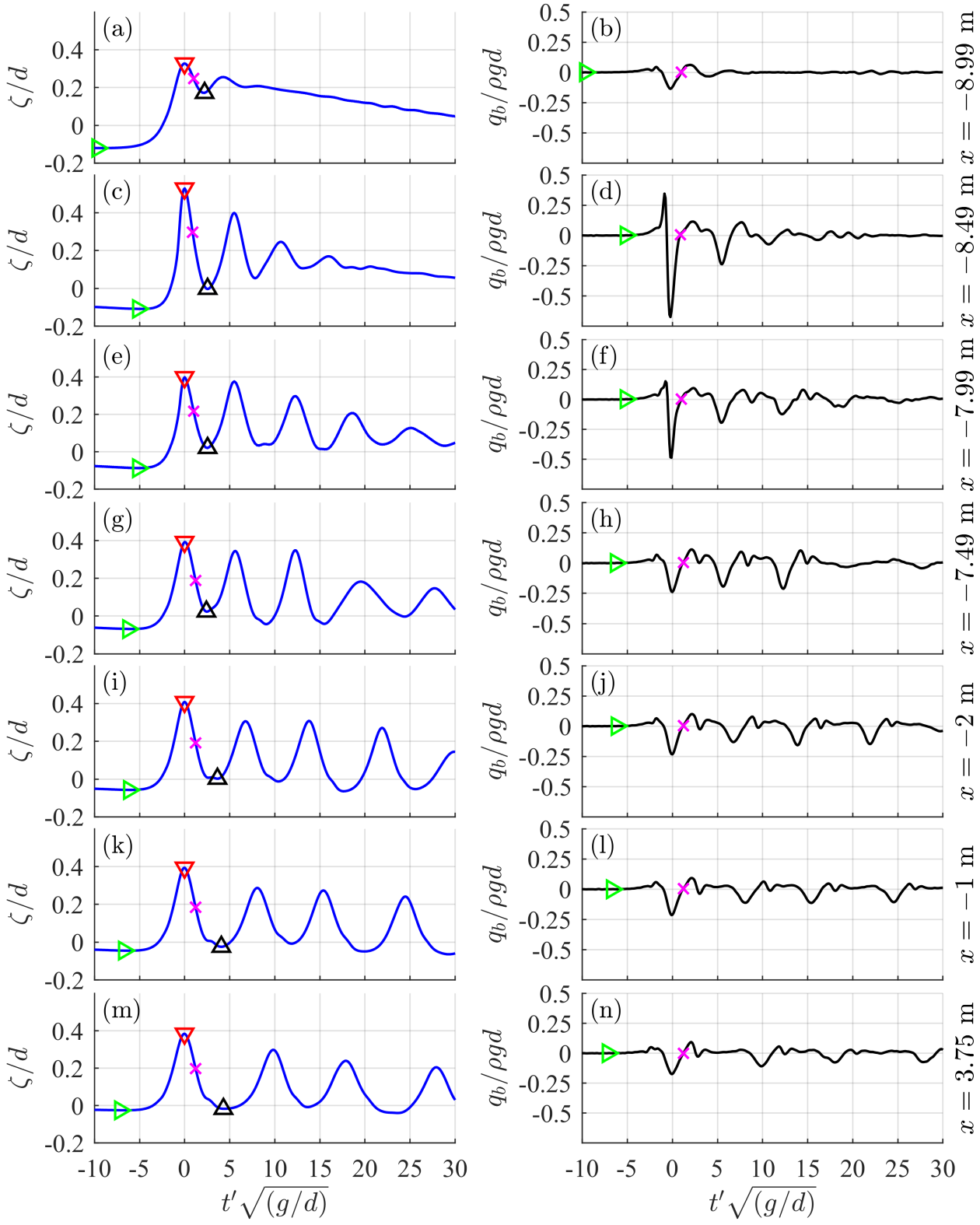

Figure 6.9: Definition of the hydrostatic point, based on measurements of test R3. The first disturbance entering still water is shown. (left) surface elevation, normalized by reef depth, (right) non-hydrostatic pressure at the bottom, normalized by hydrostatic pressure. (▷) global trough, (▽) crest of leading undulation, (△) local trough, (×) hydrostatic point.

solitary wave theory is considered, with and without taking the velocity at the preceding trough into account. Following [Bonneton, 2005], the velocity in the trough is approximated using the expression according to the method of characteristics (Eq. B.23. Note that the solitary wave speed and nonlinear shallow water wave speed are equivalent if the latter is evaluated at the crest, and if the contribution of velocity to the propagation speed is ignored. Fig. 6.10 shows how each predictor performs. All regular tests, R1-7, are included in the comparison. Simply applying one of the selected bore predictors with h_1 evaluated at the crest and h_0 at the trough yields inaccurate results for undular bores. This was to be expected because vertical acceleration leads to a significantly pressure reduction near the crest of the undulations. Taking h_1 at the hydrostatic point instead, improves results considerably. Including velocity in the trough further improves the estimates (compare for example the classical bore solution, Fig. 6.10b, with either the results using the expression of Svendsen or Bonneton, Fig. 6.10d or f). As the leading undulation becomes more developed, solitary wave theory yields increasingly accurate results — that is if the background velocity is taken into account (compare Fig. 6.10g and h).

In Fig. 6.11 it is shown how the observed propagation speed of the leading undulation changes over the reef flat. This gives better insight into the conditions under which each type of predictor performs best. The theory of [Svendsen et al., 1978] is not shown, because it performs similar to the theory of [Bonneton, 2005]. The two main theories shown here are classical bore theory and solitary wave theory. Bonneton's model for breaking waves is included to show how the result is modified with respect to classical bore theory. Bonneton's predictor, applied at the hydrostatic point, is also shown.

Notice the gradual transition from bore (or breaking wave) speed to solitary wave speed for the tests with significant turbulent breaking (R1, R2, R4 and R6). For the tests involving weaker bores (R3, R5 and linear case R7), the velocity of propagation is relatively constant. For these three tests the leading undulation peaks early on, which inferred from the fact that, already at the outer reef, the propagation speed seems to converge with that of solitary wave theory.

In addition to the introductory statements, the following conclusions can be summed up:

- The leading undulation gradually transitions from propagating at the bore speed to moving at the solitary wave speed.
- This transition is more gradual for stronger (periodic) bores and increasing wavelengths.
- Linear shallow water wave theory underestimates the velocity of propagation of the undulations, while the considered bore theories lead to a significant overestimation (if evaluated at the crest).
- Assuming $c = \sqrt{g\,(d+\zeta)}$ leads to reasonable results for the leading undulation throughout reef flat, and can be considered as the most practical predictor.

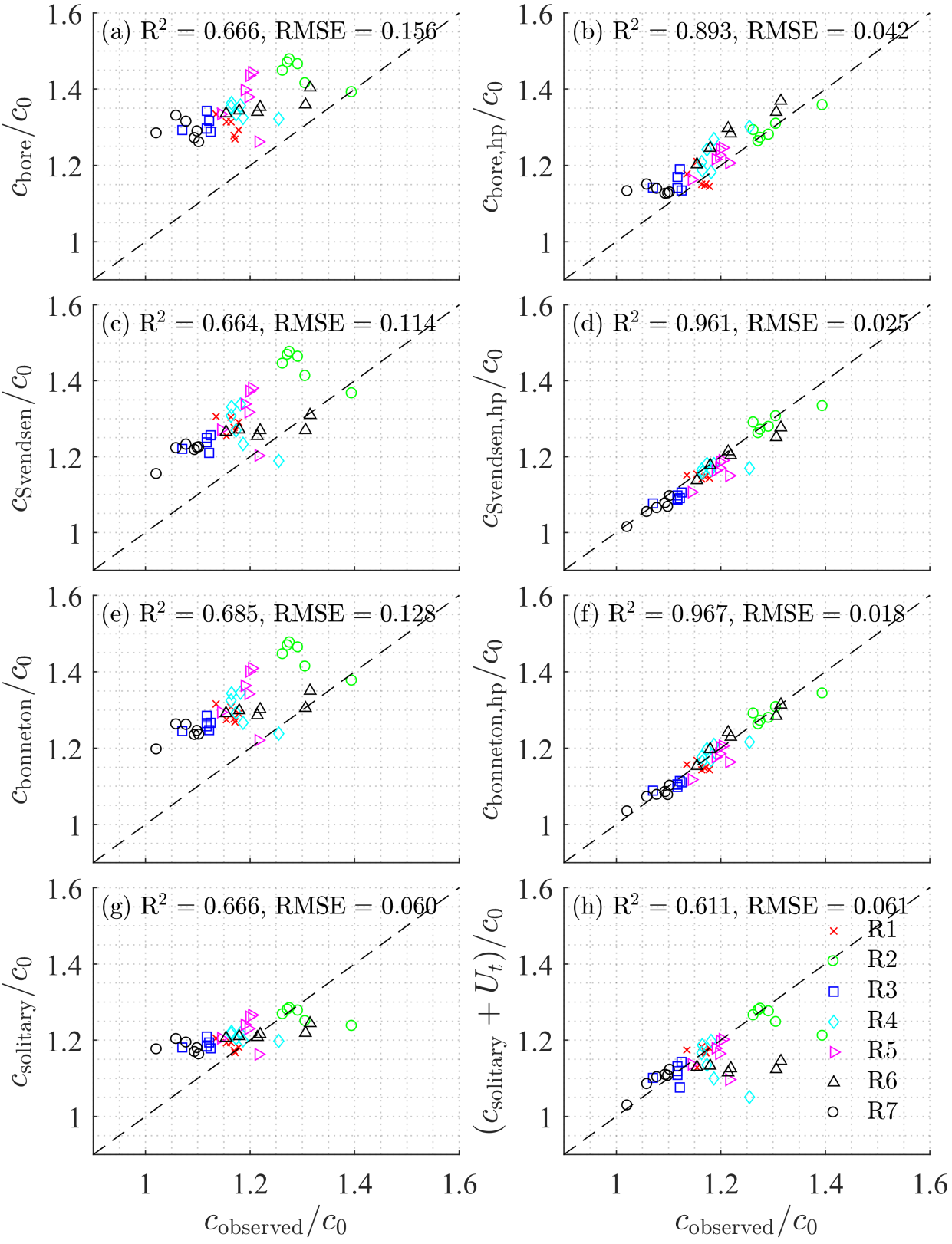

Figure 6.10: Comparison of observed and predicted propagation speed (normalized by the linear shallow water wave speed), based on different wave theories. All regular wave tests, R1-7, are included in the comparison. (a) classical bore theory, (b) classical bore theory evaluated at the hydrostatic point, (c) Svendsen's breaking wave theory, (d) Svendsen's breaking wave theory evaluated at the hydrostatic point, (e) Bonneton's breaking wave theory, (f) Bonneton's breaking wave theory evaluated at the hydrostatic point, (g) solitary wave theory, (h) solitary wave speed, taking into account the background velocity. The root-mean-square error (RMSE) and the coefficient of determination (R^2) have been computed to assess the goodness-of-fit.

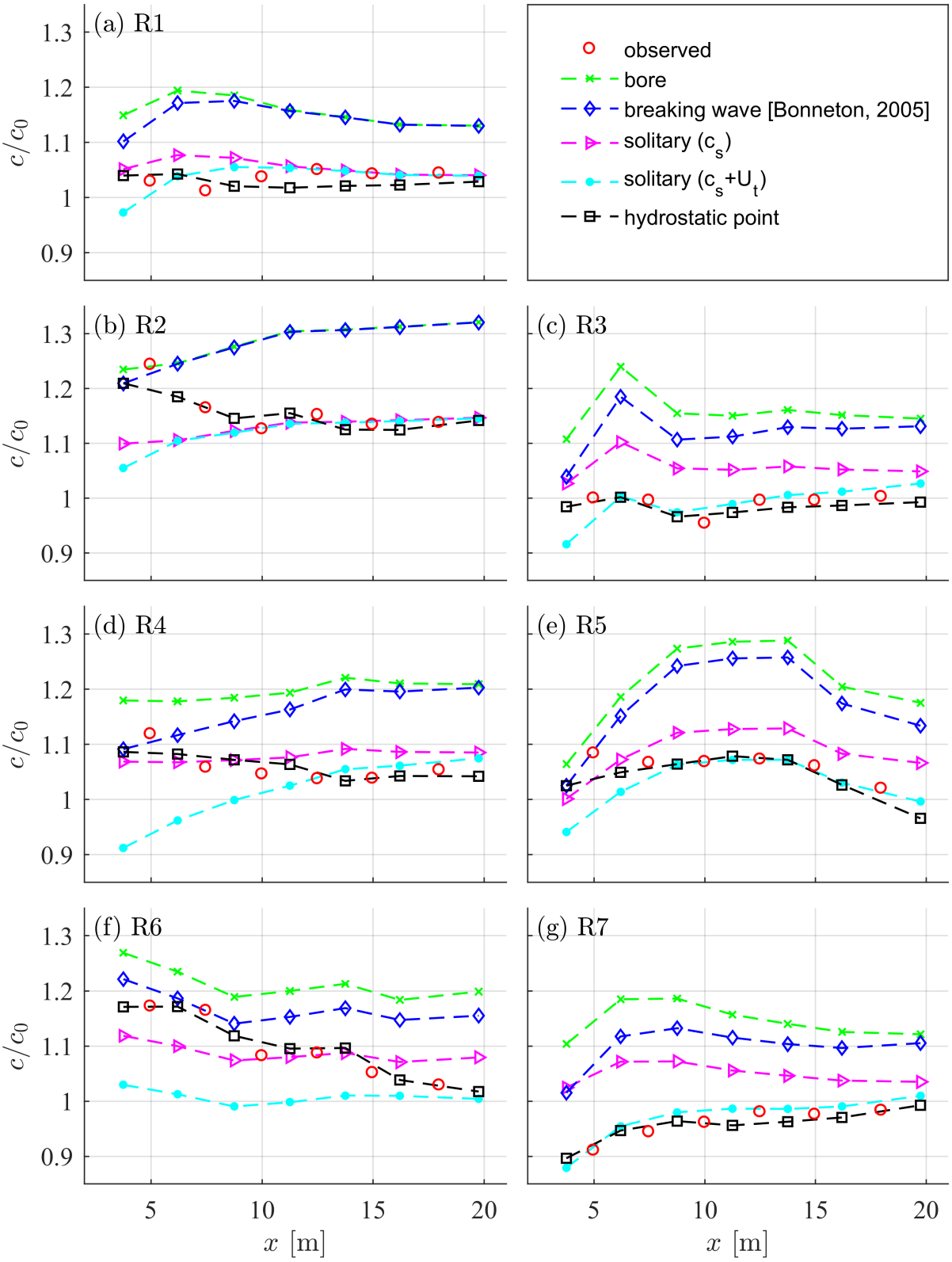

Figure 6.11: Evolution of the propagation velocity of the leading undulation over the reef flat. Notice the transition of the observed propagation speed from bore (or breaking wave) speed to solitary wave speed. Bonneton's predictor, applied at the hydrostatic point, closely follows observations.

7

Undular bore formation over a fringing reef: a frequency domain analysis

In the previous chapter, undular bore formation was studied in detail in the time domain. This chapter continues with a spectral analysis.

First, in section 7.1, the time and frequency domain representations are compared. In section 7.2, bulk energy density and bulk energy flux are calculated for all six regular wave experiments. In section 7.3, the variance density spectra are shown, for all locations on the reef flat. The peak frequency associated with the undulations is calculated. An appropriate split frequency is determined, which is used in section 7.4 to determine characteristics of the undulations based on spectral estimates, and in section 7.4.1 to quantify the relative contribution of the undulations to the total energy.

7.1. Time versus frequency domain representation

The decomposed surface elevation at several locations throughout the flume is shown in Fig. 7.10-7.11 on the left side. The corresponding amplitude spectra of the shorewards and seawards traveling waves are shown on the right side.

The amplitude spectra are obtained by application of the fast-Fourier transform for the last 1000 s of the decomposed time-series $\zeta^{\pm}$ ($f_s = 100$ Hz). The spectral resolution of $1/D = 10^{-3}$ Hz.

Nonlinear steepening is associated with generation of higher harmonics at a multiple of the primary frequency. The undulations are also higher harmonics, but form a secondary peak instead a tail of decreasing energy in the spectrum. This secondary peak shifts towards lower frequencies as the undular bore travels over the reef.

7.2. Bulk energy density, energy flux and reflection coefficient

In this section, the cross-shore evolution of energy density and energy flux is investigated.

7.2.1. Evolution of potential and kinetic energy across the reef flat

The instantaneous energy (per unit horizontal surface area $\Delta x \Delta y$, with respect to $z = -d$) is given by the sum of the kinetic and potential energy parts:

$$E = \frac{1}{2}\rho \int_{-d}^{\zeta} \left(u^2 + w^2\right) \mathrm{d}z + \rho g \int_{-d}^{\zeta} z \,\mathrm{d}z = \underbrace{\frac{1}{2}\rho \int_{-d}^{\zeta} \left(u^2 + w^2\right) \mathrm{d}z}_{E_{kin}} + \underbrace{\frac{1}{2}\rho g \left(\zeta^2 - d^2\right)}_{E_{pot}} \tag{7.1}$$

The wave-induced contribution is obtained by discarding the hydrostatic potential energy ($\rho g \int_{-d}^{0} z \,\mathrm{d}z = -\frac{1}{2}\rho g d^2$). In the linear long wave approximation, E is given by:

$$E_0 = \frac{1}{2}\rho \left(U^2 d + g\zeta^2\right) \tag{7.2}$$

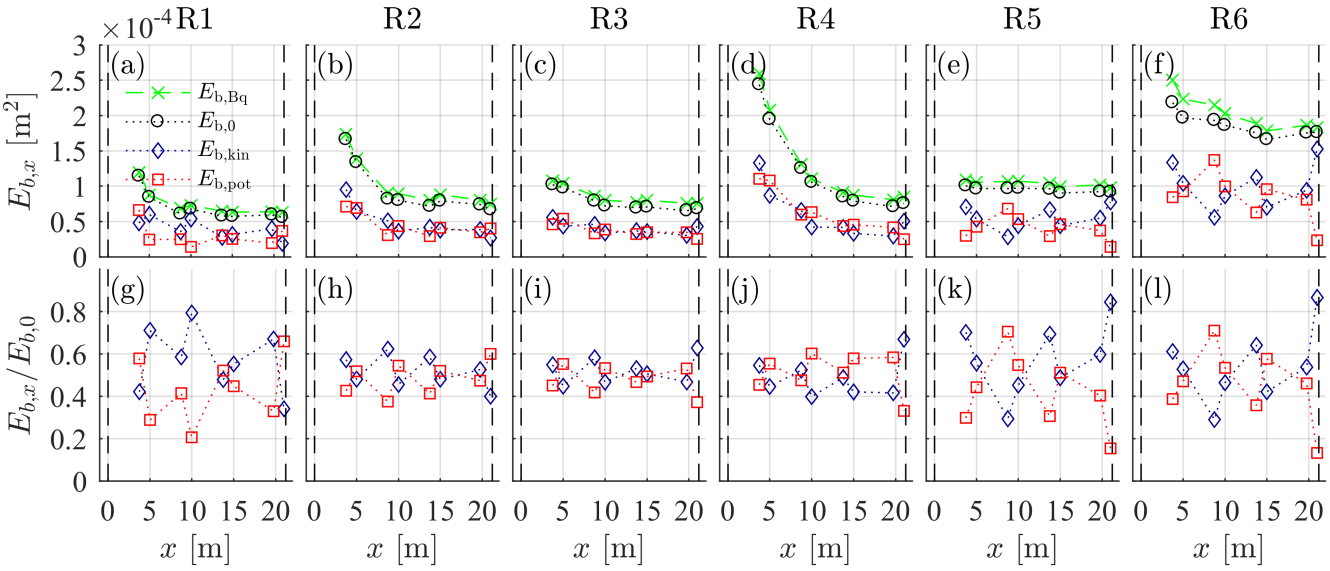

Figure 7.1: Cross-shore evolution of bulk energy for experiments R1-R6. $E_{b,0}$ according to linear shallow water theory and $E_{\mathrm{b,Bq}}$ based on Boussinesq theory have been included. (a-f) absolute potential, kinetic and total bulk energy. (g-l) Relative kinetic and potential energy with respect to the total amount of bulk energy.

In this approximation, u_α can be substituted for U. It has been shown in Ch. 5 that the discharge of the undular bores observed on the reef flat is significantly underestimated by linear shallow water theory. It can be expected that this is also the case for other physical quantities, such as the energy density and energy flux. Expressions for mass, momentum and energy (and the associated fluxes), for a general class of Boussinesq models (described in [Bona et al., 2002]), have been derived in [Ali and Kalisch, 2012]. We will use their higher-order[1] expression for the energy density to investigate whether Eq. 7.2 is sufficient for the present analysis. It is here derived in an alternative way, more in line with the rest of this thesis, namely by substituting the expressions of [Nwogu, 1993] for the horizontal and vertical velocity (Eq. 4.21) directly into Eq. 7.3. If again only the wave-related part of E_{pot} is retained, and additionally, higher order terms are discarded, we get:

$$\begin{aligned} E_{Bq} &= \frac{1}{2}\rho\int_{-d}^{\zeta}\left(u_{Bq}^2+w_{Bq}^2\right)\mathrm{d}z+\frac{1}{2}g\zeta^2 \\ &= \rho\left[\frac{1}{2}u_\alpha^2(d+\zeta)+\frac{1}{6}d^3u_{\alpha,x}^2+\left(\alpha+\frac{1}{3}\right)d^2uu_{\alpha,xx}\right]+\frac{1}{2}\rho g\zeta^2 \quad \text{where} \quad \alpha=\frac{1}{2}\left(\frac{z_\alpha}{d}\right)^2+\left(\frac{z_\alpha}{d}\right) \end{aligned} \tag{7.3}$$

Note that in contrast to [Ali and Kalisch, 2012], the expression is given in terms of z_α (the vertical position with respect to the surface) instead of θ (the height above the bottom). The bulk energy density E_b can be obtained by time-averaged energy density or by a summation over the frequencies.

Fig. 7.1 shows the cross-shore evolution of time-averaged energy density or bulk energy. Both estimates, $E_{b,0}$ according to linear shallow water theory (Eq. 7.2) and $E_{\mathrm{b,Bq}}$ based on Boussinesq theory (Eq. 7.3) have been included. The linear shallow water theory estimate deviates at most 15% from the Boussinesq estimate. While this is definitely significant, the following analysis proceeds based on the linear estimates, which is deemed sufficiently accurate for qualitative trends. Moreover, the expression for energy density, Eq. 7.2 is actually consistent with a second-order Boussinesq system [Ali and Kalisch, 2012]. In contrast, the energy flux term is different [Ali and Kalisch, 2012]

The total energy is decomposed in the kinetic and potential parts, which are approximately equal of magnitude. In the bottom plots (Fig. 7.1(g-l)) kinetic and potential energy are normalized by the total amount of energy. Locally, the contribution of kinetic and potential energy can deviate significantly from $1/2E$, as can be seen from the results of experiments R5 and R6 (Fig. 7.1e,f). This is due to significant reflection. It is crucial to use both the velocity and surface elevation measurements to determine the total amount of bulk energy.

Energy associated with dispersion becomes increasingly important towards the beach. At the beach toe,

[1] The expressions for the mechanical quantities given in [Ali and Kalisch, 2012] are obtained using a third-order Boussinesq system as starting point.

for both the swell wave experiments (R1 and R2) and the IG-scale experiments with smaller wavelengths (R3 and R4), the contribution due to dispersion is more important than the contribution to the total amount of energy due non-linearity. For R5 and R6 this is not the case (nonlinearity (still) dominates over dispersion near the beach).

7.2.2. Incident and reflected energy flux and reflection coefficient

To estimate the reflection coefficient, the energy flux has to be determined for both the incident and reflected wave. Because no higher order expression for the incident and reflected energy flux is available in literature, this section is based on the estimates following from linear shallow water theory. This is justified by the observation in the previous section that E_0 accounts for the major part of the total energy ($0.85E < E_0 \leq E$). Substituting Eq. 4.1 we have in terms of incident and reflected waves:

$$E_0 = \frac{1}{2}\rho\left[\left(U^+ + U^-\right)^2 d + g\left(\zeta^+ + \zeta^-\right)^2\right] = \underbrace{\frac{1}{2}\rho\left(\left(U^+\right)^2 d + g\left(\zeta^+\right)^2\right)}_{E_0^+} + \underbrace{\frac{1}{2}\rho\left(\left(U^-\right)^2 d + g\left(\zeta^-\right)^2\right)}_{E_0^-} + \underbrace{\rho\left(U^+U^- d + g\zeta^+\zeta^-\right)}_{E_0^i} \tag{7.4}$$

E_0^i is due to interaction. Following [Sheremet, 2002], the energy associated with the shoreward and seaward propagating waves can be obtained by substituting the linear expressions for $\zeta_0^\pm$ and $U_0^\pm$ (Guza's expressions) in Eq. 7.4:

$$E_0^\pm = \frac{1}{2}\rho\left(\left(U_0^\pm\right)^2 d + g\left(\zeta_0^\pm\right)^2\right) = \frac{1}{4}\rho\left[U^2 d + g\zeta^2 \pm 2\zeta U\sqrt{gd}\right] \tag{7.5}$$

Energy due to interaction between the incident and reflected waves turns out to be zero in this approximation. The energy fluxes are given by:

$$F_0^\pm = E_0^\pm\sqrt{gd} = \frac{\sqrt{gd}}{4}\rho\left[U^2 d + g\zeta^2 \pm 2\zeta U\sqrt{gd}\right] \tag{7.6}$$

These expressions for energy density and energy flux are due to [Sheremet, 2002] who presented the frequency domain equivalents of Eq. 7.5 and Eq. 7.6:

$$\frac{F_0^\pm(f)}{\rho g} = \frac{E_0^\pm(f)\sqrt{gd}}{\rho g} \quad \text{where} \quad \frac{E_0^\pm(f)}{\rho g} = \frac{1}{4}\left[S_{\zeta,\zeta}(f) + \left(\frac{d}{g}\right)S_{U,U}(f) \pm \left(2\sqrt{\frac{d}{g}}\right)S_{\zeta,U}(f)\right] \tag{7.7}$$

Here $S_{\zeta,U}$ is the $\zeta - U$ cospectrum, and $S_{\zeta,\zeta}$ and $S_{U,U}$ are ζ and U autospectra, respectively. See [Sheremet, 2002] for details on the method, and [Péquignet et al., 2009] and [Pomeroy et al., 2012a] for recent applications in reef hydrodynamics studies. The bulk energy fluxes $F_{b,0}^\pm$ are again obtained by summation over the frequencies. From Fig. 7.2 it can be seen that the reflection coefficient, defined by $R_{b,0}^2 = F_{b,0}^-/F_{b,0}^+$, increases with increasing offshore period (wavelength) and wave height.

7.3. Frequency distribution of the undular bore

The variance density spectra of the incident waves are shown in Fig. 7.3. Spectra are given for all IG-scale test cases, for all location on the reef flat where collocated measurements are available. Looking at the variance density spectra at the mid reef, there is a clear separation of scales. Towards the beach, the period and amplitude of undulations increase. In contrast, the underlying long wave decreases in height and the peak frequency remains constant. In this section we aim to find a practical way to separate the undulations from the underlying long wave based on the wave spectrum.

7.3.1. Peak period and split frequency

The peak frequency associated with the undulations is shown in Fig. 7.3. It has been verified that the peak period of the underlying long wave does not change as the wave propagates shoreward; $T_{p,l} = T_0$, up to the beach toe.

The peak period associated with undulation, $T_{p,u}$, is calculated as follows. For a classical undular bore, the wave-length of the leading undulation normalized by depth (L_u/d) is a function of the Froude number (or bore strength) according to experimental results by [Treske, 1994]. For low Froude numbers, $L_u/d \approx 10-20$, while for larger Froude numbers, L_u/d converges to 5. In other words, the wavelength (with respect to depth) of the leading undulation decreases with increasing bore strength (up to the point where the undulations become so steep that they start breaking).

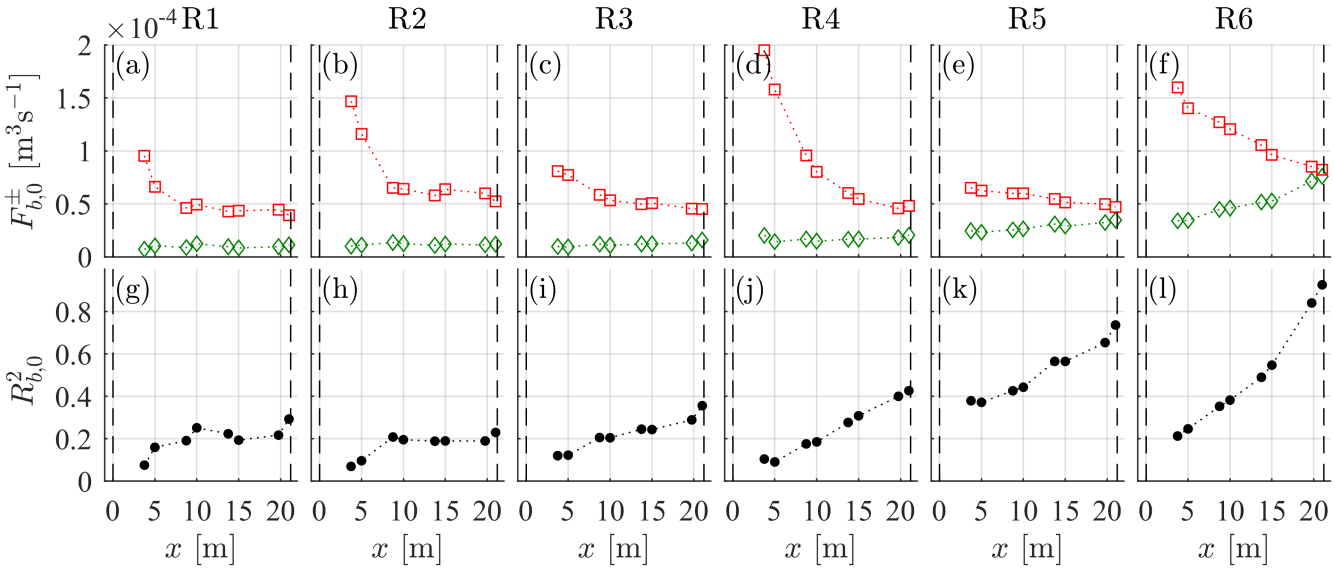

Figure 7.2: sdf

Making use of the shallow water wave speed, we can convert between wavelength and period (or frequency) using $c_0 = L/T$. $T_{p,u}$ is defined as the peak period within the frequency range $1/12.5\sqrt{(g/d)} < f \leq 1/5\sqrt{(g/d)}$. The peak frequency of the undulations $f_{p,u}$ is only defined if the energy in the associated frequency band is appreciable ($m_{0,u}/m_0 > 0.1$).

A logical split frequency would be, the frequency between the two peak frequencies $f_{p,l}$ and $f_{p,u}$, for which energy density spectrum has a minimum. However, since decomposition in sea- and shore-wards traveling waves is not perfect, it is sensitive to errors. A simple, but more robust split frequency is $f_{split} = (f_{p,l} + f_{p,u})/2$. f_{split} is shown in Fig. 7.3.

7.4. Characteristics undulations

Spectral estimates are determined for the undulations, the underlying long wave and the total incident waves. The nonlinearity parameter, $\epsilon = H/d$, the relative depth parameter, kd, and the Ursell number, N_{U} are shown in Fig. 7.4 for all locations on the reef flat. The Ursell number [Ursell, 1953], defined here as:

$$N_{\text{U}} = \frac{H/d}{(d/L)^2} = \frac{HL^2}{d^3} \tag{7.8}$$

is a non-dimensional parameter quantifying the relative magnitude of non-linearity, $\epsilon = H/d$, to dispersion, $\mu^2 = d^2/L^2$, and approximated in shallow water as:

$$N_{\text{U}} \approx \frac{HgT^2}{d^2} \tag{7.9}$$

The peak period is used to evaluate T. The root mean squared wave height $H_{\text{rms},u}$ is calculated by integrating the variance density over the frequency range $f_{1,u} < f < f_{2,u}$:

$$H_{\text{rms},u} = \sqrt{8m_{0,u}}, \quad m_{0,u} = \int_{f_{1,u}}^{f_{2,u}} E(f)\,df \tag{7.10}$$

and is used as an estimate for the wave height. Because energy is transferred to the undulations, they become increasingly nonlinear. The wavelength of the leading undulation increases and approaches a solitary wave near the beach, as will be shown in the next section. This is consistent with the decreasing kd-value of the undulations. Because nonlinearity increases and dispersion decreases, the Ursell number associated with the undulations increases. It an order of magnitude larger than used in Boussinesq scaling.

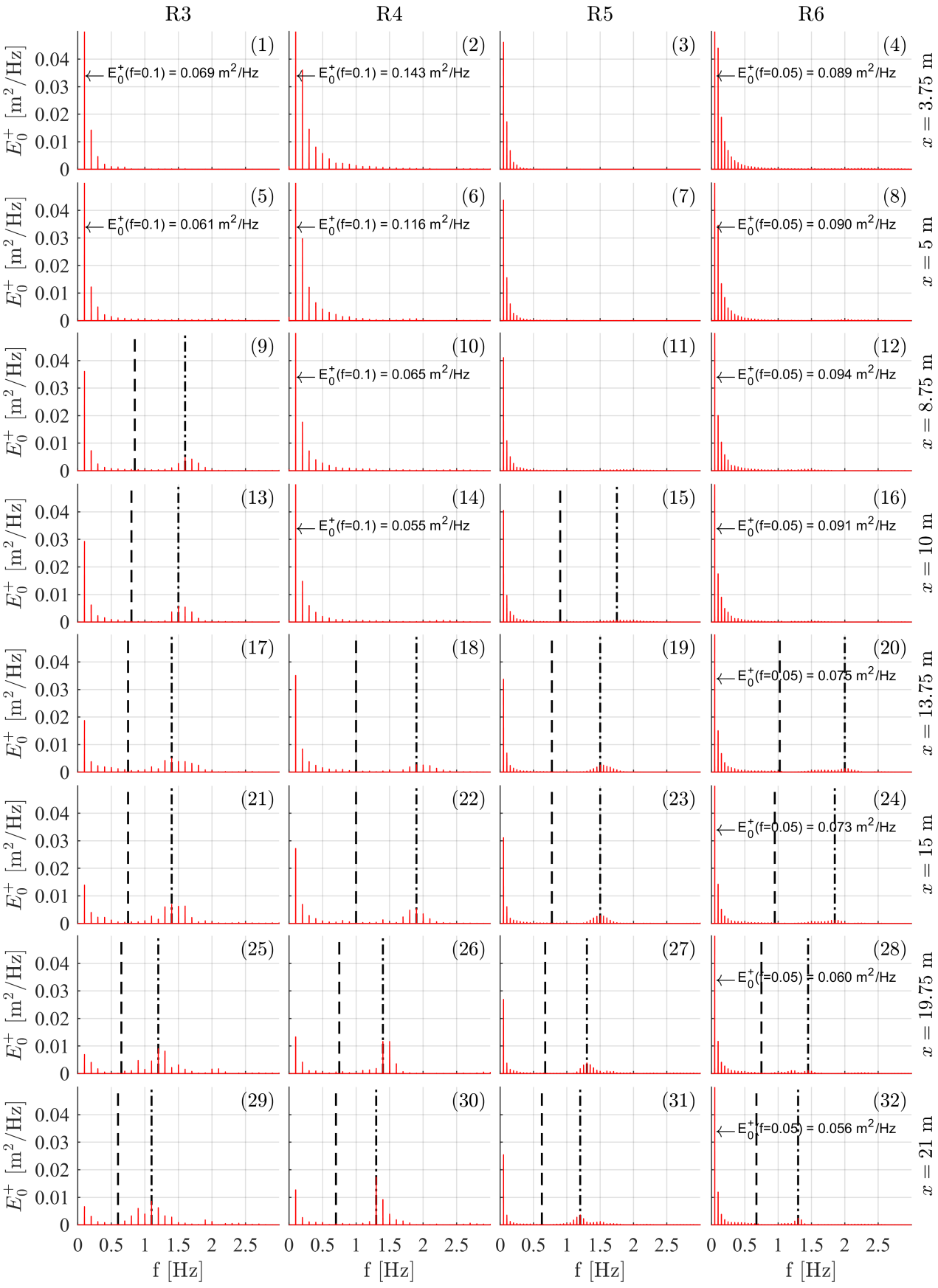

Figure 7.3: Variance density spectrum. (dash-dotted line) peak frequency associated with the undulations, (dashed line) split frequency.

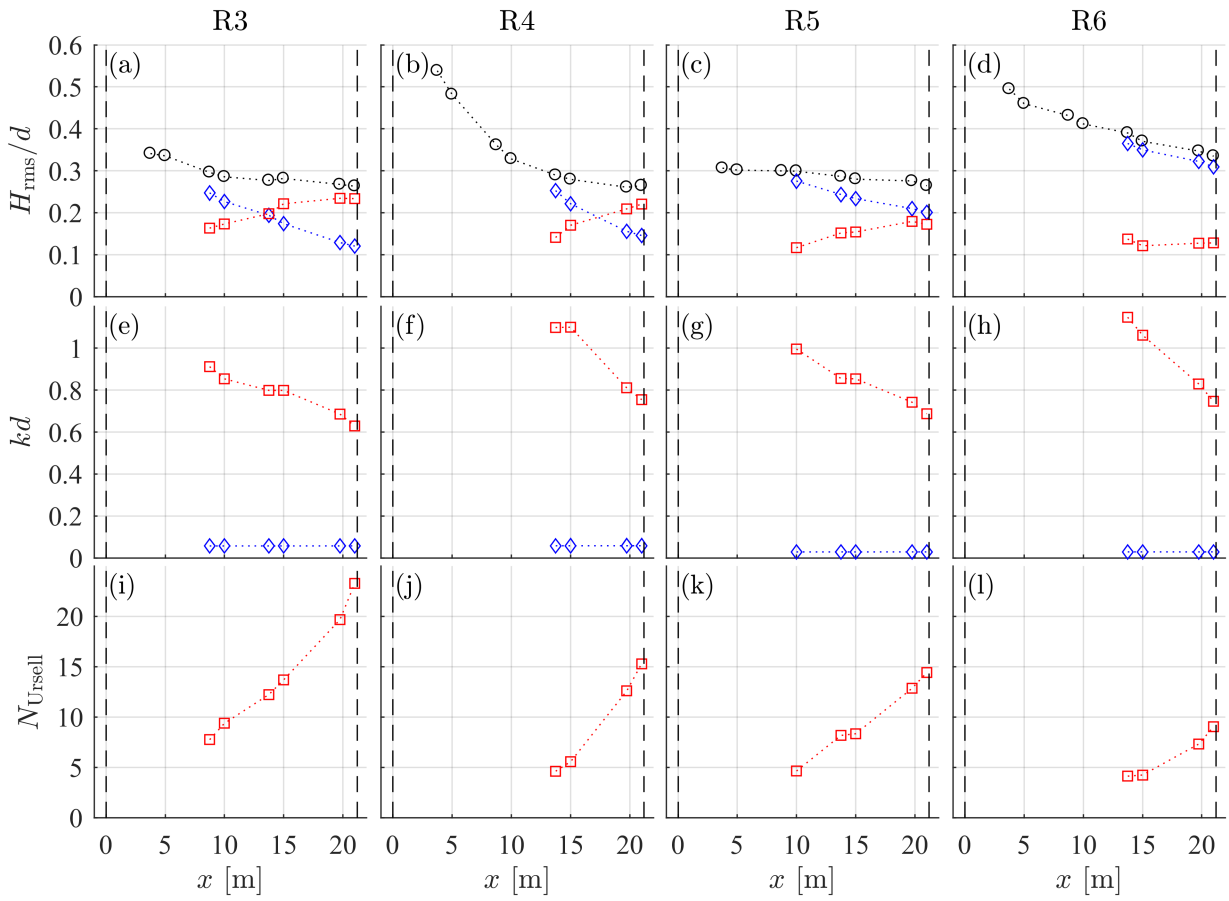

Figure 7.4: Spatial evolution of: (a-d) nonlinearity, H/d, (e-h), relative depth kd, (i-l), Ursell number, N_{Ursell}. Legend: (red) undulations, (blue) underlying long wave, (black) total incident wave.

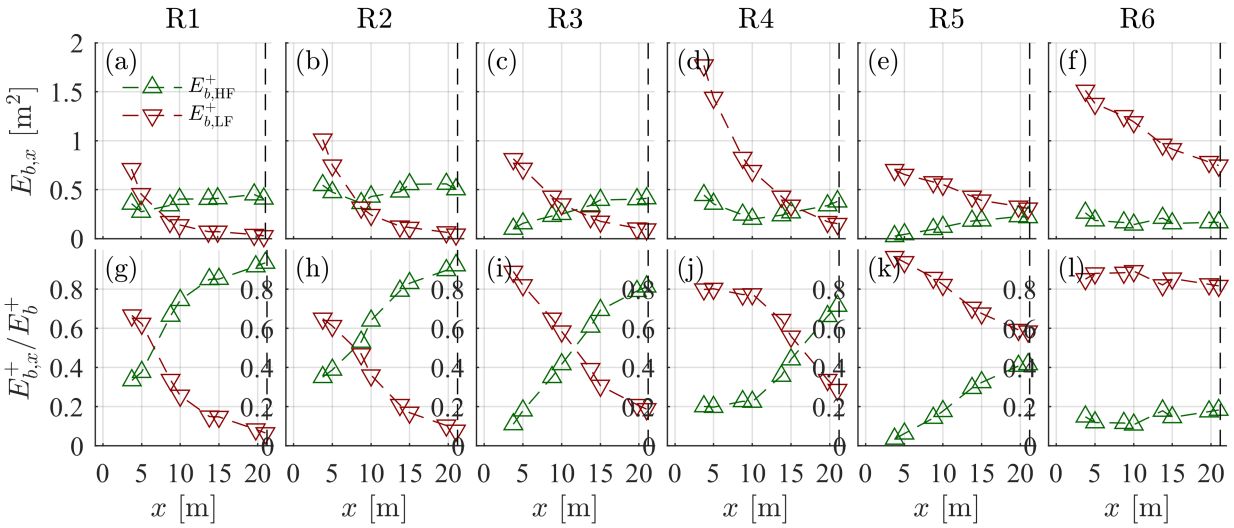

Figure 7.5: Low ($f < 0.25$ Hz) and high frequency bulk energy density ($f > 0.25$ Hz). The the relative contributions to the total amount energy is shown below.

7.4.1. Energy loss due to undular bore formation

It is common practice in spectral analysis of ocean waves to specify two frequency bands, assigning the low-frequency (LF) energy to the infragravity waves. [Gawehn et al., 2016] recently classified low frequency waves on a coral reef flat. Progressive low frequency waves were either put in the progressive-dissipative or the progressive-growing class. Energy loss in the infragravity band is commonly associated with dissipation due to bottom roughness and wave breaking [Pomeroy et al., 2012b], [Van Dongeren et al., 2013]. We would like to propose undular bore formation as a potential competing mechanism for energy loss in the infragravity band.

Fig 7.5 shows the low ($f < 0.25$ Hz) and high frequency bulk energy density ($f > 0.25$ Hz). The the relative contributions to the total amount energy are shown below. The model scale split frequency value of $f = 0.25$ corresponds to a split frequency of approximately $f = 0.05$ Hz at field scale, which is commonly used to substantiate between infragravity waves and waves in the sea-swell band. As can be seen from the top plots, the low frequency band rapidly loses energy, and the high frequency band either gains energy in shoreward direction or remains relatively constant.

The relative magnitude of HF bulk energy with respect to energy in the LF band near the beach differs per experiment. For test R5, HF and LF bulk energy are of equal magnitude. For the swell waves and IG-scale waves with smaller periods (R3 and R4) the major part of LF energy is transferred to the HF band due to undular bore formation. This can be explained due to the fact that and shorter (and higher) long waves break earlier, and developed undulations earlier on. For test R6, the underlying wave long wave still contains a significant amount of energy, and energy associated with the undulations is relatively insignificant. The hypothesis is that infragraity waves similarly lose energy due to formation of dispersive wave trains near the front. Confirmation of this hypothesis requires investigation of the bichromatic experiments at a later stage.

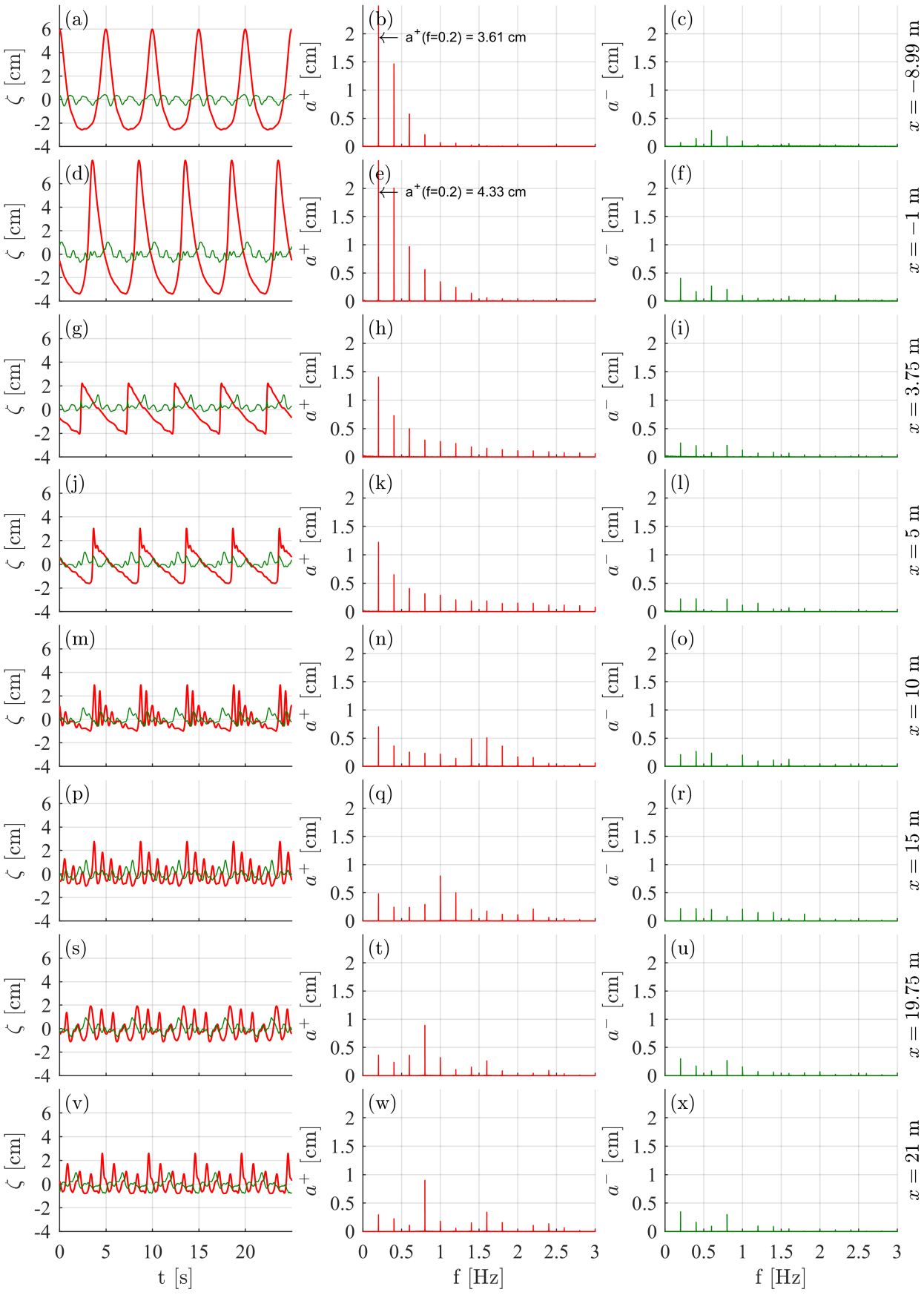

Figure 7.6: Frequency versus time domain representation for experiment R1. The decomposed incident and reflect free surface elevation is shown on the left side at several cross-reef locations. The corresponding amplitude spectra are shown on the right side.

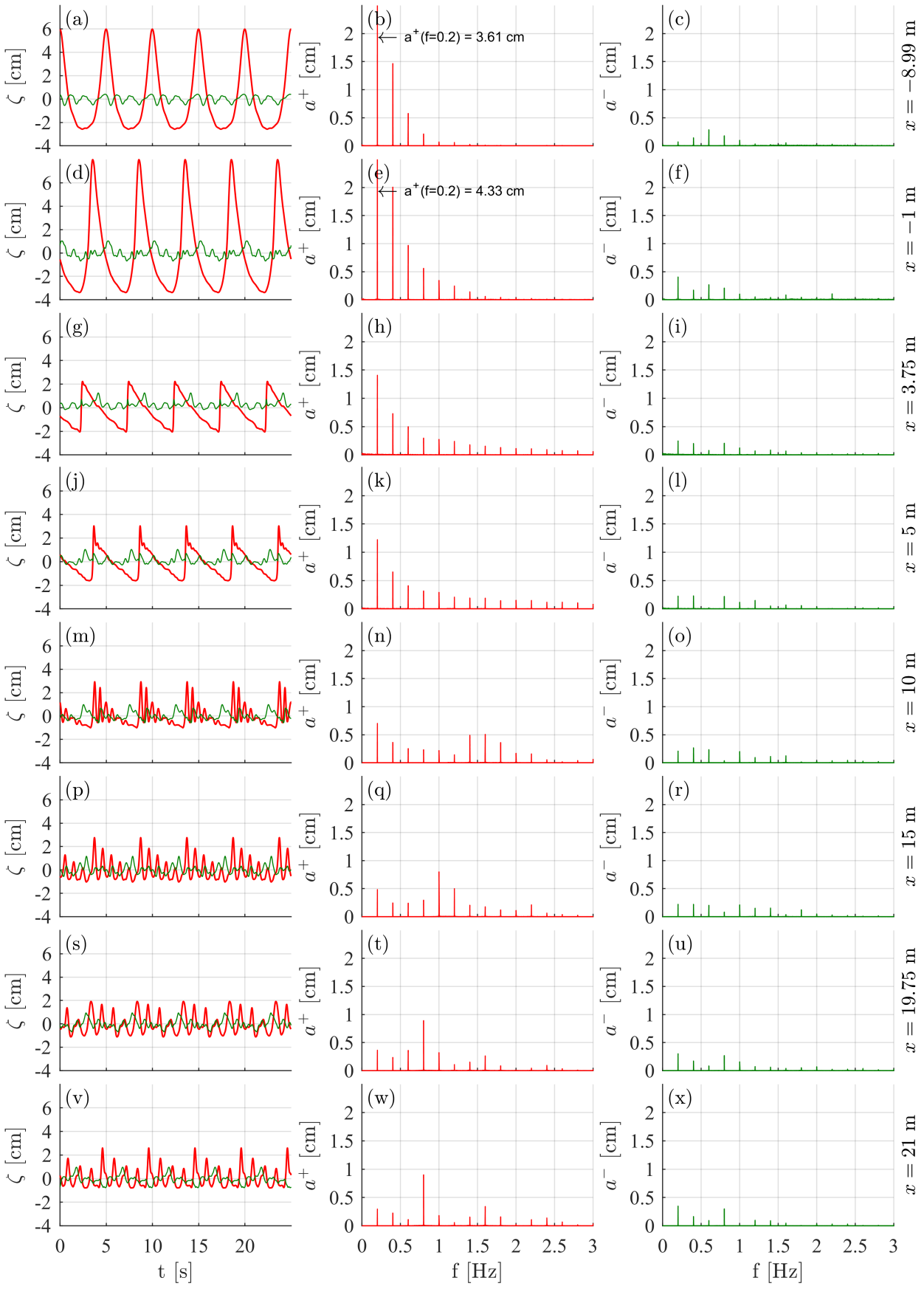

Figure 7.7: Frequency versus time domain representation for experiment R2. The decomposed incident and reflect free surface elevation is shown on the left side at several cross-reef locations. The corresponding amplitude spectra are shown on the right side.

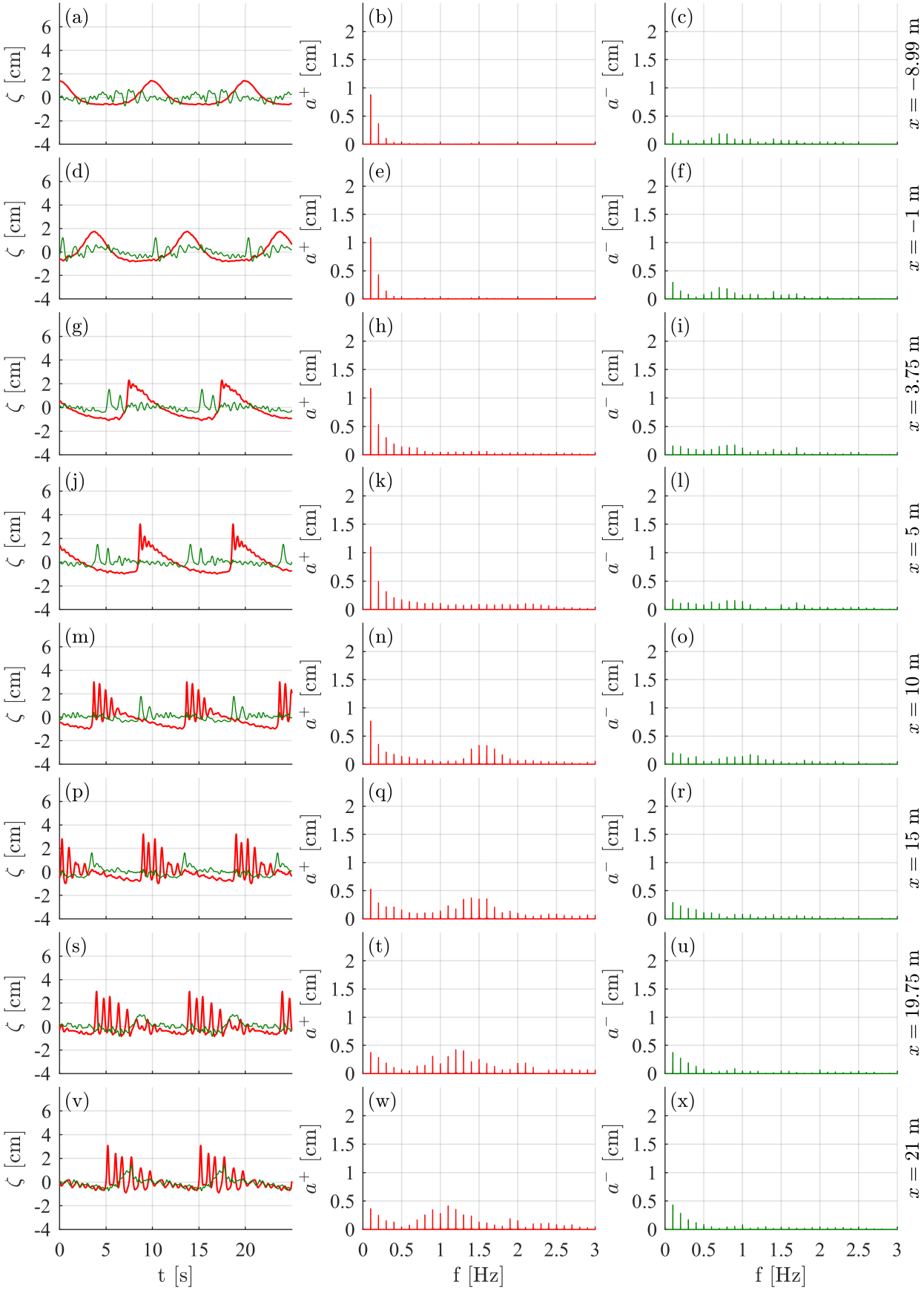

Figure 7.8: Frequency versus time domain representation for experiment R3. The decomposed incident and reflect free surface elevation is shown on the left side at several cross-reef locations. The corresponding amplitude spectra are shown on the right side.

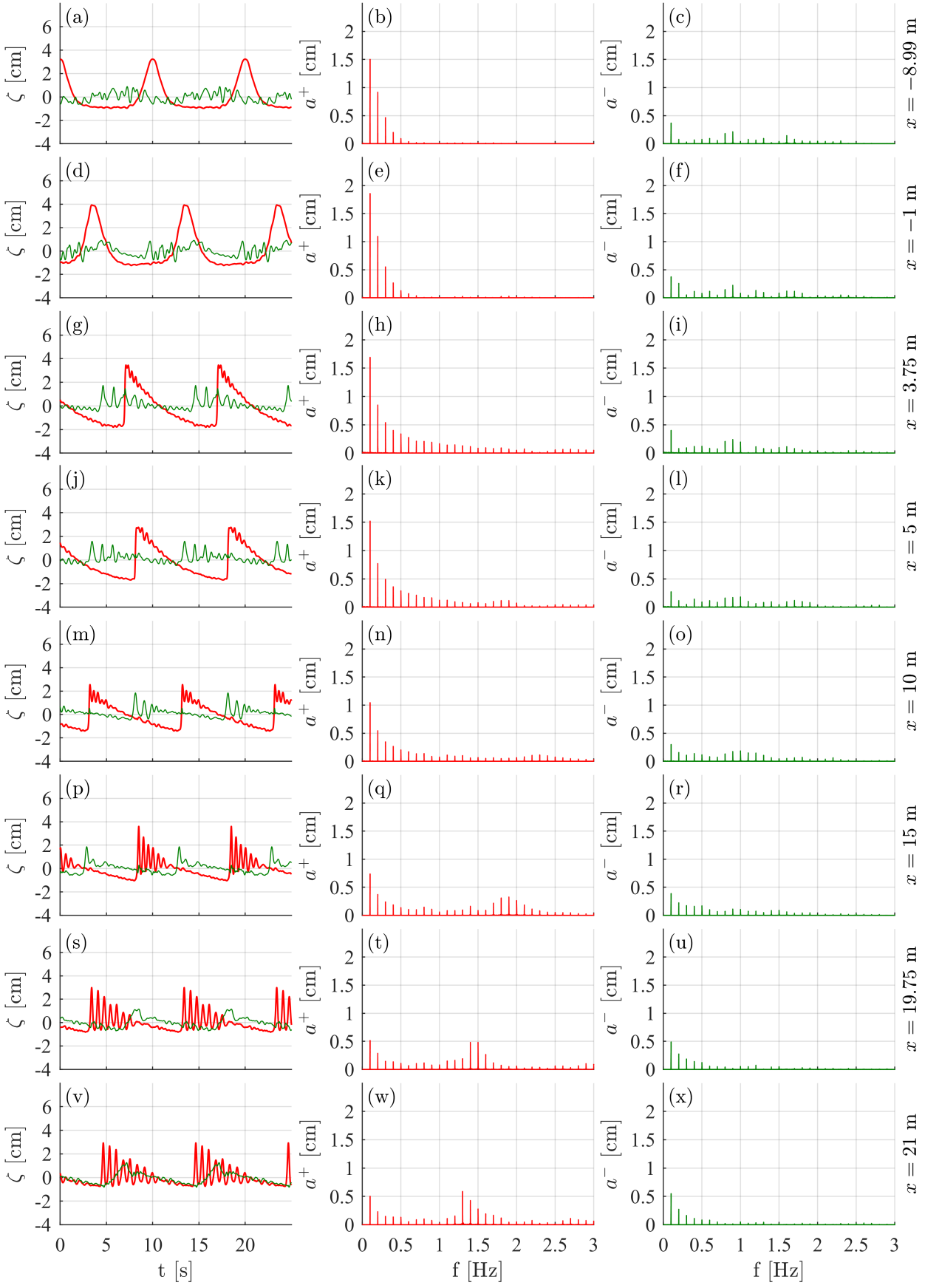

Figure 7.9: Frequency versus time domain representation for experiment R4. The decomposed incident and reflect free surface elevation is shown on the left side at several cross-reef locations. The corresponding amplitude spectra are shown on the right side.

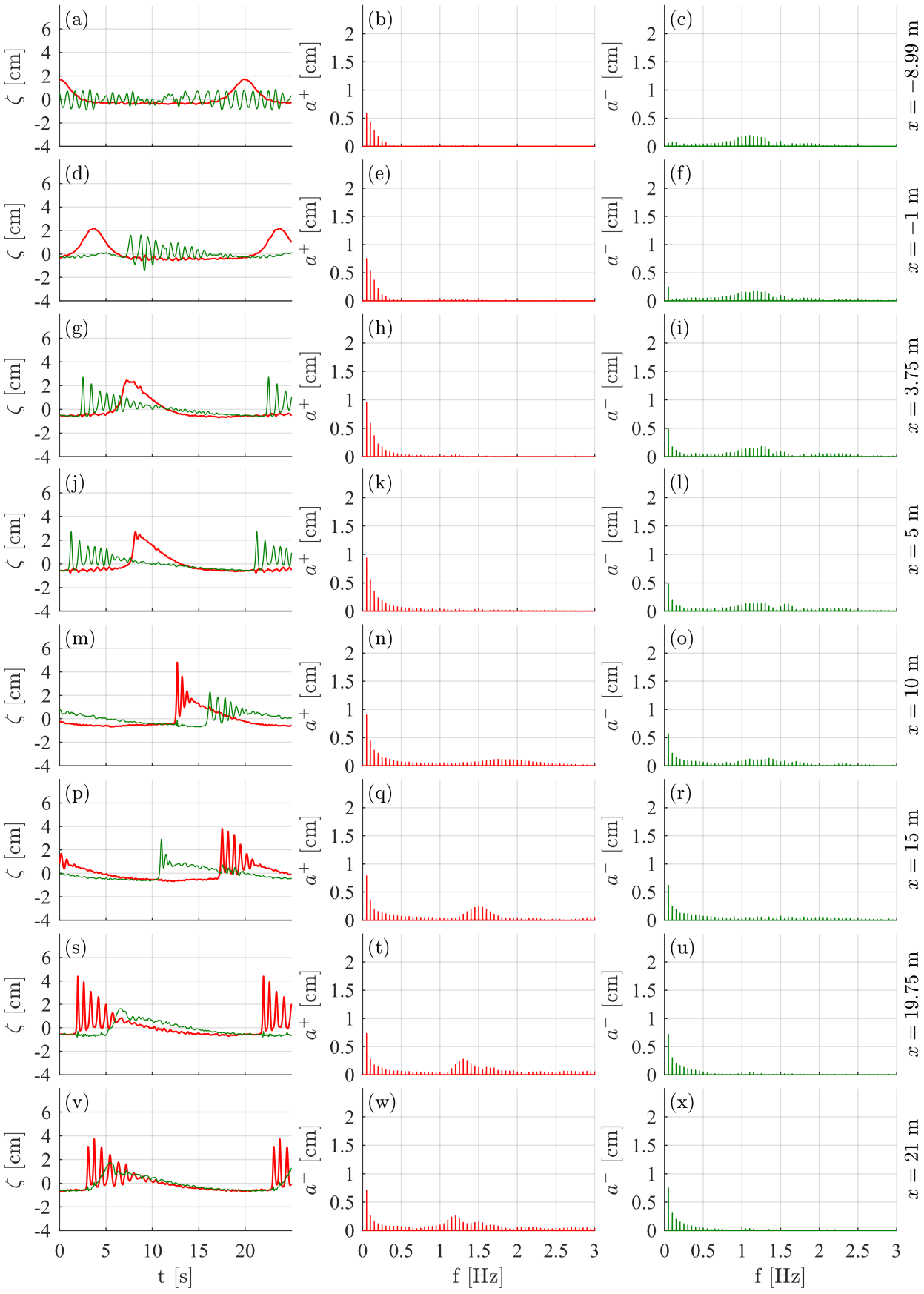

Figure 7.10: Frequency versus time domain representation for experiment R5. The decomposed incident and reflect free surface elevation is shown on the left side at several cross-reef locations. The corresponding amplitude spectra are shown on the right side.

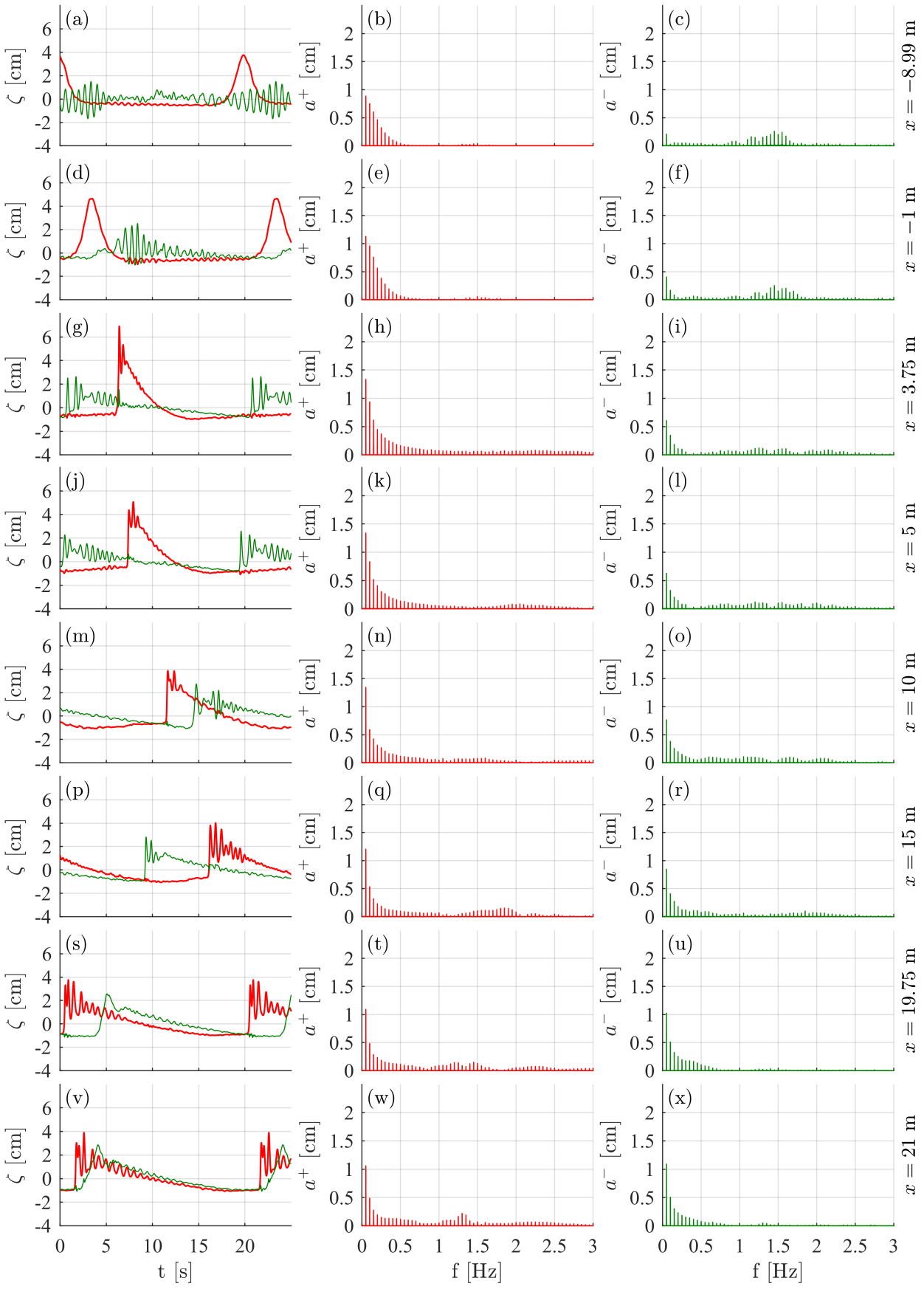

Figure 7.11: Frequency versus time domain representation for experiment R6. The decomposed incident and reflect free surface elevation is shown on the left side at several cross-reef locations. The corresponding amplitude spectra are shown on the right side.

8

Run-up of undular bores on reef-fronted beaches

In this chapter, the run-up data is analysed to get a better understanding of wave run-up of periodic undular bores on reefs. Following section 6.5 of the previous chapter, we look at the first disturbance propagating into quiescent waters. Remember that in order to get double the number of measurements with the limited number of available instruments, two sessions were carried out (see Ch. 3). To avoid any inconsistency in the analysis, the measurements obtained at the inner reef flat (i.e. gauge locations 13, 15, 17 and 19) are used to characterize the incident undular bore. These measurements are part of the same session as the run-up measurements (session 2).

8.1. Prototype wave: wave shape of leading undulation

The leading undulation that develops over the reef flat is compared with the Boussinesq solitary wave profile (Eq. 8.1), see Fig. 8.1. Time has been measured with respect to the crest of the leading undulation ($t' = t - t_c$). The measurements at wave gauge 13, 15, 17 and 19 are shown for all regular wave experiments. The solitary wave solution of Rayleigh (which has a smaller outskirt decay coefficient β) is also included in the figure for comparison. For calculation of the theoretical profile, the local depth, h_0, is used. The local depth is taken as the minimum depth within one effective period (Eq. 2.24) removed from the first crest; i.e. the depth in the trough preceding the leading undulation, $h_0 = d + \zeta_{min}$. The amplitude is measured with respect to this local level, $H = \zeta_{\max} - \zeta_{\min}$. Conceptually, the leading undulation is thus though of to be a solitary wave riding in the trough of the underlying long wave. The effective periods ($T_{e,B}$ and $T_{e,R}$) are depicted in the figure. The effect of the (negative) velocity in the trough on the solitary wave speed is ignored[1]. The nonlinearity parameter (H/h_0) is included in the figure.

The measured surface elevation during passage of the front, i.e. for $T_e < t' < 0$, has also been compared quantitatively against the solutions of both Rayleigh and Boussinesq. The normalized[2] root-mean-squared error (NRMSE), mean absolute error (NMAE) and coefficient of determination (R^2) have been computed to assess how well the front of the leading undulation can be described by a solitary wave solution. Table 8.2 lists the results. Both the NRMSE and NMAE have been included because the former gives a relatively high weight to large errors while the latter does not.

Undulation quickly approach the solitary wave shape. In general it can be said that the Boussinesq profile seems to be a good fit across mid to inner reef flat (starting from WG11 at $x = 8.75$ m). Surprisingly, this is not true for the solution of Rayleigh, for which the agreement is only good near the beach (and only for experiment R1 and R3-5). Especially the fronts of the still developing (and breaking) undulations are significantly steeper than given by Rayleigh's profile. Furthermore, it seems to be the case that for most experiments:

- For the larger part, the measured profile is situated below Rayleigh's profile.

[1] From the decomposed time-series near the beach toe (WG19, $x = 19.75$ m) it is revealed that the leading depression (almost fully) reflects against the beach slope and as a result the trough level is decreases with respect its incident value. Correspondingly, the velocity in the trough is close to zero. This suggests that the local depth should be used and the effect of the velocity on the solitary wave speed can be ignored.

[2] The root-mean-squared error has been normalized by the reef depth ($d = 0.081$ m).

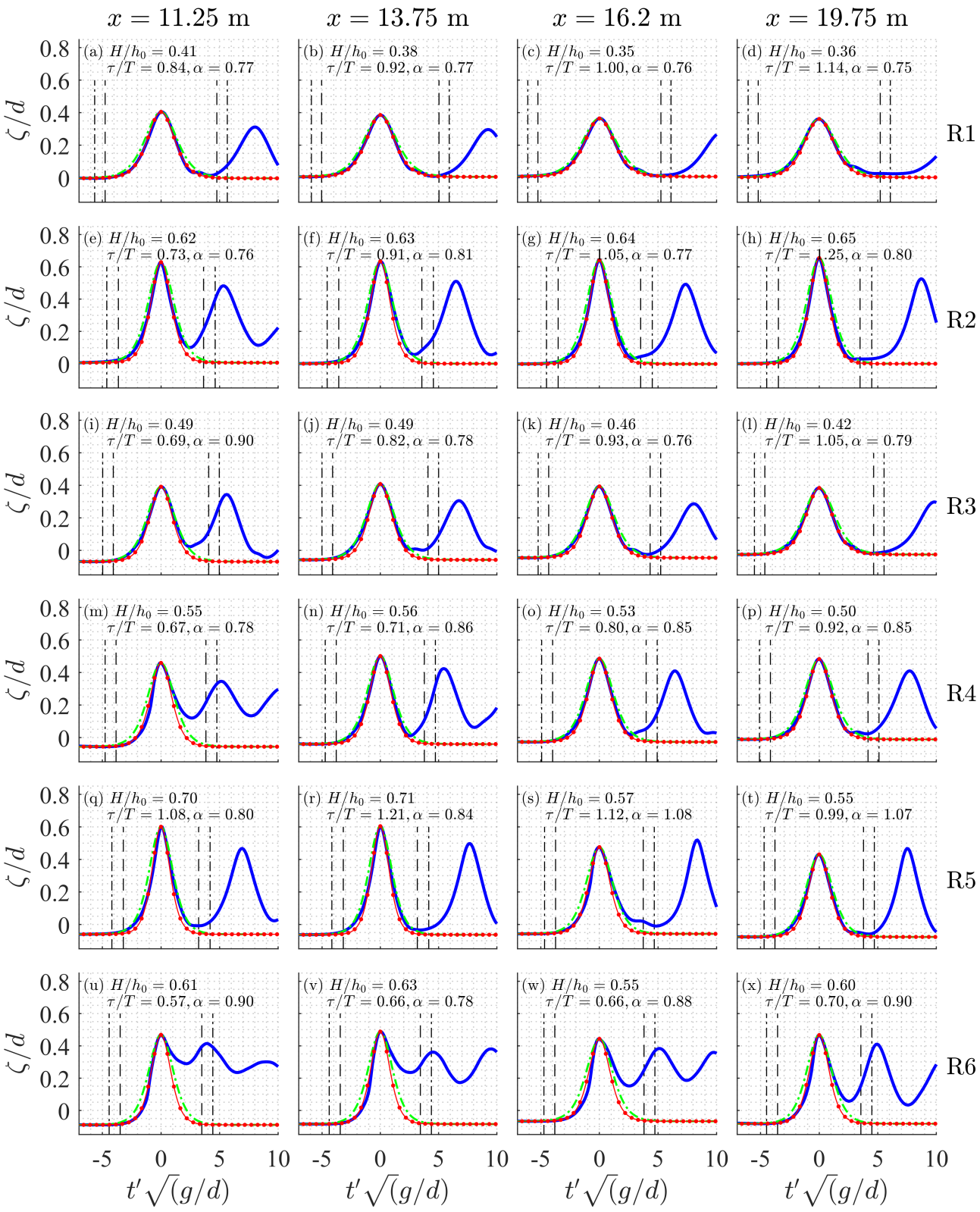

Figure 8.1: Comparison of surface elevation measurements (blue) of session 2 (at wave gauge 13, 15, 17 and 19) with the solitary wave solutions of [Boussinesq, 1872] (red) and [Rayleigh, 1876] (green). The nonlinearity parameter ($\epsilon = H_1/h_0$), amplitude ratio ($\alpha = H_2/H_1$) and the normalized separation time (normalized by the effective period T_e) with respect to the leading undulation ($\tau_{1,2}/T_{e,1}$) are indicated in each subplot.

	Boussinesq solitary wave						
	NRMSE [%]						
	WG7	WG9	WG11	WG13	WG15	WG17	WG19
R1	4.42	4.61	0.93	0.57	0.53	0.62	1.63
R2	14.33	4.93	5.74	2.23	2.30	1.95	1.74
R3	7.51	2.20	2.86	1.95	2.60	1.90	1.44
R4	19.24	2.47	2.21	2.71	1.91	1.69	1.51
R5	9.71	5.32	3.21	2.95	3.10	1.89	2.27
R6	6.57	7.59	2.30	1.34	2.83	3.71	3.10
	NMAE [%]						
	WG7	WG9	WG11	WG13	WG15	WG17	WG19
R1	3.22	3.17	0.80	0.42	0.45	0.57	1.46
R2	10.09	3.59	3.95	1.94	2.02	1.67	1.47
R3	6.79	1.68	1.79	1.61	2.23	1.64	1.27
R4	15.28	1.55	1.44	1.60	1.61	1.46	1.33
R5	8.88	4.78	2.76	2.68	2.80	1.29	2.02
R6	4.10	5.10	1.58	0.75	1.73	2.29	1.88
	R^2						
	WG7	WG9	WG11	WG13	WG15	WG17	WG19
R1	0.965	0.966	0.999	0.999	0.999	1.000	0.997
R2	0.799	0.966	0.957	0.998	0.998	0.999	0.999
R3	0.960	0.992	0.983	0.996	0.994	0.996	0.998
R4	0.719	0.989	0.991	0.985	0.998	0.998	0.998
R5	0.874	0.986	0.997	0.994	0.996	0.990	0.997
R6	0.965	0.945	0.992	0.996	0.987	0.972	0.983

	Rayleigh solitary wave						
	NRMSE [%]						
	WG7	WG9	WG11	WG13	WG15	WG17	WG19
R1	8.18	8.28	2.60	2.83	1.88	1.68	0.56
R2	9.51	9.32	10.26	4.36	4.56	4.98	5.13
R3	4.14	7.58	6.10	2.04	1.27	1.42	1.38
R4	13.02	4.36	6.61	6.72	3.28	2.67	2.42
R5	8.26	1.94	4.31	6.78	5.72	5.79	2.21
R6	4.38	3.80	7.10	6.14	7.90	7.64	7.45
	NMAE [%]						
	WG7	WG9	WG11	WG13	WG15	WG17	WG19
R1	6.50	6.65	2.15	2.41	1.59	1.33	0.47
R2	6.74	7.43	8.19	3.38	3.55	3.90	4.14
R3	3.75	5.86	4.74	1.52	0.86	1.09	1.07
R4	9.80	3.49	5.30	5.26	2.58	2.13	1.96
R5	7.55	1.63	3.14	5.20	4.25	4.38	1.67
R6	3.56	3.02	5.80	4.90	6.29	5.90	5.87
	R^2						
	WG7	WG9	WG11	WG13	WG15	WG17	WG19
R1	0.909	0.917	0.991	0.989	0.994	0.994	0.999
R2	0.894	0.908	0.898	0.985	0.984	0.981	0.982
R3	0.993	0.950	0.950	0.994	0.997	0.997	0.996
R4	0.842	0.986	0.953	0.943	0.989	0.991	0.993
R5	0.922	0.999	0.983	0.968	0.976	0.956	0.993
R6	0.987	0.982	0.952	0.963	0.939	0.921	0.939

Figure 8.2: Quantative comparison of the shape of the leading undulation with the solitary wave solution of [Boussinesq, 1872] (left) and [Rayleigh, 1876] (right). The normalized root-mean-squared error (NRMSE), normalized mean absolute error (NMAE) and coefficient of determination (R^2) have been computed to assess how well the front of the leading undulation can be described by either theory.

- For lower elevated portions of the profile, near the outskirts, the measurements are consistently above Boussinesq's solution (except for experiment R6) and align with the Rayleigh profile.

- The leading undulations are all (slightly) pitched forward.

Perhaps this pitched-forward shape contributes to the relatively good agreement with Boussinesq's solution. It is known that as an undular bore continues to propagate, undulations eventually separate; i.e. it would evolve in a train of approximate solitary waves. It is expected that, once the trailing undulations are no longer feeding the leading undulation (due to the inbalance between nonlinearity and dispersion), the leading undulation will become more symmetrical about the vertical (before it eventually separates). This of course requires a wider reef flat. It cannot be excluded that Rayleigh's solution would yield an even better estimate as it continues to become more symmetrical about the vertical.

Either way, near the beach the leading undulations quite convincingly resemble solitary waves near the beach (except for experiment R6). Hence in the following run-up analysis the solitary wave is assumed to be the governing prototype wave for run-up on the reef-fronted beach.

To investigated whether the second undulation should be considered, the amplitude ratio (α) and the separation time with respect to the leading undulation (τ/T) are also included in the figure. The amplitude ratios are in the range of $\alpha = 0.75 - 1.07$. The smallest separation time at WG19 is found for experiment R6, $\tau/T = 0.70$. Based on the experimental investigation of [Lo et al., 2013], it is concluded that the observed separation time is not large enough that the second undulation affects run-up of the leading undulation.

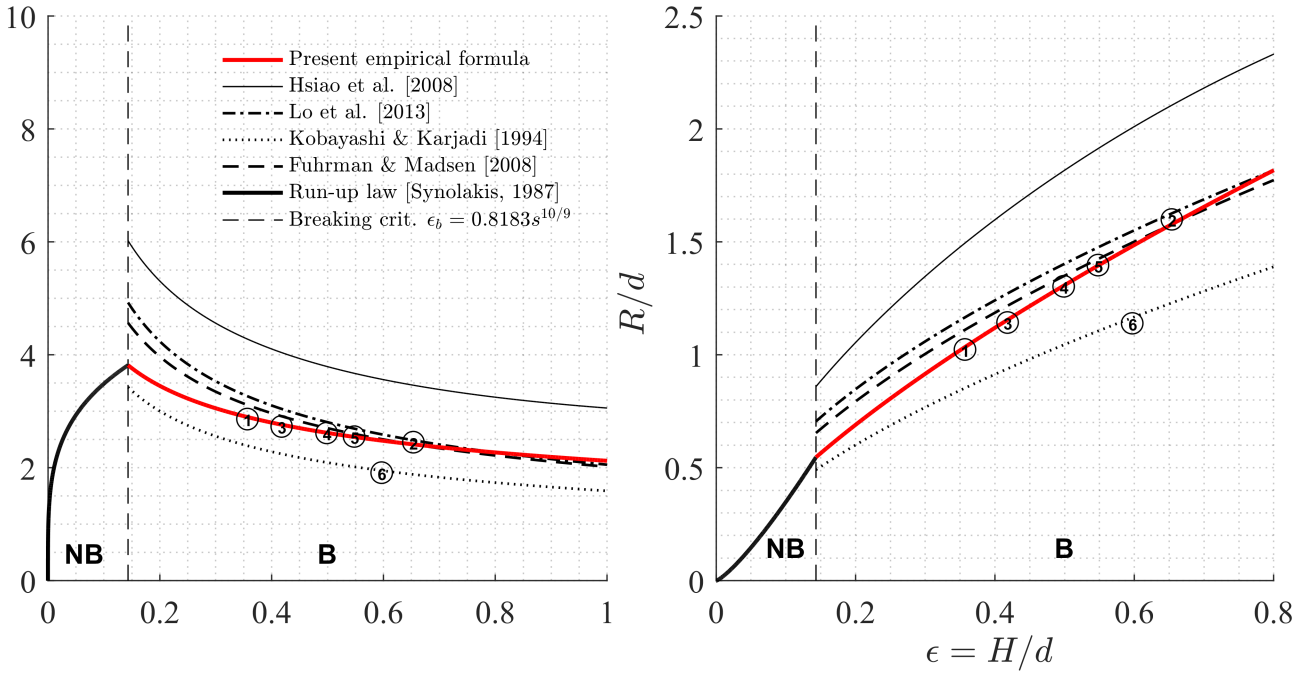

Figure 8.3: Run-up results of the six regular wave tests on the fixed 1/4.8 slope. Both fractional run-up (left), and dimensionless run-up, (right) are plotted as function of nonlinearity of the leading undulation. The run-up law for non-breaking solitary waves (Eq. 2.27 and 2.25) and the breaking criterion (Eq. 2.26) are shown in each figure. The empirical curves, developed for breaking solitary waves (Eq. 2.35 - 2.38), are also plotted in the figure. The present run-up formula (—) included for comparison.

8.2. Maximum run-up of the leading undulation

From here on h_0 is treated as the undisturbed water depth on the reef flat (i.e. $d = h_0$). This makes comparison other solitary wave run-up experiments possible[3]. For solitary waves, the wavelength is dependent on wave height. Because the beach slope is kept fixed in the present experiments, the defining variable for run-up should be $\epsilon = H/d$[4]. Fig. 8.3 shows the run-up results of the six regular (cnoidal) wave tests on the 1/4.8 slope. Both dimensionless run-up, R/d, and fractional run-up, R/H, are plotted as function of ϵ. The run-up law for non-breaking solitary waves (Eq. 2.25 for R/d and 2.27 for R/H) is included for reference. Moreover, the breaking criterion (Eq. 2.26) is graphically shown. It becomes immediately clear that, as observed in the flume, we are dealing with breaking waves. Consequently, the run-up law is not valid for our experimentally obtained results. The empirical curves, developed for breaking solitary waves (Eq. 2.35 - 2.38), are also plotted in the figure. [Hafsteinsson et al., 2017] mention that the Eq. 2.38 overestimates their obtained run-up data. This is also true for the current data set. The present empirical run-up formula (subject of section 8.3) is already included for comparison. Run-up results for experiment R1-5 follow the same trend: smaller fractional run-up and larger dimensionless run-up for increasing nonlinearity. Experiment R6 deviates from the other experiments, most likely because the leading undulation has not yet developed into a solitary wave (and is perhaps breaking moments before running up the beach). From here on, expiriment R6 is not considered.

To put the obtained results into perspective, data of several experimental studies on solitary wave run-up (featuring a range of different slopes) will be compared with the present data-set. The run-up data of [Hsiao et al., 2008], [Chang et al., 2009] and [Pujara et al., 2015] are used in addition to the widely used run-up data of [Li, 2000] and [Synolakis, 1987]. For these selected data sets, fractional run-up is plotted as a function of the three considered surf similarity parameters, ς_s, ξ_s, and χ_s (Fig. 8.4). At first, it seems that the experimental data approximately collapses onto a single line if run-up is plotted as a function of ς_s or ξ_s. This will be investigated in detail in the next section.

[3] Using the still water depth, $d_r = 0.081$ cm, instead does not change the results significantly.
[4] If the leading undulation is indeed a solitary wave, it is uniquely defined by its nonlinearity parameter $\epsilon = H/d$.

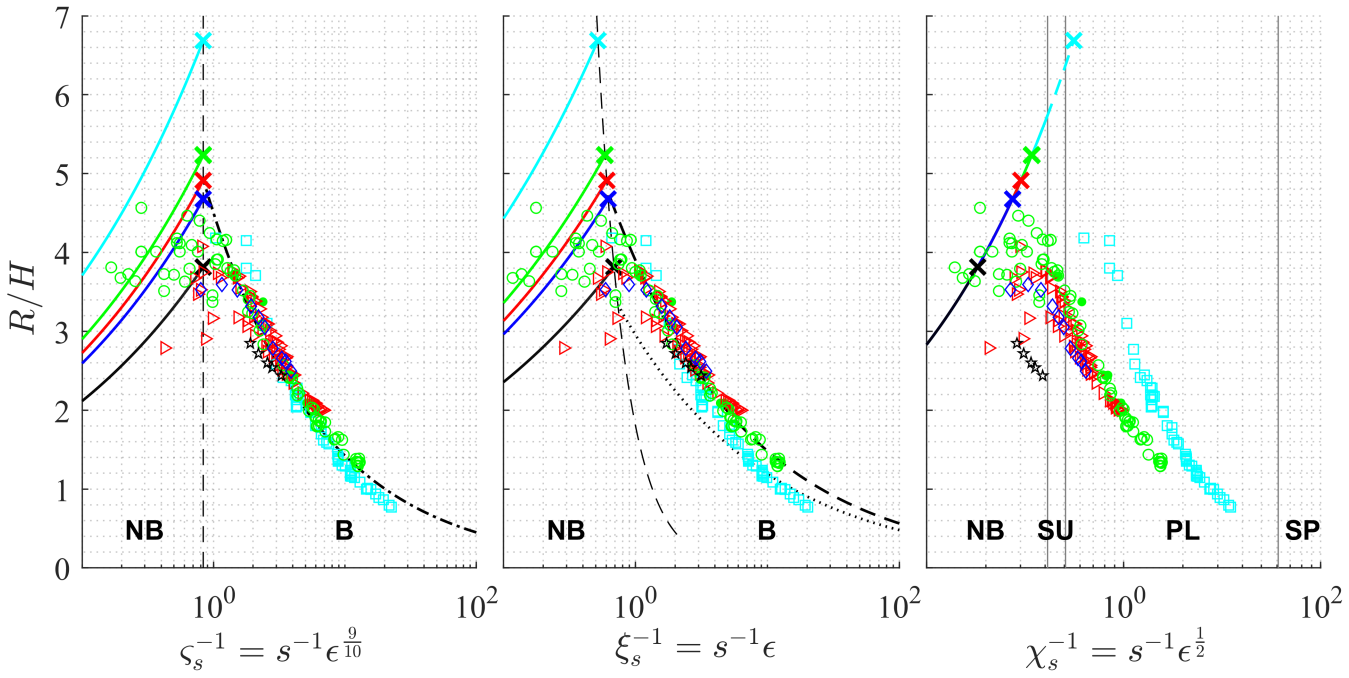

Figure 8.4: Fractional run-up is plotted as function the three considered surf similarity parameters, ς_s (left plot), ξ_s (middle), and χ_s (right). The experimental results of [Synolakis, 1987], [Li, 2000], [Hsiao et al., 2008], [Chang et al., 2009] and [Pujara et al., 2015] are shown in Fig. 8.4 are used. The run-up law (Eq. 2.27) is plotted for each experiment (thick solid lines). Note that for χ_s, the run-up law collapses onto a single line. The breaking criterion (Eq. 2.26), which demarcates the non-breaking and breaking regions, is shown in the left figure (thin vertical dashed line). The same criterion, written for ξ_s (Eq. 2.26), is shown in the middle figure. The break points are denoted by colored crosses (×). The experimental data approximately collapses for ς_s and ξ_s. The emperical curves are shown in the corresponding plots: Eq 2.35 (dotted) and 2.36 (dashed) for ξ_s and Eq.2.37 (dash-dotted) for ς_s. The right figure includes the breaker type regions according to [Grilli et al., 1997] (thin grey line).

8.3. Empirical parametrization for the run-up of breaking undular bores based on the solitary surf-similarity parameter

8.3.1. Maximum run-up

[Madsen and Schäffer, 2010] point out that for a given long wave, the worst case scenario is a beach which corresponds to $\xi = \xi_b$. If we substitute the breaking criterion (Eq. 2.26) in the run-up law for solitary waves (Eq. 2.27), we get the theoretical maximum fractional run-up for non-breaking solitary waves:

$$\left(\frac{R}{H}\right)_b = 2.831 \cdot s^{-\frac{1}{2}} \left(0.8183 s^{\frac{10}{9}}\right)^{\frac{1}{4}} = 2.831 \cdot 0.8183^{\frac{1}{4}} \cdot s^{-\frac{2}{9}} \tag{8.1}$$

which solely depends on the beach slope. According to [Lo et al., 2013], Eq. 8.1 can be treated as "the maximum fractional run-up on a given slope". The breaking limit, $\left(\varsigma_{s,b}, \left(\frac{R}{H}\right)_b\right)$, is a vertical line in the plot for ς_s, while $\left(\xi_{s,b}, \left(\frac{R}{H}\right)_b\right)$ is a curve. For a given slope, the breaking criterion can be represented as a point and from now on referred to as "the breakpoint"[5]. Because the run-up law is uniquely defined by χ_s, the breaking limit aligns with the run-up law if both are plotted as a function of χ_s. The break points are situated on the run-up law. For all experiments[6], the breakpoints are shown in Fig. 8.4 (for all three surf similarity parameters).

[Lo et al., 2013] state that Eq. 8.1 can be used as a quick estimate for maximum run-up. This seems to be in agreement with the experimental results; none of the data sets considered here (which all feature a single slope) contains fractional run-up higher than given by Eq. 8.1.

8.3.2. New empirical run-up formula for breaking solitary waves

[Madsen and Fuhrman, 2008] mention that if run-up of breaking waves follows the breaking criterion, it could be seen as a saturated breaking curve. However, they subsequently show that, based on experimental data, such a saturated breaker model is too restrictive. Furthermore, for wind waves, they show that if (a slightly modified version of) the well-known run-up relation by [Hunt, 1959] is extended up to the point where it intersects the solution of [Carrier and Greenspan, 1958], it is in much better agreement with experimental data.

Remember that run-up solutions for periodic waves and solitary waves can be written in similar form, based on their respective surf similarity parameters. Furthermore, in recent studies, fractional run-up of breaking solitary waves was assumed to be uniquely defined by a solitary surf similarity parameter (Eqs. 2.35 - 2.37. The breaking criterion was not explicitly used to constrain the solution for non-breaking waves. In addition to the breaking criterion, the mentioned empirical formulae are shown Fig. 8.4. [Fuhrman and Madsen, 2008] note that the run-up data of [Briggs et al., 1995], which features a milder 1/30 beach slope, is consistently overestimated by their empirical formula (Eq. 2.36). They hypothesize that this could be due to a mild slope dependence, or perhaps due to differences in bottom roughness. To explore this residual[7] dependence on the beach slope, the data sets of [Hsiao et al., 2008] is crucial. The data of [Hsiao et al., 2008] is obtained in a large-scale facility and features a mild 1/60 slope, which should expose any slope dependence (in case the hypothesis is true). The present data set is also interesting in the current context, as it features highly non-linear waves ($H/d = 0.35 - 0.65$) on a relatively steep slope ($s = 1/4.8$).

By including experimental data from a wider range of slopes, it becomes more convincing that run-up of breaking solitary waves is not uniquely defined by any of the three surf similarity parameters, even though the data of [Synolakis, 1987], [Li, 2000], [Chang et al., 2009] and [Pujara et al., 2015] collapses approximately onto an empirical curve (Eq. 2.36 and Eq. 2.36). It seems to be the case that, while the trend lines through each data set (considered separately) cross each other somewhere in the region where most data is obtained, the tangents to such curves differ.

It can be observed from the figure, that, for a given experiment (with a certain physical slope), the trend goes towards the corresponding breakpoint (but never reaches it). Hence, it might be natural to force an empirical fit for breaking solitary waves through this theoretical maximum. Like [Kobayashi and Karjadi, 1995], [Fuhrman and Madsen, 2008] and [Lo et al., 2013], we also assume a simple solution based on a suitable definition of the surf similarity parameter S:

$$\frac{R}{H} = \alpha S^{\beta} \tag{8.2}$$

[5] The theoretical break point is also mentioned in [Madsen and Fuhrman, 2008].

[6] Since the experiments performed by both [Chang et al., 2009] and [Synolakis, 1987] use an approximate 1/20 slope, the data is combined.

[7] Note that either definition of the surf similarity parameter (Eq. 2.28 or 2.32) already includes the beach slope.

The current approach deviates from the common approach because:

- the solution is forced through the break point,
- as a result the solution is slope dependent.

In other words, α is a dependent parameter ($\alpha = f(\beta, s)$). $beta$ is ideally a coefficient. In addition to the slope, $S = \varsigma_s$ is chosen as the independent variable because of its association with the breaking criterion. An explicit expression for the scaling coefficient, α, is obtained if Eq. 8.1 is equated to Eq. 8.2:

$$\alpha = \left(\frac{R}{H}\right)_b \varsigma_b^{-\beta} = 2.831 \cdot (0.8183)^{\frac{1}{4}} \cdot s^{-\frac{2}{9}} 0.8183^{\frac{9}{10}\beta} = 2.69258 s^{-\frac{2}{9}} \cdot 0.834875^{\beta} \tag{8.3}$$

The power β (and thus scaling coefficient α) can be estimated from the data using a nonlinear least squares method.

8.3.3. Estimation

For data close to the breaking limit ($\varsigma_s \approx \varsigma_{s,b}$), we see quite some variability in fractional run-up. In contrast, data situated further away ($\varsigma_s << \varsigma_{s,b}/2$) follows a clear trend. Hence only data for which this supposed trend can be observed ($\varsigma_s < \varsigma_{s,b}/2$) is used for estimation of α and β. Near the breaking limit, the nonlinearity parameter ϵ is relatively small (given a certain slope). Discarding part of the data is further justified by the fact that the leading undulations in all our experiments are highly nonlinear (and higher waves lead to larger (dimensionless) run-up). Moreover, there is no experimental evidence that, for a given slope, the theoretical maximum run-up value is ever reached; close to $\varsigma_{s,b}$, the data seems is lower than the value provided by the breaking limit. It turns out that β is a function of s Furthermore, it does not seem possible to capture the trend using a linear fit (for the wide range of slopes considered). The power fit,

$$\beta = a s^b = 0.2170 s^{-0.2771} \tag{8.4}$$

follows the data nicely. The coefficients a and b are estimated from the data using a nonlinear least squares method. It is stressed that the current data set is not included for estimation, because the solitary waves are not systematically generated and feature a preceding depression. Figure 8.5 shows the empirical curves based on Eq. 8.2 together with Eq. 8.3 and 8.4 for α and β.

8.3.4. Equivalent run-up expressions

A similar procedure can be ensued to obtain a run-up relations based on one of the parameters ϵ^{-1}, ξ_s or χ_s (instead of ς_s). The resulting formulations, including the corresponding coefficients, are shown in Table 8.1. It seems that all formulations are equivalent due to forcing the empirical curves through the breakpoints and assuming $\beta = a s^b$.

Because for none of the considered surf similarity parameters the run-up data totally collapses onto a single line, ϵ and s might as well be treated separately (i.e. not combined in a surf similarity parameter S). Recall that for fixed slope, Eq. 8.1 defines the maximum fractional run-up for a non-breaking solitary wave. Similarly, for a given non-breaking solitary wave (defined by ϵ) the maximum fractional run-up can be expressed as:

$$\left(\frac{R}{H}\right)_b = 2.831 \cdot 0.8183^{\frac{9}{20}} \epsilon^{-1/5} = 2.58673 \cdot \epsilon^{-1/5} \tag{8.5}$$

Hence it seems a logical choice to write fractional run-up of breaking waves in the form:

$$\left(\frac{R}{H}\right)_b = \alpha \epsilon^{-\beta} \tag{8.6}$$

where α is the corresponding expression listed in Table 8.1. Because it was shown that β depends only on the slope, we again write $\beta = a s^b$. In Fig. 8.6 both fractional and dimensionless run-up are plotted against ϵ (for each data set separately). Consider dimensionless run-up (Fig. 8.6b). For a given solitary wave (with nonlinearity parameter ϵ):

- In general, run-up is bounded by the breaking limit (Eq. 2.26).
- For non-breaking solitary waves, run-up is higher for steeper slopes (as evident from the run-up law, Eq. 2.25).

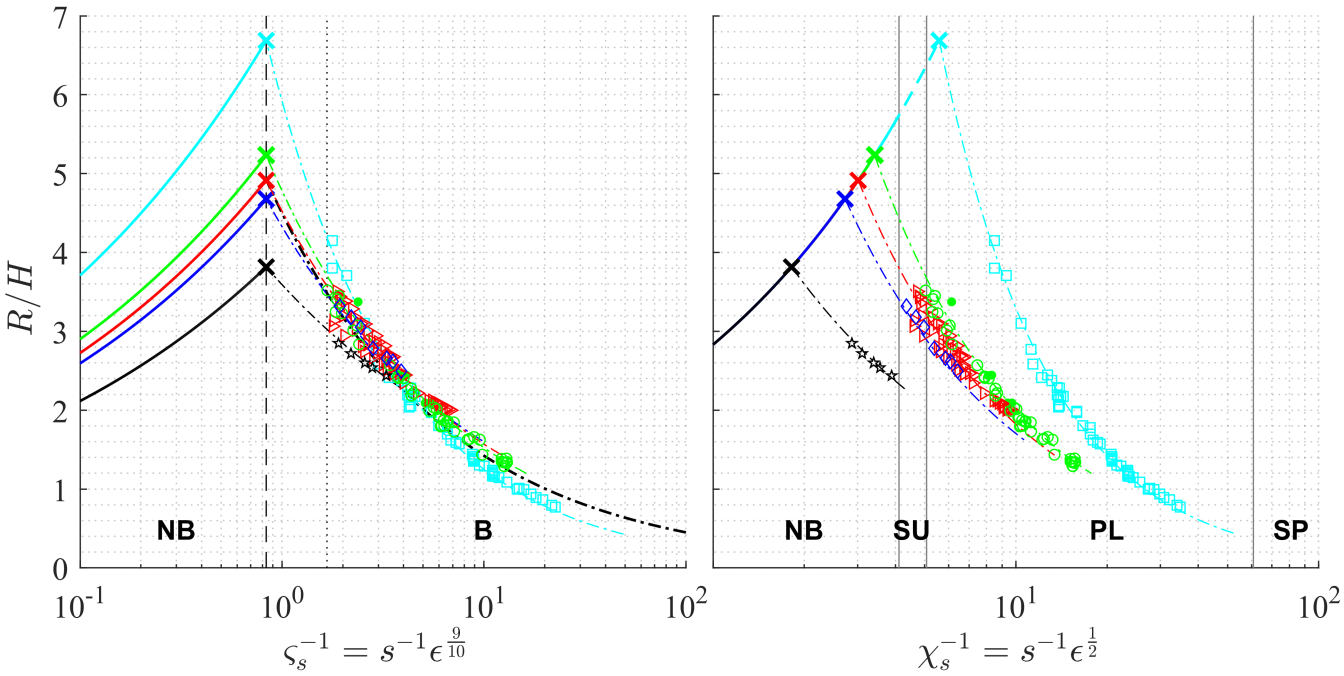

Figure 8.5: Fractional run-up is plotted as a function of two surf similarity parameters: ς_s (left plot) and χ_s (right). The experimental results of [Synolakis, 1987], [Li, 2000], [Hsiao et al., 2008], [Chang et al., 2009] and [Pujara et al., 2015] are shown. The new empirical parametrization is shown (dash-dotted colored lines). The run-up law (Eq. 2.27) is plotted for each experiment (thick solid lines). Note that for χ_s, the run-up law collapses onto a single line. The breaking criterion (Eq. 2.26), is shown in the left figure (thin vertical dashed line). The break points are denoted by colored crosses (×).

- For breaking solitary waves, run-up is higher for milder slopes (Eq. 8.2).
- Given a certain solitary wave, it can generally not be said that run-up is larger in case of either breaking or non-breaking. This is because for a certain ϵ there exists a point where a breaking solitary wave on a mild slope lead to equal run-up as a non-breaking solitary wave on a steeper slope (i.e. the run-up lines are crossing).

From Fig. 8.6a, it can be seen that this all goes together with the trends in run-up amplification: for each given slope, fractional run-up is a increasign function of ϵ up to the breakpoint, and a decreasing function for breaking solitary waves. And in both cases (breaking and non-breaking) fractional run-up is generally (without considering a certain slope) bounded by the breaking criterion.

Table 8.1: Add caption

S	R/H	α	β	a	b
ϵ^{-1}	$a\epsilon^{-\beta}$	$2.831 \cdot 0.8183^{\frac{1}{4}+\beta} \cdot s^{\frac{10\beta-2}{9}}$	as^b	0.1953	-0.2771
$\chi_s = s\epsilon^{-\frac{1}{2}}$	$a\chi_s^{\beta}$	$2.831 \cdot 0.8183^{\frac{1}{4}+\frac{\beta}{2}} \cdot s^{-\frac{4\beta+2}{9}}$	as^b	0.3907	-0.2771
$\varsigma_s = s\epsilon^{-\frac{9}{10}}$	$a\varsigma_s^{\beta}$	$2.831 \cdot 0.8183^{\frac{1}{4}+\frac{9}{10}\beta} \cdot s^{-\frac{2}{9}}$	as^b	0.2170	-0.2771
$\xi_s = s\epsilon^{-1}$	$a\xi_s^{\beta}$	$2.831 \cdot 0.8183^{\frac{1}{4}+\beta} \cdot s^{\frac{\beta-2}{9}}$	as^b	0.1953	-0.2771

8.3.5. Validation

The measured run-up and predicted run-up (Eq. 8.2 - 8.4) are plotted against each other in Fig. 8.8. This is done for both fractional (R/H) and dimensionless (R/d) run-up. The corresponding residuals are shown on the right side. The results are quite convincing. For the data of both [Li, 2000] and [Hsiao et al., 2008] our empirical fit seems to slightly overestimate the run-up for the more nonlinear waves (larger H/d). For the more nonlinear wave experiments of [Li, 2000] one could argue that this is due to the fact that these were carried out in a larger flume then the remainder of their experiments. However, this does not explain the systematic understimation of the results of [Hsiao et al., 2008].

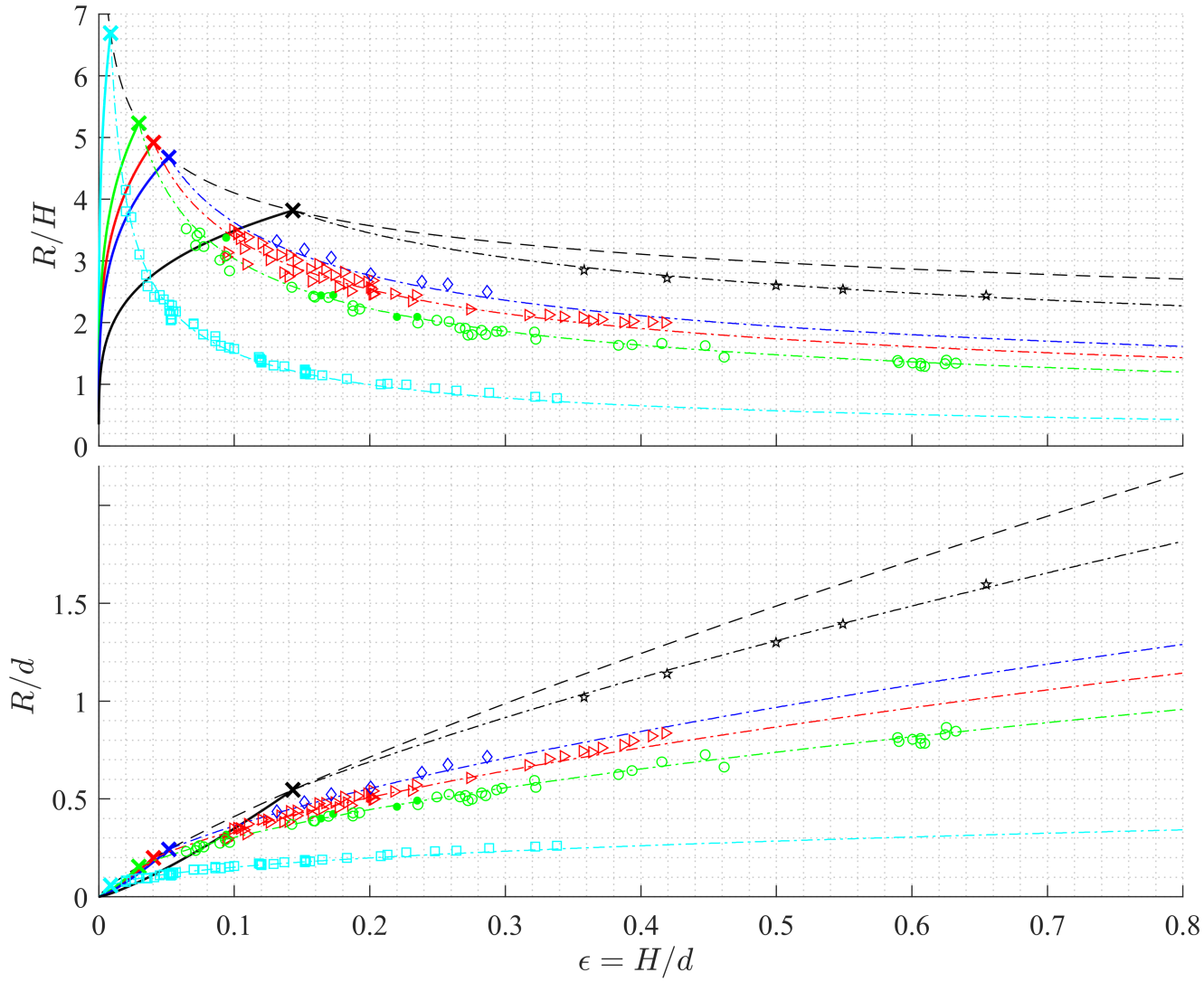

Figure 8.6: Both fractional and dimensionless run-up are plotted against ϵ.

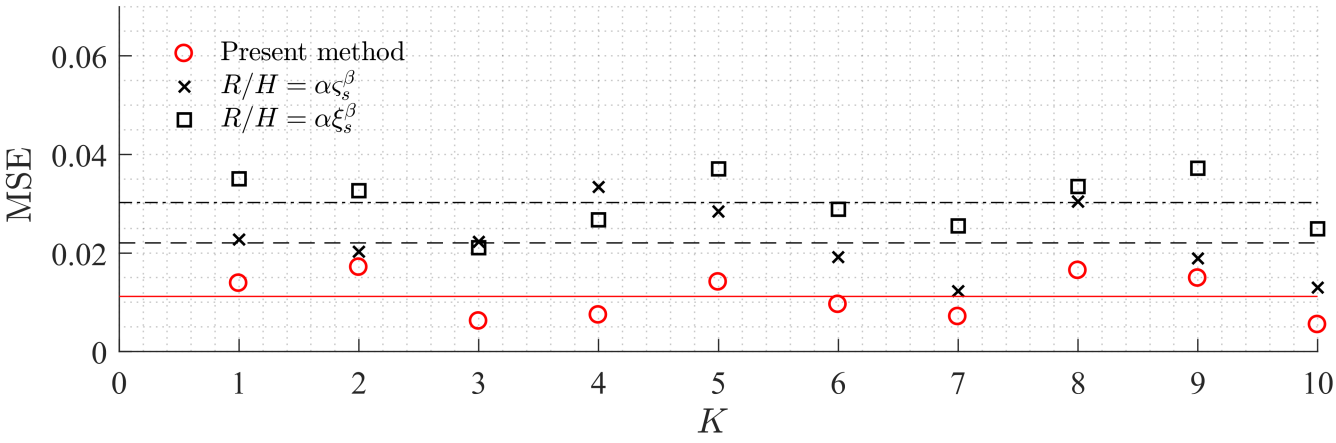

Figure 8.7: 10-fold validation results. (black square) formulation in the form of [Fuhrman and Madsen, 2008], (black cross) formulation in the form of [Lo et al., 2013], (red circle) present method.

and

8.3.6. Break point-adjusted fractional run-up

Both fractional and dimensionless run-up were treated. Moreover, it was suggested that fractional run-up was not uniquely defined by any of the surf similarity parameters. It would be interesting to see if fractional run-up can be adjusted such that this is the case. Fractional run-up, scaled by the maximum fractional run-up (Eq. 8.5), is shown as a function of both ς_s and χ_s in Fig. 8.9. It is dubbed break point-adjusted run-up. The run-up law reaches a maximum value of 1 at the breakpoint (in both figures). In the left figure, the run-up law collapses onto a single curve, and the theoretical breakpoint is a single point. The present empirical formula for fractional run-up of breaking solitary waves (Eq. 8.2), scaled by $R_{H,b}$, evaluated at a $H/d = 0.8$, can be seen as a limiting curve (i.e. an envelope). From the right figure, it can be seen that if $R_H/R_{H,b}$ is plotted against χ_s, all breaking run-up data slightly removed from the break point (i.e. $\varsigma_s < \varsigma_{s,b}/2$) follows this curve. This is interesting because, as shown by [Grilli et al., 1997], χ_s defines the breaker type. The data suggests that solitary waves with similar breaker types (similar χ_s) approximately have the same value of break point-adjusted fractional run-up. The results can be used for a simpler empirical formula than Eq. 8.2, for example:

$$\frac{R}{H} = f(\chi_s)\cdot\left(\frac{R}{H}\right)_b = K\cdot f(\chi_s)\cdot\epsilon^{-\frac{1}{5}} \quad \text{where} \quad K = 2.831\cdot 0.8183^{\frac{9}{20}} \tag{8.7}$$

Preliminary investigation reveals that an exponential function, i.e.

$$f(\chi_s) = a\left(1 - e^{-b\chi_s}\right) \tag{8.8}$$

provides a good fit through the data. The most simple formulation is obtained if the scaling coefficient is set to $a = 1$ (which means that $R_H/R_{H,b} \to 1$ as $\chi_s \to \infty$). This yields $b = 8.8468$. A two parameter model gives $a = 0.9246$ and $b = 10.2643$. Both empirical formulae are show in Fig. 8.10. The upper figure shows break point-adjusted fractional run-up as a function of χ_s. The lower figure simply shows fractional run-up, which is obtained by multiplying the adjusted fractional run-up by $R_{H,b}$. Since both models capture the data well, the two parameter model is not necessarily preferred over the single parameter model. $a = 0.9246$ in the two parameter model suggests that $R/H = 0.9246\cdot R_{H,b}$ can be seen as the empirically determined maximum fractional run-up. This is reached for very large values of χ_s for which waves are still breaking; in other words, breaking solitary waves with small relative wave heights on steep slopes. However, it has to be noted that no data close to the break point is used for estimation, hence the validity there is questionable.

8.3.7. Concluding words on the solitary surf similarity parameter

Concluding, $\chi_s = s\epsilon^{-\frac{1}{2}}$, which is the solitary wave breaker parameter of [Grilli et al., 1997] and one of the two proposed solitary surf similarity parameters of [Madsen et al., 2008], can indeed be used to estimate run-up of both breaking and non-breaking solitary waves. This is in line with [Pujara et al., 2015], who advocated that χ_s provides a credible parametrization for both run-up and breaker type. Finally, the breaking criterion of [Synolakis, 1987] and the associated theoretical maximum fractional run-up (Eq. 8.5), which were thoroughly discussed by [Lo et al., 2013], were found to be crucial for parametrization. Two types of empirical formulations were presented. While Eq. 8.2 can be used to determine the maximum run-up of breaking solitary waves, Eq. 8.7 provides a simpler and perhaps more realistic model (because the theoretical maximum run-up is never reached). In most primitive form, Eq. 8.7 only requires a single parameter (b) to be estimated from data.

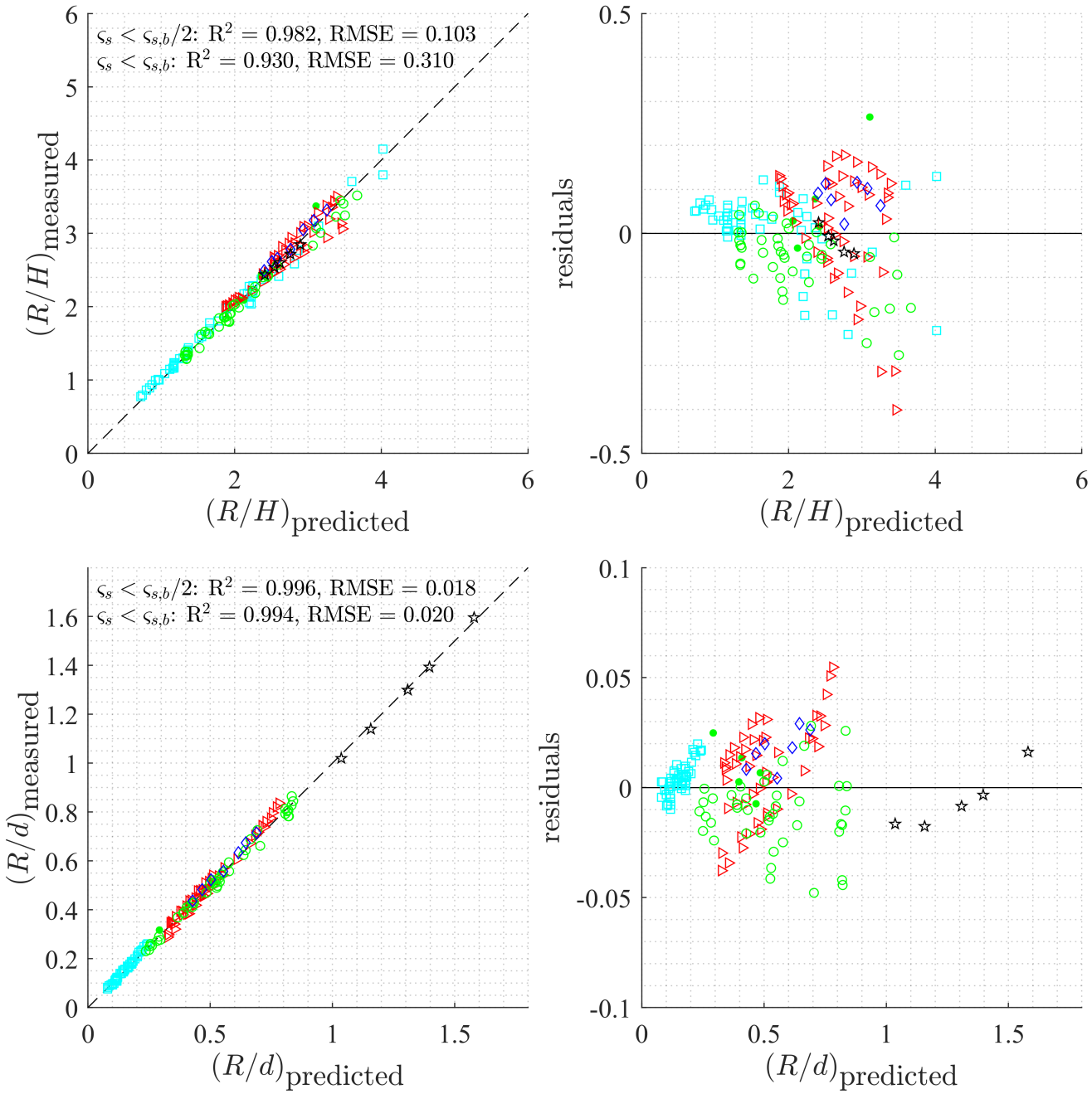

Figure 8.8: Observed versus predicted fractional and dimensionless run-up (left figures). The corresponding residuals are shown in the right figure.

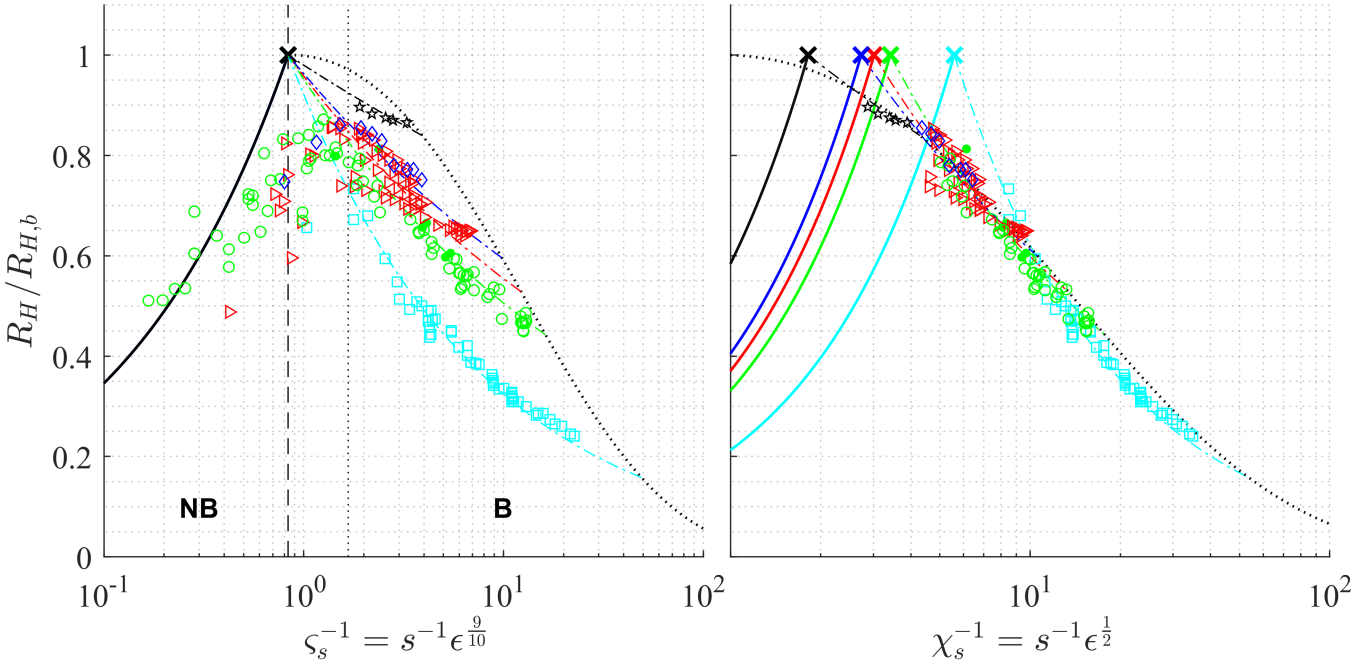

Figure 8.9: Fractional run-up, scaled by the maximum fractional run-up (Eq. 8.5) as a function of both ς_s and χ_s.

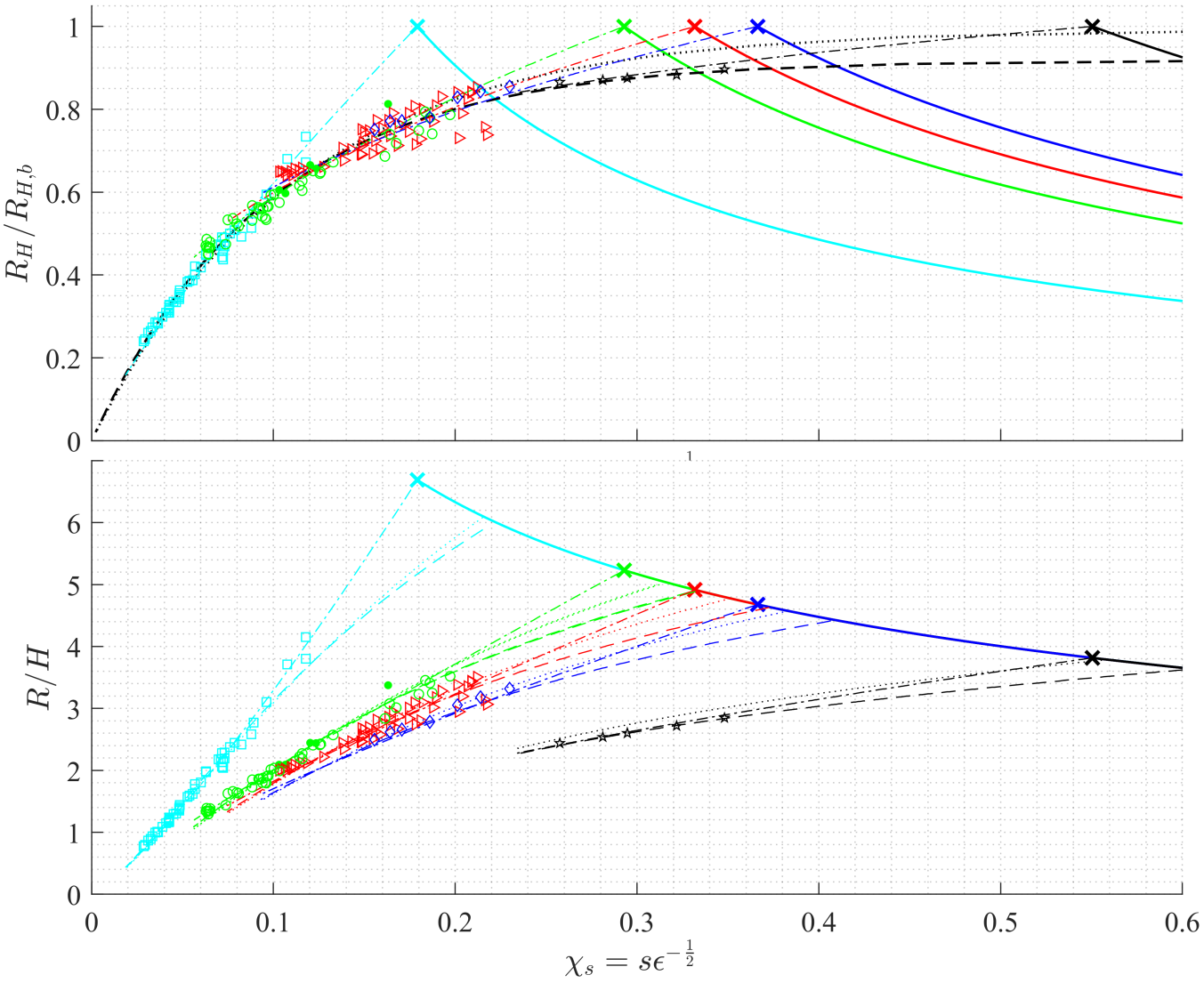

Figure 8.10: The upper figure shows the break point-adjusted fractional run-up as a function of χ_s. New parametrization based using an exponential fit: (dashed line) two parameter model, (dotted line) one parameter model. The lower figure shows fractional run-up.

9

Conclusions and recommendations

9.1. Conclusions

9.1.1. Experimental setup

In the thesis, a series of laboratory experiments were designed for a schematized 1/20 fringing reef. Both regular and bichromatic wave experiments were carried out. Bichromatic wave experiments were not analyzed in detail in this thesis; the focus lies on the regular waves experiments. Six regular wave experiments were carried out during which cnoidal waves were generated at the wave paddle. Those were of two types:

- Swell scale: wave height of 4-8 cm for a period of 5 s in model scale, corresponding to 0.8-1.6 m for 22 seconds at prototype scale (long swell)
- IG-scale: wave height of 2-4 cm for periods of 10-20 s in model scale, corresponding to 0.4-0.8 m for 44-90 seconds at prototype scale (IG-cale)

High-resolution collocated measurements of surface elevation and velocity allowed the proper separation of incoming and outgoing wave components at 11 positions along the reef. This made a detailed analysis of wave transformation over the reef flat and run-up measurements on the beach possible.

9.1.2. Decomposition of incident and reflected waves

A collocated decomposition method has been developed which takes into account the effects of nonlinearity and dispersion (non-hydrostatic pressure), and can be used for deforming waves on the reef flat.

The method requires further specification of the vertical distribution of horizontal velocity. The method can be used for experimental investigation if specification is based on the Boussinesq theory (i.e. a parabolic velocity profile is assumed), whereas it can be used for non-hydrostatic model output if both the depth-integrated velocity and non-hydrostatic pressures (at the layer interfaces) are specified.

The incoming and outgoing waves are given in terms of discharge (Q^+ and Q^-) or surface elevation (ζ^+ and ζ^-). The method is valid up to a kd-value of $kd \approx 1$, and for $H/d \approx 0.5$. If the horizontal velocity is uniform over depth and the pressure distribution is hydrostatic, the method reduces to the method of [Guza et al., 1984].

9.1.3. Wave transformation over the reef flat

For all wave conditions, well-developed undular bores are observed at the beach toe. For all these cases, a train of undulations develops behind the leading front over the reef flat. The processes leading to the development of the undulations are however quite different for the different wave conditions.

For the swell cases, the wave front steepens considerably on the fore-reef slope and the waves subsequently break violently at the reef crest. The breaking bore then decays progressively until it stops breaking and start forming undulations at mid reef, similar to field observations by Gallagher [Gallagher, 1972].

The IG-scale waves stay relatively symmetric about the vertical during the shoaling process on the fore-reef. The front only becomes steeper on the reef flat, and does not break turbulently for all IG-scale cases. For some cases the steepening process continues and is directly followed by formation of undulations. For the more energetic IG-scale cases the front first breaks turbulently. The rate at which the waves steepen on

the reef flat depends as expected on the wave height and wave length. This is in concordance with the theory of [Stoker, 1957]; larger and shorter waves steepen faster than smaller and longer waves. Consequently, the former group starts forming undulations earlier on and features more developed undulations (larger crest elevation and deeper troughs) when they arrive at the beach.

The cross-shore evolution of the total variance clearly reflects these differences in behavior. The cases involving strong breaking (swell cases) show a rapid decrease of the variance at the outer reef flat, while the IG wave cases involving no breaking experience a slow decay of energy, most probably due to bottom and wall friction. The leading undulation is generally the largest and propagates faster than the trailing undulations due to amplitude dispersion. As a result the wave length of the undulations increases while propagating towards the beach. The leading undulation progressively separate from the rest of the wave train, and ultimately resembles a solitary wave when it arrives at the toe of the beach.

9.1.4. Changes in the energy distribution

Nonlinear steepening is associated with generation of higher harmonics at a multiple of the primary frequency. The undulations are also higher harmonics, but form a secondary peak instead a tail of decreasing energy in the spectrum. This secondary peak shifts towards lower frequencies as the undular bore travels over the reef.

Due to significant reflection, it is crucial to make use of both the velocity and surface elevation measurements to determine the total amount of energy (i.e. following the method of [Sheremet, 2002]). Contributions due to potential and kinetic energy can show large differences locally. The reflection coefficient (computed using the total incident and reflected energy flux) is larger for a larger offshore period and wave height.

The relative magnitude of HF bulk energy with respect to energy in the LF band near the beach differs per experiment. For the swell waves and IG-scale waves with smaller periods, the major part of LF energy is transferred to the HF band due to undular bore formation. For the cases that involve wave breaking, energy dissipation is, at least initially, the main mechanism for energy loss in the LF band. However, as energy decay continues and the bore becomes weaker, radiation of energy at the front by means of formation of undulations can take over this role.

9.1.5. Run-up on the beach

The undulations break while running up the beach. The signature of the first undulations is clearly visible in the run-up signal. It is shown that the leading undulation governs maximum runup. More specifically, we demonstrate that empirically derived formulas for the run-up of breaking solitary waves are able to predict the maximum run-up accurately, when the characteristics of the leading undulation at the beach toe are used.

The solitary wave breaker parameter of [Grilli et al., 1997] should be used for parametrization of run-up for both breaking and non-breaking solitary waves.

Two types of empirical formulations were presented, of which only requires a single parameter to be estimated from data. This empirical formula, formally valid for solitary waves, can be used for run-up estimation of undular bores. Given the current fit, maximum run-up can be estimated for a given reef if the beach slope is known.

9.2. Recommendations and further perspectives

Based on the findings of this report, we make several recommendations for future research, formulated as potential follow-up studies.

9.2.1. Experimental and field investigation

1. **Analysis of the bichromatic wave experiments**
   Bichromatic experiments have been carried out, but have not yet been investigated in detail. It has been shown in the present study that both swell waves and IG-scale waves transform over the reef flat and form undulations. The matter that remains to be investigated in detail is whether infragravity waves — in the formal definition where they are not just long waves of $\mathcal{O}$ (100) s, but actually subharmonics of the incident short waves — also break in a dispersive manner on a reef flat. The bichomatic experiments of the present data set could provide the answer.

   Possible titles:

   - *Undular bore development over coral reefs: Part II,*

- *Dispersive wave breaking of infragravity waves on coral reefs,*
- *Progressive-dispersive infragravity waves on coral reefs.*

2. **Experimental investigation of wave run-up on coral reefs**
   It has been shown that the maximum run-up is determined by the leading undulation. For the present data set, empirical formulae developed for breaking of solitary waves, provide accurate estimates. However, run-up of turbulent bores was not investigated; all long waves considered transformed into undular bores over the reef flat, of which only experiment R6 did not yield fully developed undulations at the inner reef flat.

   A comprehensive run-up data set could be developed aimed at resolving this matter. Periodic undular bores should generated, as well as their turbulent counterparts. Various degrees should be considered, from well-developed undular bores (essentially trains of solitary waves with decreasing amplitude) to long waves with small undulations. Additionally, run-up of asymmetric long waves (steepening waves that did not yet break or for undulations) should be considered to investigate the effect of steepness of the front on run-up.

3. **Effect of bottom roughness on the formation of undulations**
   It could be investigated if bottom friction delays or even inhibits undular bore formation. Roughness elements could be placed on the reef flat and perhaps on the beach slope.

9.2.2. Decomposition

1. **Further development of collocated decomposition methods for experimental investigation**
   Collocated decomposition methods are based on the balance equations of mass and momentum, and are therefore very intuitive. The developed Boussinesq decomposition method should be verified and validated. Dispersion properties could be inproved, and it could be investigated whether it could be extended to two dimensions or uneven bottoms.

2. **Usage of different instruments**
   The Boussinesq decomposition method assumes a quadratic velocity profile. Furthermore, spatial derivatives were replaced by time derivatives. ADCP's are widely used in the field, and can be used to determine the entire velocity profile over depth. Consequently, no quadratic velocity profile has to be assumed. Furthermore, spatial gradients can be approximated numerically, and even non-hydrostatic pressure can be computed from the vertical momentum balance. Alternatively, PIV measurements can be used, see for example [David et al., 2014] and [David et al., 2015].

   A LiDaR scanner has been used in the field recently to determine the free surface during passage of an undular bore [Martins et al., 2017]. This provides a high resolution in time and space, which can be used for decomposition in order to study wave transformation in high resolution.

9.2.3. Computational modeling

1. **Impact of climate change on the importance and frequency occurrence and of undular bores**
   The wave height to depth ratio determines whether bores are of the undular or turbulent type. The submergence depth on the reef thus plays a crucial role. It could be investigated if sea level rise increases the occurrence of undular bores.

2. **Nonlinear resonance**
   Relatively deep reefs are favorable for occurrence of resonance, while shallow and wide reefs enhance nonlinear steepening of waves and undular bore formation. It could be investigated whether it is possible that resonance and (undular) bore formation occur concurrently.

3. **Application of SWASH for undular bore development over fringing reefs using a subgrid approach**
   Recently, a subgrid approach was proposed for SWASH, which is more efficient than a simulation employing a high resolution in the vertical. Unlike the HFA approximation of [Smit et al., 2013], which is typically used, it requires no additional measures to initiate wave breaking [Rijnsdorp et al., 2017]. Because the present data set contains examples of undular, intermediate and turbulent bores, it provides an interesting test case to asses both the HFA approximation and the subgrid approach.

Other recommendation:

- **Implementation of stream function theory in SWASH**
  To model the present regular wave experiments as test cases, cnoidal waves need to be generated at the boundary. Cnoidal waves can be specified in SWASH by providing time series of layer-averaged velocity. By default this does not work with the weakly reflective boundary condition. Stream funtion theory is highly accurate could prove to be a more flexible regular wave theory than cnoidal theory. It is recommended to implement stream function theory and to make it work with the weakly reflective boundary condition.

- **Implementation of an absorbing boundary condition for weakly dispersive and weakly nonlinear**
  It could be explored whether the present decomposition method can be used as a weakly reflective boundary condition. It should be explored wheter it forms an attractive alternative to the Flather/long wave radiation condition.

9.2.4. Nonlinear energy transfer and spectral analysis

1. **Bispectral analysis**
   Bispectral analysis can be performed on the regular wave measurements to study self-self interaction and to estimate energy transfers from the underlying long wave to the higher harmonics, specifically the higher harmonics associated with the undulations. This could be compared with a bispectral analysis based on the bichromatic experiments, for which the nonlinear interactions consist of sum interactions and difference interactions.

2. **Modeling the evolution of undular bores in the spectral domain**

   Theoretical modeling of triad wave–wave interactions is often based on Boussinesq-type of equations, transformed to the frequency domain [Holthuijsen, 2007]. It could be investigated whether undular bores can be modeled using a coupled energy balance equation and biphase evolution equation. Alternatively, the biphases could be estimated from the spectrum can be used instead of a biphase evolution equation.

9.2.5. Bridging the gap between theory and practice

There is an abundance of highly theoretical literature on dispersive shock waves, which is the general term for undular bore-like phenomena in various disciplines. It could be investigated if certain mathematical techniques, such as Whitham's modulation theory or the inverse scattering transform, can be applied in reef hydrodynamic studies.

Bibliography

Alfatih Ali and Henrik Kalisch. Energy balance for undular bores. *Comptes Rendus - Mecanique*, 338(2):67–70, 2010. ISSN 16310721. doi: 10.1016/j.crme.2010.02.003. URL http://dx.doi.org/10.1016/j.crme.2010.02.003.

Alfatih Ali and Henrik Kalisch. Mechanical balance laws for Boussinesq models of surface water waves. *Journal of Nonlinear Science*, 22(3):371–398, 2012. ISSN 09388974. doi: 10.1007/s00332-011-9121-2.

J.A. Battjes and R.J. Labeur. Open Channel Flow, 2014.

T B Benjamin and M J Lighthill. On cnoidal waves and bores. *Proceedings of the Royal Society A*, 244(1159):448–460, 1954.

A. M. Binnie and J. C. Orkney. Experiments on the Flow of Water from a Reservoir through an Open Horizontal Channel. II. The Formation of Hydraulic Jumps. *Proceedings of the Royal Society of London. Series A, Mathematical and Physical Sciences*, 230(1181):237–246, 1955. URL http://www.jstor.org.tudelft.idm.oclc.org/stable/99654.

Magnar Bjørkavåg and Henrik Kalisch. Wave breaking in Boussinesq models for undular bores. *Physics Letters, Section A: General, Atomic and Solid State Physics*, 375(14):1570–1578, 2011. ISSN 03759601. doi: 10.1016/j.physleta.2011.02.060. URL http://dx.doi.org/10.1016/j.physleta.2011.02.060.

J L Bona, M Chen, and J.-C Saut. *Boussinesq Equations and Other Systems for Small-Amplitude Long Waves in Nonlinear Dispersive Media. I: Derivation and Linear Theory*, volume 12. 2002. ISBN 0033200204664. doi: 10.1007/s00332-002-0466-4.

P. Bonneton, N. Bonneton, J. P. Parisot, and B. Castelle. Tidal bore dynamics in funnel-shaped estuaries. *Journal of Geophysical Research C: Oceans*, 120(2):923–941, 2015. ISSN 21699291. doi: 10.1002/2014JC010267.

P Bonneton, D Lannes, K Martins, and H Michallet. A nonlinear weakly dispersive method for recovering the elevation of irrotational surface waves from pressure measurements. *Coastal Engineering*, 138(April):1–8, 2018. ISSN 0378-3839. doi: 10.1016/j.coastaleng.2018.04.005. URL https://doi.org/10.1016/j.coastaleng.2018.04.005.

Philippe Bonneton. Wave celerity in the inner surf zone. 2005. doi: 10.1142/9789812701916.

J. Boussinesq. Théorie des ondes et des remous qui se propagent le long d'un canal rectangulaire horizontal, en communiquant au liquide contenu dans ce canal des vitesses sensiblement pareilles de la surface au fond. *Journal de mathématiques pures et appliquées*, 17(2):55–108, 1872.

L. J F Broer. On the interaction of non-linearity and dispersion in wave propagation - I. Boussinesq's equation. *Applied Scientific Research, Section B*, 11(3-4):273–285, 1964. ISSN 03657140. doi: 10.1007/BF02922007.

Mark L Buckley, Ryan J Lowe, Jeff E Hansen, and Ap R Van Dongeren. Dynamics of wave setup over a steeply-sloping fringing reef. *Journal of Physical Oceanography*, (SEPTEMBER 2015):150923131654000, 2015. ISSN 0022-3670. doi: 10.1175/JPO-D-15-0067.1. URL http://journals.ametsoc.org/doi/abs/10.1175/JPO-D-15-0067.1.

G.F. Carrier and H P Greenspan. Water waves of finite amplitude on a sloping beach. *J. Fluid Mech.*, 9:330–334, 1958.

Yu Hsuan Chang, Kao Shu Hwang, and Hwung Hweng Hwung. Large-scale laboratory measurements of solitary wave inundation on a 1:20 slope. *Coastal Engineering*, 56(10):1022–1034, 2009. ISSN 03783839. doi: 10.1016/j.coastaleng.2009.06.008. URL http://dx.doi.org/10.1016/j.coastaleng.2009.06.008.

Olivia M. Cheriton. Journal of Geophysical Research : Oceans. pages 1–14, 2016. ISSN 2169-9291. doi: 10.1002/2015JC011486.Received.

L David, L Chatellier, D Calluaud, Y J Jeon, G Rousseaux, and L Thomas. TR-PIV measurements in open channel flow for the analysis of undular tidal bores. pages 7–10, 2014.

L David, L Chatellier, D Calluaud, G Rousseaux, and L Thomas. STUDY OF DIFFERENT KIND OF TIDAL BORES IN LABORATORY. (1):2014–2016, 2015.

R G Dean. Stream function wave theory – Validity and application. *Santa Barbara Specialty Conference*, pages 269–299, 1965.

Robert George Dean and Robert A. Dalrymple. *Water Wave Mechanics for Engineers and Scientists*, volume 2. 1984. ISBN 9810204213. doi: 10.1142/9789812385512. URL http://books.google.co.uk/books/about/Water{_}Wave{_}Mechanics{_}for{_}Engineers{_}and{_}S.html?id=9-M4U{_}sfin8C{&}pgis=1.

Deltares. Programmable electromagnetic liquid velocity meter, 2016a. URL https://www.deltares.nl/app/uploads/2016/04/Programmable-electromagnetic-liquid-velocity-meter.pdf.

Deltares. Wave height meter, 2016b. URL https://www.deltares.nl/app/uploads/2016/04/Wave-height-meter.pdf.

Zeki Demirbilek, Okey Nwogu, and Donald Ward. Laboratory Study of Wind Effect on Runup over Fringing Reefs. *Test*, (July), 2007.

Henry Favre. Étude théorique et expérimentale des ondes de translation dans les canaux découverts. Technical report, Paris, 1935.

J. D. Fenton. The numerical solution of steady water wave problems. *Computers and Geosciences*, 14(3): 357–368, 1988. ISSN 00983004. doi: 10.1016/0098-3004(88)90066-0.

JD Fenton. Nonlinear wave theories. *The Sea -Ocean Engineering Science*, 9:3–25, 1990. URL http://johndfenton.com/Papers/Fenton90b-Nonlinear-wave-theories.pdf.

David R Fuhrman and Per A Madsen. Surf Similarity and Solitary Wave Runup. 134(June):195–198, 2008.

Brent Gallagher. Some qualitative aspects of nonlinear wave radiation in a surf zone. *Geophysical Fluid Dynamics*, 3(1):347–354, 1972. ISSN 0016-7991. doi: 10.1080/03091927208236086. URL http://www.tandfonline.com/doi/abs/10.1080/03091927208236086.

Matthijs Gawehn, Ap van Dongeren, Arnold van Rooijen, Curt D. Storlazzi, Olivia M. Cheriton, and Ad Reniers. Identification and classification of very low frequency waves on a coral reef flat. *Journal of Geophysical Research: Oceans*, pages 3372–3380, oct 2016. ISSN 21699275. doi: 10.1002/2016JC011834. URL http://doi.wiley.com/10.1002/2016JC011834.

D. G Goring. Tsunamis: the propagation of long waves onto a shelf. 1979:356, 1979.

Derek Goring and Frederick Raichlen. The Generation Of Long Waves In The Laboratory. *Coastal Engineering Proceedings*, 1(17):430–443, 1980. ISSN 2156-1028. URL http://journals.tdl.org/icce/index.php/icce/article/view/3470.

S. T. Grilli, I. A. Svendsen, and R. Subramanya. Breaking Criterion and Characteristics for Solitary Waves on Slopes. 123(June):102–112, 1997. doi: https://doi.org/10.1061/(ASCE)0733-950X(1997)123:3(102).

J Grue, E N Pelinovsky, D Fructus, T Talipova, and C Kharif. Formation of undular bores and solitary waves in the Strait of Malacca caused by the 26 December 2004 Indian Ocean tsunami. *Journal of Geophysical Research: Oceans*, 113(5):1–14, 2008. ISSN 21699291. doi: 10.1029/2007JC004343.

R.T. Guza, E.B. Thornton, and R.A. Holman. Swash on steep and shallow beaches. *Coastal Engineering Proceedings*, 1(19):708–723, 1984. ISSN 2156-1028. doi: 10.9753/icce.v19.%p. URL https://icce-ojs-tamu.tdl.org/icce/index.php/icce/article/view/3829.

Helgi J. Hafsteinsson, Frederic M. Evers, and Willi H. Hager. Solitary wave run-up: wave breaking and bore propagation. *Journal of Hydraulic Research*, 55(6):787–798, 2017. ISSN 00221686. doi: 10.1080/00221686.2017.1356756.

K Hasselmann. On the non-linear energy transfer in a gravity-wave spectrum. *J. Fluid Mech*, 12(481-500):15, 1962. ISSN 0022-1120. doi: 10.1017/S0022112062000373.

Holthuijsen. Waves in Oceanic and Coastal Waters. *Oceanography*, 20(3):133–135, 2007. ISSN 10428275. doi: 10.5670/oceanog.2007.42.

Shih Chun Hsiao, Tai Wen Hsu, Ting Chieh Lin, and Yu Hsuan Chang. On the evolution and run-up of breaking solitary waves on a mild sloping beach. *Coastal Engineering*, 55(12):975–988, 2008. ISSN 03783839. doi: 10.1016/j.coastaleng.2008.03.002. URL http://dx.doi.org/10.1016/j.coastaleng.2008.03.002.

Steven A. Hughes. Laboratory wave reflection analysis using co-located gages. *Coastal Engineering*, 20(3-4):223–247, 1993. ISSN 03783839. doi: 10.1016/0378-3839(93)90003-Q.

GuizieN. Katell and Barthélemy Eric. Accuracy of solitary wave generation by a piston wave maker. *Journal of Hydraulic Research*, 40(3):321–331, may 2002. ISSN 0022-1686. doi: 10.1080/00221680209499946. URL http://www.tandfonline.com/doi/abs/10.1080/00221680209499946.

G H Keulegan and G W Patterson. A CRITERION FOR INSTABILITY OF FLOW IN STEEP CHANNELS. 0(7):594–596, 1940a.

G.H. Keulegan and G.W. Patterson. Mathematical theory of irrotational translation waves. *Journal of Research of the National Bureau of Standards*, 24(1):47, 1940b. ISSN 0091-0635. doi: 10.6028/jres.024.027. URL http://nvlpubs.nist.gov/nistpubs/jres/24/jresv24n1p47{_}A1b.pdf.

Nobuhisa Kobayashi and Entin A. Karjadi. SURF-SIMILARITY PARAMETER FOR BREAKING SOLITARY-WAVE SUNUP. 120(6):645–650, 1995.

Christian Koch and Hubert Chanson. Turbulent Mixing beneath an Undular Bore Front. *Journal of Coastal Research*, 244:999–1007, 2008. ISSN 0749-0208. doi: 10.2112/06-0688.1.

R. Lemoine. SUR LES ONDES POSITIVES DE TRANSLATION DANS LES CANAUX ET SUR LE RESSAUT ONDULE DE FAIBLE AMPLITUDE. *LA HOUILLE BLANCHE*, pages 183–186, 1948. doi: http://dx.doi.org/10.1051/lhb/1948031.

Ying Li. *Tsunamis: Non-Breaking and Breaking Solitary Wave Run-Up*. PhD thesis, California Institute of Technology, 2000.

Chun Yuan Lin and Ching Jer Huang. Decomposition of incident and reflected higher harmonic waves using four wave gauges. *Coastal Engineering*, 51(5-6):395–406, 2004. ISSN 03783839. doi: 10.1016/j.coastaleng.2004.04.004.

Hong-yueh Lo, Sung Yong Park, and Philip L Liu. On the run-up and back-wash processes of single and double solitary waves — An experimental study. *Coastal Engineering*, 80:1–14, 2013. ISSN 0378-3839. doi: 10.1016/j.coastaleng.2013.05.001. URL http://dx.doi.org/10.1016/j.coastaleng.2013.05.001.

M. S. Longuet-Higgins. Integral Properties of Periodic Gravity Waves of Finite Amplitude. *Proceedings of the Royal Society of London. Series A, Mathematical and Physical Sciences*, 342(1629):pp. 157–174, 1975. ISSN 00804630. doi: 10.1098/rspa.1975.0018. URL http://www.jstor.org/stable/78694.

M. S. Longuet-Higgins and R. W. Stewart. Radiation stress and mass transport in gravity waves, with application to 'surf beats'. *Journal of Fluid Mechanics*, 13(04):481, 1962. ISSN 0022-1120. doi: 10.1017/S0022112062000877. URL http://journals.cambridge.org/abstract{_}S0022112062000877.

O.S. Madsen and C.C. Mei. The transformation of a solitary wave over an uneven bottom. *Journal of Fluid Mechanics*, 39(4):781–791, 1969. ISSN 0022-1120. doi: 10.1017/S0022112069002461. URL http://www.journals.cambridge.org/abstract{_}S0022112069002461.

Per A. Madsen and David R. Fuhrman. Run-up of tsunamis and long waves in terms of surf-similarity. *Coastal Engineering*, 55(3):209–223, 2008. ISSN 03783839. doi: 10.1016/j.coastaleng.2007.09.007.

Per A. Madsen and Hemming A. Schäffer. Analytical solutions for tsunami runup on a plane beach: single waves, N -waves and transient waves. 645:27–57, 2010. doi: 10.1017/S0022112009992485. URL https://www.cambridge.org/core/journals/journal-of-fluid-mechanics/article/analytical-solutions-for-tsunami-runup-on-a-plane-beach-single-waves-n-waves-and-transient-wav 70BDF5DD423209B400601FDF9001BDC0.

Per A. Madsen, Russel Murray, and Ole R. Sørensen. A new form of the Boussinesq equations with improved linear dispersion characteristics. *Coastal Engineering*, 15(4):371–388, jul 1991. ISSN 03783839. doi: 10.1016/0378-3839(91)90017-B. URL http://linkinghub.elsevier.com/retrieve/pii/037838399190017B.

Per A Madsen, David R Fuhrman, and Hemming A. Schäffer. On the solitary wave paradigm for tsunamis. *Journal of Geophysical Research: Oceans*, 113(12), 2008. ISSN 21699291. doi: 10.1029/2008JC004932.

Kévin Martins, Philippe Bonneton, Frédéric Frappart, Guillaume Detandt, Natalie Bonneton, and Chris Blenkinsopp. High Frequency Field Measurements of an Undular Bore Using a 2D LiDAR Scanner. *Remote Sensing*, 9(5):462, may 2017. ISSN 2072-4292. doi: 10.3390/rs9050462. URL http://www.mdpi.com/2072-4292/9/5/462.

Franc Mattioli. On the Hamiltonian decomposition of the Boussinesq equations in a pair of coupled Korteweg-de Vries equations. 28:283–296, 1998.

Robert L. Miller. Experimental determination of run-up of undular and fully developed bores. *Journal of Geophysical Research*, 73(14):4497, 1968. ISSN 0148-0227. doi: 10.1029/JB073i014p04497.

J C Van Noorloos. Energy transfer between short wave groups and bound long waves on a plane slope. (June), 2003.

Okey Nwogu. ALTERNATIVE FORM OF BOUSSINESQ EQUATIONS FOR NEARSHORE WAVE PROPAGATION. *Journal of Waterway, Port, Coastal, and Ocean Engineering*, 119(6):618–638, 1993.

Okey Nwogu and Zeki Demirbilek. Infragravity Wave Motions and Runup over Shallow Fringing Reefs. *Journal of Waterway, Port, Coastal, and Ocean Engineering*, 136(December):295–305, 2010. ISSN 0733-950X. doi: 10.1061/(ASCE)WW.1943-5460.0000050.

S. G. Pearson, C. D. Storlazzi, A. R. van Dongeren, M. F.S. Tissier, and A. J.H.M. Reniers. A Bayesian-Based System to Assess Wave-Driven Flooding Hazards on Coral Reef-Lined Coasts. *Journal of Geophysical Research: Oceans*, 122(12):10099–10117, 2017. ISSN 21699291. doi: 10.1002/2017JC013204.

Stuart Grant Pearson. Predicting Wave-Induced Flooding on Low-Lying Tropical Islands. 2016.

A. Christine N Péquignet, Janet M. Becker, Mark A. Merrifield, and Jérôme Aucan. Forcing of resonant modes on a fringing reef during tropical storm Man-Yi. *Geophysical Research Letters*, 36(3):20–23, 2009. ISSN 00948276. doi: 10.1029/2008GL036259.

D. H. Peregrine. Calculations of the development of an undular bore. *Journal of Fluid Mechanics*, 25(2): 321–330, 1966. ISSN 14697645. doi: 10.1017/S0022112066001678.

Andrew Pomeroy, Ryan Lowe, Graham Symonds, Ap Van Dongeren, and Christine Moore. The dynamics of infragravity wave transformation over a fringing reef. *Journal of Geophysical Research: Oceans*, 117(11): 1–17, 2012a. ISSN 21699291. doi: 10.1029/2012JC008310.

Andrew Pomeroy, Ryan Lowe, Graham Symonds, Ap Van Dongeren, and Christine Moore. The dynamics of infragravity wave transformation over a fringing reef. *Journal of Geophysical Research: Oceans*, 117(11): 1–17, 2012b. ISSN 21699291. doi: 10.1029/2012JC008310.

Nimish Pujara, Philip L.F. Liu, and Harry Yeh. The swash of solitary waves on a plane beach: Flow evolution, bed shear stress and run-up. *Journal of Fluid Mechanics*, 779:556–597, 2015. ISSN 14697645. doi: 10.1017/jfm.2015.435.

Ellen Quataert. Wave runup on atoll reefs. (January), 2015.

Paul A. Quinn, Marco Petti, Michele Drago, and Clive A. Greated. Velocity Field Measurements and Theoretical Comparisons For Non-Linear Waves on Mild Slopes. *Coastal Engineering*, pages 540–552, 1994.

Lord Rayleigh. XXXII. On waves. *The London, Edinburgh, and Dublin Philosophical Magazine and Journal of Science*, 1(4):257–279, 1876. ISSN 1941-5982. doi: 10.1080/14786447608639037. URL http://www.tandfonline.com/doi/abs/10.1080/14786447608639037.

Lord Rayleigh. On the Theory of Long Waves and Bores. In *Proceedings of the Royal Society of Londondon. Series A, Containing Papers of a Mathematical and Physical Character.*, volume 90, pages 324–328, 1914. URL http://www.jstor.org/stable/93519.

M. M. Rienecker and J.D. Fenton. A Fourier approximation method for steady water waves. *Cambridge University Press*, 104, 1981. doi: 10.1017/S0022112081002851.

Dirk P Rijnsdorp, Pieter B Smit, Marcel Zijlema, and Ad J H M Reniers. Efficient non-hydrostatic modelling of 3D wave-induced currents using a subgrid approach. 116:118–133, 2017. doi: 10.1016/j.ocemod.2017.06.012.

B. G. Ruessink, G. Ramaekers, and L. C. Van Rijn. On the parameterization of the free-stream non-linear wave orbital motion in nearshore morphodynamic models. *Coastal Engineering*, 65:56–63, 2012. ISSN 03783839. doi: 10.1016/j.coastaleng.2012.03.006. URL http://dx.doi.org/10.1016/j.coastaleng.2012.03.006.

A. Sheremet. Observations of nearshore infragravity waves: Seaward and shoreward propagating components. *Journal of Geophysical Research*, 107(C8):1–10, 2002. ISSN 0148-0227. doi: 10.1029/2001JC000970.

Pieter Smit, Marcel Zijlema, and Guus Stelling. Depth-induced wave breaking in a non-hydrostatic, nearshore wave model. *Coastal Engineering*, 76:1–16, 2013. ISSN 03783839. doi: 10.1016/j.coastaleng.2013.01.008. URL http://dx.doi.org/10.1016/j.coastaleng.2013.01.008.

Sandra Soares-Frazão and Vincent Guinot. A second-order semi-implicit hybrid scheme for one-dimensional Boussinesq-type waves in rectangular channels. *International Journal for Numerical Methods in Fluids*, (2008):\, 2008.

Sandra Soares Frazao and Yves Zech. Undular bores and secondary waves -Experiments and hybrid finite-volume modelling. *Journal of Hydraulic Research*, 40(July 2015):33–43, 2002. ISSN 0022-1686. doi: 10.1080/00221680209499871. URL http://www.tandfonline.com/doi/abs/10.1080/00221680209499871.

R J Sobey and Maarten W Dingemans. Rapidly varied flow analysis of undular bore. *J. Waterway Port Coastal and Ocean Engng*, 118(4):417–436, 1992. ISSN 0733950X. doi: 10.1061/(ASCE)0733-950X(1992)118:4(417).

G Stelling and M Zijlema. An accurate and efficient finite-difference algorithm for non-hydrostatic free-surface flow with application to wave propagation. *International Journal for Numerical Methods in Fluids*, 23(May 2002):1–23, 2003.

Hilary F. Stockdon, Rob A. Holman, Peter A. Howd, and Asbury H. Sallenger. Empirical parameterization of setup, swash, and runup. *Coastal Engineering*, 53(7):573–588, 2006. ISSN 03783839. doi: 10.1016/j.coastaleng.2005.12.005.

J J Stoker. *Water Waves - The Mathematical Theory with Applications*. 1957. ISBN 9780471570349.

I A Svendsen and C Staub. Horizontal particle velocities in long waves. *J. Geophys. Res.*, 86(C5):4138–4148, 1981.

I A Svendsen, P A Madsen, and J Buhr Hansen. Wave characteristics in the surf zone. *Coastal Engineering*, pages 520–539, 1978.

Ib A. Svendsen. *Introduction to Nearshore Hydrodynamics*, volume 24. 2006. ISBN 9812561420.

Ib A Svendsen, Wenkai Qin, and Bruce A Ebersole. Modelling waves and currents at the LSTF and other laboratory facilities. 50:19–45, 2003. doi: 10.1016/S0378-3839(03)00077-2.

Costas Emmanuel Synolakis. The runup of solitary waves. *J . Fluid Mech*, 185:523–545, 1987. ISSN 0022-1120. doi: 10.1017/S002211208700329X.

Costas Emmanuel Synolakis. Generation of Long Waves in Laboratory. *Journal of Waterway, Port, Coastal, and Ocean Engineering*, 116(2):252–266, mar 1990. ISSN 0733-950X. doi: 10.1061/(ASCE)0733-950X(1990)116:2(252). URL http://ascelibrary.org/doi/abs/10.1061/(ASCE)0733-950X(1990)116:2(252)http://ascelibrary.org/doi/10.1061/{%}28ASCE{%}290733-950X{%}281990{%}29116{%}3A2{%}28252{%}29.

M Tissier, P Bonneton, R Almar, B Castelle, N Bonneton, and A Nahon. Field measurements and nonlinear prediction of wave celerity in the surf zone. *European Journal of Mechanics B/Fluids*, 30(6):635–641, 2011a. ISSN 0997-7546. doi: 10.1016/j.euromechflu.2010.11.003. URL http://dx.doi.org/10.1016/j.euromechflu.2010.11.003.

M F S Tissier, P Bonneton, F Marche, F Chazel, D Lannes, De Montpellier, and Place Eugène. Nearshore Dynamics of Tsunami-like Undular Bores using a Fully Nonlinear Boussinesq Model. *Journal of Coastal Research*, Special Is(64):603–607, 2011b. ISSN 07490208.

Marion Tissier. *Etude numérique de la transformation des vagues en zone littorale, de la zone de levée aux zones de surf et de jet de rive*. Dissertation, L'UNIVERSITÉ BORDEAUX 1, 2011.

Marion Tissier, Rafael Almar, Philippe Bonneton, Hervé Michallet, Florent Birrien, Anouk de Bakker, and Gerben Ruessink. Individual wave celerity in the surf zone of a low-sloping laboratory beach. In *Coastal Dynamics*, 2013. doi: 10.1002/2015JC010708.

A Treske. Undular bores (favre-waves) in open channels - Experimental studies. *Journal of Hydraulic Research*, 32(3):355–370, 1994. ISSN 0022-1686. doi: 10.1080/00221689409498738.

Fritz Ursell. The long-wave paradox in the theory of gravity waves. *Mathematical Proceedings of the Cambridge Philosophical Society*, 49(04):685, 1953. ISSN 0305-0041. doi: 10.1017/S0305004100028887.

Ap Van Dongeren, Ryan Lowe, Andrew Pomeroy, Duong Minh Trang, Dano Roelvink, Graham Symonds, and Roshanka Ranasinghe. Numerical modeling of low-frequency wave dynamics over a fringing coral reef. *Coastal Engineering*, 73(March):178–190, 2013. ISSN 03783839. doi: 10.1016/j.coastaleng.2012.11.004.

A.R. van Dongeren and I. A. Svendsen. Absorbing-Generating Boundary Condition for Shallow Water Models. *Journal of Waterway, Port, Coastal, and Ocean Engineering*, (December):303–313, 1997.

A.R. van Dongeren, I. a. Svendsen, and F. E. Sancho. Generation of Infragravity Waves. *Proceedings of the 25th International Conference on Coastal Engineering*, Orlando:1335–1348, 1996. ISSN 08938717. doi: 10.1061/9780784402429.104.

L Verhage and A Van Dongeren. DELFT- AUKE / GENERATE Wave board computation software manual. Technical Report april, 2003.

Ge Wei, James T. Kirby, Stephan T. Grilli, and Ravishankar Subramanya. A fully nonlinear Boussinesq model for surface waves. Part 1. Highly nonlinear unsteady waves. *Journal of Fluid Mechanics*, 294:71, 1995. ISSN 0022-1120. doi: 10.1017/S0022112095002813.

G.B. Whitham. Linear and nonlinear waves, 1974. ISSN 00319228. URL http://scholar.google.com/scholar?hl=en{&}btnG=Search{&}q=intitle:Whitham,+G.B.{#}0{%}5Cnhttp://books.google.com/books?hl=en{&}lr={&}id=84Pulkf-Oa8C{&}oi=fnd{&}pg=PR7{&}dq=Linear+and+Nonlinear+Waves{&}ots=Qi8fTxiQl4{&}sig=saNJxMor1KGjcby2kLSC4RiW{_}Qo.

D.L. Wilkinson and M.L. Banner. Undular bores, 1977.

Harry H Yeh, A Ghazali, and I Marton. Experimental study of bore run-up. *Journal of Fluid Mechanics*, 206:563–578, 1989. ISSN 0022-1120. doi: 10.1017/S0022112089002417.

Haiwen Zhang and Hemming A. Schäffer. Approximate Stream Function wavemaker theory for highly nonlinear waves in wave flumes. *Ocean Engineering*, 34(8-9):1290–1302, 2007. ISSN 00298018. doi: 10.1016/j.oceaneng.2006.04.010.

M Zijlema and G.S. Stelling. Efficient computation of surf zone waves using the nonlinear shallow water equations with non-hydrostatic pressure. *Coastal Engineering*, 55(10):780–790, 2008. ISSN 03783839. doi: 10.1016/j.coastaleng.2008.02.020. URL http://www.sciencedirect.com/science/article/pii/S0378383908000380.

Marcel Zijlema. MODELLING WAVE TRANSFORMATION ACROSS A FRINGING REEF USING SWASH. (2007): 1–12, 2012.

Marcel Zijlema and Guus S Stelling. Further experiences with computing non-hydrostatic free-surface flows involving water waves. *International Journal for Numerical Methods in Fluids*, 48(2):169–197, 2005. ISSN 02712091. doi: 10.1002/fld.821.

Marcel Zijlema, Guus Stelling, and Pieter Smit. SWASH: An operational public domain code for simulating wave fields and rapidly varied flows in coastal waters. *Coastal Engineering*, 58(10):992–1012, 2011. ISSN 03783839. doi: 10.1016/j.coastaleng.2011.05.015. URL http://dx.doi.org/10.1016/j.coastaleng.2011.05.015.

A

Appendix A: Non-hydrostatic free surface flows

As mentioned in Ch. 2, vertical accelerations (dictated mainly by non-hydrostatic pressure gradients) play a crucial role in the formation and growth of undular bores. The non-hydrostatic model SWASH [Zijlema et al., 2011] is based on the mass and momentum conservative nonlinear shallow water (NLSW) equations. Since the implementation includes the vertical momentum balance, SWASH should be able to simulate the development of undular bores. This will be confirmed in Appx. C through comparison with the experimental results of [Soares Frazao and Zech, 2002]. While *computational* modeling of undular bores is not the main objective of this thesis, SWASH will be used to:

1. elucidate certain concepts regarding undular bores in general,

2. to obtain preliminary results with respect to of modeling undular bores (on reefs).

This appendix provides non-hydrostatic model equations in simplified form, which are used in Ch. 2 to explain the early stages of undular bore formation. The physical interpretation is supported by SWASH model results. Furthermore, Appx. D gives an expression for the velocity of propagation based these simplified equations.

For completeness, section A.1 first gives a short overview of SWASH and its governing equations (from the perspective focused on modeling of undular bores). In the subsequent section (section A.2), these equations are reduced to the less complex depth-integrated NLSW equations. The reader can choose to go directly to section A.2.

A.1. Governing equations

The governing equations implemented in SWASH are the Reynolds-averaged Navier–Stokes (RANS) equations for free surface flows of incompressible fluids of constant density [Zijlema et al., 2011]. They can also be considered as the NLSW equations, extended with the vertical momentum equation and the addition of non-hydrostatic pressure in horizontal momentum equation [Zijlema and Stelling, 2008]. One important difference with the conventional Navier-Stokes equations is that the free-surface elevation is single-valued[1] [Smit et al., 2013].

The equations are given here for the two-dimensional wave-motion in the vertical plane (2DV), with x and z the horizontal and vertical Cartesian co-ordinates (reference plane $z = 0$ at still water level). A detailed description of the equations and the numerical implementation is given in [Stelling and Zijlema, 2003], [Zijlema and Stelling, 2005], [Zijlema and Stelling, 2008] and [Zijlema et al., 2011]. Below follows a short overview of the governing equations.

[1] This is consistent with purely undular bores, for which the undulations are by definition not breaking. Moreover, it is most likely not very restrictive for breaking undular bores, since breaking undulations are of the spilling breaker type; the front is not overturning.

A.1.1. Continuity equation

It is assumed that density does not depend on pressure, hence density is removed from the equation for conservation of mass. The *local* continuity equation for an incompressible flow is given by:

$$\frac{\partial u}{\partial x} + \frac{\partial w}{\partial z} = 0 \tag{A.1}$$

where $u = u(x,z,t)$ and $w = w(x,z,t)$ are the mean horizontal and vertical velocities. The domain is bounded by the free surface, $z = \zeta(x,t)$ (measured upwards), and the bottom, $z = -d(x)$. The total water depth is defined as $h(x,t) = \zeta(x,t) + d(x)$.

The *global* continuity equation is obtained by integrating the local continuity equation over entire water column (applying Leibniz's integral rule), making use of both kinematic boundary conditions (the kinematic condition at the free surface, $w|_\zeta = \frac{\partial \zeta}{\partial t} + u\frac{\partial \zeta}{\partial x}$, and the bottom boundary condition, $w|_{-d} = -u\frac{\partial d}{\partial x}$), see e.g. [Stelling and Zijlema, 2003]. The global continuity equation (or free-surface condition) is given by:

$$\frac{\partial \zeta}{\partial t} + \frac{\partial Q}{\partial x} = 0 \quad \text{with} \quad Q \equiv Uh = \int_{-d}^{\zeta} u \, \mathrm{d}z \tag{A.2}$$

The discharge, Q, is obtained by integrating the horizontal velocity over depth. $U \equiv Q/h$ is the depth-averaged horizontal velocity. The global continuity equation can be regarded as an equivalent of the kinematic free surface boundary condition.

A.1.2. Momentum equations

The horizontal and vertical length scales of well-developed undulations are the same order of magnitude (as a rule of thumb, the wavelength is roughly five to ten times the depth). This means that vertical acceleration is not negligible, and the pressure distribution deviates from a hydrostatic pressure distribution. The total pressure is be split into a hydrostatic part, p_h, and a non-hydrostatic part q (see [Stelling and Zijlema, 2003]):

$$p = \underbrace{\rho_0 g\,(\zeta - z)}_{p_h} + q \tag{A.3}$$

Consequently, the forcing due to hydrostatic and non-hydrostatic pressure gradients[2] are explicitly shown in the momentum equations, which is convenient because it allows one to assess the relative importance of the forcing terms.

Horizontal momentum equation

The horizontal momentum equation for the mean flow is given by:

$$\underbrace{\frac{\partial u}{\partial t}}_{1} + \underbrace{u\frac{\partial u}{\partial x} + w\frac{\partial u}{\partial z}}_{2} = \underbrace{\frac{\partial}{\partial x}\left(\nu_h \frac{\partial u}{\partial x}\right) + \frac{\partial}{\partial z}\left(\nu_v \frac{\partial u}{\partial z}\right)}_{3} \underbrace{- g\frac{\partial \zeta}{\partial x}}_{4} \underbrace{- \frac{1}{\rho_0}\frac{\partial q}{\partial x}}_{5} \tag{A.6}$$

The terms appearing in the horizontal momentum equation are consecutively: (1) local acceleration, (2) the advective terms (here given in non-conservative form), (3) the viscosity terms[3], (4) hydrostatic pressure gradient and (5) the non-hydrostatic pressure gradient.

[2] Since a constant density ρ_0 is assumed, the influence of density differences on the flow is ignored. Using Eq. A.3, the horizontal pressure gradient can be written as:

$$\frac{\partial (p_h + q)}{\partial x} = \rho_0 g \frac{\partial \zeta}{\partial x} + \frac{\partial q}{\partial x} \tag{A.4}$$

where $\frac{\partial p_h}{\partial x}$ and $\frac{\partial q}{\partial x}$ are the forcing terms due to hydrostatic and non-hydrostatic pressure, respectively. Similarly, the vertical pressure gradient is given by:

$$\frac{\partial (p_h + q)}{\partial z} = -\rho_0 g + \frac{\partial q}{\partial z} \tag{A.5}$$

[3] The viscosity terms take into account the effect of turbulent mixing of momentum. They contain the horizontal and vertical turbulence eddy viscosities, ν_h and ν_v. The RANS equations are obtained from the instantaneous Navier-Stokes equations by means of Reynolds decomposition. The RANS equations describe the mean flow, but still have references to the fluctuating velocities in the momentum equations. These terms can be regarded as turbulent stresses, known as Reynolds stresses. The turbulence stresses can be related to the mean flow to close the system of equations (by removing any reference to the fluctuating parts of the velocities). Under the Boussinesq hypothesis, the Reynolds stresses are related to the mean flow by means of a turbulence eddy viscosity. Similar to modeling of molecular viscosity, where viscous stresses are related to shear velocities by dynamic viscosity, the turbulent stresses are related to velocity gradients using the turbulence eddy viscosities.

Vertical momentum equation and non-hydrostatic pressure

The hydrostatic balance, $\frac{\partial p_h}{\partial z} = -\rho_0 g$, is subtracted out of the total w-momentum equation (see [Stelling and Zijlema, 2003]). The resulting vertical momentum equation is given by:

$$\frac{\partial w}{\partial t} + u\frac{\partial w}{\partial x} + w\frac{\partial w}{\partial z} = \frac{\partial}{\partial x}\left(\nu_h \frac{\partial w}{\partial x}\right) + \frac{\partial}{\partial z}\left(\nu_v \frac{\partial w}{\partial z}\right) - \frac{1}{\rho_0}\frac{\partial q}{\partial z} \tag{A.7}$$

The viscosity terms are small with respect to vertical acceleration, hence it can be said that there is a balance between vertical acceleration and the vertical (non-hydrostatic) pressure gradient. The vertical and horizontal momentum equations are coupled through non-hydrostatic pressure. For a more detailed description on SWASH, one is referred to [Zijlema et al., 2011] and the references therein.

A.2. Depth-integrated nonlinear shallow water equations

SWASH gives the user the freedom to choose not to include certain terms in the momentum equations (e.g. advection terms, non-hydrostatic pressure, viscosity terms etc.), in order to speed up the computation (or perhaps reduce complexity of the problem). In this section, the RANS equations are reduced to the depth-integrated NLSW equations, retaining only the terms essential for a proper physical description of undular bore formation. This section follows a similar procedure as described in [Zijlema et al., 2011].

First of all, inclusion of viscosity is not necessary for a general description of undular bores, hence the (incompressible) Euler equations (regarded as the Navier–Stokes equations with zero viscosity) could form the starting point. Neglecting the viscosity terms in Eq. A.6 and A.7 leads to the following u- and w-momentum equations:

$$\frac{\partial u}{\partial t} + u\frac{\partial u}{\partial x} + w\frac{\partial u}{\partial z} = -g\frac{\partial \zeta}{\partial x} - \frac{1}{\rho_0}\frac{\partial q}{\partial x} \tag{A.8}$$

$$\frac{\partial w}{\partial t} + u\frac{\partial w}{\partial x} + w\frac{\partial w}{\partial z} = -\frac{1}{\rho_0}\frac{\partial q}{\partial z} \tag{A.9}$$

which, together with the continuity equation, form the mentioned Euler equations. Because a detailed description of the vertical distribution of the flow is not of interest, the equations are integrated over depth. Treatment of the vertical momentum equation and the non-hydrostatic pressure gradients (appearing in both momentum equations) is detailed below.

Consider the horizontal non-hydrostatic pressure gradient. Application of Leibniz's integral rule gives:

$$\int_{-d}^{\zeta} \frac{\partial q}{\partial x}\,\mathrm{d}z = \frac{\partial}{\partial x}\int_{-d}^{\zeta} q\,\mathrm{d}z - q|_{\zeta}\frac{\partial \zeta}{\partial x} - q|_{-d}\frac{\partial d}{\partial x} \tag{A.10}$$

If q is assumed to vary linearly over depth (from $q = 0$ at the surface to $q = q|_{-d}$ at the bottom), the non-hydrostatic forcing term can be approximated as:

$$\int_{-d}^{\zeta} \frac{\partial q}{\partial x}\,\mathrm{d}z = \frac{1}{2}\frac{\partial \left(q|_{-d} h\right)}{\partial x} - q|_{-d}\frac{\partial d}{\partial x} = \frac{1}{2}\left(h\left.\frac{\partial q}{\partial x}\right|_{-d} + q|_{-d}\frac{\partial (\zeta - d)}{\partial x}\right) \tag{A.11}$$

Substitution of this forcing term into the depth-integrated horizontal momentum equation results in:

$$\frac{\partial U}{\partial t} + U\frac{\partial U}{\partial x} = -g\frac{\partial \zeta}{\partial x} - \frac{1}{2\rho_0}\left(\left.\frac{\partial q}{\partial x}\right|_{-d} + \frac{q|_{-d}}{h}\frac{\partial (\zeta - d)}{\partial x}\right) \tag{A.12}$$

Details on the integration of the acceleration terms over depth are omitted. However, it has to be noted that the dispersion terms — that arise due to deviation of velocity from a uniform distribution — have been neglected. Their effect is normally taken into account in the viscosity terms, but as these are also neglected here, dispersion due to non-uniformity of the flow velocity is simply ignored[4].

Now consider the w-momentum equation, Eq. A.9. The advection terms are assumed to be small with respect to local acceleration, and have therefore been neglected a priori. The resulting w-momentum equation, given by:

$$\frac{\partial w}{\partial t} = -\frac{1}{\rho_0}\frac{\partial q}{\partial z} \tag{A.13}$$

[4] It has to be said that dispersion properties of SWASH are improved by increasing the number of vertical layers.

is now reduced to a balance between vertical (local) acceleration and the vertical non-hydrostatic pressure gradient. Similar to Eq. A.11, integration of the vertical non-hydrostatic pressure gradient gives:

$$\int_{-d}^{\zeta} \frac{\partial q}{\partial z}\,\mathrm{d}z = \underbrace{q|_{\zeta}}_{=0} - q|_{-d} = -q|_{-d} \tag{A.14}$$

If local accelerations are also assumed to vary linearly over depth, the following integral can be approximated as:

$$\int_{-d}^{\zeta} \frac{\partial w}{\partial t}\,\mathrm{d}z = \frac{1}{2}h\left(\left.\frac{\partial w}{\partial t}\right|_{\zeta} + \left.\frac{\partial w}{\partial t}\right|_{-d}\right) \tag{A.15}$$

Using the last two results, integration of Eq. A.13 over depth yields the reduced w-momentum equation:

$$\left.\frac{\partial w}{\partial t}\right|_{\zeta} = \frac{2}{\rho_0}\frac{q|_{-d}}{h} - \left.\frac{\partial w}{\partial t}\right|_{-d} \tag{A.16}$$

$w|_{-d}$ follows from the kinematic condition at the bottom, $w|_{-d} = -u\frac{\partial d}{\partial x}$. Since there is no equation to directly evaluate non-hydrostatic pressure, $q|_{-d}$, an extra equation is required, which is found in the local continuity equation, written as:

$$\frac{\partial u}{\partial x} + \frac{w|_{\zeta} - w|_{-d}}{h} = 0 \tag{A.17}$$

In SWASH, $q|_{-d}$ is solved for by means of the pressure-correction technique, see [Zijlema and Stelling, 2005]. In Ch. 2 a horizontal bottom is assumed to simplify the system of equations (Eq. A.17, A.2, A.12, A.16) even further.

B

Appendix B: Long waves and turbulent bores

Turbulent bores have been mentioned in the introduction of Ch. 2. Consider a positive surge propagating in downstream direction. x_1 and x_0 are the up- and downstream cross-sections, respectively. From observations it follows that a turbulent front forms, if the height of a flow transition, $\Delta h = h_1 - h_0$, is large with respect to the (undisturbed) water depth, h_0. This appendix provides a theoretical background on the turbulent bore.

Characteristic properties of turbulent bores, such as its propagation velocity, c_b, and dissipation rate, D, follow from the balance principles; conservation of mass and (horizontal) momentum. Shallow water bores are often assumed to have uniform velocities over depth and a hydrostatic pressure distribution on both sides of the bore front. Hence the Saint Venant equations form a suitable set of equations to model such bores. The shallow water equations[1] — written in conservative form — are given by:

$$\frac{\partial h}{\partial t} + \frac{\partial Uh}{\partial x} = 0 \tag{B.1}$$

$$\frac{\partial Uh}{\partial t} + \frac{\partial \left(U^2 h + \frac{1}{2} g h^2\right)}{\partial x} - gh\frac{\partial d}{\partial x} = 0 \tag{B.2}$$

For the present purpose, these equations are integrated over a control volume surrounding the a bore front. Mass conservation across the bore (per unit width) is given by:

$$\frac{d}{dt}\int_{x_0}^{x_1} h dx = [Uh]_{x_0}^{x_1} \tag{B.3}$$

and momentum conservation by:

$$\frac{d}{dt}\int_{x_0}^{x_1} Uh dx = \left[U^2 h + \frac{1}{2} g h^2\right]_{x_0}^{x_1} \tag{B.4}$$

Any wave described by Eq. B.1 and B.2 will eventually break (since dispersion, which reduces steepening of the wave, is not taken into account). As the wave front breaks, a bore is formed. A turbulent bore is usually treated as a discontinuity in the flow and so-called bore or shock conditions can be provided, which hold across the discontinuity: [Whitham, 1974]:

$$-c_b [h]_{x_0}^{x_1} + [Uh]_{x_0}^{x_1} = 0 \tag{B.5}$$

$$-c_b [Uh]_{x_0}^{x_1} + \left[U^2 h + \frac{1}{2} g h^2\right]_{x_0}^{x_1} = 0 \tag{B.6}$$

Experience learns that these shock conditions describe turbulent bores quite accurately [2].

[1] Note that these are the conventional NLSW equations; the vertical momentum balance is neglected and non-hydrostatic pressure is not included in the horizontal momentum balance.

[2] It is interesting to note that the shallow water equations are not valid if the wave front becomes too steep, but both before and after the transition (from long wave to turbulent bore form) they accurately describe the flow [Whitham, 1974].

B.1. Shallow water bore speed

Eq. B.5 and B.6 can be written explicitly for the bore speed, c_b:

$$c_b = U_0 + \sqrt{g\frac{h_0+h_1}{2}\frac{h_1}{h_0}} = U_0 + \sqrt{g\left(h_0 + \frac{3}{2}\Delta h + \frac{1}{2}\frac{\Delta h^2}{h_0}\right)} \tag{B.7}$$

or

$$c_b = U_1 + \sqrt{g\frac{h_0+h_1}{2}\frac{h_0}{h_1}} \tag{B.8}$$

c_b is the absolute speed; i.e. in a fixed frame of reference. It is clear that either U_0 or U_1 can be eliminated. The two flow velocities are related by:

$$U_1 = U_0 + \frac{h_1-h_0}{h_1}\sqrt{g\frac{h_0+h_1}{2}\frac{h_1}{h_0}} \tag{B.9}$$

The first expression for c_b, Eq. B.7, can be simplified for a bore moving in quiescent water ($U_0 = 0$):

$$c_b = \sqrt{g\frac{h_0+h_1}{2}\frac{h_1}{h_0}} \tag{B.10}$$

B.2. Froude number and bore strength

Bores can be classified based on the bore strength, either $\Delta h/h_0$ or $r = h_1/h_0$. Bores are however most often classified by their Froude number, defined as:

$$F_r = \frac{c_b - U_0}{\sqrt{gh_0}} \tag{B.11}$$

The fact that the two are often interchanged makes sense, as the ratio $r = h_1/h_0$ is a function of the Froude number:

$$r = \frac{h_1}{h_0} = \frac{1}{2}\left[\sqrt{\left(1+8F_r^2\right)} - 1\right] \tag{B.12}$$

Eq. B.12 is known as the Bélanger equation, which is a dimensionless form of Eq. B.7, making use of the definition of the Froude number. The bore speed in a reference frame with respect to the downstream current is given by:

$$c_b - U_0 = \sqrt{g\frac{h_0+h_1}{2}\frac{h_1}{h_0}} \tag{B.13}$$

To obtain the Froude number, we normalize by the downstream shallow water wave speed:

$$F_r = \frac{c_b - U_0}{\sqrt{gh_0}} = \sqrt{\frac{(2r+1)^2-1}{8}} \quad \text{where} \quad r = \frac{h_1}{h_0} \tag{B.14}$$

The Froude number defines the type of bore (purely undular, intermediate/transition, or purely turbulent) if h_1 is taken far away from the front.

B.3. Energy dissipation

The turbulent bore equations (equations B.5 and B.6) conserve mass and momentum, but for a discontinuous solution, energy is not conserved. Expressions for the total energy E and the net energy flux $\Delta F = F_1 - F_2$ can be obtained for the shallow-water energy balance in the form:

$$-\frac{dE}{dt} + \Delta P = D \tag{B.15}$$

Such a discontinuous solution resembles a turbulent bore. D is the energy loss, according to Ali and Kalisch [2010] "due to the approximate nature of the shallow water equations and the discontinuous solution". [Rayleigh,

1914] accounted this loss to turbulence at the bore front, and hence it can be called after Rayleigh. The Rayleigh dissipation rate D is given by:

$$D = \frac{\rho g}{4}\frac{|Q|}{h_0 h_1}\Delta h^3, \qquad \Delta h = h_1 - h_0, \qquad Q = h_0\left(U_0 - c_b\right) = h_1\left(U_1 - c_b\right) \tag{B.16}$$

Substitution yields:

$$D_b = \frac{\rho g}{4} h_1\left(U_1 - c_b\right)\frac{\left(h_1 - h_0\right)^3}{h_0 h_1} = \frac{\rho g}{4}\sqrt{\frac{g\left(h_0 + h_1\right)}{2 h_0 h_1}}\left(h_1 - h_0\right)^3 \tag{B.17}$$

see e.g. [Tissier, 2011]. This expression is one of the building blocks on which the theory of [Lemoine, 1948] is built on.

B.4. Propagation speed of a breaking wave

It is common practice to approximate the propagation velocity of a breaker by considering the analogy between a bore and a broken wave front. This is done by application of Eq. B.7, taking x_0 at the wave trough and x_1 at the crest. To eliminate U_t, it is assumed that the wave is of constant form, the velocity at the wave trough is then given by:

$$U_t = \frac{c_w \zeta_t}{d + \zeta} \tag{B.18}$$

Eq. B.18 is only valid if — in addition to the constant form requirement — there is no net volume flux, see Appx. D. Combination of Eq. B.7 and B.18 yields Svendsen's broken wave speed:

$$c_w = \sqrt{g\frac{h_t + h_c}{2}\frac{h_c}{h_t}\frac{h_t}{d}} \tag{B.19}$$

see for example [Svendsen et al., 1978], [Svendsen et al., 2003] or [Tissier et al., 2011a]. Evaluation of this expression requires specification of the mean water depth, d, as well as the instantaneous depth at the wave trough h_t and crest h_c. Both expressions, Eq. B.7 and **??**, will be applied to the front of a long wave transforming into an undular bore (Ch. 6). More on the velocity of propagation of undular bores in Appx. D.

B.5. Method of characteristics

For a wave entering quiescent waters, the NLSWE can be solved using the method of characteristics (MoC), see e.g. [Stoker, 1957] or [Battjes and Labeur, 2014]. Below follows a summary. The NLSWE can be decoupled and written in the form of two convection equations. For a horizontal bottom and no friction, these two equations are given by:

$$\frac{d}{dt}R^{\pm} = \partial_t R^{\pm} + \left(U \pm c_\zeta\right)\partial_x R^{\pm} = 0 \quad \text{where} \quad R^{\pm} = U \pm 2c_\zeta \quad \text{and} \quad c_\zeta = \sqrt{g\left(d + \zeta\right)} \tag{B.20}$$

for a wave traveling in the positive direction and negative direction, respectively. One can recognize the total derivative, which is stated to be zero. Hence, the functions $R^{\pm}$, called Riemann invariants, are constant for points moving through the fluid with the velocity $U \pm c_\zeta$. Equivalently stated, the following ordinary differential equations holds:

$$\frac{dx}{dt} = U \pm c_\zeta \tag{B.21}$$

for points of a constant state $U \pm 2c_\zeta$. The solution can be represented graphically by curves in the x,t-plane, called characteristics. If the Riemann invariant is known somewhere on such a characteristic, it is known along the entire characteristic. Now in the present case, at $t = 0$ the motion is undisturbed ($c = c_0$ and $U = U_0 = 0$). The undisturbed region in the x,t-plane is bounded by a positive characteristic issuing from the origin ($x = c_0 t$, the initial characteristic) is called the quiet zone [Stoker, 1957]. Anywhere in the quiet zone, $x \pm c_0 t =$ constant. All negative curved characteristics originating from the quiet zone have the same value of the Riemann invariant:

$$R_0^- = U_0 - 2c_0 \tag{B.22}$$

which, since we have assumed $U_0 = 0$, reduces to $R_0^- = -2c_0$. Since R^+ is constant, this means that in the entire domain:

$$R^+ = U - 2c_\zeta = -2c_0 \quad \text{or} \quad U = 2\left(c_\zeta - \sqrt{gd}\right) \tag{B.23}$$

Because R^+ is constant along a positive characteristic, and R^- is constant everywhere, the positive characteristics are necessarily straight. Another consequence is that the state variables U and c (and thus also Q and ζ) are constant (separately) along positive characteristics. The exact value of the slope for any positive characteristic depends on the associated Riemann invariant, which in turn is determined by the boundary condition at the time when the characteristic was issued ($t = \tau$). The slope of any of the straight positive characteristics issuing from the the left boundary at $t = \tau$, is given by either of the following two equations:

$$\frac{dx}{dt} = \begin{cases} 3/2U(0,\tau) + c_0 & \text{or} \\ 3c_\zeta(0,\tau) - 2c_0 \end{cases} \tag{B.24}$$

Where $U(0,\tau)$ or $c_\zeta(0,\tau)$ is the specified boundary condition at $x = 0$. To obtain the evolution of ζ, c_ζ, U or Q in space, Eq. B.24 can be integrated:

$$x = \begin{cases} x = (t-\tau)\,(3/2U(0,\tau) + c_0) & \text{or} \\ x = (t-\tau)\left(3c_\zeta(0,\tau) - 2c_0\right) \end{cases} \tag{B.25}$$

Hence the complete motion is determined. See for example [Madsen et al., 2008] for a application. In SWASH the boundary condition is usually given in terms of velocity, but perhaps we would like to know the evolution of the free surface, from the same velocity boundary condition as provided to SWASH. Now, the depth-averaged velocity, as a function of elevation, was determined from Eq. B.23. This expression can be inverted:

$$\zeta = U\sqrt{\frac{d}{g}} + \frac{U^2}{4g} \tag{B.26}$$

From Eq. B.26 and Eq. B.23, also the discharge can be determined.

C

Appendix C: Computational modeling of undular bores

C.1. Test case: development of an undular bore [Soares Frazao and Zech, 2002]

To validate their numerical code, [Soares Frazao and Zech, 2002] conducted laboratory experiments on undular bore development and compared the experimental results with the solution of their model. The same measurements were also used in [Soares-Frazão and Guinot, 2008] and [Tissier et al., 2011b]. Here the data will also be used, in this case to validate SWASH for undular bore development, in order to find the most suitable configuration. The bore should propagate with correct speed, and the growth (increase in amplitude and wavelength) of leading and first few subsequent undulations should follow the observed trends, in order to confidently use SWASH for the development of of undular bores on reefs.

The experimental setup is very simple. The free surface is initially at rest. A gate is almost instantly (but partially) opened and water flows (with a constant discharge) from the upstream reservoir into the channel. A bore forms and rapidly transforms into an undular bore, which are measured by six gauges at $x = 6.15, 13.15, 15.65, 18.15, 20.65, 23.15$ m. The resulting bore strength is such that generated bores are purely of the undular type, and therefore modeling wave breaking is not necessary.

Four experiments (No. 6, 15, 16, and 19) were modeled with SWASH. Velocity is imposed at the boundary, which is calculated from the given down and upstream levels h_0 and h_1, using classical bore theory (see previous Chapter). SWASH is run with default settings, in both depth-averaged and two-layer mode. Additionally, SWASH is run at higher vertical resolution (5 pressure layers, 20 velocity layers), making use of the subgrid approach by [Rijnsdorp et al., 2017]. The space increment is set to $\Delta x = 0.01$ m, which means around $100 - 200$ points per wavelength for the leading undulations. Visual inspection shows that there is not much difference with respect to $\Delta x = 0.02$ m. The maximum Courant number was set at 0.5 for stability reasons.

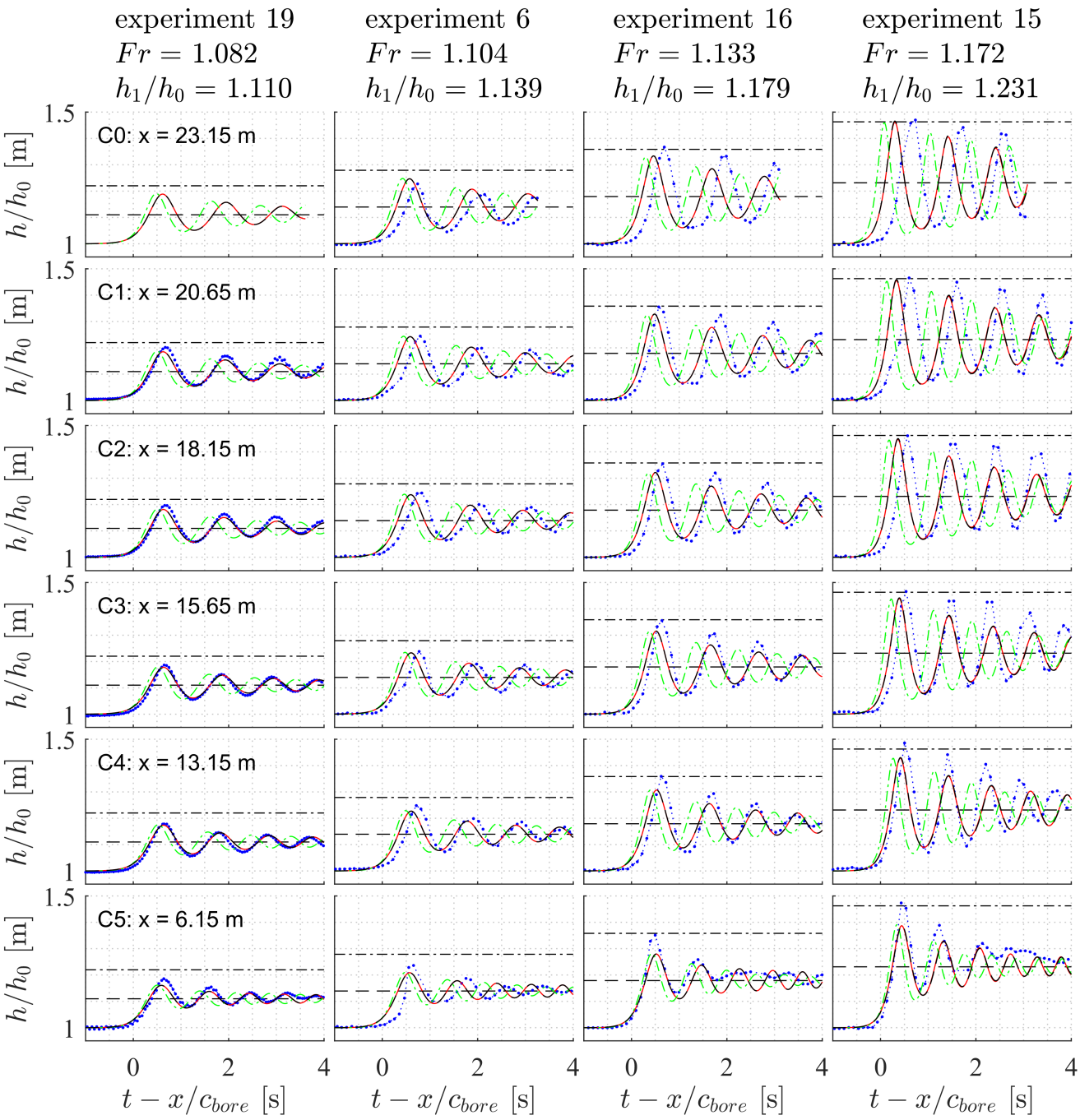

Figure C.1: Comparison of measurements by [Soares Frazao and Zech, 2002] and SWASH model results. Experiment No. 6, 15, 16 and 19 of [Soares Frazao and Zech, 2002] are shown at all available gauges (x = 6.15, 13.15, 15.65, 18.15, 20.65, 23.15 m). SWASH results are shown for (green dash-dot line) default settings, 1 layer mode, (black dashed line) default settings, 2 layers, (red) higher resolution: 5 pressure layers, 20 velocity layers. The dash-dotted line gives the theoretical maximum for the leading amplitude, and the dashed line shows the mean upstream water level.

Figure C.1 shows the measurements and the results of the numerical simulations. Similarity between measurements and model results (at higher resolution) seems quite good, even though the amplitudes of the undulations are initially underestimated (gauge C_5). This seems to improve further away from the gate. For experiment No. 16 and 19, at the final gauge (C_0), the crest level of the first undulation seems to be slightly overestimated. This is inconsistent with the results for the other two experiments, for which the crest at the final gauge is comparable in height (No. 15) or slightly underestimated (No. 6). We speculate that this is due to slight inaccuracies in the experimental procedure, since for SWASH the leading amplitude grows towards its maximum theoretical value (dash-dot line), while in the experiments the amplitude sometimes surpasses

it.

The propagation speed is overestimated for the experiments with larger Froude numbers (experiment No. 6, 15, 16); the undular bores seem to propagate faster for SWASH compared to observations. This does not improve when the number of layers is increased with respect to the two-layer simulation (two layers seems to be the absolute minimum in order to accurately model undular bore development). What we do see, as expected, is that the celerity of the dispersive trailing undulations is improved as the number of layers is increased.

Ignoring the slight inconsistencies, this case study does show that SWASH is capable of simulating undular bores with a few number of layers. Proper calibration of SWASH for undular bores requires further investigation. For example, is detailed modeling of turbulence required, or is it sufficient to introduce dissipation by means of bottom friction using a simple Manning's formulation. Perhaps Favre's results can be used for calibration, because in [Favre, 1935] detailed characteristics of the undulations are given for more developed undular bores (i.e. undular bores that have traveled a larger distance).

It has to be noted, that as the Froude number becomes larger, modeling of undular bores becomes more challenging. In addition to the fact that the wavelength of the undulations becomes smaller for stronger bores, the undulations also start breaking.

D

Appendix D: Propagation velocity of an undular bore

Throughout this thesis, the propagation velocity is used for, among other things:

1. the calculation of the to-be-generated wave profiles (Appx. E),
2. the decomposition of the free surface into incident and reflected waves (Ch. 4),
3. the analysis of the experimental results (Ch. 6).

This appendix provides some background on the matter. Section D.1 starts with two definitions of the velocity of propagation. The subsequent section (D.2) gives a criterion for instability of the flow, based on the propagation velocity. Section D.3 shows how, under certain conditions (which involves the propagation velocity), the continuity equation yields a local relation between discharge and surface elevation. The final section concerns the propagation velocity of an undular bore; an expression is given which includes the effect of non-hydrostatic pressure.

D.1. Definition of velocity of propagation

Since the definition of propagation speed can be ambiguous, this appendix starts with two definitions, based on the classical work by [Boussinesq, 1872] and the thorough review of [Keulegan and Patterson, 1940b]. We start with the definition most commonly used. Let ζ again be the surface elevation. The total derivative of ζ for an observer moving with velocity $\frac{dx}{dt} = V$ is given by:

$$\frac{d\zeta}{dt} = \frac{\partial\zeta}{\partial t} + V\frac{\partial\zeta}{\partial x} \tag{D.1}$$

If $\frac{d\zeta}{dt} = 0$, an observer moving with velocity $\frac{dx}{dt} = c$ sees no change in h locally,

$$\frac{\partial\zeta}{\partial t} + c\frac{\partial\zeta}{\partial x} = 0 \tag{D.2}$$

Eq. D.2 can be used to define the velocity of propagation, c, which does not necessarily has to be constant. "When the traveling wave is undergoing a change of form at a given instant, c is a function of h" [Keulegan and Patterson, 1940b]. This is consistent with [Svendsen and Staub, 1981], who, for a wave changing form, define c as the "horizontal velocity of a point of the surface characterized by its elevation", i.e. $c = c(\zeta)$. For a wave of constant form, all points of constant height move at the same speed, hence c = constant. Most often the definition for the velocity of propagation is used together with the assumption of waves of constant form.

A second definition is due to Boussinesq, and considers a wave moving in quiescent water. [Boussinesq, 1872] introduced the concept of a "wave volume-element"; a parcel of fluid, bound between a moving abscissa x and infinity:

$$V = \int_{x=\omega t}^{\infty} \zeta\, dx \tag{D.3}$$

The boundary moves with a velocity ω such that the volume stays constant in time:

$$\frac{\partial}{\partial t}\int_{x=\omega t}^{\infty} \zeta \, dx = 0 \tag{D.4}$$

This allowed Boussinesq to give a second definition for the velocity of propagation. Application of Leibniz integral rule yields:

$$\int_{x=\omega t}^{\infty} \frac{\partial \zeta}{\partial t} dx - \omega\zeta = 0 \tag{D.5}$$

Subsequent differentiation with respect to x finally gives:

$$\frac{\partial \zeta}{\partial t} + \frac{\partial \omega\zeta}{\partial x} = 0 \tag{D.6}$$

This defines velocity of propagation of a wave volume-element, ω, which does not necessarily has to be constant. It is essentially the continuity equation in terms of ω. Using the product rule of differentiation, this can be rewritten as:

$$\frac{\partial \zeta}{\partial t} + \omega\frac{\partial \zeta}{\partial x} + \zeta\frac{\partial \omega}{\partial x} = 0 \tag{D.7}$$

Comparison of Eq. D.2 with Eq. D.7 reveals that both definitions are identical if a wave moves without change of form ($\frac{\partial \omega}{\partial x} = 0$). Thus the propagation velocity of a wave volume-element and a "wave height-element" (defined by Eq. D.2) are related by:

$$c = \omega + \zeta\frac{\partial \omega}{\partial x}\Big/\frac{\partial \zeta}{\partial x} \tag{D.8}$$

D.2. Criterion for instability

The flow is said to be unstable if conditions are such that a disturbance of the free surface increases in magnitude as it propagates [Keulegan and Patterson, 1940a]. A simple criterion for instability is based on ω. The total derivative the height of ζ while moving with the velocity of propagation of a wave volume-element is given by:

$$\frac{d\zeta}{dt} = \frac{\partial \zeta}{\partial t} + \omega\frac{\partial \zeta}{\partial x} \tag{D.9}$$

Consider a wave-profile which is everywhere above the undisturbed surface due to a smooth increase and subsequent decrease in discharge. The flow is said to be unstable if ζ increases while moving with ω, i.e.:

$$\frac{d\zeta}{dt} > 0 \tag{D.10}$$

Combining Eq. D.7, D.9 and D.10, we get:

$$\frac{d\zeta}{dt} = -\zeta\frac{\partial \omega}{\partial x} > 0 \tag{D.11}$$

Hence for a positive disturbance ($\zeta > 0$), the flow remains unstable as long as ω decreases in positive direction ($\partial_x \omega < 0$).

In general it can be said that the flow becomes stable as the propagation velocity, ω, becomes constant (that is when ω and c are equal). It is known that the only stable wave form is a cnoidal wave, of which the solitary wave is a special case. Moreover, it is also known that near the front of an undular bore, a train of solitary waves will be formed.

D.3. Relation between discharge and free surface elevation for a progressive wave

Under certain conditions, the locally measured discharge can be written as the product of the free surface elevation and the velocity of propagation at that location. This follows from a combination of the continuity equation (Eq. A.2) with a definition for the propagation velocity (either Eq. D.2 or D.6).

We first follow the derivation presented in [Boussinesq, 1872] and [Keulegan and Patterson, 1940b]. Using Eq. D.6, $-\partial_x(\omega\zeta)$ can be substituted for $\partial_t\zeta$ in the continuity equation, which results in:

$$\frac{\partial Q}{\partial x} = \frac{\partial \omega\zeta}{\partial x} \tag{D.12}$$

If the flow is assumed to be undisturbed at infinity, i.e. for a disturbance moving in quiescent waters, integration yields:

$$Q = \omega\zeta \tag{D.13}$$

This is valid for a deforming disturbance, provided a suitable expression for ω.

Using the more commonly used definition of the propagation velocity, Eq. D.2, together with the continuity, we obtain:

$$\frac{\partial Q}{\partial x} = c\frac{\partial \zeta}{\partial x} \tag{D.14}$$

which can be written as:

$$\frac{\partial Q}{\partial x} = \frac{\partial c\zeta}{\partial x} - \zeta\frac{\partial c}{\partial x} \tag{D.15}$$

which is in similar form as Eq. D.12 if $c = \omega$ (a wave of constant form, see Eq. D.8). If we indeed assume c to be constant, integration gives:

$$Q = c\zeta \tag{D.16}$$

Eq. D.16 is not only valid for a steady bore entering quiescent water, but also for a periodic wave of constant form (provided the net volume flux to be zero). If the net volume flux were to be known, it could however be included:

$$Q = c\left(\zeta - \overline{\zeta}\right) + \overline{Q} \tag{D.17}$$

The derivation of Eq. D.17 is based on conservation of mass for a control volume between a fixed and a moving boundary (moving with a constant wave celerity as seen from a fixed frame of reference), see van Dongeren and Svendsen [1997]. $\overline{Q}$ is the net (or time-mean) volume flux, which is composed of a wave-related nonlinear volume flux $\overline{Q_w}$ contribution and the uniform current $U_c\left(d+\overline{\zeta}\right)$:

$$Q = \int_{-d}^{\zeta} u\,dz = \int_{-d}^{\zeta} (u_w + U_c)\,dz = Q_w + U_c\,(d+\zeta) \quad \text{and} \quad \overline{Q} = \overline{Q_w} + U_c\left(d+\overline{\zeta}\right) \tag{D.18}$$

If $\overline{\zeta}$ is taken with respect to mean water level, $\overline{\zeta} = 0$.Equation D.17 (and Eq. D.16 for that matter) is valid for any progressive wave of constant form (i.e. for waves in both deep and shallow water, even for highly non-linear waves) van Dongeren and Svendsen [1997]. [Svendsen and Staub, 1981] note that even for a wave changing shape, the assumption of constant form still yields a good approximation.

[Svendsen and Staub, 1981] also mention that a more general expression for Q, which does not require c to be constant, is given by:

$$Q = \int_0^{\zeta} c(\zeta)\,d\zeta \tag{D.19}$$

Eq. D.19 is the result of integration of Eq. D.14 with subsequent application of u-substitution. Quoting [Svendsen and Staub, 1981], "The change in form of the wave profile is represented by the different values of c for different surface elevations". A quick check confirms this. Assume a shallow water wave. The wave speed of a non-linear shallow water wave traveling in the positive x-direction, into still water water of constant depth is given by:

$$c = 3c_{SW} - 2c_0 \quad \text{where} \quad c_{SW} = \sqrt{g\,(d+\zeta)} \quad \text{and} \quad c_0 = \sqrt{gd} \tag{D.20}$$

see Appx. B or [Stoker, 1957] Ch. 10. c is a function of ζ. Substitution in D.19 and subsequent integration gives:

$$Q = \int_0^{\zeta} 3c_{SW} - 2c_0\,d\zeta = 2\,(c_{SW} - c_0)\,(d+\zeta) \tag{D.21}$$

which is in agreement with the method of characteristics. However, beyond the breakpoint the method of characteristics is formally invalid [Madsen et al., 2008], hence the non-linear shallow water wave speed cannot be used for either turbulent or undular bores (at least near the front). For turbulent bores, a solution is traditionally found in the shock wave speed (as detailed in Ch. B). The next section will treat the propagation velocity of undular bores. Before we move there, this section is concluded with a few remarks.

One could write Eq. D.20 as a Taylor series, and truncate the expression at the desired order, for example:

$$c = c_0\left(1 + \frac{3}{2}\epsilon - \frac{3}{8}\epsilon^2 + \frac{3}{16}\epsilon^3\right) + \mathcal{O}\left(\epsilon^4\right) \quad \text{where} \quad \epsilon = \frac{\zeta}{d} \tag{D.22}$$

More interestingly, Eq. D.21 contains an expression for ω:

$$\omega = 2\left(c_{sw} - c_0\right)\frac{d+\eta}{\zeta} \tag{D.23}$$

which can also be written as a series expansion at $z = 0$:

$$\omega = c_0\left(1 + \frac{3}{4}\epsilon - \frac{1}{8}\epsilon^2 + \frac{3}{64}\epsilon^3\right) + \mathcal{O}\left(\epsilon^4\right) \tag{D.24}$$

The first two terms of Eq. D.24 correspond to the expression of [Boussinesq, 1872], also given by [Keulegan and Patterson, 1940b], for the velocity of propagation for a wave of finite height and negligible curvature:

$$\omega = c_0\left(1 + \frac{3}{4}\epsilon\right) + \mathcal{O}\left(\epsilon^2\right) \tag{D.25}$$

Similarly, Eq. D.22 reduces to Airy's expression [Keulegan and Patterson, 1940b]:

$$c = c_0\left(1 + \frac{3}{2}\epsilon\right) + \mathcal{O}\left(\epsilon^2\right) \tag{D.26}$$

if higher order terms are neglected.

D.4. Propagation speed of an undular bore including the effect of non-hydrostatic pressure

It is clear that vertical acceleration cannot be neglected when undular bores are considered. However, since turbulent bores are often of interest, calculation of the bore or breaking wave speed is almost always based on the assumption of a hydrostatic equilibrium. For undular bores this only valid sufficiently far away from the bore front. The aim of this section is to obtain an expression for the propagation velocity, to be applied at the leading edge of an undular bore (i.e. for the first undulation).

[Svendsen et al., 1978] actually discussed the effect of non-hydrostatic pressure and non-uniformity of velocities in the wave motion on the bore speed. However, for their dataset, simply assuming the hydrostatic pressure distribution and a uniform velocity profile gave better results. Proper understanding of these expressions for the propagation speed based on the Boussinesq equations requires one to be familiar with Boussinesq's theory, which is far from trivial. They involves higher order (horizontal) derivatives, which are the result of elimination of the vertical coordinate from the equations. Because this, physical interpretation of undular bore formation based on Eq. D.34 may be hard to grasp. For a coastal engineer familiar with the non-hydrostatic model framework (which is slightly simpler), a non-hydrostatic counterpart to Boussinesq's velocity of propagation might be appreciated.

First it is assumed that the undular bore front moves at a constant speed; an expression for c is given. Then, an expression is given in line with Boussinesq velocity of propagation, ω, which allows for deformation of the wave.

D.4.1. Bore speed c_b

The mass and momentum conservation equations across a control volume are given by:

$$c_b\left(h_1 - h_0\right) = U_1 h_1 - U_0 h_0 \tag{D.27}$$

$$c_b\rho\left(U_1 h_1 - U_0 h_0\right) = F_{p,1} - F_{p,0} + \rho\left(U_1^2 h_1 - U_0^2 h_0\right) \tag{D.28}$$

The hydrostatic pressure assumption is not yet introduced, hence these equations are more general than the shock equations introduced in Appx. B. $F_{p,0}$ and $F_{p,1}$ are the total external pressure-induced forces acting on the left and right boundary of the control volume:

$$F_{p,0} = \int_{-d}^{\zeta} p_0\,\mathrm{d}z \quad \text{and} \quad F_{p,1} = \int_{-d}^{\zeta} p_1\,\mathrm{d}z \tag{D.29}$$

Assuming the bore to be of constant form, the bore speed can be obtained from these equations:

$$c_b = U_0 + \sqrt{\frac{\left(F_{p,1} - F_{p,0}\right)}{\rho\left(h_1 - h_0\right)}\frac{h_1}{h_0}} \tag{D.30}$$

An expression for F_p, acting on either boundary, is obtained by integrating pressure over depth:

$$F_p = \int_{-d}^{\zeta} \left(\rho g\left(\zeta - z\right) + q\right) \mathrm{d}z = \frac{1}{2}\rho g h^2 + \frac{1}{2} q_b h \tag{D.31}$$

It is assumed that non-hydrostatic pressure varies linearly over depth, from $q = 0$ at the surface, to q_b at the bottom. q_b can for example be obtained from pressure measurements at the bottom (by subtraction of hydrostatic pressure), approximated numerically, or requested as an output from SWASH. Substituting Eq. D.31 in Eq. D.30 yields:

$$c_b = U_0 + \sqrt{\frac{1}{2}\left(g\left(h_1 + h_0\right) + \frac{\left(q_{b,1} h_1 - q_{b,0} h_0\right)}{\rho\left(h_1 - h_0\right)}\right)\frac{h_1}{h_0}} \tag{D.32}$$

As can be seen, the expression reduces to the turbulent bore speed if non-hydrostatic pressure is set to zero. Just as the non-hydrostatic model equations can be seen as an extension to the NSW equations, Eq. D.32 can be seen as an extension of the classical shallow water bore speed (Eq. B.7), taking into account the effect of non-hydrostatic pressure. For a bore propagating propagating into quiescent water, Eq. D.32 can be written as (dropping subscript 1, and defining $d = h_0$ and $h_1 - d = \zeta$):

$$c_b = \sqrt{\frac{1}{2}\left(g\left(2d + \zeta\right) + \frac{q_b}{\rho}\frac{d+\zeta}{\zeta}\right)\frac{d+\zeta}{d}} = \sqrt{gd\left(1 + \frac{3}{2}\frac{\zeta}{d} + \frac{1}{2}\frac{\zeta^2}{d^2}\right) + \frac{q_b}{\rho}\left(1 + \frac{1}{2}\frac{d}{\zeta} + \frac{1}{2}\frac{\zeta}{d}\right)} \tag{D.33}$$

which is the equation for the bore speed, but including the effect non-hydrostatic pressure.

D.4.2. Propagation velocity ω of a deforming wave

Now the assumption of constant form is relaxed, but it is assumed from the onset that at $x \to \infty$ the flow is undisturbed.

The reduced Boussinesq equation and Boussinesq's velocity of propagation

There are expressions available for the propagation speed which take into account the effect of vertical acceleration on the flow, often based on Boussinesq-type of equations. For example, from what is known as "the Boussinesq equation", [Boussinesq, 1872] obtained:

$$\omega = c_0\left(1 + \frac{3}{4}\frac{\zeta}{d} + \frac{d^2}{6\zeta}\frac{\partial^2\zeta}{\partial x^2}\right) \quad \text{where} \quad c_0 = \sqrt{gd} \tag{D.34}$$

which is valid a wave with appreciable curvature moving into quiescent waters. The second term and third term are due to nonlinearity and dispersion, respectively. [Keulegan and Patterson, 1940b] note that if the dispersive term is neglected, Eq. D.34 reduces to Airy's expression, Eq. D.25. Eq. D.34 will be discussed briefly below (see [Keulegan and Patterson, 1940b] and [Broer, 1964] for a complete treatment). The Boussinesq equation is given by:

$$\frac{\partial^2\zeta}{\partial t^2} = gd\frac{\partial^2\zeta}{\partial x^2} + \frac{3}{2}g\frac{\partial^2\zeta^2}{\partial x^2} + \frac{1}{3}gd^3\frac{\partial^4\zeta}{\partial x^4} \tag{D.35}$$

Eq. D.35 is valid for either left or right traveling waves, but is not more generally applicable in the case where the wavefield is composed of waves coming from both directions. For a wave traveling to the right, [Broer, 1964] show that Eq. D.35 can be reduced and written in a simpler form, which, as they mention, is implicit in the work of [Keulegan and Patterson, 1940b]:

$$\frac{\partial\zeta}{\partial t} + c_0\frac{\partial\zeta}{\partial x} + \frac{3}{4}\frac{c_0}{d}\frac{\partial\zeta^2}{\partial x} + \frac{1}{6}c_0 d^2\frac{\partial^3\zeta}{\partial x^3} = 0 \tag{D.36}$$

[Broer, 1964] state that: "It is this equation which provides a simple example for the study of the interaction between nonlinearity and dispersion". Eq. D.36 can rewritten in the form of Eq. D.6:

$$\frac{\partial\zeta}{\partial t} + \frac{\partial\left(\omega\zeta\right)}{\partial x} = 0 \quad \text{where} \quad \omega = c_0\left(1 + \frac{3}{4}\frac{\zeta}{d} + \frac{d^2}{6\zeta}\frac{\partial^2\zeta}{\partial x^2}\right) \tag{D.37}$$

to highlight the velocity of propagation. These results were used in [Keulegan and Patterson, 1940b] to interpret the mechanism behind the formation of an undular bore from a positive surge.

Non-hydrostatic counterpart to Boussinesq's velocity of propagation

The same concepts will be applied to the non-hydrostatic model equations. It is stressed that for the present purpose, the resulting reduced equation does not necessarily have to be written in a single variable (for example the surface elevation), because it will not be used for modeling purposes.

The depth-integrated momentum equation — like Eq. B.2 written in conservative form, but now including a non-hydrostatic term — is given by:

$$\frac{\partial Q}{\partial t}+\frac{\partial}{\partial x}\left(\frac{Q^2}{h}+\frac{1}{2}gh^2+M_q\right)-gh\frac{\partial d}{\partial x}-\frac{q_b}{\rho}\frac{\partial d}{\partial x}=0 \tag{D.38}$$

Here M_q represents the momentum flux (per unit density) due to non-hydrostatic pressure in absence of a bottom slope. Horizontal velocity has been assumed to be uniform over depth. Pressure is assumed to vary linearly over depth, hence M_q is given by

$$M_q=\frac{1}{2}\frac{q_b}{\rho}h \tag{D.39}$$

as was already shown in the previous section D.4.1. For the present purpose, the momentum equation is slightly rewritten as:

$$\frac{\partial Q}{\partial t}+\frac{\partial}{\partial x}\left(\frac{Q^2}{h}+\frac{1}{2}g\zeta^2+M_q\right)+gd\frac{\partial \zeta}{\partial x}-\frac{q_b}{\rho}\frac{\partial d}{\partial x}=0 \tag{D.40}$$

The bottom is assumed to be horizontal (just like a reef flat). As a result, the last term on the LHS drops out:

$$\frac{\partial Q}{\partial t}=-\frac{\partial}{\partial x}\left(\frac{Q^2}{h}+g\zeta^2+M_q\right)-gd\frac{\partial \zeta}{\partial x} \tag{D.41}$$

In order to integrate this equation, the time derivative has to be replaced by spatial derivatives.

Intermezzo D.1: approximation for Q_t

Following [Keulegan and Patterson, 1940b], it is proposed to write ω as a sum of the linear shallow water speed and a small quantity:

$$\omega=c_0+\Delta\omega \tag{D.42}$$

We consider unidirectional wave propagation, specifically, waves traveling in the positive direction. Making use of Eq. D.13, this yields for $\partial_t Q$:

$$\frac{\partial Q}{\partial t}=\frac{\partial(\omega\zeta)}{\partial t}=c_0\frac{\partial \zeta}{\partial t}+\frac{\partial(\Delta\omega\zeta)}{\partial t} \tag{D.43}$$

Because $\Delta\omega$ is assumed to be a small quantity, $\partial_t(\Delta\omega\zeta)$ can be replaced by $-c_0\partial_x(\Delta\omega\zeta)$. Furthermore, making use of Eq. D.6, the first time derivative on the RHS can also be replaced by a spatial derivative:

$$\frac{\partial(\omega\zeta)}{\partial t}\approx-c_0\frac{\partial(\omega\zeta)}{\partial x}-c_0\frac{\partial(\Delta\omega\zeta)}{\partial x} \tag{D.44}$$

Substitution of $\omega=c_0+\Delta\omega$ in the first term on the RHS results in:

$$\frac{\partial(\omega\zeta)}{\partial t}\approx-c_0^2\frac{\partial \zeta}{\partial x}-2c_0\frac{\partial(\Delta\omega\zeta)}{\partial x} \tag{D.45}$$

Equating Eq. D.45 to Eq. D.41 gives:

$$c_0^2\frac{\partial \zeta}{\partial x}+2c_0\frac{\partial(\Delta\omega\zeta)}{\partial x}=\frac{\partial}{\partial x}\left(\frac{Q^2}{h}+\frac{1}{2}g\zeta^2+M_q\right)+gd\frac{\partial \zeta}{\partial x} \tag{D.46}$$

All temporal derivatives are now replaced by spatial derivatives. This makes integration possible. Note that the first term on the LHS and the last term on the RHS cancel. Carrying out the integration, and after some rewriting, the velocity of propagation of a wave volume element can be written as:

$$\omega=c_0+\Delta\omega^+=c_0+\frac{1}{2c_0\zeta}\left(\frac{Q^2}{h}+\frac{1}{2}g\zeta^2+M_q\right) \tag{D.47}$$

The main difference with Eq. D.33 is that no constant speed is assumed. Substituting Eq. D.47 in Eq. D.13, the discharge can be approximated as:

$$Q = \omega\zeta = c_0\zeta + \frac{1}{2c_0}\left(\frac{Q^2}{h} + \frac{1}{2}g\zeta^2 + M_q\right) \tag{D.48}$$

under the condition of unidirectional wave propagation. The non-hydrostatic counterpart to the reduced Boussinesq equation (Eq. D.37) is thus given by:

$$\frac{\partial\zeta}{\partial t} + \frac{\partial Q}{\partial x} = 0 \quad \text{where} \quad Q = \omega\zeta = c_0\zeta + \frac{1}{2c_0}\left(\frac{Q^2}{h} + \frac{1}{2}g\zeta^2 + M_q\right) \tag{D.49}$$

If in Eq. D.47, Q^2/h is replaced by $Q^2/d \approx g\zeta^2$, an expression is obtained which similar to the expression for ω obtained by Boussinesq (Eq. D.34):

$$\omega = c_0\left(1 + \frac{3}{4}\frac{\zeta}{d} + \frac{q_b}{4\rho g}\left(\frac{1}{d} + \frac{1}{\zeta}\right)\right) \tag{D.50}$$

but written in terms of ζ and q_b instead of ζ and its second order derivative ζ_{xx}. The corresponding discharge, which can be obtained without flow measurements, is given by:

$$Q = c_0\left(\zeta + \frac{3}{4}\frac{\zeta^2}{d} + \frac{q_b}{4\rho g}\left(1 + \frac{\zeta}{d}\right)\right) \tag{D.51}$$

D.4.3. Non-hydrostatic pressure

In the present experimental investigation, no pressure sensors were installed. It is however, possible to approximate q_b from free surface measurements in time. For a horizontal bottom, using the equations presented in section A.2, q_b can be written as:

$$q_b = \frac{1}{2}\rho h\frac{\partial w_\zeta}{\partial t} = -\frac{1}{2}\rho h\frac{\partial}{\partial t}\left(h\frac{\partial u}{\partial x}\right) \tag{D.52}$$

Making use of the (global) continuity equation (Eq. A.2) and the definition of velocity of propagation (Eq. D.2), one can write for a bore entering quiescent waters:

$$\frac{\partial w_\zeta}{\partial t} = \frac{d}{h}\frac{\partial^2\zeta}{\partial t^2} - \frac{d}{h^2}\left(\frac{\partial\zeta}{\partial t}\right)^2 \tag{D.53}$$

hence

$$q_b = \frac{1}{2}\rho\left(d\frac{\partial^2\zeta}{\partial t^2} - \frac{d}{h}\left(\frac{\partial\zeta}{\partial t}\right)^2\right) \tag{D.54}$$

It has been verified that Eq. D.33 yields a good results for undular bores and dispersively breaking long waves, simulated by a depth-averaged non-hydrostatic model (as described in section A.2). Since Eq. D.54 is consistent with a single layer non-hydrostatic model, its validity is limited to slightly disperse waves; in other words, waves with small kd values.

Appendix E: Long wave generation

Unfortunately, second-order Stokes wave theory is not suitable for generation of long waves. For high (Stokes-)Ursell numbers ($N_{Ursell} = HL^2/d^3 > 10-20$), Stokes theory is not valid; the second-order correction results in the generation of a secondary crest in the wave trough. On the other hand, using linear wave theory for wave generation of non-linear waves does not result in a well-defined wave of permanent form; spurious waves are additionally generated.

Goring [1979][1] solved this non-linear long wave problem by matching the wave-paddle velocity and the horizontal particle velocities under the wave (according to a suitable wave theory of choice) *as the board moves*. Since the velocity-profile of a long wave is approximately uniform over depth, the wave paddle velocity $\frac{dX(t)}{dt}$ is equated to the depth-averaged horizontal velocity $U(X(t),t)$:

$$\frac{dX}{dt} = U(X,t) \tag{E.1}$$

Eq. E.1 requires specification of the depth-averaged velocity. The depth-averaged velocity is defined as the discharge (per unit width) divided by the total depth:

$$U = \frac{Q}{d+\zeta} \tag{E.2}$$

Q is provided by Eq. D.16. It is repeated that Eq. D.16 is valid for any progressive wave of constant form (i.e. for waves in both deep and shallow water, even for highly non-linear waves) van Dongeren and Svendsen [1997]. Substitution yields:

$$U = \frac{c\zeta}{d+\zeta} \tag{E.3}$$

ζ and c can be obtained from a suitable wave theory. In the present study they are provided by cnoidal theory (see for example [Mei, 1989]). Notice that we do not include a net volume flux, i.e. $\overline{Q} = 0$, which is suitable for a flume setting[2]. The next section describes how to integrate Eq. E.1. in order to obtain the paddle displacement X.

E.0.1. Wave generation & Wave paddle displacement

The depth-averaged velocity, Eq. E.3, is evaluated at the paddle position $X(t)$:

$$U(X,t) = \frac{c\zeta(X,t)}{d+\zeta(X,t)} \tag{E.4}$$

[1] Goring [1979] developed his non-linear wave-maker theory for tsunami wave propagation onto a shelve, and used both the solutions of cnoidal and solitary wave theory. In this study the method by Goring [1979] will be used (together with cnoidal theory) to investigate the propagation and transformation of long waves — both (long) swell waves, and long waves at the infra-gravity wave scale — onto a reef.

[2] In a closed region (such as a wave flume), the net mass flux is zero after sufficient spin-up time. In other words, once the motion is established in the flume, the wave-induced mass flux (between trough and crest) is compensated by a return current (below the trough level) [Svendsen, 2006].

Combination of Eq. E.1 and Eq. E.4 gives:

$$\frac{dX}{dt} = \frac{c\zeta(X,t)}{d+\zeta(X,t)} \tag{E.5}$$

The trajectory equation has to be time-integrated in a Lagrangian manner; i.e. following the paddle position. "Including the position of the plate, $X(t)$, in the velocity, $U(X,t)$, takes into account that during the generation process the wave is propagating away from the plate", [Goring and Raichlen, 1980]. As opposed to Goring [1979], differential equation E.5 is directly integrated numerically (using the classical Runge-Kutta method of order 4, as in Synolakis [1990]). In this thesis the differential equation is solved with a constant small time step ($\Delta t = 0.001$ s) for accurate computations, and subsequently interpolated to match the required frequency of the wave paddle ($\Delta t = 0.04$ s or $f = 25$ Hz).

Figure E.1 depicts resulting wave paddle displacement, $X(t)$. Note the deformed shape of $X(t)$ for a cnoidal wave, and even for the generation of a linear wave. See Goring [1979] for an interpretation of the paddle position.

Zhang and Schäffer [2007] have extended the method of Goring [1979] to deeper water, by making a correction for dispersion. Moreover, they use stream function theory for calculation of the horizontal velocity. However, since we are only interested in shallow water waves (i.e. $L/h > 20$), the dispersion correction should be negligible in our case, and thus the method by Goring [1979] in combination with a cnoidal theory wave solution should suffice.

To compute the the movement of the board, the paddle position has to be converted to rotation (in degrees). Conversion and compilation is done using a small excecutable Asc2BinPifg.exe (supplied by A.R. van Dongeren). The resulting .dat file has to be accompanied with an .ifg file, which provides additional generation information, such as: number of time-samples, active reflection compensation mode, frequency , and other facility/waveboard information (see figure E.2). An amplification factor of 1.00 (instead of the default 0.80 used for second-order theory) seems to result in correct wave heights.

To avoid extreme accelerations (due to a finite velocity at $t = 0$), and to start start the paddle smoothly (in order to avoid large disturbances), the paddle position signal is multiplied by a tangent hyperbolic with a timescale of one wavelength.

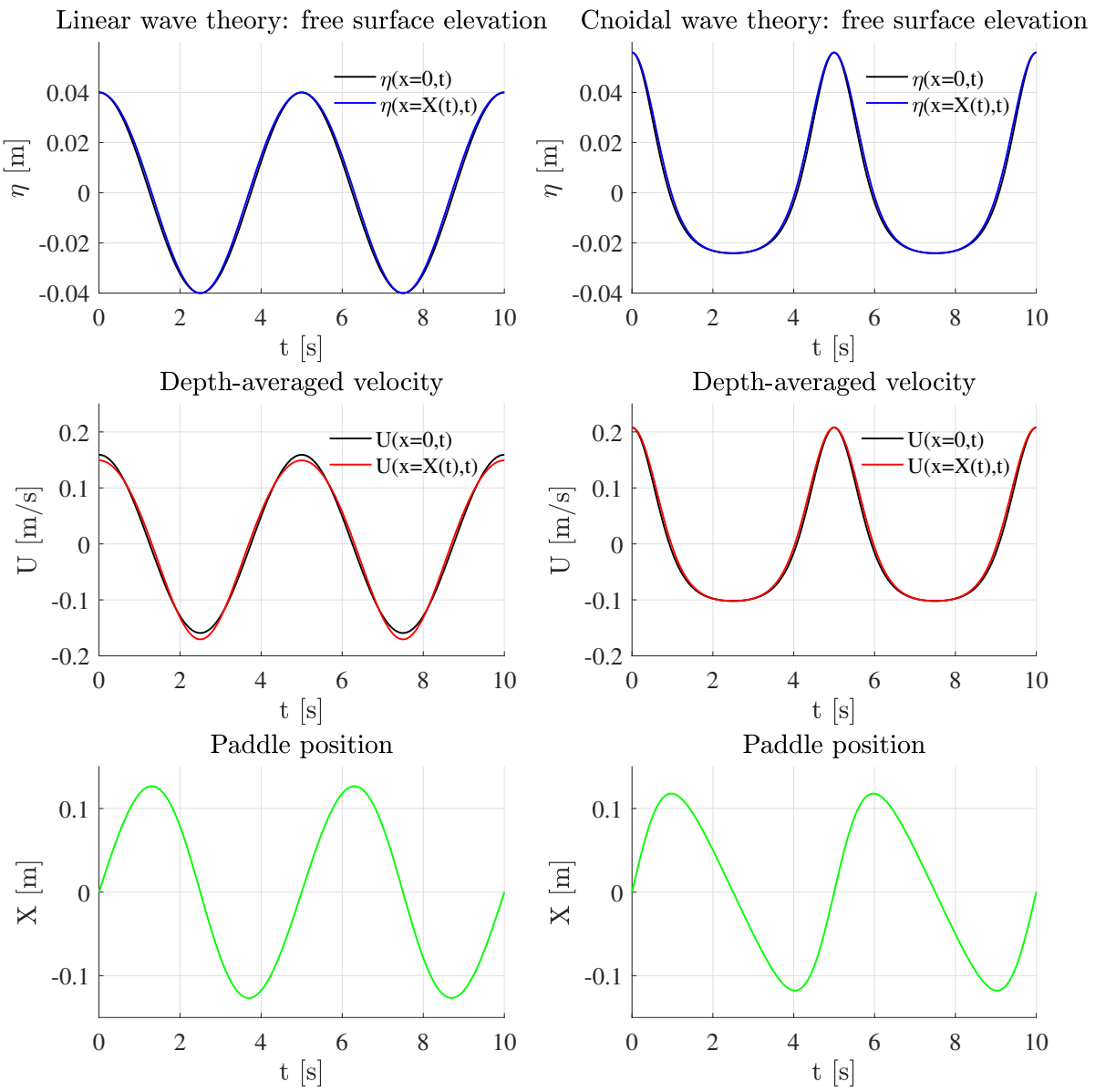

Figure E.1: Non-linear (long) wave generation. Calculation of wave paddle position $X(t)$ according to Goring [1979]. Left three plots: linear wave generation; right three plots: cnoidal wave generation. (top two figures) free surface elevation at x=0 and x = X(t), (middle) horizontal depth averaged velocity at at x=0 and x = X(t), (bottom) wave paddle position $X(t)$

```
FACILITY-FILE , E-WAVE. POS
SETPOINT-RESOLUTION, 0.00005
FREQUENCY,   25.000000
AMPLIFICATION, 1.00
TIME-SAMPLES, 0054001
CYCLIC , NO
WAVEBOARD, E-WAVE
    USE, YES
    SEGMENTS, 001
    IDLE , n
    ARC-MODE, SHORTWAVE-THEORY-2D
END: WAVEBOARD
```

l

Figure E.2: Example of an .ifg file, which provides generation information.

Appendix F: Stream function theory

The Stream function method was first developed by Dean [Dean, 1965]. While initially developed by Dean for analytical validity of other wave theories, Dean's stream function theory (also called a the Fourier approximation method [Fenton, 1990]) itself provided a better fit to measurements than other theories. See Dean [1965], Rienecker and Fenton [1981], Fenton [1988] or Svendsen [2006] for details. Below follows a short introduction. The stream function, defined by:

$$(u, w) = \left(\frac{\partial \psi}{\partial z}, -\frac{\partial \psi}{\partial x} \right) \tag{F.1}$$

satisfies both the Laplace equation (the field equation for an incompressible, irrotational fluid),

$$\frac{\partial^2 \psi}{\partial x^2} + \frac{\partial^2 \psi}{\partial z^2} = 0 \tag{F.2}$$

throughout the fluid and the kinematic bottom boundary condition (for a horizontal bottom). A Stream-function solution can be expressed as a truncated Fourier series:

$$\psi(x, z) = B_0 z + \sum_{i=1}^{N} \frac{B_i}{ik} \frac{\sinh(ik(d+z))}{\cosh(ikd)} \cos(ikx) \tag{F.3}$$

where N[1] is the order or the approximation. A solution can be found numerically, by satisfying the free surface conditions, both kinematic,

$$\psi_\zeta = -q \tag{F.4}$$

and dynamic boundary condition at the surface,

$$g\zeta + \frac{1}{2}\left(u^2 + w^2\right) = R \tag{F.5}$$

at N+1 points (evenly spaced over half a wavelength from crest to trough). The system is closed with three additional equations:

1. a definition for the wave height, $H = \zeta_0 - \zeta_N$;
2. an equation prescribing the mean water level to be zero, $\overline{\zeta} = \frac{1}{2L}\int_0^{L/2} \zeta \, dx = 0$, approximated numerically by a trapezoidal type of rule, $\zeta_0 + 2\sum_{i=1}^{N-1} \zeta + \zeta_N = 0$;
3. (a) an equation relating the absolute wave speed c, the time mean Eulerian velocity and the mean velocity at each level within the fluid, $U_{Euler} = c + B_0$ (where U_{Euler} has to be specified),
   (b) or a relation which requires specification of the Stokes drift velocity $U_{Stokes} = c + B_0 - q/d$.

[1] N = 64 is used in this thesis

The wave number is defined by $k = \frac{2\pi}{L}$ and the phase speed by $c = L/T$, hence $k = \frac{2\pi}{cT}$. Once the system is solved numerically for the unknowns (c, k, ζ, B, R), the velocity and discharge can be calculated. The velocity $u(t,x,z)$ is obtained by differentiating the stream function with respect to the vertical coordinate:

$$u = c + B_0 + \sum_{i=1}^{N} \frac{\cosh(ik(d+z))}{\cosh(ikh)} \cos(i(kx - \omega t)) \tag{F.6}$$

The velocities are calculated in a frame of reference moving with the wave; hence the absolute wave speed c is added to obtain the solution in a fixed reference frame. The discharge follows from the kinematic boundary condition at the surface:

$$Q = (c + B_0)(d + \zeta) + \sum_{i=1}^{N} \frac{B_i}{ik} \frac{\sinh(ik(d+\zeta))}{\cosh(ikd)} \cos(i(kx - \omega t)) \tag{F.7}$$

F.1. Velocity response function

For the decomposition method in section 4.5, the definitions for Q and u are compared to estimate the discharge Q from the measured horizontal velocity u and a velocity response function, K. For each harmonic component, $i = 1 - N$, the velocity response function is given by:

$$K_i = Q_i / u_i = \frac{\sinh(k_i(d+\zeta))}{k_i \cosh(k_i(d+z))} \tag{F.8}$$

where $k_i = ik$. k is computed numerically (using the procedure above) for the primary incident component; i.e. for given T, d and H. Note that K_0 is simply the total depth, $d + \zeta$.

F.2. SWASH stream function boundary condition

Wave generation in SWASH relies heavily on linear wave theory, which is sufficient for most coastal applications. By default, regular waves can be specified by means of Fourier series or time series. Because the conditions for the regular long wave experiments fall outside of the region of validity of linear wave theory, we have to resort to a non-linear wave theory. Since the wave number is calculated according to the linear dispersion relation, non-linear permanent waves cannot be correctly specified by means of the Fourier series option. Instead, for each layer, a time-series of layer-averaged velocity is imposed at the wavemaker boundary.

In the physical model tests, cnoidal theory is used. Therefore, this would also be the most obvious choice for long wave generation in SWASH. However, stream function theory (see [Fenton, 1988]) has a larger region of validity; it can be applied to high waves in both deep water (Stokes' region) and water of finite depth (where cnoidal wave theory is appropriate). Stream function theory seems to be a more versatile choice.

As described above, a mean mass-flux velocity (Stokes' vertically integrated mean transport velocity) or, alternatively, a mean current velocity (Eulerian time-mean velocity) has to be be specified. A zero net mass flux ($U_{Stokes} = 0$) is appropriate for flume simulations. Using stream function theory to obtain the unknowns (wave number k, wave speed c, coefficients B_i), the layer-averaged horizontal velocity is readily calculated by evaluating the following expression:

$$u_k(t) = c + B_0 + \frac{1}{z_{k+\frac{1}{2}} - z_{k-\frac{1}{2}}} \sum_{i=1}^{N} \frac{B_i}{ik} \frac{\sinh\left(ik\left(d + z_{k+\frac{1}{2}}\right)\right) - \sinh\left(ik\left(d + z_{k-\frac{1}{2}}\right)\right)}{\cosh(ikd)} \cos(-i\omega t) \tag{F.9}$$

Here $z_{k-\frac{1}{2}}$ and $z_{k+\frac{1}{2}}$ are the layer interfaces associated with layer k. Consistent with SWASH, the layers are equidistantly distributed over the total depth $d + \zeta$. For depth-averaged simulations, $z_{k-\frac{1}{2}} = -d$ and $z_{k+\frac{1}{2}} = \zeta$. As a check, the solution (Eq. F.9) is compared with the depth averaged velocity according to Eq. E.3.

G

Appendix G: Integral Flux Equations

The wave-averaged mass, momentum and energy fluxes, see e.g. [Sobey and Dingemans, 1992], [Fenton, 1990], are given by:

$$\overline{\int_{-d}^{\zeta} \rho u dz} = \underbrace{\overline{\int_{-d}^{0} \rho U dz}}_{\rho U d} + \underbrace{\overline{\int_{-d}^{\zeta} \rho \tilde{u} dz}}_{\text{wave mass flux } I} \tag{G.1}$$

$$\overline{\int_{-d}^{\zeta} \left(p + \rho u^2\right) dz} = \underbrace{\overline{\int_{-d}^{0} \overline{p} dz}}_{\frac{1}{2}\rho g d^2} + \underbrace{\overline{\int_{-d}^{0} \rho U^2 dz}}_{\rho U^2 d} + \underbrace{\overline{\int_{-d}^{\zeta} \left(\tilde{p} + \rho \tilde{u}^2\right) dz}}_{\text{radiation stress } S} + 2U \underbrace{\overline{\int_{-d}^{\zeta} \rho \tilde{u}^2 dz}}_{I} \tag{G.2}$$

$$\begin{aligned}
&\overline{\int_{-d}^{\zeta} u\left(p + \frac{1}{2}\rho u^2 + \frac{1}{2}\rho w^2 + \rho g(d+z)\right) dz} = \\
&\qquad \overline{\int_{-d}^{0} U\left(\frac{1}{2}\rho U^2 + \rho g d\right) dz} + \overline{\int_{-d}^{\zeta} U\left(\overline{p} + \tilde{p} \frac{3}{2}\rho \tilde{u}^2 + \frac{1}{2}\rho \tilde{w}^2 \rho g z\right) dz} \\
&+ \overline{\int_{-d}^{\zeta} \tilde{u}\left(\frac{3}{2}\rho \tilde{U}^2 + \rho g d\right) dz} + \overline{\int_{-d}^{\zeta} \tilde{u}\left(\overline{p} + \tilde{p} + \frac{1}{2}\rho \tilde{u}^2 + \frac{1}{2}\rho \tilde{w}^2 + \rho g z\right) dz} \\
&\qquad = \rho g d^2 U + \frac{1}{2}\rho U^3 d + \left(g d + \frac{3}{2}U^2\right) I + U(T + V + S) + F
\end{aligned} \tag{G.3}$$

where T and V are the the wave-averaged kinetic and potential energy of the wave motion respectively. F is the mean energy flux by the wave motion. Furthermore, $u = U + \tilde{u}$, $w = \tilde{w}$, U is the mean flow, $\tilde{u}$ and $\tilde{w}$ are deviations from the mean flow, $\overline{p}$ is the hydrostatic pressure and $\tilde{p}$ the residual wave-related pressure (non-hydrostatic pressure). The overbar here means time-averaging over a single wave period.

Appendix H: Energy transport in undular bores

As described in Ch. 2, Ali and Kalisch [2010] confirmed the suspicion of [Lemoine, 1948] and [Benjamin and Lighthill, 1954], that during the formation of an undular bore, the dispersive wave-train appearing at the bore front indeed absorbs the energy which according to classical theory is otherwise liberated, by showing that the net influx of energy to the region is equal to the rate of change of energy in the region surrounding the bore front. Ali and Kalisch [2010] used a Boussinesq-type of model to confirm the notion that no energy is lost during the formation of an undular bore.

Here we would also like to investigate the dispersive wave-breaking of long waves, but this time using a non-hydrostatic model (SWASH). First, approximations for the depth-integrated energy and energy flux are given (section H.1). Then, in section H.2, we would like to revisit the energy budget of an undular bore during its development (essentially (partially) repeating the experiment of [Ali and Kalisch, 2010]).

H.1. Energy & energy flux

The energy density, composed of kinetic and potential energy density, is given by:

$$\frac{1}{2}\rho\left(u^2+w^2\right)+\rho g z \tag{H.1}$$

H.1.1. Depth-integrated energy and horizontal energy flux

In depth-averaged mode, SWASH can output the required quantities (d, ζ, U, w_z q_b), to approximate the depth-integrated energy E and the depth-integrated energy flux F. The depth-integrated energy (energy per unit horizontal surface area) is given by:

$$E=\int_{-d}^{\zeta}\left(\frac{1}{2}\rho\left(u^2+w^2\right)+\rho g z\right)dz=\int_{-d}^{\zeta}\frac{1}{2}\rho\left(u^2+w^2\right)dz+\frac{1}{2}\rho g\left(\zeta^2-d^2\right) \tag{H.2}$$

and here approximated numerically by:

$$E\approx\frac{1}{2}\left(d+\zeta\right)\rho\left(U^2+\frac{1}{3}\left(w_{-d}^2+w_{-d}w_\zeta+w_\zeta^2\right)\right)+\frac{1}{2}\rho g\left(\zeta^2-d^2\right) \tag{H.3}$$

w_ζ is the vertical velocity at the surface and w_{-d} at the bottom ($w_{-d}=-u\frac{\delta d}{\delta x}$ but $w_{-d}=0$ for a horizontal bottom). The wave-induced contribution is obtained by discarding the hydrostatic potential energy ($-\frac{1}{2}\rho g d^2$):

$$E_{wave}\approx\frac{1}{2}\left(d+\zeta\right)\rho\left(U^2+\frac{1}{3}\left(w_{-d}^2+w_{-d}w_\zeta+w_\zeta^2\right)\right)+\frac{1}{2}\rho g\zeta^2 \tag{H.4}$$

The depth-integrated horizontal energy flux at any given vertical section is given by:

$$\begin{aligned} F &= \int_{-d}^{\zeta} u\left(p+\frac{1}{2}\rho\left(u^2+w^2\right)+\rho g(d+z)\right)dz \\ &= \int_{-d}^{\zeta} u\left(\rho g\left(\zeta-z\right)+q+\frac{1}{2}\rho\left(u^2+w^2\right)+\rho g(d+z)\right)dz \end{aligned} \tag{H.5}$$

where $p=\rho g\left(\zeta-z\right)+q$ is total pressure, composed of a hydrostatic and non-hydrostatic contribution. Eq. H.5 is approximated numerically by:

$$F \approx Q\left(\rho g\left(d+\zeta\right)+\frac{1}{2}q_b+\frac{1}{2}\rho\left(U^2+\frac{1}{3}\left(w_{-d}^2+w_{-d}w_\zeta+w_\zeta^2\right)\right)\right) \quad \text{where} \quad Q\equiv U\left(d+\zeta\right) \tag{H.6}$$

q_b is the non-hydrostatic pressure at the bottom $z=-d$, and Q is the discharge. Lastly, discarding the term $Q\rho g d$ gives the wave-induced depth-integrated horizontal energy flux:

$$F_{wave} \approx Q\left(\rho g\zeta+\frac{1}{2}q_b+\frac{1}{2}\rho\left(U^2+\frac{1}{3}\left(w_{-d}^2+w_{-d}w_\zeta+w_\zeta^2\right)\right)\right) \tag{H.7}$$

H.1.2. Layer-integrated energy and horizontal energy flux

Because SWASH can also output the quantities per layer, it is possible to approximate the layer-integrated energy and energy flux. Similar to Eq. H.2, the layer-integrated horizontal energy density is given by:

$$E_k = \int_{z_{k-\frac{1}{2}}}^{z_{k+\frac{1}{2}}}\left(\frac{1}{2}\rho\left(u^2+w^2\right)+\rho g z\right)dz \tag{H.8}$$

Eq. H.8 is approximated numerically. w is assumed to vary linearly over a layer, and u is assumed to be constant in the layer. The layer-integrated kinetic energy is approximated by:

$$E_{kin,u,k} \approx \frac{1}{2}\rho\left(z_{k+\frac{1}{2}}-z_{k-\frac{1}{2}}\right)u_k^2 \quad \text{and} \quad E_{kin,w,k} \approx \frac{1}{6}\rho\left(z_{k+\frac{1}{2}}-z_{k-\frac{1}{2}}\right)\left(w_{k-\frac{1}{2}}^2+w_{k-\frac{1}{2}}w_{k+\frac{1}{2}}+w_{k+\frac{1}{2}}^2\right) \tag{H.9}$$

where u_k is the layer-averaged velocity, located at the center of the cell faces, and $w_{k\pm\frac{1}{2}}$ are the vertical velocities at the layer interfaces $k\pm\frac{1}{2}$. E_{wave} is obtained by summing up $E_{kin,u,k}$ and $E_{kin,w,k}$ over the layers and adding the wave-induced depth-integrated potential energy $\frac{1}{2}\rho g\zeta^2$:

$$E_{wave} \approx \sum_{k=1}^{K}\left(E_{kin,w,k}+E_{kin,u,k}\right)+\frac{1}{2}\rho g\zeta^2 \tag{H.10}$$

Similar to Eq. H.5, the layer-integrated horizontal energy flux at any given vertical section is given by:

$$F_k = \int_{z_{k-\frac{1}{2}}}^{z_{k+\frac{1}{2}}} u\left(\rho g\left(\zeta-z\right)+q+\frac{1}{2}\rho\left(u^2+w^2\right)+\rho g(d+z)\right)dz \tag{H.11}$$

The layer-integrated horizontal transport of kinetic energy,

$$F_{kin,k} = \int_{z_{k-\frac{1}{2}}}^{z_{k+\frac{1}{2}}} u\frac{1}{2}\rho\left(u^2+w^2\right)dz \tag{H.12}$$

is approximated by:

$$F_{kin,k} \approx Q_k\left(\frac{1}{2}\rho u_k^2+\frac{1}{6}\rho\left(w_{k-\frac{1}{2}}^2+w_{k-\frac{1}{2}}w_{k+\frac{1}{2}}+w_{k+\frac{1}{2}}^2\right)\right) \tag{H.13}$$

where $Q_k = u_k\left(z_{k+\frac{1}{2}}-z_{k-\frac{1}{2}}\right)$ is the discharge in layer k. The work done by the (non-hydrostatic part of the) pressure,

$$F_{nhp,k} = \int_{z_{k-\frac{1}{2}}}^{z_{k+\frac{1}{2}}} uqdz \tag{H.14}$$

is approximated by:

$$F_{nhp,k} \approx \frac{1}{2}Q_k\left(q_{k-\frac{1}{2}}+q_{k+\frac{1}{2}}\right) \tag{H.15}$$

$q_{k\pm\frac{1}{2}}$ are the non-hydrostatic pressures at the layer interfaces. The (wave-related) contribution to the total depth-integrated horizontal transport of energy due to hydrostatic pressure and potential energy combined, $F_{wave,hp+pot}$, is not calculated per layer (and then summed up), but directly calculated by integration over the total depth:

$$F_{wave,hp+pot} = \int_{-d}^{\zeta} u\left(\rho g\left(\zeta - z\right) + \rho g(d+z)\right) dz - Q\rho g d = Q\rho g\zeta \tag{H.16}$$

Finally, the wave-induced horizontal energy flux is given by:

$$F_{wave} \approx \sum_{k=1}^{K} \left(F_{kin,w,k} + F_{kin,u,k} + F_{nhp,k}\right) + F_{wave,hp+pot} \tag{H.17}$$

H.2. Energy budget during undular bore formation

In this section we analyze the energy budget during the transformation of a stepped bore into an undular bore.

H.2.1. Numerical setup

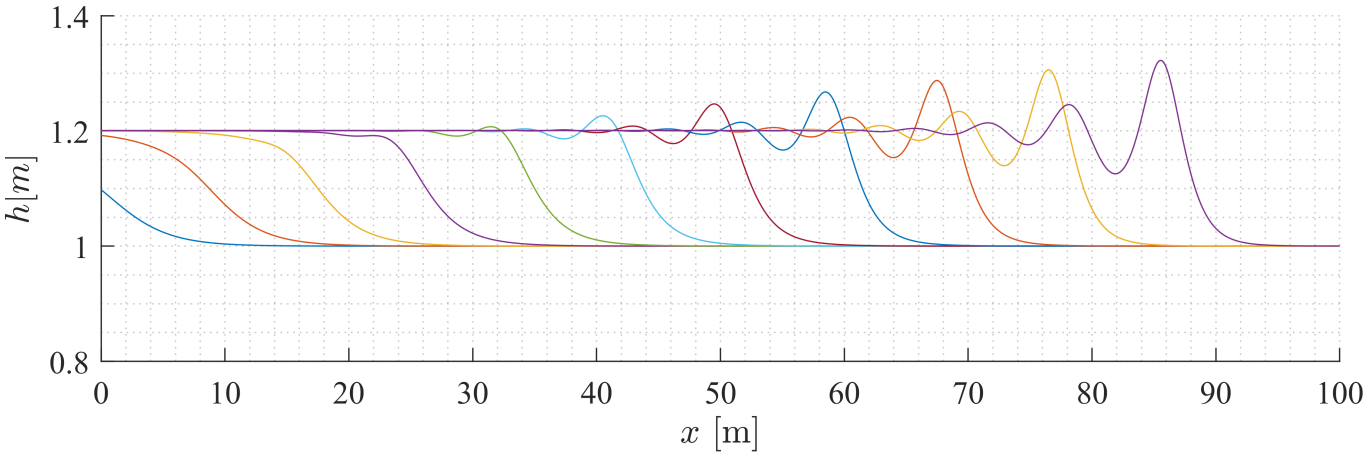

Figure H.1: Snapshots of the free surface elevation of the stepped bore, transforming into an undular bore. The free surface is shown at several moments in time, as it propagates across the domain. $t = 20 - 45$ s, with an interval Δt of 2.5 s.

To smoothly start the simulation, we impose a hyperbolic tangent boundary condition at the left boundary of the computational domain:

$$U(0,t) = U_0 + \frac{U_1 - U_0}{2}\left(1 + \tanh a\left(t - b\right)\right) \tag{H.18}$$

where $a = 2\pi/T$, $b = T$. T is the characteristic time scale of the front, and is taken sufficiently large ($T = 10$ s). The conjugate depths are $h_0 = 1$ m and $h_1 = 1.2$ m. U_1 is again calculated using Eq. B.9. We run SWASH in six-layer mode for good representation of dispersion, and $dx = 0.02$ m (at least 250 ppwl for the leading undulation). The duration of the simulation is $D = 45$ s.

H.2.2. Visualization of the flow and pressure field

Figure H.1 shows snapshots of the free surface elevation of the undular bore at several moments in time as it propagates across the domain. Fig. H.2 visualizes the flow in an undular bore, and shows the magnitude of non-hydrostatic pressure q.

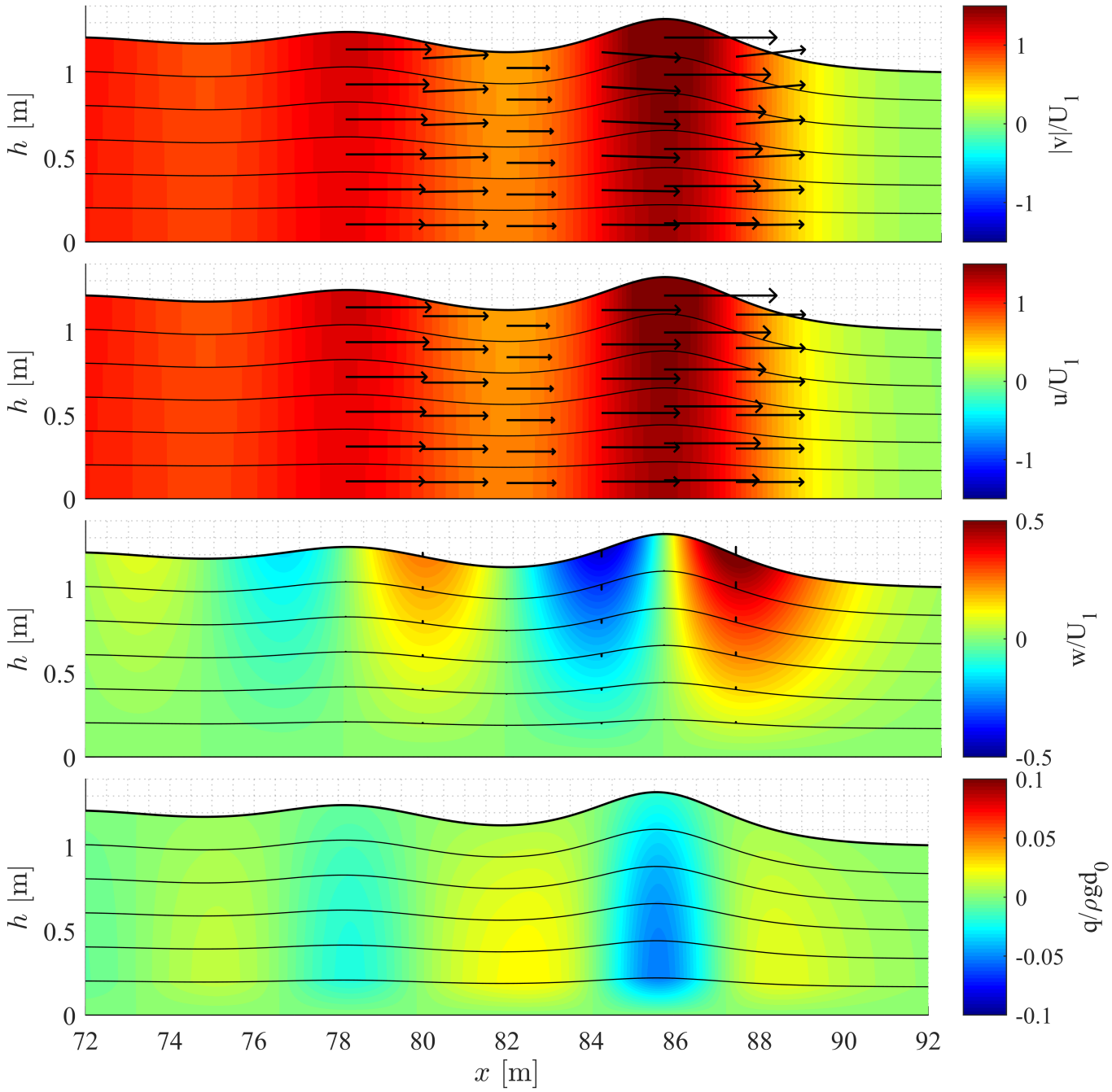

Figure H.2: Visualization of the flow in an undular bore. The following quantities are shown: (a) the total velocity magnitude in each layer, $|u| = \sqrt{u_k^2 + \overline{w_k}^2}$, normalized by the upstream velocity U_1, (b) the normalized layer-averaged horizontal velocity, u_k/U_1, (c) the vertical velocity at the layer interfaces, $w_{k\pm\frac{1}{2}}/U_1$, (d) non-hydrostatic pressure q, normalized by the initial hydrostatic pressure at the bottom $\rho g d_0$. The arrows show the relative magnitude of the horizontal and vertical velocities in the layers.

H.2.3. Energy & energy transport

Fig. H.3 shows the depth-integrated energy (top) and energy flux (bottom), for two moments in time: at $t = 28$ s, when the first undulation starts to appear; and when the wave-train more developed, at $t = t_{end} = 45$ s. The different contributions to the total energy and energy flux are shown. It is clear from the first two figures, that potential and kinetic energy are roughly equal. $E_{kin,w}$ is negligibly small[1], but not unimporant in this analysis.

[1] Near the front, where it is maximum, $E_{kin,w}$ contributes for less than 5% to E_{tot} (evaluated at the end of the simulation, when the bore is most developed).

The energy transport due to non-hydrostatic pressure, F_{nhp}, contributes significantly to the total transport due to work done by pressure ($F_{press} = F_{hp} + F_{nhp}$). Near the troughs, F_{press} is larger than the transport due to hydrostatic pressure F_{hp} only. Around the crest region, F_{hp} effectively reduces the energy transport due to pressure. Interestingly, F_{nhp} is the only contribution to the total energy flux that works against the direction of propagation.

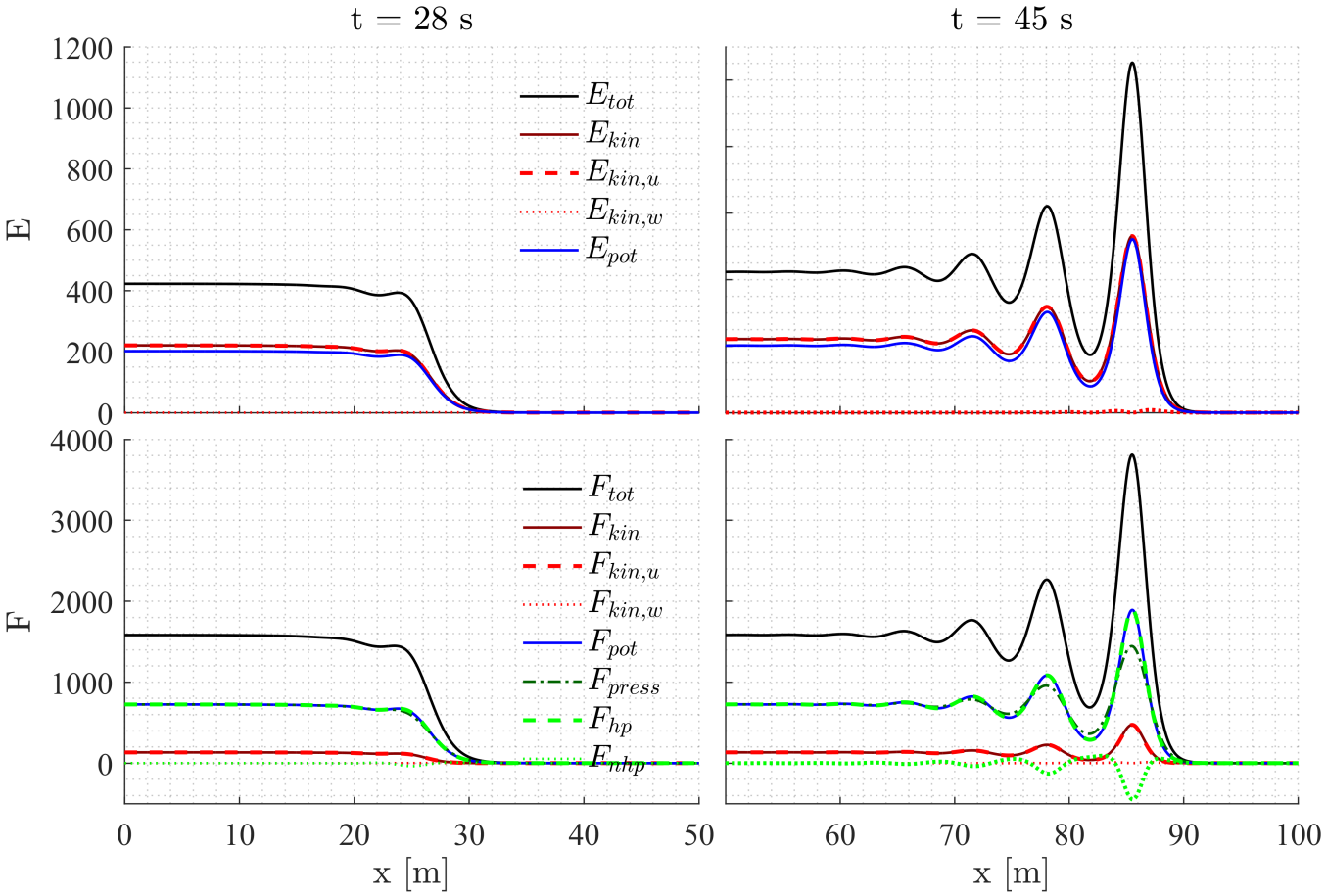

Figure H.3: Depth-integrated energy (top subplots) and energy flux (bottom subplots) as the bore travels across the domain. Both quantities are shown at two moments in time: at $t = 28$ s, when the first undulation starts to appear; and when the wave-train more developed, at $t = t_{end} = 45$ s. The total depth-integrated energy E_{tot} is decomposed in potential (E_{pot}) and kinetic energy ($E_{kin,u}$ and $E_{kin,w}$). The total energy flux is decomposed in F_{pot}, $F_{kin,u}$, $F_{kin,w}$, F_{hp} and F_{nhp} (see section H.1).

H.2.4. Energy budget

In this section we study the energy budget for a control volume surrounding the undular bore. The energy balance is given by:

$$\frac{d}{dt}\int_{x_1}^{x_2} E_{wave}\,dx + \Delta F_{wave} + D = 0 \tag{H.19}$$

The boundaries of the control volume are set at $x_1 = 0$ and $x_1 = 100$ m. We would like to known if the net influx of energy $\Delta F = F_2 - F_1$ at the boundaries x_1 and x_2 of a control volume equals the rate of change of energy $\frac{d}{dt}\int_{x_1}^{x_2} E\,dx$ in the control volume surrounding the bore region. In other words, is energy conserved ($D = 0$), or is it dissipated ($D \neq 0$). To that end, H.19 is integrated numerically.

Fig. H.4a shows both the net influx of energy and the rate of change of energy as a function of time. At all times both seem approximately equal[2], hence the undular bore dissipates little to no energy. See Fig. H.4b for a zoomed-in version. The black dash-dotted line shows the total rate of change of energy if we would neglect the contribution due to $E_{kin,w}$, as we often do for shallow water flows. The mismatch (if $E_{kin,w}$ were to be neglected) becomes larger as the undulations develop.

[2]The net energy flux does seem to be slightly decreasing in time (and so does the rate of change of energy), which is most likely due to the numerical approximations involved.

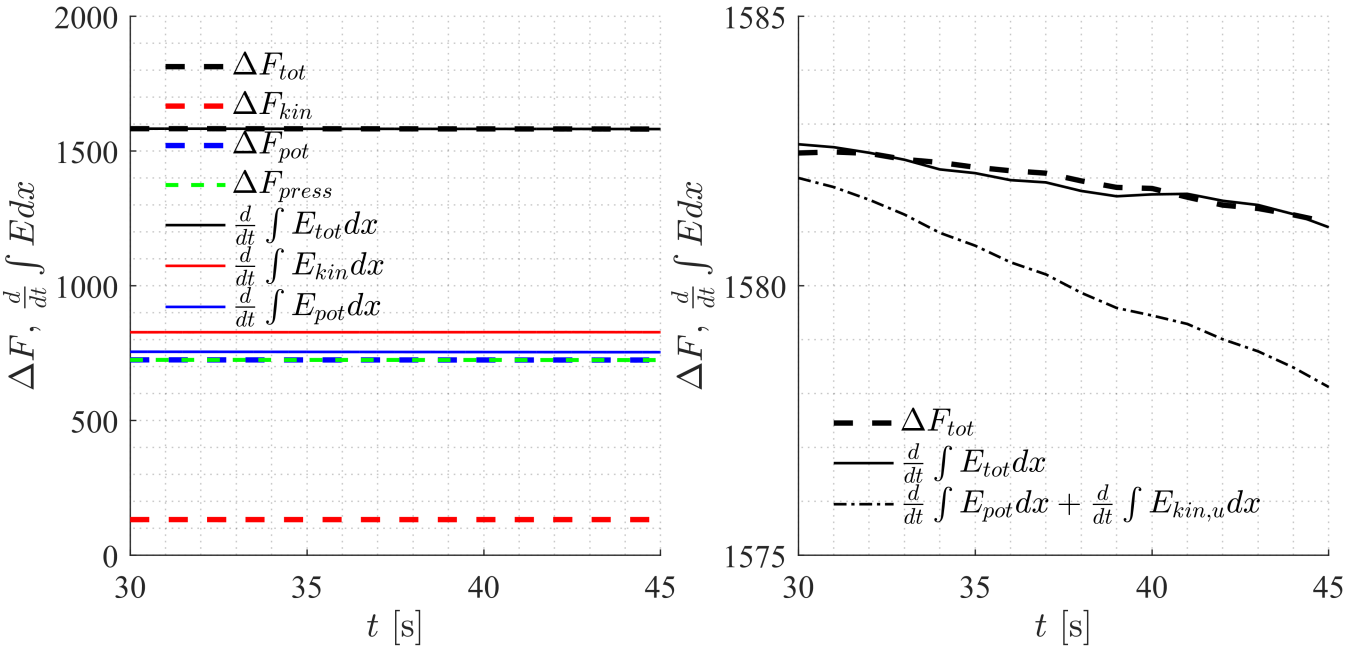

Figure H.4: Energy budget for a control volume surrounding the undular bore: (left) decomposition of the net energy flux and rate of change of energy, (right) zoomed in.